Optical control of polariton condensation

and

Dipolaritons in coupled quantum wells

Peter Cristofolini

Trinity College

Cavendish Laboratory

University of Cambridge

A thesis submitted for the degree of

Doctor of Philosophy

13th February, 2015

Abstract

Polaritons are short-lived and lightweight bosonic quasiparticles that result from the strong coupling of light with an exciton transition inside a microcavity. A sufficiently dense cloud of polaritons condenses into a single state with macroscopic coherence, a so called polariton condensate. This state of matter has superfluid properties and its non-linear dynamics are influenced by the cycle of constant pumping and decay of polaritons.

Chapters 1 and 2 give an introduction on polaritons and how they are excited, manipulated and detected in experiments, with special focus on particle and wave properties of the polariton condensate. Theoretical description of polaritons is presented in chapter 3, alongside Bose-Einstein condensation (BEC) and its peculiarities in two dimensions, followed by a section on how to simulate polariton condensates. Chapter 4 explains the optical setup and the microcavity sample. Holographic laser shaping with a spatial light modulator (SLM) is introduced, which allows to excite the microcavity with arbitrarily shaped pump geometries.

Experimental results in this thesis comprise two related topics: optical control of polariton condensates and dipolaritons, i.e. polaritons with a permanent dipole moment. Chapter 5 introduces optical blueshift trapping and phase-locking, a mechanism by which condensates synchronise their energy. The transition from phase-locked condensates to an optically trapped condensate is investigated for a configuration of N pump spots arranged on a circle of varying diameter d. Differences between these two condensate types are highlighted in the discussion. Another interesting pump geometry is presented in chapter 6: two parallel laser lines with small separation, which create a 1D waveguide with strong uniform gain. These optically guided polaritons are investigated with respect to coherence, flow speed, temperature and chemical potential both below and above the condensation threshold, posing the question whether coherence can arise simply from the geometry of the system. Finally chapter 7 is dedicated to dipolaritons which arise when a polariton strongly couples to an indirect exciton in coupled quantum wells. In this system quantum tunnelling of electrons can be controlled with a bias voltage, allowing us to tune the dipolariton properties optically and electrically, with exciting prospects for future experiments. A conclusion and outlook in chapter 8 rounds off this work.

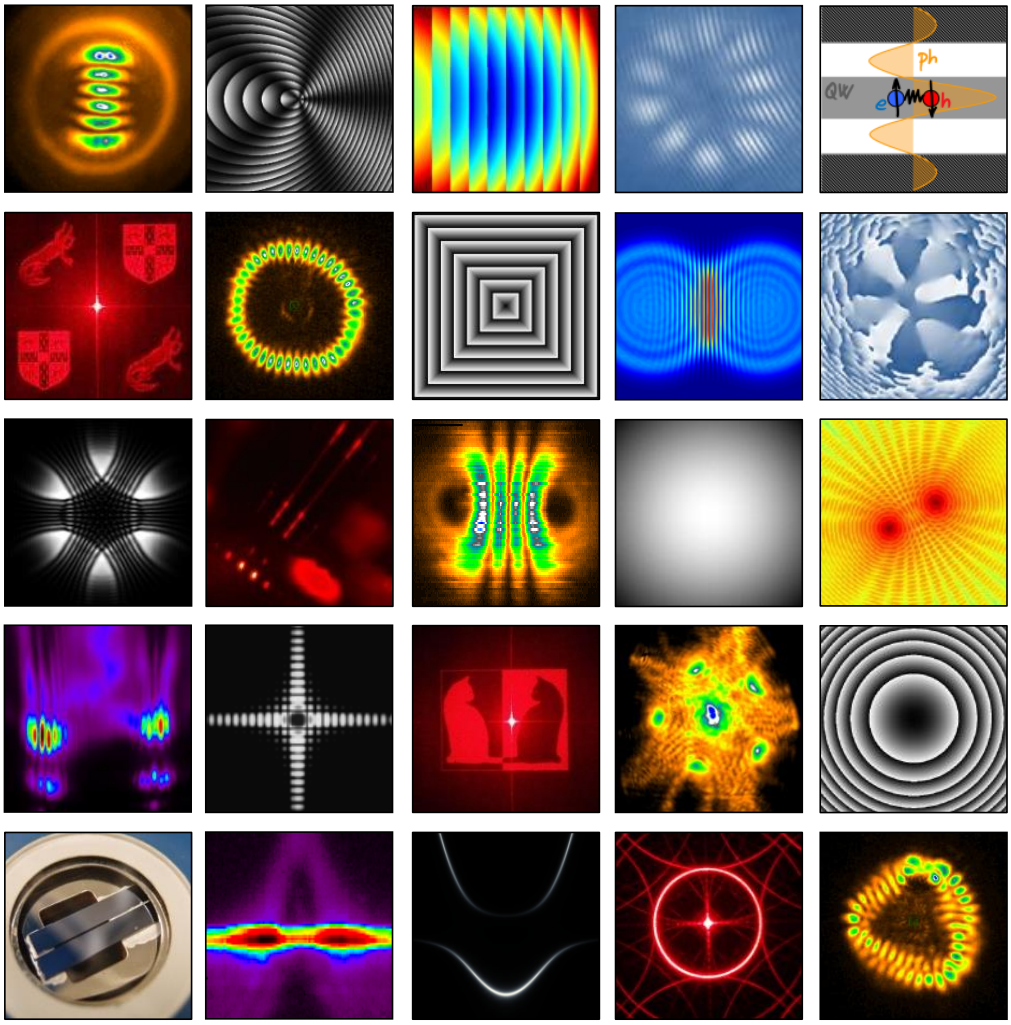
ph
QW
e
h

Contents

Declaration

This thesis is the result of my original work and a product of my own research endeavours. It contains no material which has been accepted for the award of any other degree or diploma in my name, in any university or other tertiary institution and, to the best of my knowledge and belief, contains no material previously published or written by another person, except where due reference has been made in the text. I acknowledge that copyright of published works contained within this thesis resides with the copyright holders of those works. Permission to use images of other researchers in this thesis was obtained directly from the author or from the publisher, as marked in the respective captions.

Results presented in chapters 5 and 7 were attained in close collaboration with my colleagues Alexander Dreismann and Gabriel Christmann, respectively. Some ideas for the setup presented in chapter 4 were borrowed from Guilherme Tosi's experiment. Simulations in chapter 5 (including theoretical derivation of the cGLE equation) were preformed by our collaborators Florian Pinsker, Guido Franchetti and Natasha Berloff from DAMTP at the University of Cambridge. Microcavity samples for this research and their optical characterisation were provided by the group of Pavlos Savvidis from the University of Crete. Many fruitful ideas developed in discussions with Prof. Jeremy Baumberg have shaped and influenced chapters 5 and 7. All other work is my own creation.

This thesis does not exceed the word limit of sixty thousand words, including tables, footnotes, bibliography and appendices, as set out by the Faculty of Physics and Chemistry.

Peter Cristofolini
13^{th} February, 2015

List of publications

H. Ohadi, A. Dreismann, F. Pinsker, P. Cristofolini, R. B. Balili, Z. Hatzopoulos, P. G. Savvidis, and J. J. Baumberg. **Spontaneous and long-lived antiferromagnetic coupling of exciton-polariton condensates.** *Unpublished*, 2014.

A. Dreismann, P. Cristofolini, R. Balili, G. Christmann, F. Pinsker, N. G. Berloff, Z. Hatzopoulos, P. G. Savvidis, and J. J. Baumberg. **Coupled counterrotating polariton condensates in optically defined annular potentials.** *Proceedings of the National Academy of Sciences*, 111(24):8770-8775, 2014. doi: 10.1073/pnas.1401988111.

P. Cristofolini, A. Dreismann, G. Christmann, G. Franchetti, N. G. Berloff, P. Tsotsis, Z. Hatzopoulos, P. G. Savvidis, and J. J. Baumberg. **Optical superfluid phase transitions and trapping of polariton condensates.** *Phys. Rev. Lett.*, 110(18):186403, May 2013. doi: 10.1103/PhysRevLett.110.186403.

C. Coulson, G. Christmann, P. Cristofolini, C. Grossmann, J. J. Baumberg, S. I. Tsintzos, G. Konstantinidis, Z. Hatzopoulos, and P. G. Savvidis. **Electrically controlled strong coupling and polariton bistability in double quantum wells.** *Phys. Rev. B*, 87:045311, Jan 2013. doi: 10.1103/PhysRevB.87.045311.

P. Cristofolini, G. Christmann, S. I. Tsintzos, G. Deligeorgis, G. Konstantinidis, Z. Hatzopoulos, P. G. Savvidis, and J. J. Baumberg. **Coupling quantum tunneling with cavity photons.** *Science*, 336(6082):704-707, May 2012. ISSN 1095-9203. doi: 10.1126/science.1219010.

Acknowledgements

This thesis is an account of the work performed during my PhD at the Cavendish Laboratory and it is the result of my personal interest in physics and the many people that have influenced and encouraged me along the way, from the teachers at school to my friends and colleagues at university and in the Nanophotonics group. My PhD has had its ups and downs, but overall it was a lot of fun and I have learned so many things during these four years, both scientifically and on a personal level.

Here I want to say a big thank you to all of you, first and foremost to Prof. Jeremy Baumberg, who has given me the opportunity to study physics in such a unique and historical university. Scientific research needs a stimulating environment to flourish, and the Nanophotonics group is such a special place with lots of freedom for creative and autonomous development as a researcher and as an academic, and full of enthusiastic people with interesting stories and bright ideas. The winter schools are brilliant and I have enjoyed being part of the Royal Society Summer Exhibition and other outreach activities. The electronic lab environment is very helpful to keep data and collaborations organised.

Next on my list is Gabriel Christmann, thanks for all the advice and help, without you I would have been so lost at the beginning of my PhD. Gabdalph will always be remembered and `huss` will live forever in the depths of the SLM code on "R-twopoint". Hamid Ohadi, thanks for the big improvements of the experiment setup and all the help with the thesis. Alex Dreismann, it was good fun to be your lab buddy for so long. Zoltán Vörös, I have learned a lot from you and you have tried to answer every single one of my many questions. Immo Söllner, I'm missing the times when we played our lab anthem at full blast at 1 a.m. in the dark lab!

I'm very grateful to all our collaborators, starting from the theoreticians Florian Pinsker, Natasha Berloff and Guido Franchetti who skilfully tamed the Ginzburg-Landau equations to reproduce our experiment condensates and have helped me understand the deeper connections in the physics of polariton condensates. Further

I'm thankful to everyone in the team of Pavlos Savvidis, because polariton physics is a tough world: no good sample, no condensate. I want to include Anthony, Colin and Angela here, who have resolved every problem with computers, mechanics & DIY or of administrative nature.

Christian and Lars, thanks for the unforgettable experience in Iceland and outdoors in other places, all the funny pranks and the philosophical rants on science, politics and college life. Thanks to my best friends Anna, Silvia and Jan for the company and for keeping me grounded. Cooking dinner together and playing Bang! was a lot of fun and your encouragements have helped to finish my PhD. Thanks also to everyone who has read and corrected this thesis. Finally a big thank you goes to my parents, for supporting my studies for nine years, to my brother and sister for all the adventures in the Dolomites, and to Anitha for every precious moment spent together.

Chapter 1

Preface

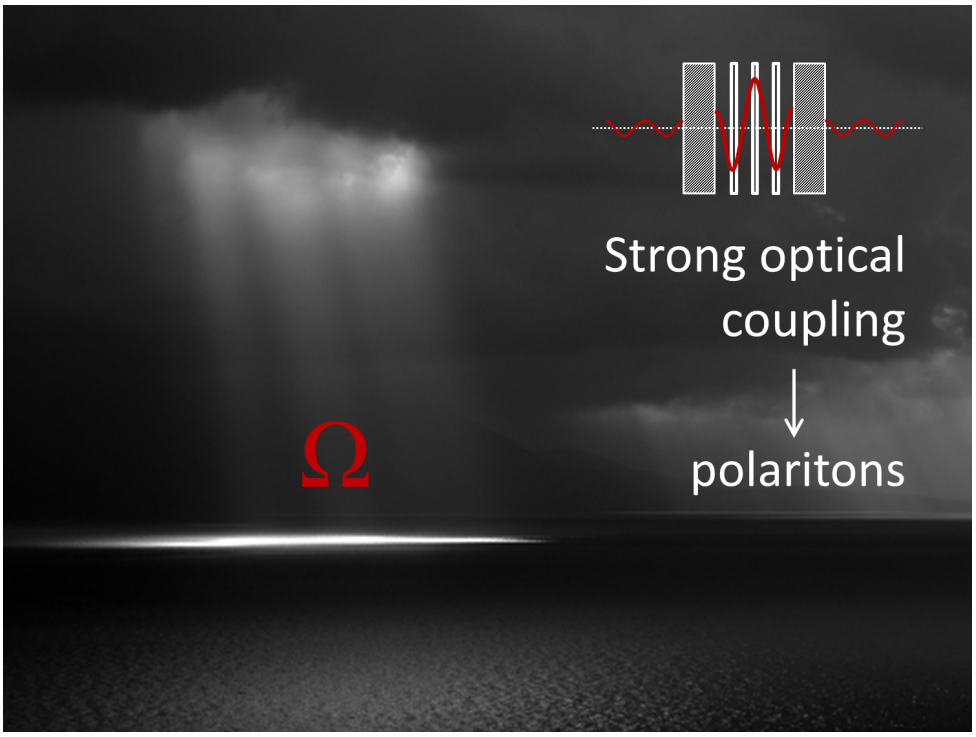

Figure 1.1: Sketch of an optical microcavity which amplifies the light field (red) to enable strong light-matter coupling, represented by the vacuum Rabi frequency Ω.

1.1 What is a polariton?

> *"A polariton is a bosonic quasiparticle resulting from strong coupling between a light mode and an exciton transition in a semiconductor material."*

This succinct and rather complicated sentence is the description of a polariton in physics. It is not easy to explain to a layman what my research is about, so most of the time I tell my friends I work with lasers (exciting!), semiconductors (ah, computers!) and liquid helium (cool!) to study

quantum physics (complicated kind of science!). This is by no means a sufficient description of the work contained in this thesis but it describes the ingredients used for my research pretty well.

A polariton is a bosonic quasiparticle[1] that has mass, momentum, lifetime, charge and spin associated to it. It is a fuzzy object, delocalised in space and hence better described in momentum space. Furthermore it shows very strong wave properties due to being so lightweight – the description as a matter wave is often more fitting than that of point-like particle. A cloud of polaritons favours populating one single energy state, with all their matter waves aligned and moving in unison. This state of matter is linked to the bosonic nature of the polariton and will be referred to as a polariton condensate throughout this thesis. Due to its quantum and wave nature, a polariton condensate shows coherence in time and space. Similar to laser light, it becomes possible to "cancel out" matter at a specific location in space by destructive interference of the probability amplitudes of two matter waves. An excellent review on polariton condensation by Deveaud-Pledrán [1] is recommended for further study.

Creating a polariton is simple: shine a laser beam of resonant wavelength onto a specially layered structure of semiconductor material, the microcavity, and the photons get absorbed and turn into polaritons. What differentiates a polariton from an exciton is the presence of strong optical coupling: while an exciton simply stores the energy received from the photon until it decays, in a polariton this energy is cycled back and forth continuously at THz-rate between the light mode (photon) and the matter excitation (exciton). Since many polaritons are involved at once in this process, it is a classical effect. In analogy to the two-level system in atom optics, this oscillation frequency is called the vacuum Rabi frequency Ω_{R}. A polariton is thus a mixed light-matter excitation. Many tricks are necessary to reach the strong coupling regime where energy cycling and hence polariton formation occurs. In addition to cryogenic cooling down temperatures of 10 K (for GaAs-based systems), many thoughts have gone into the design of the microcavity, a microscopic marvel of an optical resonator. It strongly amplifies the light between its mirrors and it is exactly matched to resonate with the excitons created in the active material by this light field. Despite all this, the polariton remains a short-lived excitation, surviving for typically 10 ps. Direct investigation of its actions requires therefore an ultra-high-speed streak camera or interferometric measurements.
After having introduced the concept of a polariton, two questions arise: why are they interesting and what can you do with them? The first question is answered below and I will present my view on the second one in the concluding chapter 8.

[1] Here a quasiparticle is an electronic excitation in the semiconductor, induced by absorbing a quantity of energy, which *behaves like a particle* in free space.

1.2 Visualising quantum mechanics

Polaritons are an interesting object of study because of the rich physical phenomena they combine. They are a manifestation of light interacting so strongly with a semiconductor that the system cannot be described by its original modes (exciton and photon). Instead two polariton modes arise, split in energy by the coupling strength of the light-matter interaction. The dual light-matter nature of polaritons gives them unusual properties: very light mass, high mobility and speed, large spatial extension and wave-like attributes. They interact with other semiconductor excitations, their spin can be easily controlled with magnetic fields and their very short lifetime implies dynamics on the picosecond scale or THz range, making them interesting for switches. Polaritons carry momentum and can interact with phonons, they can be guided by electric fields or optical potentials induced by a strong pumping laser. The beauty of polaritons lies in the ease with which they can be created and studied. All polariton dynamics are restricted to the two-dimensional world of the microcavity plane, hence the out-of plane direction offers free access for excitation beams, optical detection and direct manipulation with electric and magnetic fields. In fact, when a polariton decays into a photon, this photon carries all the information necessary to reconstruct the original state the polariton was in.

Polariton systems are well suited to study a variety of many-body phenomena in lower dimensions (2D, 1D, 0D): bosonic condensation and coherence of matter waves, thresholdless polariton lasing, semiconductor excitations including vortices and solitons, non-equilibrium physics of bosonic ensembles (polaritons decay quickly and hence require continuous pumping) and spin transport electronics, including transistors, spin gates and memories. Recently a lot of progress has been made in the development of organic semiconducting materials and in epitaxial growth techniques of conventional semiconductors, enabling polariton condensation at room temperature and allowing fabrication of much higher quality microcavities. The goal of electrical excitation of polaritons has also been solved with stable room temperature operation now being possible.

In summary, polaritons are easy to excite and very tuneable and responsive to electromagnetic signals, they can be controlled in a variety of ways and detection of changes in their quantum state is possible by optical means. The most fascinating feature of polaritons in my perspective is a more educational one. In no other physical system it is so easy to manipulate and image a macroscopic quantum object. Such a quantum object Ψ, a polariton condensate extending over 100 micrometres, glows by itself via photoluminescence emission. With a spatial light modulator the excitation beam can be modulated into any shape in real time and the condensate will adapt to fit the restrictions imposed by it. The objective of this thesis is to explore the possibilities and

limits of all-optical potentials to generate and control the propagation of polariton condensates.

This is experimenting with visual quantum mechanics and it is what this thesis primarily is about. A conventional microscope snapshot of the real space photoluminescence records the density $|\Psi|^2$, revealing wells and sinks within the condensate, while an interferometric image measures the spatial dependence of the quantum phase. A k-space picture, the far field of the photoluminescence, directly reveals most of the dynamics of the system (polariton flow velocities and directions) while a streak camera can record picosecond dynamics directly. The "digital" nature of quantum physics leaps to the eye from phase maps of polariton vortices with quantised winding number.

Chapter 2

Fundamentals

In our material system, which is based on the direct bandgap semiconductor material GaAs, polaritons are rather fragile bosonic quasiparticles that dissociate at room temperature and hence require cryogenic cooling in the experiments presented herein. Because of their exciton component, polaritons interact strongly with most kinds of excitations (other polaritons and excitons [2, 3, 4] and phonons [5, 6]), with its semiconductor environment (charges and defects [7]) and they are affected by electric [8, 9] and magnetic fields [10, 11]. Polaritons are excellent objects to study as (non-equilibrium) Bose-Einstein condensates due to their bosonic character and unusually light effective mass. While a single polariton barely survives more than a few picoseconds, constant excitation of polaritons forms stable condensate clouds with spatial coherence extending over a hundred micrometers, a very large distance for a single quantum object.

This chapter introduces the polariton in Sec. 2.1 based on the concepts of strong coupling of light and matter, and energy-momentum conservation in 2D systems. The combination of both properties allows for direct polariton state readout and imaging of quantum wavefunctions in a single shot. The planar microcavity is described in Sec. 2.2 and constitutes a miniature laser: a high quality optical resonator encloses a gain medium that is excited optically or electrically to form polaritons.
Polaritons are coherent superpositions of photons and excitons as explained by the harmonic oscillator model in Sec. 2.3. The polariton eigenmodes are introduced in Sec. 2.3.2, followed by an inspection of their properties (composition, effective mass, lifetime) and the meaning of strong coupling in Sec. 2.3.4. Mechanisms for polariton excitation and methods for detecting and studying polariton clouds and condensates are presented in Sec. 2.3.5. The following Sec. 2.3.6 lists various ways to change the polariton properties using angle, position, stress or temperature tuning, static electromagnetic fields, acoustic vibrations and surface patterning.
The intriguing concept of coherent matter with strong wave properties, i.e. the Bose-Einstein condensate, is discussed in Sec. 2.4. The implications of a condensate of polaritons, short-lived and highly interacting as opposed to inert cold atomic gases, is highlighted in Sec. 2.4.3. Finally, in Sec. 2.5, optical potentials called “blueshift potentials” are introduced, which allow to trap or set a polariton condensate in motion in a similar fashion to light in a waveguide, thus allowing us to study polariton dynamics in detail.

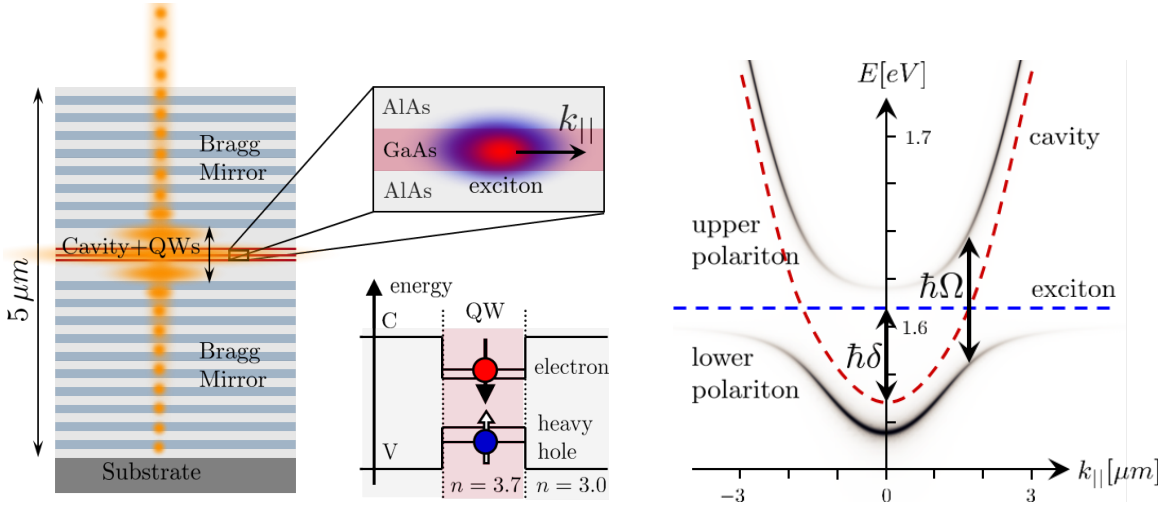

Figure 2.1: Left: Semiconductor microcavity with QWs positioned at the intensity maxima of the light mode. Inset: The exciton can move only inside the QW, its state of motion is described by the in-plane momentum $k_{||}$. Middle: Scheme of a QW, which constitutes a square potential well that traps electron and hole in the growth direction. Right: Calculated polariton dispersion curve: the strong light-matter coupling splits the two polariton modes by an energy $\hbar\Omega$ at the crossing points of exciton and photon mode. Here δ is the detuning, while the black-level and thickness of the polariton line represent the photon fraction and the polariton linewidth.

2.1 The basics

A polariton is a quasiparticle that arises when light strongly interacts with an elementary excitation in a resonant medium. The elementary excitation can be an exciton, a phonon, a surface plasmon or any other induced-dipole-carrying excitation in the medium. The polariton is thus a coherent superposition of light and matter, a bosonic quasi-particle that inherits properties from both worlds.

In a semiconductor, optical excitation can produce either free electron-hole pairs, harvested in photovoltaic solar cells or in CMOS and CCD sensors, or it can lead to the formation of excitons. Excitons are correlated electron-hole pairs[1] that travel across the crystal, bound by Coulomb interaction, similar to a positronium atom. They are the elementary electronic excitations in a semiconductor and appear as sharp peaks in the photoluminescence spectrum. An exciton can be treated as a single bosonic quasi-particle in the low density limit, when the separation between excitons is much larger than the radial extension of their wavefunction. In the case of polaritons, the matter component is usually a Wannier-Mott exciton, for which the electron wavefunction extends over many lattice sites, thus screening out the local crystal structure.

[1]Electron and hole have the same momentum, opposite charge and their wavefunctions overlap strongly.

Hence this type of exciton can be treated as a freely propagating and interacting excitation in a semiconductor with an associated energy, momentum, mass, spin and lifetime.

Excitons are polarisable, meaning they interact with electromagnetic radiation. They are usually excited optically and can decay under emission of a photon. In semiconductor microcavities (microscopic optical resonators of size comparable to the wavelength of light) two limits of exciton-light coupling are distinguished: the weak and the strong coupling regime [12] (see Sec. 2.3.4). For weak coupling the average linewidth of an exciton and a photon is larger than the coupling constant (vacuum Rabi frequency) $\frac{\gamma_\mathrm{x}+\gamma_\mathrm{c}}{2} > \Omega_\mathrm{R}$ [13] and the exciton decays in a spontaneous emission event. The microcavity can enhance or reduce this emission rate by orders of magnitude compared to the spontaneous emission rate for bulk semiconductor material. However, in the strong coupling regime the interaction (reversible energy exchange between exciton and photon) is much faster than the decay processes of either of them. Consequently the energy stored in the exciton starts to oscillate coherently back and forth between the exciton and the photon state at a rate faster than the decay rate, $\Omega_\mathrm{R} > \frac{\gamma_\mathrm{x}+\gamma_\mathrm{c}}{2}$, as observed experimentally by Jacobson et al. [14] for a single quantum well inside a microcavity. In this regime the coupling is so dominant that it becomes impossible to speak of "photon" or "exciton" – this combined matter excitation is known as a polariton, the coherent superposition of an exciton and a photon.

While polaritons do exist in bulk semiconductors[1], the system of choice to study them is the planar microcavity, which allows to study fundamental light-matter interactions in the strong coupling regime in a two dimensional solid state system. Microcavities are essentially a pair of highly reflective planar mirrors for light (DBRs, Sec. 2.2), separated by about one wavelength of visible light and with one or many layers of active material sandwiched in between. The resulting optical resonator restricts the photon wavevector k_z to quantised values in the out-of-plane direction, in addition to greatly amplifying the intensity of the light within the resonator. The quantum well (QW), the thin layer of active (semiconductor) material, constitutes a tight potential well in the band structure for electrons and holes, and traps excitons within its 2D plane.

All the dynamics of exciton and photon are hence restricted to a two-dimensional plane with particle motions described by the so-called in-plane momentum $k_{||}$ (also called "k-parallel", see Fig. 2.2). This leaves the out-of-plane dimension z free for optical and electrical access, to excite and study the behaviour of polaritons. In terms of physics, a QW exciton inside a microcav-

[1] Bulk polaritons without microcavity have a photon-like linear dispersion curve of the lower polariton. Momentum conservation implies a full match of the $\vec{k}$ vectors of photon and exciton [15] - consequently strong optical coupling is much harder to achieve in bulk semiconductor.

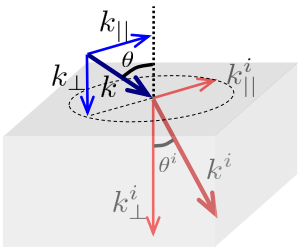

in-plane momentum

$$k^i_{||} = \frac{n_i\,\omega_{ph}}{c}\sin\theta_i$$

Figure 2.2: The in-plane momentum of photon, exciton or polariton is conserved in each layer of the microcavity (Snell's law).

ity is a somewhat "messy" (continuum of excited states, interactions with the semiconductor lattice, weak binding energy, continuous pumping negates quasiparticle conservation) but also richer analogue of the neat two-level system of an atom in an optical resonator in atomic physics.

A very important quantity in the microcavity system is the in-plane momentum $k_{||} = \sqrt{k_x^2 + k_y^2}$ of the polariton, the projection of the photon momentum $\vec{k}$ onto the quantum well plane (Fig. 2.2). Due to momentum conservation only $k_\perp$ changes at interfaces and a photon with in-plane momentum $k_{||}$ can only couple to an exciton state with identical $k_{||}$. This coupling results in a polariton with the same in-plane momentum and angular momentum as the photon. This one-to-one correspondence $k_{||,\mathrm{pol}} \leftrightarrow \{\omega, \theta\}_{\mathrm{ph}}$ makes it possible to retrieve the polariton momentum through examination of the photon that was created when the polariton decayed. Thus, $k_{||} = \frac{2\pi n}{\lambda_0}\sin\theta$ is a conserved quantity since it remains the same value regardless of the medium through which the photon travels (Snell's law). Energy is conserved in a similar way: the photon frequency ω is fully set by the transition energy of the polariton state. Hence, the photon escaping from the microcavity carries valuable information about the polariton state, which allows one to study the polariton dynamics inside the resonator. In reality, due to the finite linewidth of the exciton and the photon, a slight mismatch in the energy-momentum conservation is allowed.

Microcavity exciton-polaritons, from here on simply called polaritons, are uncharged composite bosons in 2D that freely move across the crystal (in the absence of strong sample disorder), carrying energy E, momentum $p = \hbar k_{||}$ and one quantum of angular momentum $s = \pm\hbar$, known as polariton spin. The state of a polariton can be reconstructed from the three quantities $\{E, k_{||}, s\}$. By recording angle-resolved photoluminescence or reflection spectra it is possible to directly measure the full dispersion curve of polaritons (Fig. 2.1 right), from which a multitude of important parameters can be deduced: effective mass, density of states, photon-to-exciton fraction, coupling strength, detuning and coherence.

Polariton experiments are ideal to study fundamental quantum physics properties like long-range matter coherence [16, 17, 18] and superfluid flow dynamics [7, 19, 20] in a relatively simple and easily accessible system. Due to their very low mass m^* condensation of polaritons occurs standard cryogenic temperatures and recently even at room temperature [21, 22]. In contrast to atomic quantum gases, polariton-based systems are not in thermal equilibrium: they have to be constantly pumped, optically or electrically, because the decay of polaritons will provide a steady stream of photoluminescence (PL) light. The correspondence $\{\omega, \theta\}_{\mathrm{ph}} \leftrightarrow k_{||,\mathrm{pol}}$ entails that a simple PL image records the squared wavefunction $|\Psi(\vec{x})|^2$ of a polariton condensate, while an interferometer allows detecting singularities or discontinuities in its phase, to study quantised vortices [23, 24] and solitons [25].

The out-of-plane direction of the microcavity can be used to introduce perpendicular electric or magnetic fields into this 2D polariton world. Two QWs stacked on top of each other, separated by a thin layer of semiconductor material, form a coupled quantum well system. The coupling is mediated by quantum tunnelling of electrons or holes through the thin spacer layer. In such a system selective electron tunnelling can be combined with strong coupling to the microcavity mode, leading to the formation of "dipolaritons" [8]. These new quasiparticles possess an intrinsic static dipole moment pointing out of the QW plane, whose magnitude can be controlled directly with an electric field, with interesting physical properties, as shown in chapter 7.

2.2 Microcavity design and sample fabrication

A typical high quality GaAs Fabry-Pérot microcavity, as used in the experiments presented in this thesis, consist of a highly reflective bottom and top thin-film mirror. A cavity layer containing multiple QWs, the active gain medium of the microcavity, is sandwiched in between the two mirrors. All semiconductor materials apart from the substrate have to be transparent at the resonance wavelength of the microcavity. Microcavities are grown in ultra-high vacuum chambers by atomic vapour deposition with a technique called molecular beam epitaxy (MBE). Typically $\sim$ 100 layers of semiconductor have to be grown on top of each other at very low deposition rate to ensure a highly regular crystalline structure of each layer, thus requiring 12 or more hours to fabricate. The deposited semiconductor materials have to be strain matched[1], that is their lattice constants should be nearly identical to avoid dislocations due to build-up of strain when two materials with different lattice constant are grown on top of each other. This

[1]There is a residual 0.13% difference in the lattice constant of GaAs and AlAs, resulting in some residual strain.

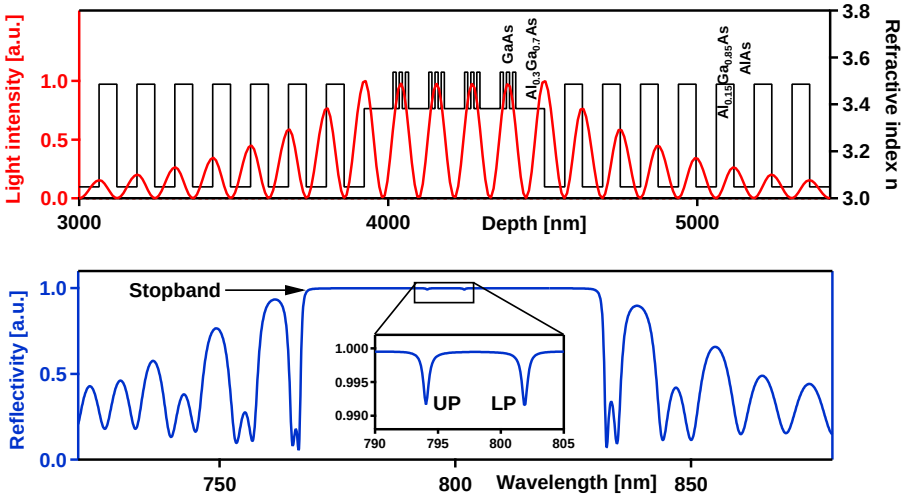

Figure 2.3: Top: Refractive index profile of the central part of the microcavity with the top and bottom DBR mirrors (left and right) and the $\frac{5}{2}\lambda_c$ cavity with 4 sets of 3 QWs. The red line depicts the light field intensity inside the microcavity. Bottom: Calculated microcavity reflectivity spectrum. Inset shows the upper and lower polariton mode. Image courtesy of Pavlos Savvidis.

problem is particularly prominent in multilayer structures like microcavities.

The reflected and transmitted electric field of a microcavity can be calculated using transfer matrix formalism with boundary conditions [26] or an impedance matching method [27] which is suitable also for out-of-plane waveguide modes as produced by gratings. Fig. 2.3 presents the refractive index profile and the light field inside the microcavity studied in this thesis, calculated with the impedance matching method. The bottom graph presents the simulated reflection spectrum with the two polariton dips (inset in bottom graph of Fig. 2.3).

The microcavity mirror, called **distributed Bragg reflector (DBR)**, is a stack of $20-35$ pairs of semiconductor material with a distinct refractive index contrast $\Delta n \sim 0.1-0.2$. Each layer in the DBR has an optical thickness of $n_i d_i = \frac{\lambda_c}{4}$ where d_i is the thickness of the layer i and λ_c is the design wavelength of the microcavity in vacuum. This means the mirrors have a period of half a wavelength, which is the condition for constructive thin film interference in reflection at normal incidence, just as for multilayer reflection coatings on dielectric mirrors. Due to the small refractive index contrast Δn a large number of layer pairs is necessary to fabricate highly reflective mirrors of $R > 99.8\%$, which are necessary to reach quality factors $Q \sim 16000$ that allow polariton condensation in GaAs-based microcavities.
Two such highly reflective mirrors separated by a spacer layer of optical thickness $m\frac{\lambda_c}{2}$, m being

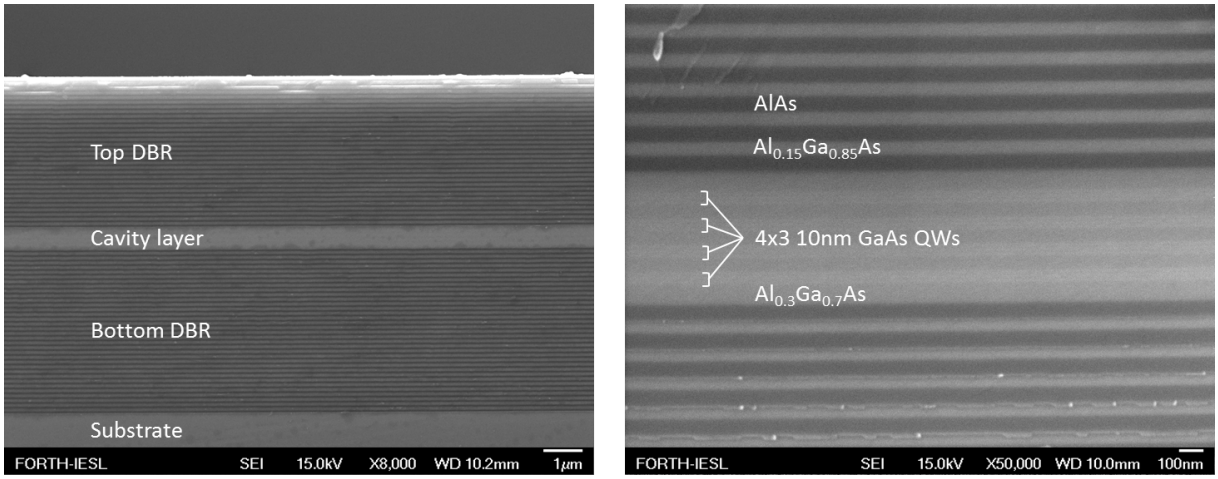

Figure 2.4: Left: SEM image of the microcavity cross section. The flatness of various layers is impressive, although small defects start to appear at the top end of the DBR. Right: Magnified view of the cavity layer with its 4×3 QWs positioned at the field antinodes. Image courtesy of Pavlos Savvidis.

an integer, form a highly selective filter. Via destructive interference of the reflections off both mirrors, a wide stopband with a very sharp transmission resonance, the cavity mode C, appears in the transmission spectrum. The top mirror is intentionally less reflective, so that most photons exit through the upper side of the microcavity, rather than being absorbed by the substrate.

For a Fabry Pérot cavity, the spacing of the mirrors L_c has to be an integer multiple m of the resonance wavelength $\lambda_{\text{FP}} = 2n_\mathsf{c}L_\mathsf{c}\cos\theta/m$ with n_c the refractive index of the medium between the mirrors and θ the incidence angle of the light inside the cavity. While this condition still holds for planar microcavities, the exact thickness of the cavity layer is less important since the cavity resonance wavelength is a weighted average $\lambda_\mathsf{c} = (1-\alpha)\lambda_{\text{DBR}} + \alpha\lambda_{\text{FP}}$ of the stopband wavelength λ_{DBR}, determined by the DBR period, and the Fabry-Pérot resonance of the cavity layer λ_{FP}, with typically $\alpha \ll 1$ [28].
The number of "antinodes" (maxima of the light field) inside the cavity layer depends on the layer pair arrangement in the DBRs: there are m or $m-1$ antinodes, spaced by a distance $\frac{\lambda_\mathsf{c}}{2}$. Our microcavity is of thickness $\frac{5}{2}\lambda_\mathsf{c}$ which has the advantage that 4 sets of 3 QW per antinode can be fitted to ensure strong coupling of the photon to the exciton mode. For N QWs the light-matter coupling is enhanced by a factor $\sqrt{\text{N}}$ [29] (Eq. 2.4).

A **quantum well (QW)** is a few nanometre-thick slab of semiconductor with a conduction band lower and a valence band higher in energy than any of the surrounding layers, so that the

QW bandgap is fully within the bandgap energy range of any other layer of the microcavity (Fig. 2.1 middle and Fig. 2.3 top). QWs are essentially two-dimensional square potential wells that trap excitons in the maxima of the cavity light field. The bandgap, or more precisely the exciton transition energy of the QW material, is matched to be equal to the resonance frequency ω_{C} of the microcavity (Eq. 2.25) to enable strong coupling between excitons and photons. The small QW thickness $d_{\mathrm{QW}} \sim 10$ nm entails a confinement in the z-direction tight enough to ensure quantised energy levels, that is the level separation is larger than the (broadened) linewidth of the quantum state (the thermal energy $k_{\mathrm{B}}T$). In this picture the exciton can be viewed as a 2D version of a hydrogen-like atom, with discrete energy levels, lower binding energy and travelling only in the QW plane. The quantised motion out of the QW plane is frozen out because of the large energy spacing of the levels compared to the exciton kinetic and thermal energy.
QW excitons have a higher binding energy (13 meV for a typical 10 nm GaAs QW [30]) than bulk excitons due to better overlap of electron and hole wavefunctions. The QW width can be chosen freely within limits but the spacing between QWs should be substantially thick to prevent quantum tunnelling of electrons between them. Wide QWs show lower binding energy and level spacing, approaching the bulk values. In very narrow QWs linewidth broadening due to well width disorder is a problem. Furthermore the first exciton level is close in energy to the conduction band of the cavity spacing layer, thus reducing the binding energy due to increased leakage of the exciton wavefunction into adjacent spacer layers. To ensure the highest possible coupling strength Ω_{R} special care has to be taken to make all of the QWs of equal thickness and with minimal surface roughness.

2.3 Microcavity polariton - a coherent superposition of light and matter

In a microcavity light is trapped between the two DBR mirrors for a few picoseconds. The intensity of the light field becomes high enough to amplify the dipole interaction of the photon with the exciton (both have the same momentum $k_{||}$) to values that reach the strong coupling regime (see Sec. 2.3.4). At this point the two original modes of the system (red lines in Fig. 2.5) couple strongly and an avoided crossing with energy splitting $\hbar\Omega_{\mathrm{R}}$ becomes visible at the intersection of the photon with the exciton line. The dispersion curve of the system now shows two coupled resonance lines (black solid lines in Fig. 2.5) that tune with the emission angle θ (i.e. with $k_{||}$) and with the cavity detuning δ_{C}. These new eigenmodes are the upper (UP) and the lower (LP) polariton mode, a coherent mixture (superposition) of the exciton (X) and the microcavity photon (C).

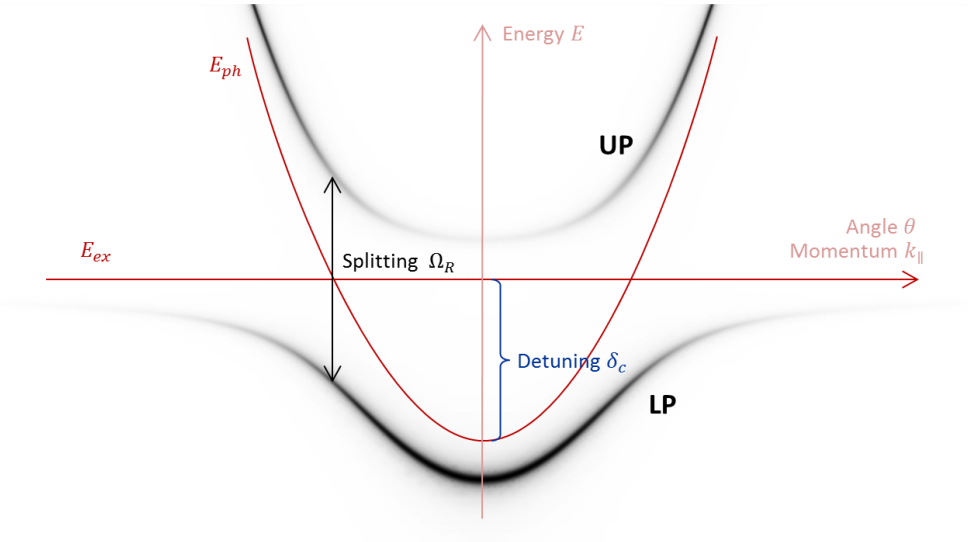

Figure 2.5: Angle-dependent dispersion of the upper (UP) and lower (LP) polariton branch with exciton and photon mode (red lines). The grey scale codes the photon fraction of the polariton, Ω_R is the full Rabi splitting between the two polariton modes at the crossing point of exciton and photon, δ_C if the detuning of the cavity with respect to the exciton line at $k_{||} = 0$.

2.3.1 Coupled oscillator model

A very simple but instructive way to describe polaritons is the coupled oscillator model, which treats both the exciton X and the cavity photon C as a harmonic oscillator with resonance energies $E_\mathsf{x} = \hbar(\omega_\mathsf{x} - i\gamma_\mathsf{x})$ and $E_\mathsf{c} = \hbar(\omega_\mathsf{c} - i\gamma_\mathsf{c})$ that are coupled by the coupling constant Ω_R. Despite its simplicity this analytical model explains most of the striking properties of polaritons. In matrix notation, in the basis $\{|\mathsf{X}\rangle, |\mathsf{C}\rangle\}$ of the exciton and the cavity mode, the (non-Hermitian) Hamiltonian can be written as

$$H = \hbar \begin{pmatrix} \omega_\mathsf{x} - i\gamma_\mathsf{x} & -\Omega_\mathrm{R}/2 \\ -\Omega_\mathrm{R}/2 & \hbar\omega_\mathsf{c} - i\gamma_\mathsf{c} \end{pmatrix} \qquad \text{coupled oscillator model} \tag{2.1}$$

Solving for the normal modes of this matrix one obtains the energies of the upper and lower polariton and their exciton and photon fraction. The model presented here is rather simple; more detailed theoretical descriptions (TE/TM splitting, coupled microcavities) can be found in [3, 28].

Cavity and Exciton Dispersion

In semiconductor theory excitons in a QW are described in the effective mass approximation as two dimensional electronic excitations with dispersion

$$\begin{aligned} \mathsf{Re}[E_{\mathsf{x}}(k_{||})] &= E_g - E_{\mathrm{B}}^{\mathrm{2D}} + \frac{\hbar^2 k_{||}^2}{2m_{\mathsf{x}}^{\mathrm{2D}}} \qquad \text{exciton energy} \\ \mathsf{Im}[E_{\mathsf{x}}(k_{||})] &= \hbar\gamma_{\mathsf{x}} = \frac{h}{\tau_{\mathsf{x}}} \end{aligned} \tag{2.2}$$

where E_g is the gap energy of the QW material, $m_{\mathsf{x}}^{\mathrm{2D}}$ is the in-plane effective mass of the QW exciton and $E_{\mathrm{B}}^{\mathrm{2D}}$ is its binding energy, caused by Coulomb attraction of the electron and the hole, and enhanced due to the tight exciton confinement in the QW [31]. From emission spectra of our microcavity we have obtained $E_g - E_{\mathrm{B}}^{\mathrm{2D}} = 1.553$ eV and $h/\tau_{\mathsf{x}} \approx 1$ meV. The last term proportional to $k_{||}^2$ is the kinetic energy of the exciton and describes its motion in the microcavity plane as a free particle with effective mass $m_{\mathsf{x}}^{\mathrm{2D}}$.

The cavity dispersion is imposed by the resonance condition of the mirrors and constitutes, compared to the small curvature of the exciton parabola, a very steep hyperbola

$$\begin{aligned} \mathsf{Re}[E_{\mathsf{c}}(k_{||})] &= \hbar c\sqrt{k_{\perp}^2 + k_{||}^2} \approx E_{\mathsf{c}}(0) + \frac{\hbar^2 k_{||}^2}{2m_{\mathsf{c}}^*} \qquad \text{photon energy} \\ \mathsf{Im}[E_{\mathsf{c}}(k_{||})] &= \gamma_{\mathsf{c}}(k_{||}) \approx \frac{h}{\tau_{\mathsf{c}}(k_{||})} \end{aligned} \tag{2.3}$$

where $k_{||}$ is connected to the angle of incidence of the photon through Fig. 2.2, $m_{\mathsf{c}}^* = 3.6{\cdot}10^{-35}$ kg is the mass of the microcavity photon of Eq. 2.24 and $E_{\mathsf{c}}(0) = 1.544$ eV, $\tau_{\mathsf{c}} \approx 7$ ps is the cavity photon lifetime (the last two parameters depend on the cavity detuning δ_{c} and the angle θ). The approximation on the right hand side of Eq. 2.3 is valid for angles $\theta < 45°$, so for the whole light cone permitted by the microcavity. Because of the small curvature of the exciton dispersion in the region of interest, around the centre of the cavity mode, the exciton energy can safely be treated as $k_{||} = 0$, so that the kinetic energy term in Eq. 2.2 is neglected.

Induced dipole Coupling

Light inside the microcavity with energy $hc/\lambda_0 > E_{\mathsf{x}}$ can be absorbed by the QW material, thereby forming excitons. The coupling between the two harmonic oscillators, the exciton X and microcavity photon C, is due to the polarisability of the exciton (induced dipole-coupling),

described by the coupling constant[1] Ω_R [28, 29]

$$\frac{\Omega_\mathrm{R}}{2} = \sqrt{\frac{e^2 f_{\mathrm{osc,x}} N_\mathrm{QW}}{2\varepsilon_0 n_\mathrm{eff}^2 m_\mathsf{x}^\mathrm{2D} L_\mathrm{eff}}} \qquad \text{Rabi frequency dependence} \tag{2.4}$$

where e is the electron charge, $f_{\mathrm{osc,x}} N_\mathrm{QW}$ is the total oscillator strength for N_QW identical QWs, n_eff is the effective cavity layer refractive index and ε_0 is the vacuum permittivity. The oscillator strength contains the dipole matrix element for the exciton transition between the valence band state $|v\rangle$ and the conduction band state $|c\rangle$: $f_{\mathrm{osc,x}} \propto |\langle c|e\,\vec{x}_\mathsf{x} \cdot \vec{E}_\mathsf{C}|v\rangle|^2$, $e\vec{x}_\mathsf{x}$ is the induced exciton dipole moment and $\vec{E}_\mathsf{C}$ is the electric field vector of the light mode inside the microcavity. Eq. 2.4 shows that in order to achieve strong coupling it is necessary to fabricate microcavities with large number of QWs, large oscillator strength and small cavity size, that means putting multiple QWs per antinode of the intracavity light field. The measured full splitting of our microcavity is $\hbar\Omega_\mathrm{R} = 9$ meV.

2.3.2 Polariton eigenmodes

The characteristic equation of the Hamiltonian matrix in Eq. 2.1 is

$$(\omega - \omega_\mathsf{x} + i\gamma_\mathsf{x})(\omega - \omega_\mathsf{c} + i\gamma_\mathsf{c}) = \frac{\Omega_\mathrm{R}^2}{4} \qquad \text{characteristic polynomial} \tag{2.5}$$

and its roots are the eigenenergies[2] of the two polariton modes

$$E_{\substack{\mathsf{UP}\\\mathsf{LP}}} = \hbar\left(\tilde{\omega}_k \pm \tfrac{1}{2}\sqrt{\tilde{\delta}_k^2 + \Omega_\mathrm{R}^2}\right) \qquad \text{polariton energies} \tag{2.6}$$

$$\tilde{\omega}_k = \tfrac{1}{2}[\omega_{\mathsf{c},\mathrm{k}} + \omega_\mathsf{x} - i(\gamma_{\mathsf{c},\mathrm{k}} + \gamma_\mathsf{x})] \tag{2.7}$$

$$\tilde{\delta}_k = \omega_{\mathsf{c},\mathrm{k}} - \omega_\mathsf{x} - i(\gamma_{\mathsf{c},\mathrm{k}} - \gamma_\mathsf{x}) \tag{2.8}$$

where $\hbar\tilde{\omega}_k$ is the average energy and $\tilde{\delta}_k$ is the detuning of the cavity mode from the exciton mode. The index $...k$ denotes quantities that depend on the in-plane momentum $k_{||}$. The eigenvectors, the lower (LP) and upper (UP) polariton, can be written conveniently in the form

$$|\mathsf{UP}\rangle = C_{\mathsf{c},\mathrm{k}}\,|\mathsf{X}\rangle - C_{\mathsf{x},\mathrm{k}}\,|\mathsf{C}\rangle \qquad \text{upper polariton} \tag{2.9}$$

$$|\mathsf{LP}\rangle = C_{\mathsf{x},\mathrm{k}}\,|\mathsf{X}\rangle + C_{\mathsf{c},\mathrm{k}}\,|\mathsf{C}\rangle \qquad \text{lower polariton} \tag{2.10}$$

[1] The dependence of Ω_R and L_eff on the light polarisation and the angle of the cavity mode θ are neglected here but can be found in [28].

[2] Simpler but less compact formulae for eigenenergies and eigenvectors can be found in [3, 32].

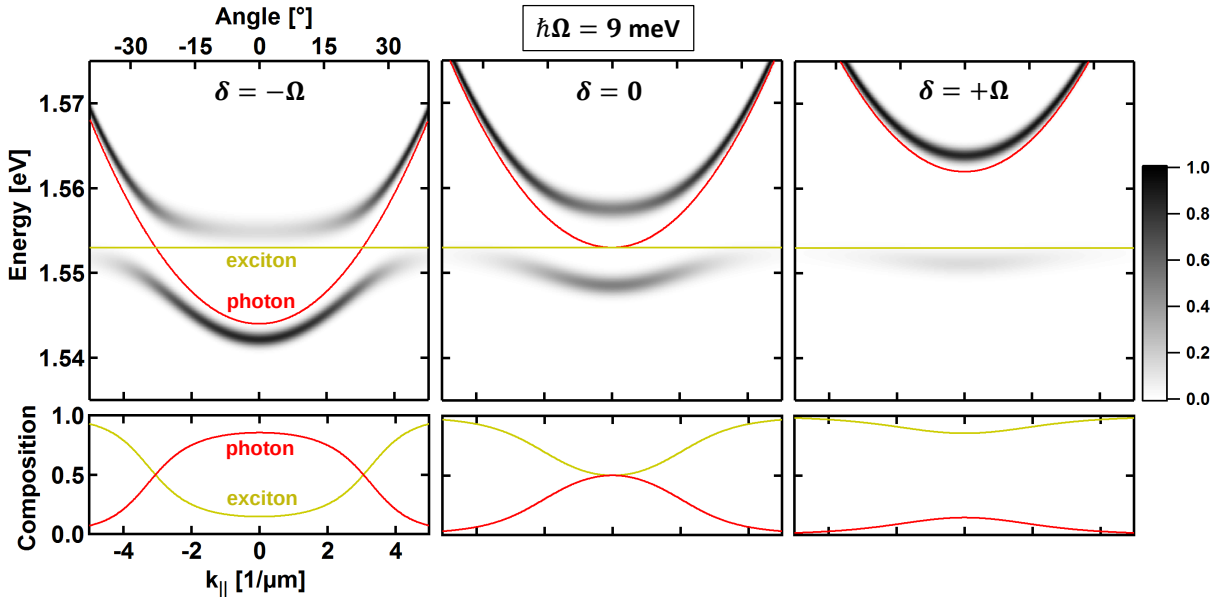

Figure 2.6: Dispersion relation of the LP and UP branch for negative, zero and positive detuning δ_c. The lower row shows the composition of the LP. The grey-scale codes the photon fraction and the line thickness represent the linewidth of the polariton. Experiments presented in this thesis where performed with strong negative detuning as depicted in the left column. Simulation parameters: $E_x = 1.553$ eV, $m_c = 3.6 \cdot 10^{-35}$ kg, $\hbar\Omega_R = 9$ meV; linewidths $\gamma_x = 1$ meV, $\gamma_c = 0.5$ meV

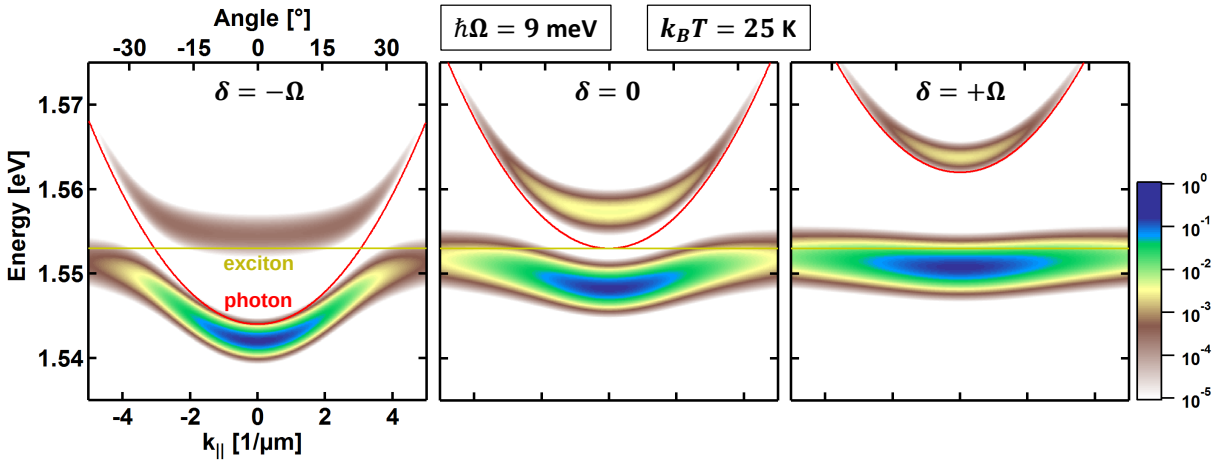

Figure 2.7: Difference between reflection spectroscopy (Fig. 2.6) and PL emission intensity (shown in logarithmic colour scale in this graph). Same parameters as in Fig. 2.6, with the intensity multiplied by a Boltzmann factor $\exp\left[\frac{E-E_c(k_{||}=0)}{k_B T}\right]$ with $T = 25$ K. It can be seen that the UP branch is three orders of magnitude more faint than the LP emission for $\delta_c = -\Omega_R$.

whereby $|C_{\mathrm{x,k}}|^2 + |C_{\mathrm{c,k}}|^2 = 1$. All physical properties of these polaritons are governed by the Hopfield coefficients $|C_{\mathrm{x,k}}|^2$ and $|C_{\mathrm{c,k}}|^2$, which describe the exciton and photon content of the LP and vice versa for the UP. They depend on Ω_{R} and $\tilde{\delta}_k$ [33]

$$C_{\mathrm{c,k}} = \sin\frac{\phi_k}{2} = \sqrt{\frac{\Delta_k - \tilde{\delta}_k}{2\Delta_k}} \equiv \frac{\Omega_{\mathrm{R}}}{\sqrt{2\Delta_k(\Delta_k + \tilde{\delta}_k)}} \qquad \text{photon coefficient} \tag{2.11}$$

$$C_{\mathrm{x,k}} = \cos\frac{\phi_k}{2} = \sqrt{\frac{\Delta_k + \tilde{\delta}_k}{2\Delta_k}} \equiv \frac{\Omega_{\mathrm{R}}}{\sqrt{2\Delta_k(\Delta_k - \tilde{\delta}_k)}} \qquad \text{exciton coefficient} \tag{2.12}$$

with the effective splitting $\Delta_k = \sqrt{\Omega_{\mathrm{R}}^2 + \tilde{\delta}_k^2}$ and the mixing angle ϕ defined by $\tan\phi_k = \Omega_{\mathrm{R}}/\tilde{\delta}_k$. With the detuning $\tilde{\delta}_k$ the polariton properties can be controlled, e.g. for the LP at $k_{||} \approx 0$ from exciton-like at $\tilde{\delta}_k \to \infty$ to photon-like at $\tilde{\delta}_k \to -\infty$.

$\tilde{\delta}_k$	ϕ	$\lvert C_{\mathrm{x,k}}\rvert^2$	$\lvert C_{\mathrm{c,k}}\rvert^2$	detuning
$+\infty$	0	1	0	$\omega_{\mathsf{c},k} > \omega_{\mathsf{x}}$
0	$\pi/2$	1/2	1/2	$\omega_{\mathsf{c},k} = \omega_{\mathsf{x}}$
$-\infty$	π	0	1	$\omega_{\mathsf{c},k} < \omega_{\mathsf{x}}$

A simulation of the coupling between the exciton mode X and the microcavity mode C is shown in Fig. 2.6 for negative, zero and positive detuning of the cavity mode. In the left column the LP is highly photonic at $k_{||} = 0$ (normal conditions for the experiments presented in this thesis) as shown in the composition graph ($\tilde{\delta}_k = -\infty$). At the crossing point of the exciton and photon mode at 23° polaritons are half light, half exciton. Finally, at very high $k_{||}$ the polariton are predominantly excitonic ($\tilde{\delta}_k = \infty$) and hence their PL emission is very weak.

2.3.3 Polariton lifetime and effective mass

Excitons and photons have physical properties like mass, lifetime, speed, interaction strength and wavefunction size that differ by orders of magnitude between the two entities. A polariton is a mixed light-matter particle and hence its character is strongly dependent on the weight of the two constituents, $|C_{\mathrm{x,k}}|^2$ and $|C_{\mathrm{c,k}}|^2$. The dispersion curve (Eq. 2.6 and Fig. 2.6) is a very important relation in polariton physics that depicts the dependence of the polariton branches $E_{\mathsf{LP}}, E_{\mathsf{UP}}$ on the in-plane momentum $k_{||}$. It is measured by tracking the shift of the polariton dips/peaks in the reflection/photoluminescence spectrum with collection angle θ. Through fitting with the model in Eq. 2.1 important quantities like the polariton composition, the coupling strength Ω_{R}, the cavity detuning δ_{c} and the exciton energy in the QW can be retrieved. The effective mass

is inversely proportional to the curvature of the dispersion curve

$$M_{ij}^{-1} = \frac{1}{\hbar^2}\frac{d^2E(\mathbf{k})}{dk_i\,dk_j} \quad \xrightarrow[\text{crystal}]{\text{isotropic}} \quad m^*_{\text{pol}} = \hbar^2\left[\frac{d^2}{dk_{||}^2}E_{\text{pol}}(k_{||})\right]^{-1} \tag{2.13}$$

The large curvature of the cavity mode results in an extraordinarily small effective mass of the polariton for states close to the centre of the Brillouin zone, where its photonic component is large. In fact the LP mass is $10^4 - 10^5$ times lighter than an exciton and about 10^9 times lighter than a Rb atom, making it very interesting for condensation at room temperature. Around the minimum of the dispersion curve, for low momenta $k_{||} \ll k_z$, the energy-momentum relation of the polariton can be approximated by a constant term with the common quadratic form of the kinetic energy

$$E_{\mathsf{LP/UP}}(k_{||}) = E_{\mathsf{LP/UP}}(0) + \frac{\hbar^2 k_{||}^2}{2m^*_{\mathsf{LP/UP}}} \qquad \text{polariton kinetic energy} \tag{2.14}$$

The polariton effective mass for $k_{||} \ll k_z$ is the weighted mean of the mass of the exciton and the photon components [32]

$$m^*_{\mathsf{LP}} = \left(\frac{|C_{\mathsf{x,k}}|^2}{m^{2\text{D}}_{\mathsf{x}}} + \frac{|C_{\mathsf{c,k}}|^2}{m^*_{\mathsf{c}}}\right)^{-1} \approx \frac{m^*_{\mathsf{c}}}{|C_{\mathsf{c,k}}|^2} \qquad \text{LP effective mass} \tag{2.15}$$

$$m^*_{\mathsf{UP}} = \left(\frac{|C_{\mathsf{c,k}}|^2}{m^{2\text{D}}_{\mathsf{x}}} + \frac{|C_{\mathsf{x,k}}|^2}{m^*_{\mathsf{c}}}\right)^{-1} \approx \frac{m^*_{\mathsf{c}}}{|C_{\mathsf{x,k}}|^2} \qquad \text{UP effective mass} \tag{2.16}$$

where the approximations can be made because of $m^*_{\mathsf{c}} < 10^{-4} \cdot m^{2\text{D}}_{\mathsf{x}}$ and the high photonic (excitonic) fraction of the LP (UP). A similar expression holds for the polariton lifetime

$$\tau_{\mathsf{LP}} = \left(\frac{|C_{\mathsf{x,k}}|^2}{\tau^{2\text{D}}_{\mathsf{x}}} + \frac{|C_{\mathsf{c,k}}|^2}{\tau_{\mathsf{c,k}}}\right)^{-1} \approx \frac{\tau_{\mathsf{c,k}}}{|C_{\mathsf{c,k}}|^2} \qquad \text{LP lifetime} \tag{2.17}$$

$$\tau_{\mathsf{UP}} = \left(\frac{|C_{\mathsf{c,k}}|^2}{\tau^{2\text{D}}_{\mathsf{x}}} + \frac{|C_{\mathsf{x,k}}|^2}{\tau_{\mathsf{c,k}}}\right)^{-1} \approx \frac{\tau_{\mathsf{c,k}}}{|C_{\mathsf{x,k}}|^2} \qquad \text{UP lifetime} \tag{2.18}$$

In our high quality microcavity sample the LP polariton mass is $m^*_{\text{LP}} = 5.4 \cdot 10^{-34}$ kg and the lifetime is 7 ps.

2.3.4 Weak and strong coupling regime

There is some controversy in the literature as to what strong coupling means. From a pragmatic point of view strong coupling is when the polariton decay time (at resonant cavity) is much

longer than the time of a Rabi oscillation cycle, $\gamma_{\mathsf{LP}}, \gamma_{\mathsf{UP}} < \Omega_{\mathrm{R}}/(2\pi)$:

> "If the coupling strength between two same-energy oscillators exceeds the mean of their decay rates, then the coupled system has two eigenenergies – that is their energies split." [13]

This argument is easily checked in a polariton spectrum: if two peaks are clearly separated by a splitting[1] S *at the resonance point*, then the system is in strong coupling regime:

$$S \lessgtr \gamma_{\mathsf{LP}} + \gamma_{\mathsf{UP}} \quad \text{for} \quad \begin{cases} \text{weak} \\ \text{strong} \end{cases} \text{coupling} \tag{2.19}$$

This is the case in Fig. 2.8(h), in all other cases (e-g) it is not. However, following the coupled oscillator model, there is another criterion that separates the two regimes [12], namely if $\Delta_k = \sqrt{\Omega_{\mathrm{R}}^2 + \tilde{\delta}_k^2}$ in Eq. 2.6 is imaginary or real. Assuming the cavity is resonant with the exciton, $\omega_{\mathsf{c,k}} = \omega_{\mathsf{x}}$, the criterion becomes

$$\Omega_{\mathrm{R}} \lessgtr |\gamma_{\mathsf{c,k}} - \gamma_{\mathsf{x}}| \quad \text{for} \quad \begin{cases} \text{weak} \\ \text{strong} \end{cases} \text{coupling} \tag{2.20}$$

In the calculation in Fig. 2.8(a-d) this means that the real part of the polariton energy splits in the strong coupling regime whereas the splitting will occur in the linewidths (imaginary part) in the weak coupling regime. According to the condition given above, the system is in strong coupling even if both linewidths are equal $\gamma_{\mathsf{c,k}} = \gamma_{\mathsf{x}} > \Omega_{\mathrm{R}}$ and *larger* than the Rabi frequency [Fig. 2.8(c)], where there would be no visible splitting in the spectrum [Fig 2.8(g)]. As an experimentalist I prefer Eq. 2.19 to define strong coupling, which is present only if the modes are clearly split in the spectrum (at the resonance point).

2.3.5 Polariton excitation and detection

Polaritons can easily be excited optically, resonantly or non-resonantly, or electrically by carrier injection in a semiconductor diode heterostructure. For **non-resonant optical excitation**, the microcavity is excited with a laser beam at high energy, usually at the first minimum on the high energy side of the DBR spectrum [~ 100 meV higher in energy (50 nm shorter wavelength) than the microcavity resonance] to get maximum coupling efficiency to the intracavity field. The excitation produces a population of coherent free electron-hole pairs that thermalise under

[1] For small linewidths $\gamma_{\mathsf{x}}, \gamma_{\mathsf{c}} \ll \Omega_{\mathrm{R}}$ the splitting between the LP and the UP mode is indeed equal to $\hbar\Omega$ at resonance: $S = \hbar\sqrt{\Omega_{\mathrm{R}}^2 - (\gamma_{\mathsf{c,k}} - \gamma_{\mathsf{x}})^2}$. With increasing difference between the linewidths the splitting S gradually diminishes, until it reaches $S = 0$ for $\Omega_{\mathrm{R}} = |\gamma_{\mathsf{c,k}} - \gamma_{\mathsf{x}}|$.

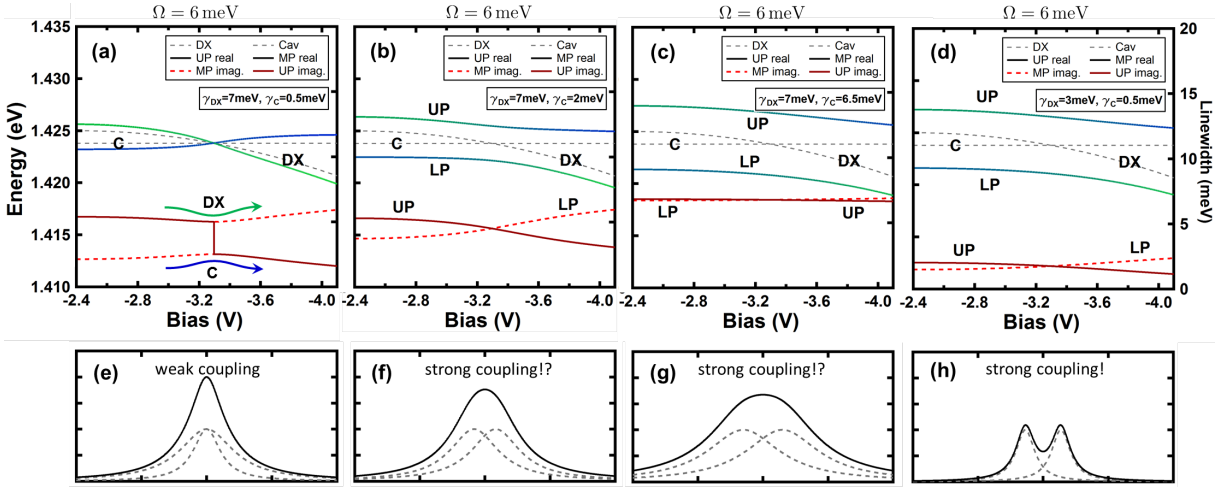

Figure 2.8: Examples of weak and strong coupling in bias tuning of the exciton mode. Top row: coupled oscillator model calculations after Eq. 2.6. Bottom row: computed spectrum at the resonance point with linewidths and splitting as calculated above. In weak coupling the two modes have equal energy but different linewidth (e) whereas in strong coupling they split in energy but have the same broadening (h). Notation: C is the cavity mode, DX is the exciton which tuned as a function of applied bias (see Sec. 7.2).

emission of longitudinal optical phonons [5] to form high $k_{||}$ polaritons on the LP branch. These highly excitonic polaritons form a reservoir (often simply called exciton reservoir) from which they relax further towards the centre of the dispersion curve by scattering with other polaritons, QW disorder and free charge carriers, thus gaining a higher photonic component. A second and very effective way of relaxation is stimulated scattering, which provides a direct way to transfer polaritons from a reservoir at high $k_{||}$ on the LP polariton branch into the final (condensed) state. The stimulation rate is proportional to $(1 + N_0)$ and stems from the bosonic nature of polaritons and the high final state population N_0. This relaxation process is very important in polariton condensation [1, 16, 32] and parametric amplification processes [4, 34].

Below a certain pump power threshold, the created polariton population is incoherent for continuous wave pumping and not polarised with respect to the excitation, due to the many scattering interactions in the energy relaxation process. The luminescence originates from all states of the lower polariton branch, whose population decreases exponentially with increasing energy for non-resonant below-threshold pumping (Eq. 2.21). However, above the so called condensation threshold, the PL stems predominantly from a single condensed or macroscopically populated state, the polariton condensate. Hence the emitted light is coherent and some effects of the pump laser polarisation can be seen, especially for circularly polarised non-resonant pumping [35], less so for linearly polarised pumping.

For **resonant optical excitation** the laser beam wavelength and the excitation angle have to be tuned to match one of the states on the polariton dispersion curve (Sec. 2.1). The resulting polariton population is inherently coherent, i.e. polariton condensation occurs if the threshold polariton density is exceeded [16]. Furthermore it is spin polarised identically to the laser: σ^+ or σ^- for circularly polarised excitation laser; for linearly polarised light half the polaritons are excited with $s = +\hbar$ and half with $s = -\hbar$, so as a whole the population is not spin polarised[1] [36]. An important note is that the polariton dispersion shifts to higher energy with increasing pump power (applies also to non-resonant excitation): this requires resetting the pump laser to a shorter wavelength to be again in resonance with the blueshifted polariton branch (Sec. 2.5.1).

Electrical formation of polaritons has been shown in VCSEL-like (Vertical Cavity Surface Emitting Laser) structures close to room temperature [9, 37]. Here electrons and holes are injected electrically through doped DBRs of a *p-i-n* diode structure to the undoped central cavity region where they drop into the QWs and form excitons that are resonant with the cavity, i.e. polaritons. A revolutionary approach to electrical pumping has been demonstrated by Bhattacharya et al. in their GaN-based room temperature polariton laser [21, 22], in which the electrons and holes are injected orthogonally to the direction of laser emission.

Optical detection of polaritons is performed by monitoring the peaks or dips in photoluminescence (PL), reflection (R), transmission (T) or absorption (A) spectroscopy. Reflection, transmission and photoluminescence are measured directly, while absorption can be calculated from energy conservation $\mathrm{R} + \mathrm{T} + \mathrm{A} = 1$ (assuming no scattering). Usually angle-, bias voltage- or position-dependent measurements of R,T,A,PL are recorded, in which the cavity or exciton modes tune with respect to one another. For convenience either reflection or transmission is measured, even though the real signatures of strong coupling should be measured in absorption [38]. Photoluminescence is easy to measure but tricky to interpret: it depends on the absorption A but does not directly correspond to the polariton population inside the cavity. First, the PL signal depends on the photonic content of the polaritons which diminishes with increasing $k_{||}$ on the LP branch (it increases on the UP branch). Second, only a fraction of the polaritons annihilate in a radiative decay, while the rest decays into waveguide modes of the microcavity or nonradiatively via interactions with defects and phonons. Additionally, the photoluminescence is often thermalised [39], meaning that even if the LP and the UP are equally half photon and

[1] Unless the polarisation symmetry is broken by effects intrinsic to the microcavity, such as TE/TM splitting or strong anisotropic properties of the semiconductor crystal

half exciton, the emission from the UP will be weaker than the one from the LP by a factor (see also Fig. 2.7)

$$\frac{I_{\mathrm{PL,UP}}}{I_{\mathrm{PL,LP}}} = \exp\left(-\frac{E_{\mathsf{UP}}(k_{||}) - E_{\mathsf{LP}}(k_{||})}{k_{\mathrm{B}}T}\right) \tag{2.21}$$

This Boltzmann factor accounts for the diminishing population of higher energy states in a thermalised system. Polariton systems are often not in thermal equilibrium due to continuous pumping and relaxation rates slower than the inverse polariton lifetime. However the fact that a simple intensity measurement is not sufficient to determine the state's population remains true, because the photonic fraction has to be taken into account. Besides optical detection, photocurrent measurements give a sensitive record of the polariton population [40, 41].

Measurement techniques to study polaritons

Insight into the dynamics of polaritons is gained from PL emission images in real and k-space. Mapping $I_{\mathrm{PL}}(x, y)$ records the spatial positions of strong PL emission and therefore images directly the polariton cloud (assuming all polaritons have the same photon fraction). It shows where defects and cracks are present and, in the case of a condensate, directly images the polariton condensate wavefunction. Introduction of a k-space lens (L5 in Fig. 4.1) allows us to record the k-space properties of the PL, $I_{\mathrm{PL}}(k_x, k_y)$, which gives the flow directions and speed $v = \hbar\sqrt{k_x^2 + k_y^2}/m^*_{\mathrm{pol}}$ of polaritons, where k_x, k_y are measured from the origin of the image.

Specialised and more complicated instruments are used to measure coherence and dynamics of polaritons. Streak camera images can record one spatial or spectral dimension of a periodic process with picosecond time resolution, allowing direct studies of dynamics. Such measurements are fundamental to study relaxation and coupling effects of polaritons [24, 42]. Interferometers are used in polariton research to study correlations in space (condensate phase, phase locking, vortex detection) [7, 43] and time (frequency locking of condensates, temporal coherence) [44].

2.3.6 Polariton tuning

Polaritons can be tuned in a number of ways and a very detailed list can be found in Sec. D of [45]. The simplest way is to change the **excitation/detection angle** θ which blueshifts the cavity energy E_{c} (Fig. 2.5) due to the Fabry-Pérot resonance condition fixing the orthogonal polariton momentum: $k_{\perp,\mathsf{c}} \cdot 2L_{\mathrm{eff}} = 2\pi\, m$ with the perpendicular component of the photon

momentum in a medium[1] $k_\perp = n|\vec{k_0}|\cos\theta = \frac{2\pi n}{\lambda_{c,0}}\cos\theta$ and the effective cavity length $n_c L_{\text{eff}} = \frac{m}{2}\lambda_{\text{design}}$ with $m = 5$ for our cavity design. Using the continuity of the in-plane momentum $k_{||} = \frac{2\pi}{\lambda_0} n_c \sin\theta_c \equiv \frac{2\pi}{\lambda_0}\sin\theta_0$, the result for the cavity dispersion relation E_c is

$$E_c(k_{||}) = \frac{\hbar c}{n_c}\sqrt{k_{\perp,c}^2 + k_{||}^2} = \hbar c\sqrt{\left(\frac{2\pi}{\lambda_{\text{design}}}\right)^2 + \left(\frac{2\pi}{n_c\lambda_0}\sin\theta_0\right)^2} \tag{2.22}$$

$$\approx \hbar c k_{\perp,0} + \frac{\hbar^2 k_{||}^2}{2m_c^*} = E_c(0) + \frac{1}{2E_c(0)}\left(\frac{hc}{n_c\lambda_0}\right)^2 \sin^2\theta_0 \tag{2.23}$$

An example of this near-parabolic photon dispersion inside a 2D microcavity is depicted by the red line in Fig. 2.5. The quantities in Eq. 2.23 can easily be measured: $E_c(0)$ is the energy at the apex of the cavity dispersion curve, λ_0 is the photon wavelength and θ_0 is its emission angle outside the microcavity. The in-plane effective mass of the photon is

$$m_c^* = \hbar k_{\perp,0}\, n_c^2/c = E_c(0)\, n_c^2/c^2 = 3.6\cdot 10^{-35}\text{ kg} = 4\cdot 10^{-5}\, m_e \tag{2.24}$$

for our structure. The bottom of the LP branch inherits to a large extent this light mass. The exciton mass, on the other hand, is 4-5 orders of magnitude heavier and hence tunes much slower (flat line in Fig. 2.5), so that it can be regarded as dispersionless within the light cone accepted by the microcavity.

A common method to tune the **cavity resonance wavelength** without changing the polariton momentum $k_{||}$ is to spatially vary the cavity layer thickness in between the DBR mirrors [37, 44]. A microcavity is designed so that its resonance frequency $\omega_c/2\pi$ matches the exciton transition energy at normal incidence $\theta = 0°$ at the centre of the sample $\vec{x}_0$:

$$\hbar\omega_c(\theta = 0, \vec{x} = \vec{x}_0) = E_x \qquad \text{resonant microcavity} \tag{2.25}$$

By stopping the spinning of the substrate in the MBE growth process, the cavity layer acquires a slight wedge which allows tuning the cavity mode to lower (higher) energies by changing sample position, thus moving the resonance point to higher (lower) angles $\theta > 0$, to find the desired detuning value $\hbar\delta_c = \hbar\omega_c(\vec{x}) - E_x$.
With a change in detuning the polariton interactions can also be altered directly via the recently observed polariton **Feshbach resonance**: two polaritons with anti-parallel spin produce a molecule at the bound state resonance. These two polariton populations with anti-parallel

[1] Quantities $n_0, k_0, \lambda_0, \theta_0$ indicate the values in vacuum $n = 1$, e.g. $k = nk_0 = n\frac{2\pi}{\lambda_{c,0}}$, while $n_c, k_c, \lambda_c, \theta_c$ denote quantities in the cavity layer with refractive index n_c.

spins show an enhancement of attractive interactions and a prompt change to repulsive interactions as the system is tuned across the biexciton bound state energy [46]. Optical tuning of polaritons can also be achieved by deposition of **perforated gold masks** with regular hole patterns on top of a microcavity, thus altering the boundary conditions for the photon mode [47]. This leads to periodic polariton wavefunctions with energy shifts of a fraction of a meV. Recently a hybrid microcavity with a sub-wavelength diffraction grating on the top DBR has achieved polariton lasing on a small footprint of 8×8 μm [48]. The $Al_{0.15}Ga_{0.85}As$ diffraction grating is suspended by a 300 nm air gap over the 2.5 periods of the top DBR. This configuration shows polarisation-selective strong coupling in 0D geometry. There is no need to etch through the active layers of the microcavity, as opposed to etched micropillars [49], so that coupling of neighbouring "condensation centres" is unrestricted.

There are several approaches to tune the exciton energy, the most popular one being **temperature tuning**. A rise in sample temperature shifts and lowers the QW bandgap and hence lowers the exciton transition energy [9]. The cavity mode shifts in the same direction with temperature, albeit by a much smaller amount. A flexible approach is **electrical tuning** of the exciton resonance by applying a voltage perpendicular to the microcavity plane [8]. The voltage tilts the band structure of the QW, thus changing the wavefunction of the excitons (centres of mass of electron and hole become increasingly separated, slowly morphing into an indirect exciton) and hence lowering their resonance energy. For this technique, voltage is applied by gold electrodes or ohmic contacts which are evaporated on the substrate and on top of the DBR mirror, through which the voltage is applied. Often the sample is processed into mesas using reactive ion etching or wet etching to form polaritonic devices such as the electrically injected polariton LED [9, 37] or the polariton laser [21, 22]. If the sample contains tunnel-coupled QWs, it becomes possible to electrically change the relative content of direct and indirect excitons [8]. Application of a **magnetic field** perpendicular to the microcavity plane splits the exciton levels due to Zeeman splitting, which tunes linearly with the magnetic field strength. The oscillator strength increases with magnetic field, in contrast to electric fields, which reduce it [50].

Stress tuning [17] was used to achieve one of the first experimental signatures of polariton condensation in a harmonic trap. Pressing the tip of a needle against the sample builds up mechanical stress in the QW crystal. This in turn shifts the exciton line to lower energies, while the photon mode remains unchanged. Similar to patterned gold masks, which affect the optical component of the polariton, the exciton mode can be modulated spatially with a sinusoidal potential by **surface acoustic waves** [18] using a surface-acoustic wave transducer, leading again to dynamic periodic polariton potentials which move at the speed of sound.

2.4 Wave properties: condensation and lasing

The powerful properties that make laser light more useful than conventional incandescent or fluorescent light are its large spatial and temporal coherence and its strict monochromatic nature. A plane wave, for example, has a fixed and predictable relationship for the phase of all the photons in the light field given by $\phi(\vec{x},t) = \vec{k}\cdot\vec{x} - \omega t$. This correlation of the photon phases over long spatial and temporal distances enables constructive and destructive interference, low-divergence beam propagation, high intensity light focussing and coherent optical excitation of dipole transitions. Precise control of the phase of laser light has found widespread applications [51, 52] ranging from homodyne and heterodyne measurements, interferometric positioning, high-precision laser cutting and lithography to miniaturised data storage on DVDs, medical applications and high-speed large-bandwidth optical data transmission.

Laser light is a collection of identical photons with near equal frequency, polarisation and phase. Moreover, the momentum of each light particle is identical in magnitude and often also in direction, for instance in a collimated laser beam with very low divergence. Coherence of photons in a laser light field is achieved through a stimulated decay process of electrons from an excited energy level in a gain medium. In a gas laser a necessary condition for stimulated (coherent) light emission is the presence of an electron population inversion, whereas in a diode laser a different mechanism[1] is at work. The process of phase-coherent amplification of light was first described by Albert Einstein in 1916 and experimentally demonstrated in 1960 with the first pulsed laser, followed soon after by the first continuous wave laser source, the HeNe gas laser, which is still one of the most widely used laser types to date for its simplicity and good coherence properties. Commercial success of laser-based technology came about in the 1970s with the development of efficient diode lasers operating at room temperature.

A very similar phenomenon to laser light, the proposition of coherent matter, was postulated by Louis de Broglie in his PhD thesis in 1924. He stated that electrons, just like photons, should have wave properties related to their particle or de Broglie wavelength

$$\lambda_{\mathrm{dB}} = \frac{h}{p} = \frac{h}{mv}\sqrt{1-\frac{v^2}{c^2}} \qquad \text{matter wavelength} \tag{2.26}$$

which is equal to the ratio of the Planck constant h, appearing in all quantum phenomena, and the particle momentum p. The smaller p is, the more prominent the wave nature becomes. Macroscopically visible effects of matter waves with $\lambda_{\mathrm{dB}} > 1\ \mu$m are only possible in the quan-

[1] Bernard-Durraffourg condition, the distance between the quasi-Fermi levels for electrons and holes is larger than the energy gap of the semiconductor [1].

tum regime, for very light and nearly-static ($v \approx 0$) particles which are hence delocalised over a large area in real space (Heisenberg uncertainty principle $\Delta x \Delta p \geq \frac{\hbar}{2}$). Polaritons are therefore good candidates for matter wave phenomena.

Still in the year 1924, Indian physicist Satyendra Nath Bose sent a research paper to Albert Einstein which derives the quantum statistics of photons without any reference to classical physics. At the heart of his manuscript was the uncertainty principle, stating that every Bosonic particle occupies a volume h^3 in phase space, and the indistinguishability of identical particles, leading to quantum statistics and, in the case of integer spin particles, to preferential occupation of the same quantum state. Impressed by Bose's work, Einstein personally translated Bose's manuscript to German and published it in Bose's name in "Zeitschrift für Physik". It was Einstein who realised that the same formalism can be extended to all bosonic matter with integer spin (bosons), not just massless photons, predicting the existence of a new state of matter in which a large number of identical bosons occupy the very same quantum state [53]. The matter waves of individual bosons in this cloud add up constructively to form a fully coherent macroscopic quantum object, later called a Bose-Einstein-condensate. Similarly to a laser, such forms of matter show coherence and interference effects, as proven by various ground breaking experiments in the last two decades (see for example [54]).

2.4.1 Conventional Bose-Einstein condensation

Bose-Einstein condensation is a quantum phase transition in which an unordered dense cloud of bosons "condenses" into a new matter state in which the matter-wave properties dominate and long-range quantum-mechanical order is present. In such a Bose-Einstein condensate (BEC) all particles reside in the lowest energy state of the system and the phases of the single bosons follow a fixed relation across the cloud, just as for photons in laser light. A BEC is a highly coherent matter state that shows self-interference and is described by a single wavefunction Ψ. The response of the condensate of N bosons to an external force or an electric/magnetic field will always be proportional to the wavefunction Ψ of the whole condensate, i.e. all the particles in the BEC respond in unison (in phase), thus amplifying the response signal by a factor N. This allows us to see, measure and manipulate quantum effects on a macroscopic scale.

At high temperatures or low densities a cloud of bosons behaves like a classical ideal gas with high momentum $p \gg 0$ and billiard ball trajectories, as shown in Fig. 2.9(a). As the temperature T is lowered their matter waves of size $\lambda_{\mathrm{dB}} = h/p$ increase and the bosonic wave nature becomes progressively more prominent (b) while the particle properties slowly vanish. Past a critical temperature T_c the bosonic matter waves spread to the point where they overlap with

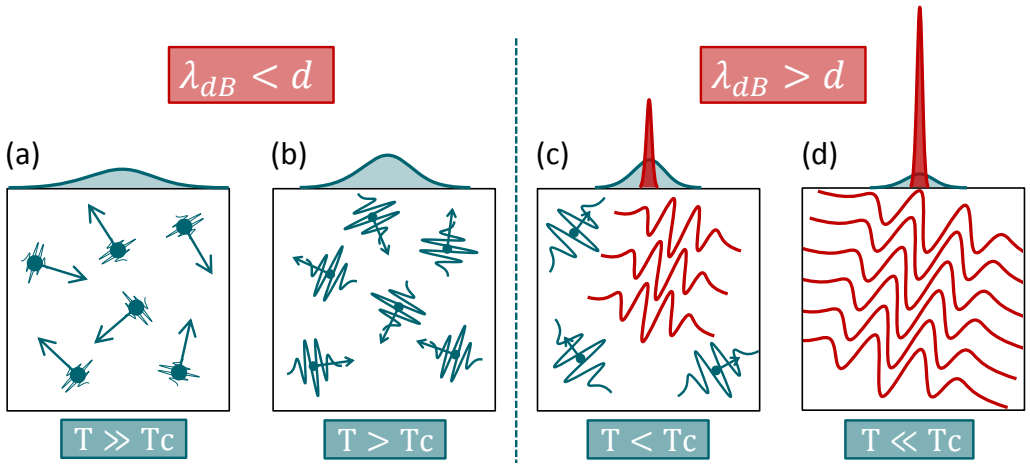

Figure 2.9: BEC formation in a box. As the temperature of the system is lowered (a → d) the wave nature in (d) of the bosons dominates over the particle properties in (a). Past a critical temperature T_c (dashed line) the matter waves overlap, leading to correlation of their phases and formation of a coherent matter cloud in the lowest energy state of the system, the Bose-Einstein condensate (red). The curves on top of the boxes represent the momentum distribution: the red spike is the condensate and the green Gaussian the uncondensed thermal boson population.

their neighbours and consequently their phases become correlated - matter coherence emerges. This is accompanied by a strong increase of the population N_0 in the lowest quantum state, exceeding the condensation threshold occupancy $N_0 > 1$, and a BEC is formed [sharp red peak at $p = 0$ in the momentum distribution of (c,d)]. Finally, for $T \ll T_c$ the lion's share of the population ends up being in the ground state of the system and forms a macroscopic quantum object Ψ.

BEC formation spontaneously breaks the symmetry of the uniform system in a second order phase transition. Above a critical temperature (or at low density) the cloud behaves as a classical gas, following Boltzmann statistics at a temperature T, with an order parameter $\Psi = 0$. When the system transits past this condensation threshold a non-zero order parameter $\Psi = \rho \exp(i\phi)$ emerges and builds up gradually, as more and more atoms from the thermal gas cloud join the condensate. Ψ is the wavefunction of the condensate with the phase ϕ, which is picked randomly[1] during the phase transition. ϕ being approximately constant across the full extension of the condensate. A BEC is mono-energetic (at the ground state energy E_0) and hence its time evolution in the absence of external perturbations is simply a linear increase of the global phase $\phi = E_0 t/\hbar$ with time t, a rotation of the phasor Ψ in the Hilbert space with constant angular frequency $\omega_0 = E_0/\hbar$.

[1] In the absence of external factors skewing the potential of the Gibbs free energy as function of the parameter driving the transition (temperature T, density N, etc.).

2.4.2 Short history of BEC

The quest for experimental realisation of the first Bose-Einstein condensate has a long history. The concept of BEC was proposed theoretically by Bose and Einstein in 1924-25 [53] and was followed by the discovery of superfluidity of ^{4}He in 1938 by Kapitza and Allen. When ^{4}He (a bosonic atom with integer spin) is cooled below the λ-point temperature of 2.17 K it becomes a superfluid, a liquid with zero viscosity and the lowest energy level of a Bose fluid [55]. In this state it shows two intriguing phenomena: quantised rotation and the "creeping" or Rollin or Onnes effect. Quantised rotation appears in a stirred superfluid in form of vortices arranged in a regular honeycomb pattern. The second effect is driven by surface tension and results in the superfluid creeping out of an unsealed container by itself, to lower its overall chemical potential, thereby crossing obstacles and overcoming gravity. At the time of discovery it was not clear that superfluidity and BECs share many properties.

In the following decades a lot of effort was put into achieving BE condensation in various systems, most notably Rb and Na atoms and excitons, which were proposed due to their much higher critical temperature. The problem of producing a BEC lies in the fact that quantum degeneracy has to be reached, i.e. the boson gas has to be cooled or "densified" until the matter waves of individual bosons overlap (see Sec. 3.1). For atomic BEC this requires temperatures below 1 μK, which were attained only after special techniques like laser cooling and magnetic evaporative cooling had been developed. Following many unsuccessful attempts, finally in 1995 three different research groups in the USA succeeded independently to produce the first atomic condensate [56, 57]. In 2001 Cornell, Wieman and Ketterle were awarded the Nobel Prize in physics for the achievement of BEC. Evidence for condensation of direct or indirect excitons has been shown recently [58, 59] but the proof is still debated after several premature claims.

	Atomic Gases	Excitons	Polaritons
Effective mass m* [m_e]	10^3	10^{-1}	10^{-5}
Bohr Radius a$_B$ [nm]	10^{-2}	10	10
Particle spacing [nm]	10^2	10	10^3
Critical temperature [K]	$10^{-9} - 10^{-6}$	$10^{-3} - 1$	$1 - 300$
Thermalisation time [ps]	10^9	10^1	$1 - 10$
Lifetime [ps]	10^{12}	10^3	$1 - 10$

Table 2.1: Parameter comparison for BEC in atomic gases, excitons and polaritons; from [32].

2.4.3 Polariton condensation

Polariton condensation is the appearance of long-range spatial order in a cloud of polaritons. It is usually achieved by increasing the laser pump power to the point where the critical polariton density inside the microcavity is exceeded (Eq. 3.11). Signatures of polariton condensation [1] include coherent photoluminescence (indeed the full polariton cloud is coherent), a well defined but randomly oriented polarisation of the emitted light (spontaneous symmetry breaking for each condensate realisation), narrowing of the emission linewidth (increased temporal coherence) at the condensation threshold and a strong rise in the luminescence output (non-linear emission).

As mentioned earlier, polaritons are good candidates for BEC formation due to their very low mass and naturally large spatial extension. Table 2.1 summarises typical parameters for systems showing Bose-Einstein condensation (BEC) in dense ultracold gases and solid state environments (excitons, polaritons and magnons). Three properties of polaritons clearly stand out. First, their effective mass is eight orders of magnitude smaller than for atomic systems, leading to a drastically higher critical temperature, allowing condensation even at room temperature. Second, the ratio of inter-particle spacing to Bohr radius is comparable for atomic gases and polaritons, as opposed to excitons. This means that efficient condensation can take place at relatively high temperatures, and densities well below the Mott density [7, 20, 44]. Third, the thermalisation time is comparable to the lifetime for polaritons, meaning that is harder for polaritons to reach thermal equilibrium, compared to atoms or excitons.

Formation of a condensate in GaAs QWs typically necessitates a high quality microcavity that supports long-lived polaritons based on two parameters: a photon lifetime exceeding ~ 5 ps and strong light matter coupling with Rabi splitting of $\hbar\Omega > 5$ meV (see strong coupling in Sec. 2.3.4). This could be achieved in mid 2000 with a new breed of microcavities with quality factors $Q \sim 10000$ and higher, in which typically 10-12 CdTe [16] or GaAs [7, 20, 44] QWs are fitted in 3-4 antinodes to space out the oscillator strength and to avoid the Mott transition limit.

The concept of a polariton condensate, the first proof of BEC formation in solids, was embraced more openly than exciton condensation and was established with the paper by Kasprzak [16] in 2006 and numerous papers from research groups in Europe (Lausanne [60, 61, 62], Cambridge/Southampton [63], Paris [20, 49, 64]) and the USA (Pittsburgh [17] and Stanford [32, 65]) collecting good evidence. From this point on the majority of polariton research is carried out on polariton condensates.

As a final remark, a recent publication has shown very convincing data of polariton condensation in an organic microcavity [66] consisting of a single 120 nm thick film of TDAF which is sandwiched between two SiO_2/Ta_2O_5 dielectric mirrors. The observed energy blueshift with increasing density is the first proof of a *strongly interacting* Frenkel-exciton-polariton condensate, which is highly stable at room temperature. In such inorganic systems completely different key figures lead to the strong coupling regime: a low cavity quality factor $Q \sim 600$, a giant Rabi splitting $\hbar\Omega = 520$ meV, a very short polariton lifetime $\tau = 55$ fs, blueshifts of ~ 15 meV and room temperature, all owing to the very large exciton binding energy of ~ 1 eV. Another promising result of organic strong coupling was obtained with a thin structured polymer film [67], and again condensation was observed only at strong negative detuning. The future of such high bandgap organic materials promises to remain very interesting in the view of room temperature condensation now being feasible, with the major limitations being the photostability of the organic active materials and the stronger localisation of Frenkel-exciton condensates.

Polariton condensation differs from atomic BEC formation in a number of ways:

1. Polaritons are metastable and hence **continuous pumping** is required to keep the polariton condensates alive for more than the polariton lifetime. A steady state of continuous decay and recreation is formed, in which condensation can be studied in quasi-equilibrium. Small intensity fluctuations of the laser are transferred to and amplified in the condensate [68], hence a stable and single-mode laser should be used for pumping for good temporal stability.

2. Polariton condensates exist naturally in **two dimensions**, as opposed to the three dimensional atomic BEC. This property allows for good direct optical access to the system and interesting low-dimensional physics (e.g. spinor condensate [69]).

3. Polaritons are strongly interacting and repel each other at high densities, thus pushing the polariton cloud apart and shifting the LP branch to higher energies. This is known as **"polariton blueshift"** (see Sec. 2.5.1).

4. At high densities polaritons lose their bosonic character due to excitons undergoing a **Mott transition** [7, 20, 44], i.e. the dense insulating cloud of excitons dissociates to become a conducting metallic plasma of electrons and holes. The oscillator strength decreases as a consequence of increased electron-hole pair screening due to fermionic exchange interactions [32, 70]. This effect also deteriorates the coherence properties of the condensate.

5. Polariton properties **can be tuned** in a number of ways (see Sec. 2.3.6) and they "glow", meaning the condensate cloud can directly be imaged, with **full access to the k-space**

dynamics.

6. For a long time **thermalisation** was a big issue, preventing polaritons from relaxing to the bottom of the LP branch quickly enough to achieve above unity occupation of the ground state. Polaritons have to reach the low momentum states in a time shorter than the polariton lifetime, which is prevented by the bottleneck effect [5, 35, 71] that can be overcome in the new breed of microcavities with increased **bosonic stimulated scattering** [72] due to better DBR mirrors and longer polariton lifetime.

7. Coherence of polaritons can occur in the ground state $k_{||} = 0$ or in states with higher energy ($k_{||} > 0$, meaning the condensate moves with uniform speed). Due to the peculiar relaxation dynamics, **multiple polariton states can show coherence simultaneously** [44, 73] and in the same spatial location [74]. Theoretically the formation of multiple condensates has been studied in [75, 76].

Strictly speaking point 7 contradicts the definition of a BEC, which demands a single ground state condensate[1] in an arbitrary frame of reference. Hence the term "polariton condensate" is used in this thesis for any polariton population showing coherence in an interferogram.

2.4.4 Photon lasing, polariton condensation and non-linearities

A polariton microcavity and a vertical cavity surface emitting laser (VCSEL) are built from GaAs-based materials, and are both made of a set of QWs embedded in a high quality Fabry-Pèrot-type microcavity. Furthermore the VCSEL has doped contact layers for electrical operation and is fabricated into mesas. In fact they both show the same threshold behaviour, increase of first order coherence, appearance of spatial order and linewidth narrowing. This poses the question whether polariton BEC is the same as VCSEL or photon lasing [1].

The answer can be given from the dispersion curve in Fig. 2.10 which depicts various photoluminescence mechanisms present in a microcavity system. Coherent emission stemming from the uncoupled cavity mode (red) is purely photonic and is called photon lasing, the light generation mechanism employed by all VCSEL lasers. In the same way exciton emission, which can have very broad linewidth, stems from the exciton line and shows that the system is in the weak coupling regime. In contrast polariton emission, and especially the presence of blueshift of the LP (see Sec. 2.5.1), indicates the strong coupling regime. Hence a polariton condensate can be differentiated from photon lasing if it appears on the blueshifted LP curve, as opposed to the uncoupled cavity parabola (red) at even higher energy.

[1] Unless there are other degrees of freedom like spin.

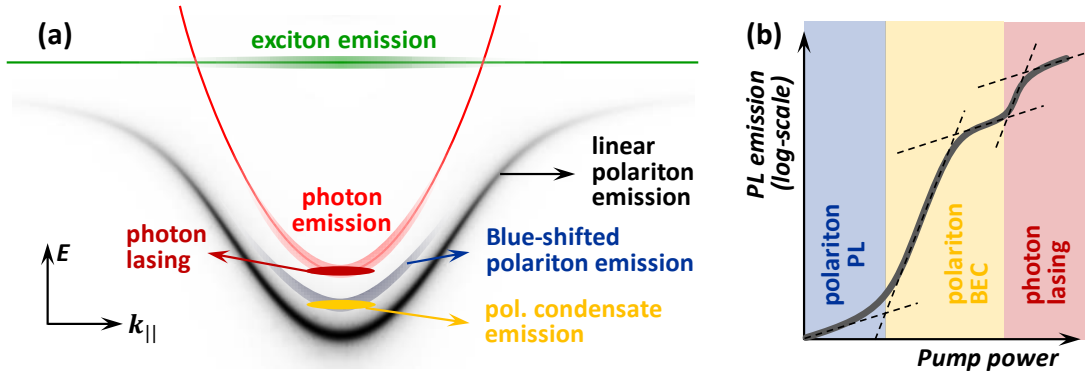

Figure 2.10: (a) Various emission mechanisms expected from a microcavity, depicted in an E vs $k_{||}$ diagram. Exciton and photon emission, originating from the uncoupled modes, belong to the weak coupling regime. Polariton emission is a signature of strong light-matter coupling. Coherent emission (polariton condensate, photon lasing) can be identified by its mono-energetic nature. (b) Power dependence of the PL emission of a non-resonantly pumped microcavity. Two thresholds are visible as kinks in the PL response: condensation threshold (blue to yellow) and photon lasing threshold at higher pump power (yellow to red).

For strongly negatively detuned cavity mode the lower branch polaritons are highly photonic and the distinction between photonic and polaritonic emission can be tricky due the proximity in energy of LP and cavity mode. Another good indicator [49] for "polariton operation" is the **power dependence of the PL response** ("input-output curve") of the microcavity. For such a measurement the total emitted light is recorded as a function of pump power [77], resulting in a curve with two kinks in a logarithmic plot as shown in Fig. 2.10(b). The first kink separates the regime of sub-threshold polariton PL (blue) from the zone of polariton condensation (yellow, also called polariton lasing), in which a strongly non-linear response of the PL emission is seen. Stimulated scattering into a single polariton state becomes dominant, followed by an exponential jump in luminosity of the forming condensate and significant blueshift of the polariton mode.

The second transition at higher pump power marks the onset of photon lasing (shaded in red). Here the emission is still coherent but originates from the bare cavity mode (red line in (a)), i.e. the strong coupling regime is lost due to bleaching of the oscillator strength. Important differences between a photon laser and a polariton condensate arise from the strong interactions between polaritons and excitons, which are present only in the condensate. In photon lasing, coherent emission is limited to the excited area without substantial propagation features, while a polariton condensate spreads over long distances, accelerating away from the pump spot due to the blueshift potential (see Sec. 2.5.1).

At high pump powers the intensity correlation function, measured with an interferometer,

$$g^{(2)}(\Delta t) = \frac{\langle I_1(t) I_2(t+\Delta t)\rangle}{\langle I_1(t)\rangle\langle I_2(t)\rangle} \tag{2.27}$$

shows a jump from $g^{(2)}(0) > 1$ in the condensate regime to $g^{(2)}(0) = 1$ for photon lasing. This is a result of increased polariton pair scattering in the former and can be used to distinguish the two regimes. Photon lasers always remain at a value of $g^{(2)}(0) = 1$, while below threshold both systems operate at $g^{(2)}(0) = 2$. With this method it was shown experimentally [42] that even highly photonic polariton condensates differ significantly in this respect, thus implying that a polariton condensate is not a version of photon lasing. It has to be mentioned that several experiments, especially signatures often identified as solitons, can be reproduced in a microcavity with negligible polariton non-linearity [78], hinting that some effects attributed to polariton condensation and superfluidity actually happen in the linear polariton regime, well below the condensation threshold. However this result is still strongly debated in the community.

Finally, Fig. 2.11 shows a comparison of the properties of a photon laser (coherent emission, weak coupling), a polariton LED (electrically pumped with incoherent polariton emission, blue polariton PL region in Fig. 2.10(b), strong coupling) and a polariton laser (coherent polariton emission, strong coupling). The important feature of the polariton laser, compared to an ordinary laser, is the much lower lasing threshold (Bernard-Durraffourg condition, no population inversion argument [1]), which is orders of magnitude below the Mott density. A good recent review of polariton lasers can be found in [22].

2.4.5 Superfluidity

Polaritons are bosons with strong interactions and hence show superfluidity, which is the striking property of a liquid to flow past obstacles without friction. According to the Landau theory a polariton condensate can only support excitations if the flow velocity of the condensate, $v_p = \hbar k_{||}/m^*$ (Eq. 3.14), exceeds the critical value of the local sound velocity in the condensate

$$c_s = \sqrt{\frac{\hbar g |\Psi|^2}{m^*}} \qquad \text{condensate sound velocity} \tag{2.28}$$

This critical velocity depends on the polariton-polariton interaction strength g, the effective mass m^* and can be easily tuned by changing the local superfluid density $|\Psi(\vec{x})|^2$. If the condensate flows past a fixed sized obstacle with a velocity lower than the speed of sound ($v_p < c_s$) it behaves as a superfluid and no ripples or other scattering effects are visible. Superfluidity of

	Normal laser	*Polariton LED*	*Polariton laser*
	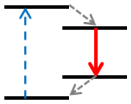	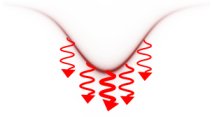	
Excited population	electrons incoherent	polaritons incoherent	ground state pol. coherent
Light emission	stimulated, coherent	spontaneous incoherent	spontaneous coherent
Excitation	electrical, optical	electrical	electrical, optical
Popul. inversion	yes	no	no
Strong coupling	no	yes	yes
High power	yes	no	no
Room temp. op.	yes	yes	yes

Figure 2.11: Comparison of a traditional laser, a polariton LED and a polariton laser.

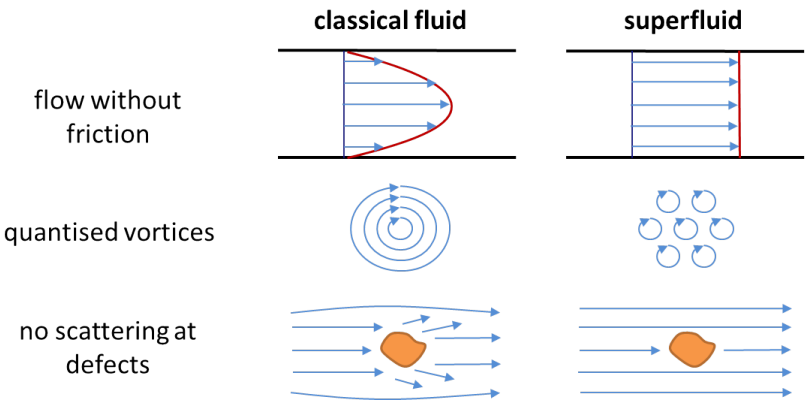

Figure 2.12: Differences between a classical fluid and a superfluid, which shows frictionless flow, quantised rotation and unperturbed flow past small defects.

polaritons was demonstrated experimentally in a resonantly excited polariton condensate with injected momentum $k_{||}$ that impinges on a defect of the microcavity [7]. For low $k_{||}$, i.e. low flow velocity, full suppression of scattering in k-space is seen. On the contrary for $v_p > c_s$ excitations become energetically possible and the condensate shows a clear Cherenkov-like wake pattern, from which c_s and the polariton coupling constant g can be deduced [7]. Below the condensation threshold the real space image of the condensate shows parabolic-shaped wavefronts around the defect. These result from interference of the incident polariton wave with the spherical ripples scattered by the defect.

Another very striking property of a superfluid is the absence of true rotation: a stirred condensate shows no global circulation ("tornado in water glass") because the curl of the superfluid velocity v_p is zero. Rotation energy in a superfluid can only be stored by creation of a quantum vortex (see Sec. 3.1.3), a phase singularity in the quantum liquid wavefuntion. Theoretical arguments show that it is energetically favourable for the superfluid to create a regular array of single-charged vortices [79], which is depicted in Fig. 2.12. In a polariton condensate such vortices appear spontaneously due to the continuous flow of polaritons from areas of high gain to regions with high loss, like defects. In these flows pinned vortices have been observed [23]. Further studies have shown that a vortex can be imprinted by a pump laser beam carrying orbital angular momentum [24, 80]. Since polaritons have two possible spin configurations, vortices can appear independently in both spin components and are called half vortices [81].

2.5 Particle properties: localisation and propagation

While it comes more natural to describe the polariton state and its dynamics in the frame of k-space which highlights its wave nature, it is equally true that polaritons show strong particle properties in real space. They can be excited with a well defined momentum (resonant excitation) and in absence of defects and external forces they travel on a straight line from A to B without dispersion, similar to wave-packet or polariton bullet [19].

Deterministic trajectories of polaritons have been exploited to show the principle of an all optical polariton transistor [82], in which switching is triggered by exceeding the condensation threshold of a near-degenerate polariton cloud with an additional weak control pulse. Another prototype polariton transistor was demonstrated recently [83], where the polariton condensate is created at one end of a 20 μm wide etched channel. Following the detuning gradient to lower energies, polaritons ejected from the condensate travel ballistically to one end of the channel, unless they are blocked by a blueshift potential that can be created by a weak control beam.

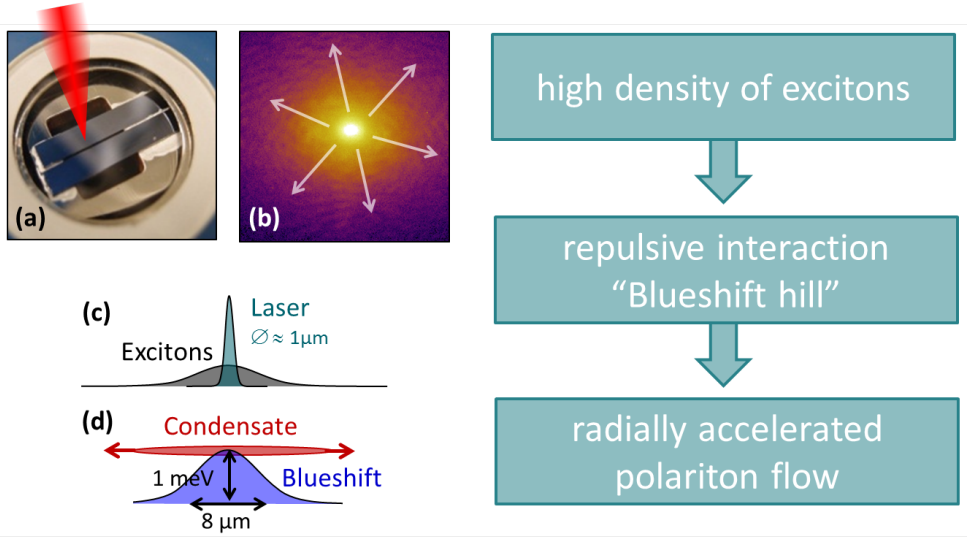

Figure 2.13: The blueshift potential sets non-resonantly excited polaritons in motion. A strong and focussed laser beam hitting the microcavity (a) produces a radially expanding polariton condensate (b). Simplistic sketch of the exciton reservoir (c) formed by the laser beam, resulting in a blueshift potential (d) that expels the condensate from the pumped area.

Work is in progress to develop electrically controlled gating.

Both implementations rely on the supreme control properties offered by a coherent polariton condensate, compared to a below threshold polariton cloud. Polariton transistors allow operation frequencies of tens of GHz [83], much faster than modern electron-based switches, and can be cascaded into large arrays [82]. Unfortunately, a high packing density is constrained by the limitations of independent directional control of multiple addressing beams and, more fundamentally, by the large extension of a polariton wavefunction over several micrometers.

2.5.1 Blueshift potential

In general a polariton condensate forms in a sink of the overall potential landscape, in the vicinity of the pumped region of the sample. This potential landscape is the combination of intrinsic sample disorder[1], the detuning gradient, the structural design of the microcavity (lateral confinement by channels or mesas for lower dimensionality, or patterned microcavites), external electric or magnetic fields and surface acoustic waves or strain potentials, as summarised in Sec. 2.3.6. There is however another important factor that determines the shape of the polariton condensate: the **blueshift potential**, a consequence of mutual repulsion of polaritons and

[1]Which can lead to spatially highly localised condensation but is negligible in our system.

excitons (self-interaction).

At high densities polaritons overlap and the fermionic constituents - electron, hole, photon - start to interact directly [84, 85]. In pair scattering events small dipole moments are induced in the excitons via charge separation, which can be identified as an average repulsive dipole-dipole potential with a direct and an exchange Coulomb interaction term [86] (exciton-exciton interaction). Additionally, there is a similar direct and exchange interaction term for an exciton and a photon [86] (exciton-photon coupling), which saturates for densities on the order of the Mott density n_{sat}, causing a reduction ("bleaching") of the oscillator strength of the exciton (also known as screening). A theoretical estimation for both blueshift effects in a polariton condensate can be obtained from [3]

$$E_{\mathrm{BS}} \approx \underbrace{\frac{3e^2 a_{\mathsf{x}}}{\varepsilon A}|C_{\mathsf{x}}|^4 N_{\mathsf{x}}}_{\text{exc - exc}} + \underbrace{\frac{2\hbar\Omega_{\mathrm{R}}}{n_{\mathrm{sat}} A}|C_{\mathsf{c}}||C_{\mathsf{x}}|^3 N_{\mathrm{pol}}}_{\text{screening}} \qquad \text{blueshift potential} \tag{2.29}$$

where a_{x} is the exciton Bohr radius, $n_{\mathrm{sat}} = 7/(16\pi a_{\mathsf{x}}^2)$ is the exciton saturation density and $N_{\mathsf{x}} = n_{\mathsf{x}} A$ is the number of excitons in the microcavity (A is the excited sample area). The Hopfield coefficients $C_{\mathsf{x}}(k_{||}, \Omega_{\mathrm{R}}, \delta_{\mathsf{c}})$, $C_{\mathsf{c}}(k_{||}, \Omega_{\mathrm{R}}, \delta_{\mathsf{c}})$ from Eqs. 2.11 and 2.12 are assumed to be mostly in the condensate state $k_{||} \approx k_c$.

In experiments using non-resonant pumping, as presented in chapter 5, each pump laser spot excites first a cloud of static excitons[1] at high $k_{||}$. This so called exciton reservoir forms in a circle of radius $r \approx 2-4$ μm around each tightly focussed pump spot and repels polaritons, making it the driving force of radial expansion in a free polariton condensate (Fig. 2.13). The second effect is direct self-repulsion among the condensed polaritons, which leads to spreading of the wavefunction[2] to fill out as much of the trap as possible, while retaining good overlap with the pump and avoiding areas of high loss (defects). Around the laser spot the entire polariton dispersion is blueshifted compared to areas of low polariton or exciton density due to these repulsive interactions. The gradient of the exciton density maps onto a diminishing blueshift the polaritons feel as they move outwards [87], and it is the driving force of condensate expansion. Its effect on polaritons can be described by an effective repulsive blueshift potential, which accelerates polaritons in a similar way to a ball rolling down the slope of a hill. Polaritons are expelled from the excitation area and convert their potential energy into kinetic energy [20, 60, 88]. For

[1] Static excitons are technically high $k_{||}$ polaritons with very large exciton component. They are very slow compared to polaritons due to their much higher mass.

[2] In atomic BE condensation such a condensate is described as being in the Thomas-Fermi limit and its wavefunction will assume the inverse shape of the trapping potential.

example, the polaritons gain a momentum equal to $k_{||} = 1.3/\mu$m from a blueshift potential of a tightly focussed pump spot with maximum energy blueshift $E_{\mathrm{BS}} = \max_{\vec{x}} V_{\mathrm{BS}}(\vec{x}) = 1$ meV:

$$k_{||} = \frac{\sqrt{2m^* E_{\mathrm{BS}}}}{\hbar} \qquad \text{momentum from blueshift potential} \tag{2.30}$$

Blueshift hills are directly visible in spectrally resolved images of PL emission in real space. Experimental observation shows that there are two contributions to the blueshift potential [66], one from the exciton reservoir n_{x} (exc.-pol. repulsion) and another from the polariton population $n_{\mathsf{pol}} \approx |\Psi(\vec{x})|^2$ itself (pol.-pol. repulsion). Both are repulsive [89] and proportional to the density (at least in first order approximation). The blueshift potential is therefore

$$V_{\mathrm{BS}}(\vec{x}) = \hbar g_{\mathsf{x}} n_{\mathsf{x}}(\vec{x}) + \hbar g |\Psi(\vec{x})|^2 \qquad \text{blueshift potential} \tag{2.31}$$

with respective interaction constants $g_{\mathsf{x}}, g > 0$. There is no general consensus on which contribution dominates; a thorough study of blueshift potentials can be found in [89]. Exciton reservoir related blueshift [90] seems to prevail for 1D and 2D polariton condensates that can expand freely [20, 87] while for tightly trapped polaritons [43, 49, 73] and in situations where the polariton condensate is spatially separated from the exciton reservoir [73, 89] the polariton non-linearities are stronger. For inorganic microcavities the blueshift within the pumped region stems predominantly from exciton-polariton interaction [66]. The linear regime $E_{\mathrm{BS}} \propto P$ in Eq. 2.31 is correct only up to medium pump powers, above which a saturation of the blueshift kicks in (logarithmic dependence in 0D polariton condensate [48]). Additionally, the trapping geometry has a strong effect on the observed blueshift, which differs strongly at the pump spots and in the trap centre (see Sec. 5.4).

2.5.2 Trapping and motion control of polaritons using optical and structural potentials

Good control over creation, motion and trapping of polaritons is of high importance for most experiments, especially for the development of polariton logic circuits. There are several approaches to manipulate the motion of polaritons: through resonant excitation, which generates polaritons directly in the desired state of motion $k_{||}$ [19], by acceleration in a blueshift potential in non-resonant excitation [20, 89] or via a detuning gradient of the microcavity [83]. Specially designed waveguides can be used to efficiently restrict polariton motion along the channel over several hundred micrometres [20, 83]. Newly developed waveguide techniques allow us to build directional couplers and interferometers for polaritons, with gate operations (phase shift, switching, transmission regulation) that are controlled electrically (still to be shown) or optically [91].

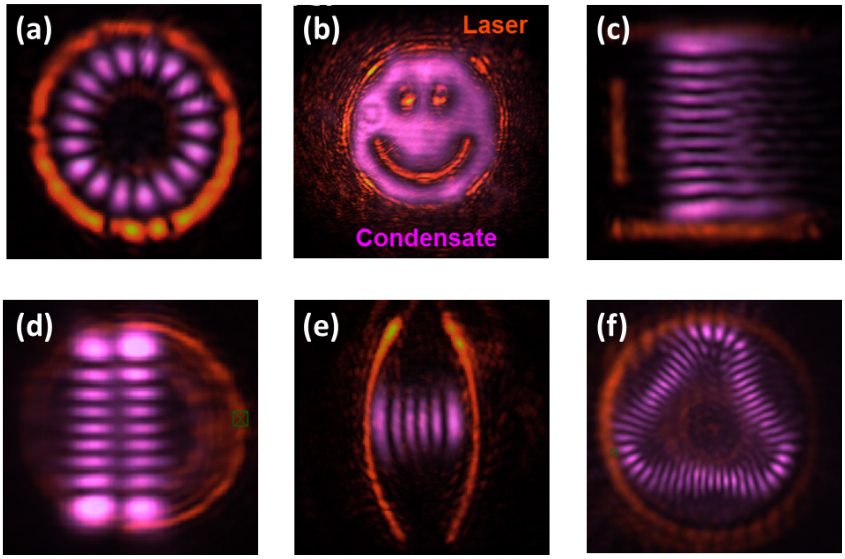

Figure 2.14: PL images of polariton condensates (purple) formed by differently shaped pump laser beams (orange). The presence of ripples indicates coherence and mono-dispersity (a,c-f). For very high pump powers the trap area is evenly filled out with polaritons at different energies (b). The imaged area is roughly 50×50 μm.

Polariton excitation in a trap can be achieved in multiple ways. A widely used method is to provide lateral confinement by etching small mesa structures such as micropillars [77, 89], in addition to patterning the microcavity itself [47] or by using stress traps [17]. The recent approach of replacing the top DBR by a sub-wavelength diffraction grating (photonic crystal confinement) to localise the region of strong coupling is very promising [48]. Active and reconfigurable ways to confine polaritons include optical potentials [20, 73, 83, 89] and surface acoustic waves [18, 92]. Using blueshift potentials, it is possible to create semi-permeable "walls" that allow quantum tunnelling of the condensate wavefunction in addition to controlled phase-locking [20]. These blueshift walls can be ramped up to form a deep optical trap [73] simply by increasing the optical power of the pump laser.

More intricate polariton circuits can be created by spatial modification of the pumping laser with a spatial light modulator. Fig. 2.14 presents a selection of laser shapes (orange) obtained with this method, along with the resulting PL from the polariton condensates (purple)[1]. It can clearly be seen that polaritons form inside the optical trap (a,b,d,f). The condensates seek a compromise between avoiding the pump laser (blueshift repulsion) and ensuring good gain

[1]PL emission is at longer wavelength and appears purple on a colour CCD (hue changed for better contrast)

overlap (vicinity to pump lines). For this reason stable condensates can be formed also in semi-trapped configurations (c,e) (see also Sec. 5.3). Polariton condensates formed at threshold pump power show regular ripples in their wavefunction, which signifies that they are coherent and mono-energetic (a,c-f). Opposed to this is high power pumping, which excites multiple polariton states simultaneously (b), resulting in polaritons filling out all available space in the trap with a smooth density profile without fringes. In addition, the condensate does not necessarily follow the exact symmetry imposed by the pumping geometry (d,f). This observation is not understood but may be related to defects in the microcavity, which makes other condensate shapes extremely lossy.

There is however a catch in this blueshift potential approach: gain and confinement are not independent, since the non-resonant pumping laser creates both the polariton population and potential to trap it. This effect is especially problematic for small geometries creating channels that are less than $5 - 10$ μm wide. One way to overcome part of this problem is to create large-sized pump geometries, with tightly focussed laser lines. This creates more localised and higher blueshift potentials which repel the condensate stronger, for a better separation of condensate and pumping area. At the same time the gain experienced by the condensate is reduced compared to a spread out pump laser because of smaller spatial overlap.

In summary, non-resonantly pumped blueshift potentials created by a single tightly focussed laser beam have been used successfully in combination with etched microcavity structures as the gate of a polariton transistor [83]. With the same mechanisms of structural confinement and optical control a phase shift can be imprinted in a polariton Mach-Zehnder interferometer [91], allowing to switch the output flow and polarisation at the exit of the interferometer. Furthermore all optical control of polariton condensates is a very promising development despite the limitations mentioned above. Its main advantages are the versatility to reconfigure the design continuously and in real time, and the simple control of the potential height by adjusting the power of the laser beam directed into a specific area of the sample. The tools needed to shape the laser beam into the desired form are explained in Sec. 4.2.

Chapter 3

Theory

Research in physics is an increasingly complex task and often real understanding is obtained when the problem is tackled from three side simultaneously: the experiment provides relations between physical quantities, the theoretical model gives analytical insight to show connections to related physical phenomena, and simulations are employed where analytical solutions cannot be found, and to test the system in the full parameter space not reachable in the experiment.

The aim of this chapter is to lay out the theoretical foundations of polariton condensation. In the first half of this chapter the theory of Bose-Einstein condensation is presented (Sec. 3.1), starting with a 3D box of ideal bosons and then moving on to the richer 2D world of microcavity polaritons. Excitations in a 2D polariton condensate are discussed in Sec. 3.1.3 and the BKT transition, separating the condensate state with long-range spatial correlations from the disordered phase at higher temperature, is outlined in Sec. 3.1.4.

The second part, Sec. 3.2, is dedicated to simulations of polariton condensates, with their peculiar dynamics arising for continuous pumping and decay of polaritons. The complex Ginzburg-Landau equation is introduced in Sec. 3.2.2, a highly versatile differential equation developed for superconductors and very useful to explain pattern formation within the polariton condensate. The effect of coherent and incoherent polariton pumping is discussed in Sec. 3.2.2.1. The last two sections deal with specific aspects relevant to polariton condensates covered in the results chapters of this thesis, namely the shape of a polariton condensate in non-resonant pumping (Sec. 3.2.3) and the mode competition and frequency locking of multiple condensates in a trap (Sec. 3.2.4).

3.1 Theory of polariton condensates

3.1.1 BEC theory in a 3D box

Bosons are identical particles with integer spin. Since they are indistinguishable, the wavefunction of a bosonic ensemble is symmetric under exchange operation $P_{j,k}$ of any two particles j and k (with sets of coordinates $\underline{x}_j, \underline{x}_k$ for position, momentum, spin, charge etc.)

$$P_{j,k}\Psi(...,\underline{x}_j,...,\underline{x}_k,...) \equiv \Psi(...,\underline{x}_k,...,\underline{x}_j,...) = +\,\Psi(...,\underline{x}_j,...,\underline{x}_k,...) \qquad (3.1)$$

symmetric bosonic wavefunction

and an infinite number of bosons are allowed to occupy the same quantum state, as opposed to fermions which have to follow the Pauli exclusion principle (either 0 or 1 fermions per state). Bosons obey the Bose-Einstein (BE) distribution function

$$\bar{\mathrm{n}}_i(\epsilon_i) = \frac{\mathrm{g}_i}{\exp\left(\frac{\epsilon_i-\mu}{k_\mathrm{B}T}\right)-1} \qquad \text{Bose-Einstein statistics} \qquad (3.2)$$

where $\bar{\mathrm{n}}_i(\epsilon_i)$ is the mean occupation number of the single-particle state i with energy ϵ_i and degeneracy g_i in a certain trapping potential, $\mu < \epsilon_0$ is the chemical potential (the free energy cost of adding one more boson to a large ensemble) and $k_\mathrm{B}T$ is the reference thermal energy at temperature T. Given a number N of bosons, the ground state population N_0 (the number of bosons in the lowest energy state ϵ_0) can then be calculated from

$$N = N_0 + \int_{\epsilon_0}^{\infty} d\epsilon\, \mathrm{g}(\epsilon)\, \bar{\mathrm{n}}(\epsilon) \qquad \text{condensate occupancy } N_0 \qquad (3.3)$$

where $\mathrm{g}(\epsilon)$ is the density of states (DOS), which for a 3D box potential with N bosons in a volume V equals to $\mathrm{g}(\epsilon) = Vm^{\frac{3}{2}}\sqrt{\epsilon-\epsilon_0}/(\sqrt{2}\pi^2\hbar^3)$. The integral in this equation gives the number $N_{\epsilon>\epsilon_0}$ of bosons in the excited states. Evaluating it and setting it equal to the total number N of particles in the box gives an expression that can be solved to obtain $\mu(N,T)$ at the condensation threshold.

$$N_{\epsilon>\epsilon_0} = \int_{\epsilon_0}^{\infty} d\epsilon\, \mathrm{g}(\epsilon)\, \bar{\mathrm{n}}(\epsilon) = V\left(\frac{mk_\mathrm{B}T}{2\pi\hbar^2}\right)^{\frac{3}{2}} \mathrm{Li}_{\frac{3}{2}}\left[\exp\left(\frac{\mu-\epsilon_0}{k_\mathrm{B}T}\right)\right] \stackrel{!}{=} N \qquad (3.4)$$

Lets define $\mathrm{Li}_\alpha(z)$ as the polyalgorithm function[1] which is zero for $z = 0$, monotonically increasing for $0 \le z \le 1$ and complex for $z > 1$; $\zeta(\alpha)$ is the Riemann zeta function[2]. Then the

[1] The polyalgorithm function is defined as $\mathrm{Li}_\alpha(z) = \sum_{n=1}^{\infty}\frac{z^n}{n^{-\alpha}} = \frac{1}{\Gamma(\alpha)}\int_0^\infty \frac{x^{\alpha-1}dx}{\exp(x)/z-1}$

[2] The Riemann zeta function is defined as $\zeta(\alpha) = \sum_{n=1}^{\infty} n^{-\alpha} = \frac{1}{\Gamma(\alpha)}\int_0^\infty \frac{x^{\alpha-1}dx}{\exp(x)-1}$ and $\zeta(\alpha) = \mathrm{Li}_\alpha(1)$.

condition 3.4 can be simplified to

$$\varrho = \frac{N}{V}\lambda_{\mathrm{dB}}^3 = \mathrm{Li}_{\frac{3}{2}}(z) \xrightarrow[\max]{z\to 1} \zeta(\tfrac{3}{2}) \approx 2.612 \qquad \text{phase space density 3D box} \tag{3.5}$$

$$\lambda_{\mathrm{dB}} = \sqrt{\frac{2\pi\hbar^2}{m k_{\mathrm{B}} T}} \qquad \text{thermal de Broglie wavelength} \tag{3.6}$$

In the thermodynamic limit $\{N \to \infty,\ V \to \infty,\ N/V \to n_0\}$ the left hand side of Eq. 3.5 becomes very large for small T and large n_0, and so should the polygeometric function $\mathrm{Li}_{\frac{3}{2}}(z) \gg 1$. This is however not possible for two reasons: first this function reaches its (real) maximum at $Li_{\frac{3}{2}}(1) = 2.612$ after which it becomes complex and second this would require $z > 1$ or $\mu > \epsilon_0$ which contradicts the requirement for BE statistics $\mu < \epsilon_0$. Both reasons are strong hints for a phase transition.

The expedient is as follows: in a system with large N at low temperature T not all bosons can be accommodated in the excited states $N_{\epsilon>\epsilon_0}$ permitted by the BE distribution. The population in the excited states saturates at a critical temperature T_c, corresponding to $\mu \to \epsilon_0^-$. A remedy is the fact that the ground state population N_0 can become arbitrarily large (the BE distribution diverges for $\mu \to \epsilon_0^-$) hence it has to be counted separately in Eq. 3.3. Past the condensation threshold all "homeless" bosons pile up in the ground state ϵ_0, forming a massive cloud of identical overlapping and phase-correlated bosons, the BEC.

The phase space density ϱ in Eq. 3.5 defines a very useful quantity, the number of particles within a volume λ_{dB}^3, with the thermal de Broglie wavelength λ_{dB} being the size of the matter wave at a given temperature T. When ϱ exceeds unity the matter wavelength becomes comparable to the interparticle spacing and the bosons start to overlap: the system has reached quantum degeneracy. ϱ is the ratio of the number of particles N in the system and the number of states with energy less than $\sim 1.2\, k_{\mathrm{B}}T$[1] and is hence a measure for the occupancy of low energy states. In a 3D box Bose-Einstein condensation takes place when $\varrho \geq 2.612$, when all excited states are filled according to BE statistics and the remaining fraction of the bosons are forced to all occupy the lowest energy state, which becomes massively populated: $N_0 = N - N_{\epsilon>\epsilon_0} \gg 1$. A critical temperature, or an equivalent critical density, can be formulated from the condensation

[1] This can be verified from the number of states $D(\epsilon) = \int_{\epsilon_0}^{\epsilon} d\epsilon'\, \mathrm{g}(\epsilon') = V\frac{4\pi}{3}\left(\frac{\sqrt{2m\epsilon}}{2\pi\hbar}\right)^3$ which gives $D(1.2\, k_{\mathrm{B}}T) = V/\lambda_{\mathrm{dB}}^3$

condition Eq. 3.5

$$k_{\mathrm{B}}T_{\mathrm{c}} = \frac{2\pi\hbar^2}{m}\left(\frac{N}{V\zeta(\frac{3}{2})}\right)^{\frac{2}{3}} \qquad \text{critical temperature for condensation in 3D} \tag{3.7}$$

which shows that low mass bosons at high densities are ideal candidates for BECs. A typical BEC of ^{87}Rb atoms has to be cooled to temperatures of a few nK to μK above the absolute zero point. Polariton systems are advantageous in this respect as they have a 10^9 times lower mass which brings the condensation temperature up to values of $T_c = 1 - 300$ K (see Tab. 2.1). The ground state occupancy N_0 is obtained from Eqs. 3.4 and 3.7 as

$$N_0 = \begin{cases} N\left[1 - \left(\frac{T}{T_c}\right)^{\frac{3}{2}}\right] & T < T_c \\ 0 & T > T_c \end{cases} \qquad \text{cond. population / order param.} \tag{3.8}$$

This quantity N_0 is directly proportional to the order parameter Ψ mentioned before, in that it is zero above the transition temperature and increases below T_c until all bosons end up in the condensate Ψ for $T \to 0$ K. Similar expressions for T_c and N_0 in a harmonic trap can be found in the standard literature on BEC formation. A recommended book on this topic is [79].

3.1.2 Condensation in 2D

According to BEC theory condensation is not possible in an infinite 2D system since the required phase space density is infinitely large, or the temperature of the system has to be infinitely close to the absolute zero point. With the two-dimensional DOS $\mathrm{g}^{\mathrm{2D}}(\epsilon) = Am/(2\pi\hbar^2)$ the number bosons in excited states is

$$N^{\mathrm{2D}}_{\epsilon>\epsilon_0} = \int_{\epsilon_0}^{\infty} d\epsilon\, \mathrm{g}^{\mathrm{2D}}(\epsilon)\, \mathrm{n}(\epsilon) = -\frac{Amk_{\mathrm{B}}T}{2\pi\hbar^2} \ln\left[1 - \exp\left(\frac{\mu - \epsilon_0}{k_{\mathrm{B}}T}\right)\right] \stackrel{!}{=} N \tag{3.9}$$

which gives a phase space density ϱ with the matter wavelength defined in Eq. 2.26 and the boson area density N/A:

$$\varrho^{\mathrm{2D}} = \frac{N}{A}\lambda^2_{\mathrm{dB}} = -\ln\left[1 - \exp\left(\frac{\mu - \epsilon_0}{k_{\mathrm{B}}T}\right)\right] \qquad \text{phase space density in 2D} \tag{3.10}$$

Unlike the 3D case there is no upper bound of the phase space density in 2D since the right-hand side of Eq. 3.10 diverges as $\mu \to \epsilon_0^-$. This implies that quantum degeneracy is reached ($\varrho \gg 1$, matter waves overlap) but there will always be a suitable chemical potential at finite temperature $T > 0$ K to fit all N bosons in the BE-allowed high energy states, so that macroscopic occupation of N_0 and hence BEC formation will never occur in an infinite 2D system. The

critical temperature for quantum degeneracy can be readily calculated from $\varrho \stackrel{!}{=} 1$ and gives:

$$k_{\mathrm{B}} T^{2\mathrm{D}} = \frac{2\pi\hbar^2 N}{mA} \qquad \text{quantum degeneracy in 2D} \tag{3.11}$$

As will be explained in Sec. 3.1.3, true condensation is possible in a finite 2D system under the condition $T \ll T^{2\mathrm{D}}/\ln N$ and an additional phase transition exists in 2D, the BKT transition, which is based on massive creation of quantum vortices past a critical temperature $T_{\mathrm{BKT}} = \frac{1}{4} T^{2\mathrm{D}}$.

3.1.3 Excitations in a cold 2D boson gas

There are three kinds of excitations in a BEC: sound waves (phonons) at low energy, rotational excitations (quantised vortices) at intermediate energies and thermal dissociation of composite bosons (creating free electrons and holes in the case of polaritons). Excitations are mediated via elastic particle interactions and the interaction energy of a many-body system is commonly simplified to $U_{\mathrm{int}}(\vec{x}) = \hbar g N\,|\psi(\vec{x})|^2$ (see Sec. 3.2.2). Here $\psi(\vec{x})$ is a single boson wavefunction $\psi(\vec{x})$. All the details about the scattering process are hidden in the interaction constant g which is positive in polariton systems, stating that polariton-polariton interactions are repulsive and increase the total energy of the system proportionally to number N of the polaritons in it (polariton blueshift).

Phonons are long-wavelength (compared to the healing length ξ) thermally induced vibrations of the bosons in the BEC. They can be seen as sound waves that propagate in the condensate via local variations of the condensate density[1] $N|\psi(\vec{x})|^2$ travelling at a speed

$$c_s = \sqrt{\frac{\hbar g N |\psi(\vec{x})|^2}{m^*}} \qquad \text{speed of sound in condensate} \tag{3.12}$$

with m^* being the polariton mass. Phonons are bosons that obey the BE statistics (Eq. 3.2) and the number of phonons is not conserved, hence $\mu = 0$ (cost of creating a new phonon is zero), just like for photons. In 1D or 2D infinite systems phonons induce phase fluctuations that destroy the long-range phase correlation in the BEC ([79] p. 447-451), despite the fact that the condensate density is non-zero. This leads to the formation of islands of locally coherent condensate without long-range correlation (quasi-condensates). The size $L_\phi = \xi \exp[T^{2\mathrm{D}}/(2T)]$

[1] The normalisation of the single particle wavefunction ψ is as usual $\int_{\mathbb{R}^2} d^2x |\psi(\vec{x})|^2 = 1$, see Eq. 3.20.

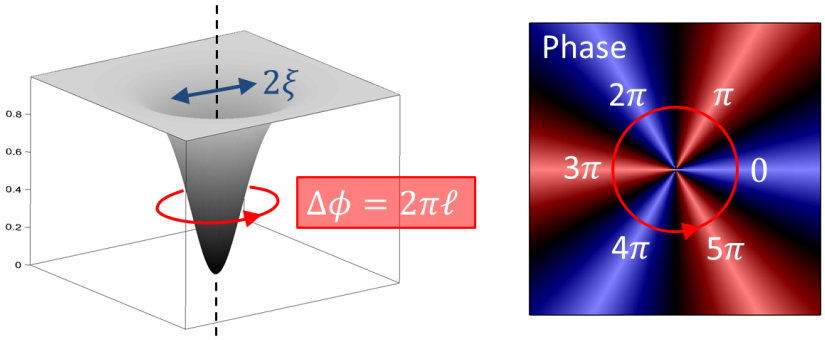

Figure 3.1: Quantum vortex in $|\Psi(\vec{x})|^2$ (left) with phase winding equal to an integer multiple of 2π (right).

of these islands is temperature dependent, with the healing length ξ

$$\xi = \frac{\hbar}{\sqrt{2}m^* c_s} = \frac{\hbar}{\sqrt{2m^* g N |\psi(\vec{x})|^2}} \qquad \text{healing length of the condensate} \qquad (3.13)$$

being the typical length scale on which the condensate screens out spatial constraints, the length on which Ψ varies from 0 to its average value, for example at a vortex or the edge of the condensate. It is also the fastest permissible spatial variation of Ψ and hence the highest energy phonon wavelength. In finite systems the phase is well correlated if the size of the system $A < L_\phi^2$ which implies $T \ll T^{2\mathrm{D}}/\ln N$.

The local velocity in a condensate $\Psi = \sqrt{\rho}\exp(i\phi)$ is the gradient of its phase

$$\vec{v}(\vec{x}) = \frac{\hbar}{m^*}\vec{\nabla}\phi(\vec{x}) \qquad \text{local condensate velocity} \qquad (3.14)$$

This fact has profound implications on its motion, as the flow has to be irrotational ($\vec{\nabla} \times \vec{v} = 0$) unless the phase ϕ contains singularities. Indeed these singularities are observed as **quantum vortices** in rotating or turbulent superfluids: they are punctures in a smooth surface Ψ, around which the phase revolves by multiples of 2π (Fig. 3.1). Vortices of the same charge in a uniform superfluid are all identical and have fixed size ξ (the healing length). The circulation around such a vortex is:

$$\Gamma = \oint \vec{v} \cdot d\vec{l} = \frac{\hbar}{m^*} \oint \vec{\nabla}\phi \cdot d\vec{l} = \frac{\hbar}{m^*} 2\pi\ell \qquad \text{quantised vortex circulation} \qquad (3.15)$$

In order for the condensate to be continuous in both phase and amplitude the change in phase $\Delta\phi = 2\pi\ell$ along any closed loop around the vortex core has to be an integer multiple ℓ times

2π and the wavefunction $\Psi \to 0$ has to vanish at the core position. The first condition implies that angular momentum $L = \ell\hbar$ is quantised in units of the reduced Planck constant $\hbar$, as are the rotation energies $E = L^2/(2I)$. The second requirement happens via a gradual fall-off of Ψ on the length scale of the healing length ξ (Eq. 3.13 and Fig. 3.1) towards the vortex core at (0,0): $\Psi(\vec{x}) \propto \tanh[\sqrt{x^2+y^2}/(\sqrt{2}\xi)$.

3.1.4 BKT transition

Vortices are particularly important in 2D systems, where they give rise to large local variations in the condensate density and phase. Vortices are the driving force behind many quantum phase transitions: driven by a thermodynamic energy argument, bound vortex-antivortex pairs with total vorticity charge zero dissociate in large numbers at temperatures above the phase transition point to form free vortices, thereby destroying the long-range order of the quantum state at lower temperatures. This is referred to as the Berezinskii-Kosterlitz-Thouless (BKT) transition [93], which is specific to 2D systems and is also found in Josephson junction arrays, thin disordered superconducting granular films and more recently has been applied to the 2D superconductor insulator transition.
The cost of creating a free vortex of size ξ in a uniform condensate of area A is ([79] p. 452)

$$E = \frac{\pi\hbar^2 N|\psi|^2}{2m^*} \ln\left(\frac{A}{\xi^2}\right) \tag{3.16}$$

The number of possible positions of this vortex in the condensate area is approximately A/ξ^2, so its entropy becomes $S = k_\mathrm{B}\ln(A/\xi^2)$. It follows that the Helmholtz free energy cost $F = E - TS$ associated with the presence of a vortex in a uniform condensate is approximately

$$F \approx \left(\frac{\pi\hbar^2 N|\psi|^2}{2m^*} - k_\mathrm{B}T\right)\ln\left(\frac{A}{\xi^2}\right) \qquad \text{energy cost of a vortex} \tag{3.17}$$

At low temperatures the density of vortices is exponentially small, and their only effect is to reduce the superfluid density. However, above a certain temperature

$$k_\mathrm{B}T_\mathrm{BKT} \approx \frac{\pi\hbar^2 N|\psi|^2}{2m^*} \iff \frac{N}{A}\lambda_\mathrm{dB}^2 = 4 \qquad \text{BKT transition temperature} \tag{3.18}$$

the number of vortices proliferates because $F < 0$, thereby giving rise to a sudden drop in the superfluid density and a drastic reduction in the coherence length. Vortices of opposite charge can form bound pairs thereby reducing the energy cost E by a factor $\ln(\frac{d}{\xi})/\ln(\frac{\sqrt{A}}{\xi})$ with d the vortex separation. In this picture the BKT transition can be viewed as the unbinding of vortex pairs to independent free vortices at $T > T_\mathrm{BKT}$.

The BKT transition is no second-order phase transition with a continuous increase of an order parameter Ψ below the critical point. However, one finds a low-temperature quasi-ordered phase with a first order correlation function $g^{(1)}$ that decreases with the distance r like a power, where the exponent depends on the temperature T:

$$g^{(1)}(\vec{r}) = \langle \Psi^*(\vec{x})\Psi(\vec{x}+\vec{r})\rangle \propto \left(\frac{\xi}{r}\right)^{\frac{T}{T^{2D}}} \qquad \text{BKT phase correlation} \tag{3.19}$$

There is no long-range ($r \to \infty$) correlation but short-range phase order – no BEC but local superfluidity. At high temperatures the disordered phase presents an exponential drop of the correlation function. Such a transition is said to be of infinite order and its underlying mechanism is not yet fully understood [93].

3.2 Simulation of polariton condensates

The vast majority of simulations of polariton condensates describe the spatial dependence and time evolution of a single condensate Ψ, with continuous pumping and decay of polaritons and intrinsic self-interaction term $\hbar g|\Psi|^2$. Two very similar non-linear partial differential equations have proven particularly useful in simulations, the complex Ginzburg-Landau equation (cGLE) and the generalised Gross-Pitaevskii equation (GPE). In this section we concentrate on the first one, although the GPE, adapted to describe polariton condensates, gives analogous results (Sec. 3.2.2).

The complex Ginzburg-Landau equation was originally proposed as a phenomenological model by Vitaly Ginzburg and Lev Landau in 1950 to describe type-I superconductors without examining their microscopic properties. It is now widely used to simulate a vast variety of phenomena from nonlinear waves to second-order phase transitions, from superconductivity, superfluidity and Bose-Einstein condensation to pattern formation in liquid crystals and strings in field theory [94]. The cGLE and modified versions of it [95] are widely used to simulate polariton condensates and show very good qualitative agreement for condensate shapes and time evolution with the right choice of parameters. Computational studies in the field of polariton condensates include vortex formation and decay, phase-locking and Josephson oscillation of two condensates, spin interactions and formation, propagation and decay of vortices and solitons.

Simulating a polariton system remains challenging due to its non-equilibrium and highly interactive nature. The cGLE can be extended with rate equation terms to incorporate the effects of (spatially varying) pumping and decay channels and a saturation term is necessary to prevent

the condensate wavefunction Ψ from growing infinitely. Additional effective potentials describe interactions with reservoir excitons and other semiconductor excitations. Still, both adaptations of the cGLE and GPE do not describe the energy relaxation and the scattering processes of non-resonantly excited polaritons in detail, nor can uncondensed polariton clouds be treated, because the equations work only for a coherent macroscopically occupied state Ψ. In recent years a lot of progress has been made to address these issues, as summarised in the excellent review by Carusotto [45].

3.2.1 Stationary solution in thermal equilibrium

The starting point is the N-particle condensed bosonic wavefunction Ψ for which all single particle wavefunctions $\psi(\vec{x}_i)$ reside in the ground state

$$\Psi(\vec{x}_1, \ldots, \vec{x}_N) = \prod_{i=1}^{N} \psi(\vec{x}_i) \qquad \int_{\mathbb{R}^2} d^{2N}x \, |\Psi(\underline{\vec{x}})|^2 = N \int_{\mathbb{R}^2} d^2x \, |\psi(\vec{x})|^2 = N \tag{3.20}$$

The normalisation of Ψ is defined such that the squared wavefunction corresponds to the condensate density: $\rho(\vec{x}) = |\Psi(\vec{x})|^2$. A many-body system with mutual interactions between all N particles is generally very difficult to solve and therefore often replaced by a 1-body problem where the Hamiltonian becomes

$$\hat{H} = \sum_{i=1}^{N} \left[\frac{\vec{p}_i^2}{2m^*} + V(\vec{x}_i) \right] + U_0 \sum_{i<j} \delta(\vec{x}_i - \vec{x}_j) \tag{3.21}$$

the sum of kinetic and potential energy for each particle plus the pairwise interactions between the particles. $\vec{p}_i = -i\hbar\vec{\nabla}_i$ is the momentum operator, $V(\vec{x}_i)$ is the external potential.

Pairwise interactions have been reduced[1] to an effective contact potential $U_0(\vec{x}_i, \vec{x}_j) = U_0 \, \delta(\vec{x}_i - \vec{x}_j)$, which is valid in a dilute (range of interparticle forces $r_0 \ll d = \sqrt{A/N}$ are much smaller than particle spacing) and cold ($T < T_c$ and only single state is highly occupied, scattering amplitude becomes independent of particle energy and scattering angle) boson gas [45, 79]. In 3D the contact potential $U_0 = \frac{4\pi\hbar^2}{m} a_0$ is related to an s-wave scattering length a_0 which can be positive or negative, depending on whether the pair scattering is repulsive or attractive. In scattering theory, when a_0 diverges, a scattering resonance is found and a bound state is formed. A more complicated dependence is seen 2D: with tight confinement in the z-direction $L_z \ll L_x, L_y$

[1] In general, interactions are mediated via elastic scattering of two particles $\phi(\vec{x}_i)$, $\phi(\vec{x}_j)$ of the form $\iint d^3x_i \, d^3x_j \, |\phi^*(\vec{x}_i)|^2 \, U(\vec{x}_i, \vec{x}_j) \, |\phi(\vec{x}_j)|^2$ where $U(\vec{x}_i, \vec{x}_j)$ is the interaction potential.

the scattering potential becomes [96]

$$U_0^{\mathrm{2D}}(a_0, E) \approx \frac{4\pi\hbar^2}{m^*}\left[\sqrt{2\pi}\frac{L_z}{a_0} + \ln\left(\frac{\hbar\omega_z}{\pi E}\right)\right]^{-1} \qquad \text{scattering potential in 2D} \tag{3.22}$$

with $\omega_z = \hbar/(m^* L_z^2)$ and E the average energy per particle ($k_{\mathrm{B}}T$ for a thermalised 2D bose gas). The interactions change in magnitude and sign from repulsive ($E < E_b^{\mathrm{2D}}$) to attractive ($E > E_b^{\mathrm{2D}}$), depending on whether the energy of the scattering polaritons is smaller or larger than the bound state resonance energy $E_b^{\mathrm{2D}} = \frac{\hbar\omega_z}{\pi}\exp\left(\frac{\sqrt{2\pi}L_z}{a_0}\right)$ (the ln[...] diverges to $\pm\infty$). The bound state corresponds to the formation of a bi-exciton "molecule" which is strongly coupled to the optical field. This so called **Feshbach resonance** was recently observed for polaritons [46], where the energy E of the two polaritons is scanned past the resonance with a change from negative to positive cavity detuning with respect to the bi-exciton transition. In typical experiments the single polariton energies $E(k_{||} = 0)$ are slightly lower than the bi-exciton energy, $E \lesssim E_b^{\mathrm{2D}}$, so that Eq. 3.22 reduces to $U_0^{\mathrm{2D}}(a_0) \approx +\frac{\sqrt{8\pi}\hbar^2}{m^*}\frac{a_0}{L_z}$, i.e. the interactions are repulsive and stronger for tighter QW confinement L_z.

The stationary shape of a condensate in thermal equilibrium[1] is obtained by finding the Ψ (as defined in Eq. 3.20) that minimises the total free energy functional of the system $\mathrm{F}[\Psi] = \langle\Psi|\hat{H} - \mu|\Psi\rangle$ for the lowest μ eigensolution of the stationary Gross-Pitaevskii equation (GPE) [97]

$$\mathrm{F}[\Psi] = \int d^3x\, N\left[-\frac{\hbar^2}{2m}|\vec{\nabla}\psi|^2 + V(\vec{x})|\psi|^2 - \mu|\psi|^2\right] + \frac{N(N-1)}{2}U_0|\psi|^4 \tag{3.23}$$

where the terms are, from left to right, the kinetic energy, the potential energy (including exciton reservoir blueshift, trapping potentials and disorder), the chemical potential and the non-linear polariton-polariton interaction energy. The last term contributes to the blueshift energy and is conventionally rewritten as

$$U_{\mathrm{NL}}|\Psi(\vec{x})|^2 = \frac{N(N-1)}{2}U_0|\psi(\vec{x})|^4 = \hbar g|\Psi(\vec{x})|^4 = \hbar g\,\rho^2(\vec{x}) \qquad \text{interaction energy } g \tag{3.24}$$

where $\hbar g \approx \frac{1}{2}U_0$ is the interaction polariton constant and $\rho(\vec{x}) = N(\vec{x})/A$ is the condensate density. In typical polariton condensates at high pump density $g > 0$ is positive, stating that polariton-polariton interactions are repulsive and increase the total energy of the system (polariton blueshift). The global phase of the wavefunction $\Psi(\vec{x})$ is freely chosen at each realisation of a new condensate (spontaneous U(1) symmetry breaking). In free space the condensates is

[1] This is not really the case for polaritons, which are subject to continuous pumping and decay.

spatially uniform, with a featureless flat shape linked to the chemical potential, $|\Psi_0|^2 = \mu/g$, while in a trap it will assume the inverse shape of the trapping potential. Even in the trapped case $\Psi(\vec{x})$ is purely real, meaning that the phase ϕ_0 of the wavefunction is constant in space and there is no macroscopic current flow [45]

$$\vec{\mathrm{J}} = \frac{1}{2im^*}[\Psi_0^* \vec{\nabla} \Psi_0 - \text{h.c.}] = 0 \tag{3.25}$$

This is not the case in polariton condensates, where the shape $\Psi(\vec{x})$ is determined by the dynamical balance of pumping and losses, which leads to non-zero polariton currents $\vec{\mathrm{J}}$ and a spatially varying wavefunction phase $\phi(\vec{x})$ [see Fig. 5.12(b,f)].

3.2.2 Complex Ginzburg-Landau equation (cGLE)

The most generic form of the complex Ginzburg-Landau equation [94, 95] is a non-linear second-order partial differential equation describing the time evolution of a complex field $A(\vec{x}, t)$:

$$\frac{d}{dt}A = \alpha A + \beta \vec{\nabla}^2 A + \gamma A|A|^2 \qquad\qquad \alpha, \beta, \gamma \text{ complex} \tag{3.26}$$

For polariton simulation a pumping term $\mathcal{P}$ is added and some complex terms are neglected, so that this equation simplifies to what we refer here as the cGLE equation. It describes the time evolution of a BEC with complex order parameter $\Psi(\vec{x}, t)$ in a potential landscape $V(\vec{x})$ with self-interaction $\hbar g|\Psi|^2$ and pumping $\mathcal{P}$ at $T \approx 0$ K (limit of excitations being only a perturbation of the system):

$$i\hbar \frac{d}{dt}\Psi = (1 + i\eta)\underbrace{\left[-\frac{\hbar^2}{2m}\vec{\nabla}^2\Psi + V(\vec{x})\Psi \right]}_{\hat{H}_0\Psi} - \hbar g|\Psi|^2\Psi - i\,\frac{\hbar\gamma_{\text{pol}}}{2}\Psi + i\,\mathcal{P} \tag{3.27}$$

complex Ginzburg-Landau equation

All parameters here are real. The generalised GPE[1] [98] is obtained from Eq. 3.27 by setting the energy relaxation parameter $\eta \to 0$. Since most simulations use $\eta \ll 1$ it becomes obvious why both equations produce similar results and are equally well suited to describe polariton systems. By setting $\eta, \gamma_{\text{pol}}, \mathcal{P} = 0$ the cGLE reduces to conventional GPE and further setting $g = 0$ yields the time-dependent Schrödinger equation $i\hbar\frac{d}{dt}\Psi = \hat{H}_0\Psi$.

The cGLE is based on the mean field approximation, the fact that for a system of many particles

[1] The time dependent GPE is derived in second quantisation formalism from the Heisenberg equation $i\hbar\frac{d}{dt}\hat{\Psi} = [\Psi, \hat{H}]$ with $\hat{H}$ as in Eq. 3.21.

all quantum field operators for photons and excitons $\hat{\Psi}(\vec{x}), \hat{\Psi}(\vec{x})^\dagger$, which are sums of creation and annihilation operators $\hat{a}(k_{||}), \hat{a}^\dagger(k_{||})$ respectively, can be replaced by their expectation values $\Psi(\vec{x}) = \langle\hat{\Psi}(\vec{x})\rangle$. This approximation is made on the pair interaction terms $\hat{\Psi}^\dagger\hat{\Psi}^\dagger\hat{\Psi}\hat{\Psi}$ and breaks down in the photon blockade regime, where a single interacting photon has a non-linear response strong enough to pull the system off resonance, so that no further photon can be absorbed as long as the first one is trapped [45].

Depending on the excitation method, different approaches are used for the pumping term [45] for resonant (or quasi-resonant, i.e. parametric) and non-resonant pumping:

$$\mathcal{P}(\vec{x},t) = \begin{cases} \hbar\beta\, E_{\text{in}}(\vec{x},t) & \text{coherent pumping} \\ \frac{\hbar R}{2}\, n_{\text{R}}(\vec{x},t)\, \Psi(\vec{x},t) & \text{incoherent pumping} \end{cases} \tag{3.28}$$

3.2.2.1 Coherent (resonant) pumping

For coherent pumping $E_{\text{in}}(\vec{x},t) = E_0 \exp[i(\vec{k}_{\text{in}} \cdot \vec{x} - \omega_{\text{in}} t)]$ is the amplitude of the incident laser field and β is the coupling efficiency of the pump light to the polariton mode, which depends on the DBR design, the detuning in E and $\vec{k}$ with respect to the polariton state $(E_{\mathsf{LP}}, k_{||})$ on the dispersion curve and the light polarisation. Resonant excitation will directly excite polaritons with the momentum $k_{||}$ that corresponds to the laser energy, $\hbar\omega_{\text{in}} = E_{\mathsf{LP}}(k_{||})$, rather than gaining the laser momentum k_{in} directly. Thus these polaritons are launched with an initial group velocity $v_g = \vec{\nabla}_k E_{\mathsf{LP}}(k_{||}) \approx \frac{\hbar}{m^*} k_{||}$ and experience ballistic propagation thereafter.

The system response for quasi-resonant pumping is very different depending if the laser is below or above the polariton dispersion curve: in the first case $\hbar\omega_{\text{in}} < E_{\mathsf{LP}}(\vec{k}_{\text{in}})$ (red-detuned pump laser) the condensate density $\rho(\vec{x})$ grows monotonically with pump power P (optical limiter regime), while in the second case $\hbar\omega_{\text{in}} > E_{\mathsf{LP}}(\vec{k}_{\text{in}})$ (blue-detuned) an optical bistability is observed. Here the blueshift suddenly brings the LP branch into resonance with the laser for rising P through a positive feedback mechanism. When P is lowered again the system is kept in resonance for longer by the same feedback, resulting in a hysteresis loop in the PL intensity vs pump power plot. A detailed description of this process and parametric pumping can be found in [45].

3.2.2.2 Incoherent (non-resonant) pumping and reservoir coupling

For incoherent pumping the laser is so far blue-detuned that no direct excitation of the polariton is possible. Instead, the deposited laser energy is converted into high energy excitons which end up populating the incoherent exciton reservoir around the bottleneck region. Polarisation from

the laser is lost in multiple scattering events [99] as the excitons relax in energy, although some polarisation preserving effects are still present for circularly polarised pump laser. At low pump power further relaxation towards the LP ground state through phonon-polariton scattering is slow and a whole range of polariton states around the inflection point and the apex are populated, with state occancies $N \ll 1$. At higher P stimulated pair scattering kicks in, an energy and momentum preserving process where one bottleneck polariton is transferred to a lower $k_{||}$ state, while the other one ends up in the high momentum tail of the LP branch. When stimulation overcomes the losses in a polariton state, then a condensate is formed with $N \gg 1$.

In Eq. 3.28 the feeding of the condensate Ψ from the exciton reservoir of density $n_{\mathrm{R}}(\vec{x},t)$ is described by a relaxation rate R. The condensation threshold is reached for a reservoir population $n_{\mathrm{R}}^{\mathrm{thr}}$ for which $R\,n_{\mathrm{R}}^{\mathrm{thr}} = \gamma_{\mathrm{pol}}$, i.e. gain and loss in Eq. 3.27 balance each other. The population of the reservoir is accounted for by a separate rate equation [100]

$$\frac{d}{dt}n_{\mathrm{R}}(\vec{x},t) = P(\vec{x},t) - \left(\gamma_{\mathrm{R}} + R\,|\Psi(\vec{x},t)|^2\right) n_{\mathrm{R}}(\vec{x},t) + D\vec{\nabla}^2 n_{\mathrm{R}}(\vec{x},t) \qquad (3.29)$$

exciton reservoir population

which balances laser pump rate $P(\vec{x},t)$ with boson-stimulated scattering rate into the condensate $R\,|\Psi(\vec{x},t)|^2$, other reservoir relaxation channels γ_{R} and diffusion $D\vec{\nabla}^2 n_{\mathrm{R}}(\vec{x},t)$ in the plane. According to [45] the relaxation rate γ_{R}, which includes exciton redistribution among the reservoir states, is typically much faster than all other processes so that n_{R} can be adiabatically eliminated ($\frac{d}{dt}n_{\mathrm{R}} = 0$). Neglecting diffusion (D is much smaller for excitons than for polaritons) allows us to rewrite the incoherent pumping term in Eq. 3.27 as:

$$\mathcal{P}(\vec{x},t) = \frac{\hbar R}{2}\frac{P(\vec{x},t)}{R\,|\Psi(\vec{x},t)|^2 + \gamma_{\mathrm{R}}}\,\Psi(\vec{x},t) \qquad \text{incoherent pumping} \qquad (3.30)$$

This expression can be further linearised under the assumption $R\,|\Psi(\vec{x},t)|^2 \ll \gamma_{\mathrm{R}}$ to give a pumping term of the form

$$\frac{\mathcal{P}(\vec{x})}{\hbar\,\Psi(\vec{x},t)} = \alpha(\vec{x}) - \sigma(\vec{x})|\Psi(\vec{x},t)|^2 = \frac{RP(\vec{x})}{2\gamma_{\mathrm{R}}} - \frac{R^2P(\vec{x})}{2\gamma_{\mathrm{R}}^2}\,|\Psi(\vec{x},t)|^2 \qquad (3.31)$$

as used in Eq. 5.12.

3.2.3 Condensate shapes for incoherent pumping

From polariton experiments it is well known that the geometry of the pump spot has a strong influence on the shape in real and k-space of the forming condensate. For a single pump spot

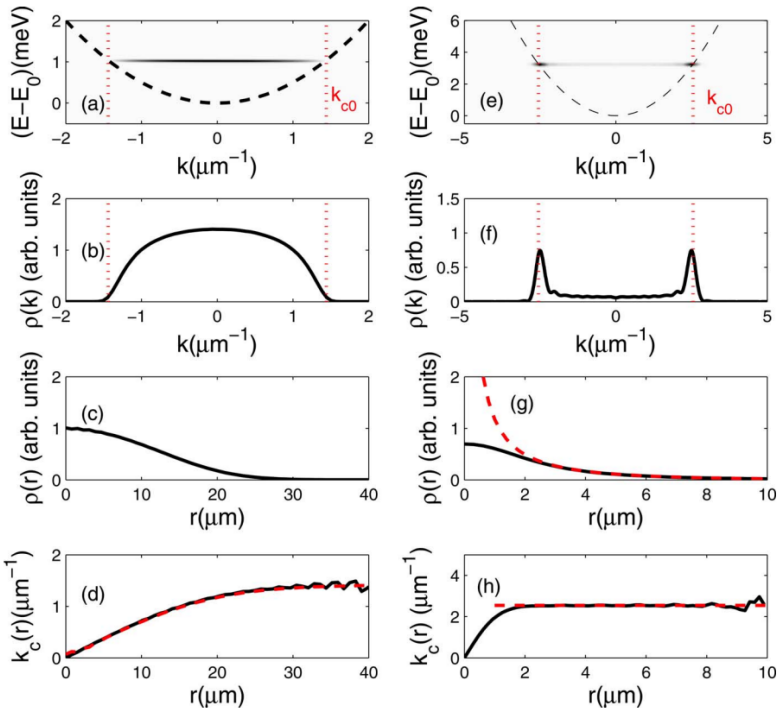

Figure 3.2: Numerical results of generalized GPE simulations in the absence of disorder for (a-d) a large $\varnothing = 20$ μm and (e-h) a small $\varnothing = 2$ μm circular excitation pump spot, respectively. (a,e) give the (k, E) emission pattern, (b,f) the polariton distribution in momentum space, (c,g) the polariton distribution in real space, and (d,h) the local wave vector $k_c(r)$, The wave vector k_{c0} of a free polariton at ω_c is indicated by the dotted lines in (a,b,e,f); the dashed line in (g) is the analytical approximations to the density tail, and the dashed lines in (d,h) are the LDA predictions to the local wave vector. All quantities in real (momentum) space depend only on the radial coordinate $r = |\vec{x}|$ ($k = |\vec{k}_{||}|$). The values of the parameters used in the simulations are as follows: $\hbar g = 0.015$ meV $\cdot$ μm^2, $\hbar\gamma_c = 0.5$ meV, $\hbar\gamma_R = 2$ meV, $\hbar R = 0.05$ meV $\cdot$ μm^2, $\hbar g_R = 0$, $\mathcal{G} = 0.0175$ μm^2, and $P/P_{\text{thr}} = 2$ (left panels) and $P/P_{\text{thr}} = 8$ (right panels). Taken from [88].

the condensate is formed at energy E_c, the highest value of the blueshift energy [88]

$$E_c = E - E_{\mathsf{LP}}(k_{||} = 0) = \max_{\vec{x}} \left[\hbar g_{\mathsf{x}} n_{\mathsf{x}}(\vec{x}) + \hbar g |\Psi(\vec{x})|^2 \right] \tag{3.32}$$

whereby the momentum k_c of the condensate depends sensitively on the size of the pumping spot. A large Gaussian pump spot of diameter $\varnothing \sim 20$ μm or more [88, 101] leads to a stationary condensate in time with spatially varying phase $\phi(\vec{x})$, contrary to an atomic condensate whose phase ϕ_0 is constant in space. The momentum of the condensate is associated to this phase gradient

$$k_c(\vec{x}) = \vec{\nabla}\phi(\vec{x}) \qquad\qquad \text{momentum = phase gradient} \tag{3.33}$$

As shown in the simulation in Fig. 3.2, it increases monotonically with distance $r = |\vec{x}|$ (d), from 0 at the centre to $k_c(\vec{x}) \lesssim \sqrt{2m^* E_c}/\hbar$ at the edges of the condensate, bounded by the free polariton dispersion curve (a). This indicates the presence of non-zero polariton flows $\vec{J} \neq 0$ from gain regions to loss areas, i.e. from the centre of the pump spot to the edge of the condensate. The momentum distribution of the condensate for large pump spot is broad and centred around the origin (b).

On the contrary, focussed excitation spots of $\varnothing \sim 2$ μm or smaller have been shown experimentally [60, 87] and theoretically [88] to form condensates which feature a narrow PL ring in k-space with radius $k_c = \sqrt{2m^* E_c}/\hbar$, whose energy E_c is again fixed by the maximum blueshift at the pump spot (Eq. 3.32). Outflow in this case is still radial, however the acceleration stage is much faster and restricted to the immediate surroundings of the pump spot [Fig. 3.2(h)], so that most of the condensate extends past the exciton blueshift potential and hence expands ballistically at constant end velocity k_c. In this region an analytical solution can catch the asymptotic behaviour of the condensate wavefunction [88]:

$$\Psi(r \to \infty) \approx \frac{\exp(-2\kappa_c r)}{r} \exp(ik_c r) \qquad \kappa_c = \frac{\gamma_{\text{pol}}}{2v_c} = \frac{m^* \gamma_{\text{pol}}}{2\hbar k_c} = \sqrt{\frac{2m^*}{E_c}}\, \gamma_{\text{pol}} \tag{3.34}$$

Most of the condensate density is in the state k_c, directly on the free polariton dispersion curve (e,f), and forms the observed ring in k-space. Furthermore there is a weak pedestal at all momenta from 0 up to $\pm k_c$ stemming from the short acceleration phase around the pump spot. The latter is considerably smaller than the typical spatial decay length $1/\kappa_c \approx 5$ μm of the condensate.

Experimentally measured polariton dispersion curves have more washed out features than the

images presented in Fig. 3.2(a,e). Apart from the mono-energetic condensate mode a "smeared out" dispersion curve is seen [Fig. 6.6(a)]. This is due to the contribution of non-condensed polaritons, which are distributed on dispersion curves with varying blueshift at different locations in space. Monte Carlo simulations of the classical field equations for the Wigner distribution function $P_W[\Psi(\vec{x})]$ [102] describe the polariton dynamics coupled to the exciton reservoir with unprecedented detail. In contrast to earlier cGLE or gGPE simulations, this model includes fluctuations of Ψ, making it suitable to treat also condensates of low density, i.e. to account for the effects of reservoir and non-condensed polaritons [88].

3.2.4 Trapped states: mode competition and mode locking

A very simple and instructive model of two interacting polariton condensates in a 1D trap with incoherent pumping and decay was studied in [75], using the cGLE in Eqs. 3.27 and 3.31. All parameters $g, \gamma_{\mathrm{pol}}, \alpha, \sigma$ are assumed to be homogeneous in space and confinement is provided by a hard wall potential well of length a, with a trap of size b and depth V at its centre [Fig. 3.3(a)]. Two limits are found, depending on whether the non-linear interactions are weak or strong compared to the single-particle level spacing, which is set by the size a of the confining trap.

Strong trapping regime

The first case, $\hbar(g-\sigma)|\Psi_n|^2 \ll E_2 - E_1$, corresponds to tightly confined condensates in a hard-well trap, e.g. a micropillar, and can be treated analytically in perturbation theory. Considering only the two lowest energy states, the overall wavefunction of the systems is

$$\Psi(r,t) = c_1(t)\Psi_1(r) + c_2(t)\Psi_2(r) \tag{3.35}$$

where Ψ_1, Ψ_2 are the first two eigenstates of the linear Hamiltonian $\hat{H}_0$. With a rotating wave approximation $c_1(t) = \exp(-i\frac{g\alpha}{\sigma}t)\sqrt{\rho_1(t)}\exp[-i\phi_1(t)]$ (and analogous for Ψ_2, $1 \leftrightarrow 2$) the density and phase dynamics separate:

$$\frac{d}{dt}\rho_1 = 2\sigma\rho_1\left(\frac{\alpha}{\sigma} - \eta_1\rho_1 - 2\beta\rho_2\right) \qquad (1 \leftrightarrow 2) \tag{3.36}$$

$$\frac{d}{dt}\phi_1 = \frac{E_1}{\hbar} - g\left(\frac{\alpha}{\sigma} - \eta_1\rho_1 - 2\beta\rho_2\right) \tag{3.37}$$

$$\eta_1 = \int dr\,|\Psi_1(r)|^4 \qquad \beta = \int dr\,|\Psi_1(r)|^2|\Psi_2(r)|^2 \tag{3.38}$$

The values η_1, η_2 describe the spatial homogeneity[1] or spread of the state Ψ_1, Ψ_2 and β quantifies the overlap of the trap states Ψ_1 and Ψ_2. Eq. 3.36 describes the population of state Ψ_1 (and Ψ_2), with the terms being stimulated pumping from the reservoir (α is the effective pump rate, σ the gain saturation parameter), spontaneous decay and gain competition (Ψ_2 depletes the same reservoir). There are three steady state solutions ($\frac{d}{dt}\rho_1 = \frac{d}{dt}\rho_2 = 0$) in this system

$$\rho_1^s = \frac{\alpha}{\sigma\eta_1} \qquad \rho_2^s = 0 \qquad \mathrm{S}_1 : \eta_1 < 2\beta \tag{3.39}$$

$$\rho_1^s = 0 \qquad \rho_2^s = \frac{\alpha}{\sigma\eta_2} \qquad \mathrm{S}_2 : \eta_2 < 2\beta \tag{3.40}$$

$$\rho_1^s = \frac{\alpha}{\sigma(\eta_1 - 2\beta)} \qquad \rho_2^s = \frac{\alpha}{\sigma(\eta_2 - 2\beta)} \qquad \mathrm{T} : \eta_1, \eta_2 > 2\beta \tag{3.41}$$

This is illustrated in Fig. 3.3(b) where the parameter space η_1, η_2 can be divided in four regions, S_1, S_2, S_1/S_2 and T, depending on the overlap of the trap states β with respect to the homogeneity η_1, η_2. In T both states Ψ_1 and Ψ_2 are populated simultaneously and share the reservoir resources. In the regime S_1 and S_2 either Ψ_1 or Ψ_2 exceeds condensation threshold while the other state remains without macroscopic population (the more localised state wins). In the dark grey region S_1/S_2, for large overlap β or $\eta_1, \eta_2 < \beta$, the system picks to populate only one of the two states, depending on the initial conditions [75]. For widely separated and/or strongly localised states ($\beta \to 0$ or $\eta \to \infty$, regime T) both states coexist, as also seen for a double well trap with Josephson coupling [103].

Coexistence of condensates can happen with substantial overlap and in traps of widely different shape [Fig. 3.3(a)]. As the diagram in (c) shows, depending on the dimensions of the smaller trap (b and V) the three regimes T, S_2 and S_1/S_2 are possible. For similar trap size $b \lesssim a$ the state overlap is large and initial conditions pick the condensing state. On the other hand, narrow deep traps with $b \ll a$ and $bV > \frac{\hbar^2}{ma}$ allow both condensates to survive at the same time due to small overlap (regime T). In the region S_2 the state Ψ_2 with higher homogeneity survives. The energies E_1, E_2 in the tight trapping case are both blueshifted by the same amount, set purely by the non-resonant pump, as can be seen from inserting the stationary solutions in Eq. 3.27: $E_1 = E_1^0 + \frac{g\alpha}{\sigma}$ and analogous for E_2, independent of the regimes T or S_1 or S_2.

An interesting side note arises from the relations for the lowest three quantum harmonic oscillator functions $\Psi_1^{\mathrm{ho}}, \Psi_2^{\mathrm{ho}}, \Psi_3^{\mathrm{ho}}$ (see Sec. 5.3.2): $\eta_1^{\mathrm{ho}} = 2\beta_{12}^{\mathrm{ho}}, \eta_1^{\mathrm{ho}} > \eta_2^{\mathrm{ho}}, (\eta_2^{\mathrm{ho}} = 2\beta_{13}^{\mathrm{ho}})$. In a perfect harmonic trap with two states the system is exactly on the boundary between the regimes S_2

[1] Small $\eta \ll 1$ means homogeneous density distribution, large $\eta \gtrsim 1$ means high spatial localisation of the density in a single narrow peak.

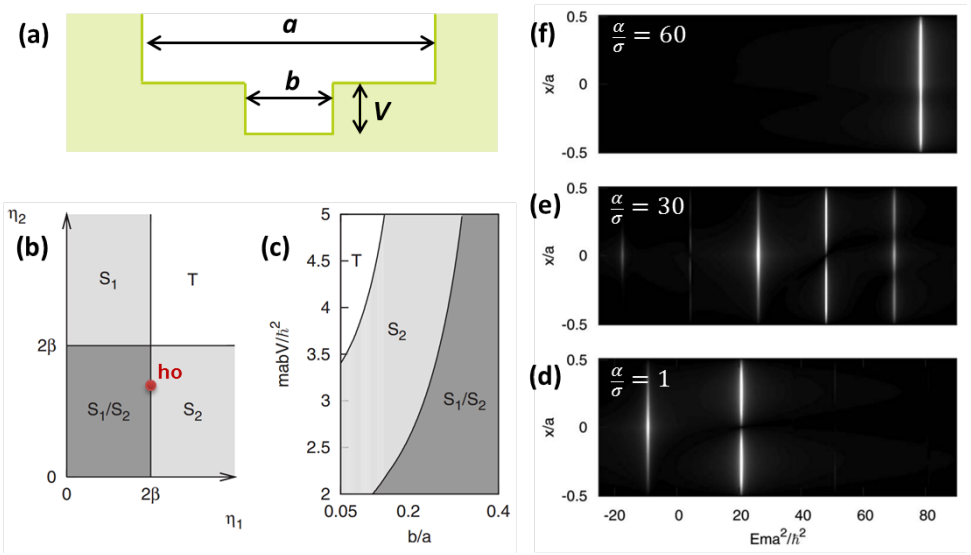

Figure 3.3: (a) Hard-wall trap of length a with a trap of length b and depth V at its centre. (b) Three regimes are present in the tight single trap with $b = V = 0$: T – both states Ψ_1 and Ψ_2 are populated; S_1 and S_2 – either Ψ_1 or Ψ_2 exceed condensation threshold; S_1/S_2 – the system picks to be in Ψ_1 or Ψ_2 depending on initial conditions. (c) Steady state regimes in the two-well trap depicted in (a) as a function of trap geometry a/b and depth. (d-f) Simulated PL emission spectra for the double-well trap for increasing pump power $\alpha = 1, 30, 60$. (b-f) taken from [75].

and S_1/S_2 as marked by the red dot in Fig. 3.3(b), an inherently unstable configuration. Considering that disorder will lead to more localised wavefunctions and reduced overlap, the system might choose to lase from the higher energy state Ψ_2^{ho}. Indeed we see this effect for trapped condensates (see Sec. 5.5.2).

Strong non-linearity regime

The strong non-linearity regime on the other hand, $\hbar(g-\sigma)|\Psi_n|^2 \gtrsim E_2 - E_1$, can only be calculated numerically. The simulation [75] in Fig. 3.3(d-f) shows how the spatial emission spectrum develops with increasing pump power $\frac{\alpha}{\sigma} = 1, 30, 60$ ($\frac{\alpha}{\sigma} = 0$ is the condensation threshold). Parameters used in the simulation are normalised $a = m^* = \sigma = 1$, $\frac{b}{a} = 0.05$, $\frac{Vma^2}{\hbar^2} = 25$, and they highlight strong non-linearities: $g = \sigma$. For low pump power (d) the system is in regime T and the higher energy state is predominantly occupied due to $\eta_2 < \eta_1$. With increasing P additional states become weakly populated in the spectrum (e), a blueshift acts equally on all states and the energy spacings reduce and become equidistant. The third trap state in (e) could be generated by parametric scattering from the two lower states. For high pump power $\frac{\alpha}{\sigma} = 60$ the spectrum suddenly switches to emission at a single frequency (f).

Both effects seen in (e) an (f) can be traced down to the non-resonant terms of the rotating wave approximation, which are neglected in Eqs. 3.36 and 3.37 but not in the simulation. In the two-mode model with states of opposite parity additional Josephson terms

$$i\frac{d}{dt}c_1 = \cdots + \beta(g - i\sigma)(c_1^* c_2)c_2 \qquad (1 \leftrightarrow 2) \tag{3.42}$$

couple the phases of the two condensates, leading to frequency pulling and eventually synchronisation for strong enough interactions. Coupled oscillators synchronise to a common frequency when the phase-phase couplings become comparable with with their energy splitting $E_2 - E_1$, which happens above a critical condensate density, related to a critical pumping strength [75]

$$\frac{\alpha_c}{\sigma} \sim \frac{E_2 - E_1}{\hbar\sqrt{g^2 + \sigma^2}} \tag{3.43}$$

which is at around $\frac{\alpha_c}{\sigma} \approx 40$ for the parameters used in this simulation. The presence of strong interaction in polariton condensates, as opposed to lasers, favours frequency pulling and mode locking. It is expected that at high enough condensate densities, or for large shallow traps, all trap states synchronise to a single frequency. This effect has not been seen experimentally yet, presumably because the polariton-polariton non-linearities $\hbar g$ play a much smaller role within the condensates than previously assumed.

Chapter 4

Experimental Methods

Traditionally, polaritons are excited optically by focussing a single - more or less focussed - laser beam onto the microcavity sample. Instead, in our experiments we employ a spatial light modulator (SLM) to precisely control the excitation laser in position, shape and intensity. This technique is very flexible and present several advantages:

- mechanical beam control is replaced by computerised electrical steering
- intensity control is digital, so that power can be set in a very repeatable way
- multiple (N $>$ 10) laser beams can be steered precisely and independently in 3D (x, y positions and focus z)
- arbitrary laser shapes can be created with a phase pattern generation algorithm
- this system allows to correct for aberrations of the optical setup

Disadvantages of this technique are the lower light efficiency (depending on the type of phase pattern), the need to properly calibrate the SLM for the laser wavelength (it works for one wavelength only) and the necessity for a well aligned optical setup.

This chapter is entirely dedicated to technical aspects of our experiments and starts with a thorough description of the setup (in functional groups) and the microcavity sample in Sec. 4.1. The process of creating laser images using an SLM is illustrated in Sec. 4.2, in which a digital phase modulation (kinoform) is imposed onto the laser beam and subsequently Fourier transformed by a lens, so that the desired laser image forms in the far field. Techniques and algorithms for phase and complex beam modulation are presented in Sec. 4.3, with special focus on iterative algorithms for phase-only modulation of the laser beam. For pure phase modulation there is no jack of all trades algorithm, hence Sec. 4.4 discusses which algorithm performs best for a certain type of laser image. Finally, Sec. 4.5 explains the technique of phase retrieval from an interferogram, which is used to measure the spatial variation of the phase of the polariton condensate cloud.

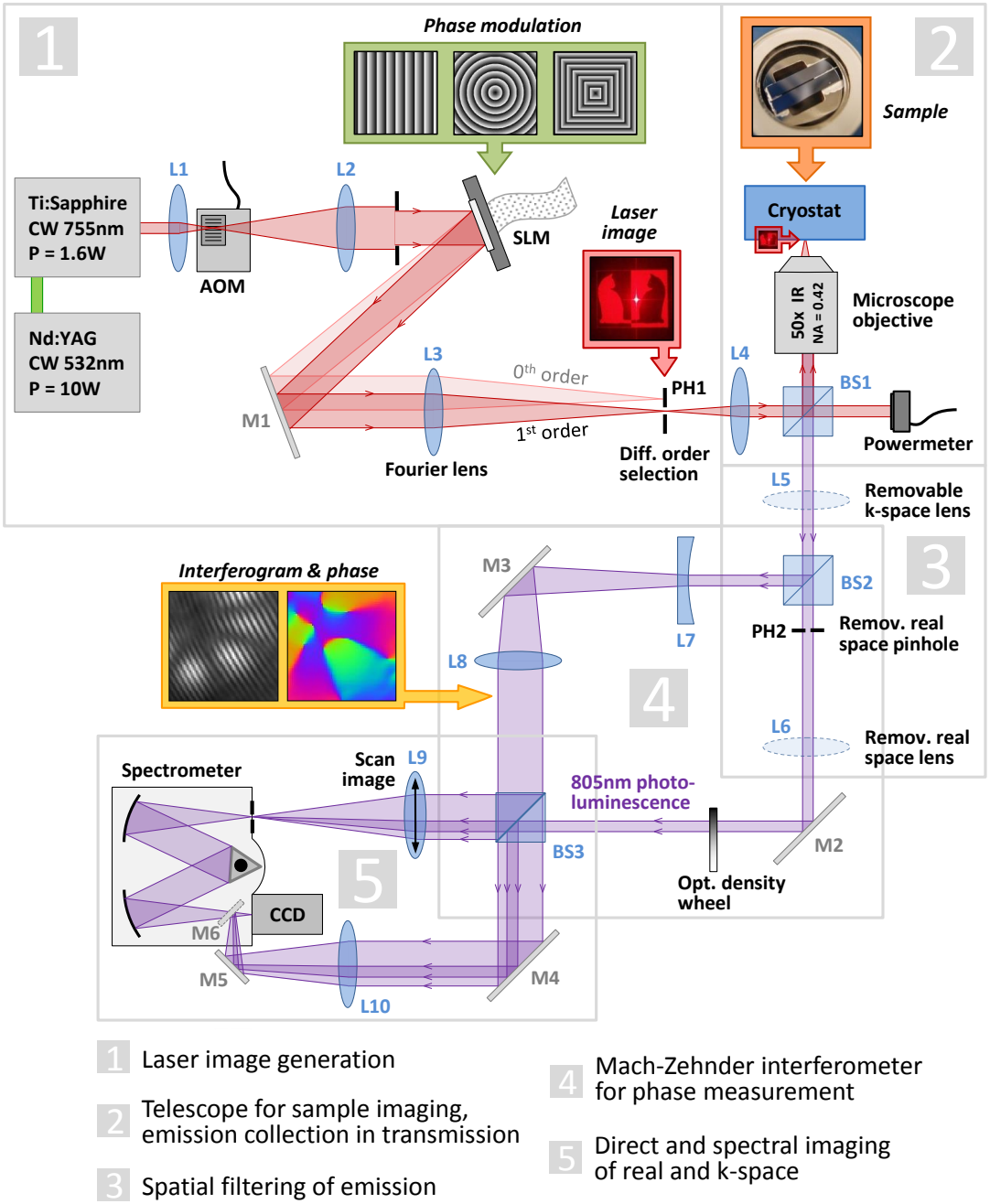

Figure 4.1: Experimental Setup: A laser image, phase-modulated onto the pump beam, is projected on the sample inside the cryostat to produce polaritons. The photoluminescence is collected with the microscope objective and analysed with a real and k-space imaging setup including a spectrometer and an interferometer. Details on the optical elements and acronyms are collected in Tab. B.1. A detailled picture of the interferometer in rectangle nr 4 with the delay stage (omitted here) is shown in Fig. 4.3.

4.1 Experimental Setup

The experimental setup is depicted in Fig. 4.1 and consist of five main parts:

1. **Laser image generation.** The pump laser beam (red) is expanded and directed onto the spatial light modulator (SLM, explained in Sec. 4.1.1). This computer controlled device modulates the wavefront of the Gaussian beam by adding a spatially varying phase shift. A Fourier lens then transforms the modified beam to the far field in which the laser image is obtained. The spatial phase modulation imprinted by the SLM is generated with an iterative algorithm that uses the desired laser image as input, or calculated directly using grating functions.

2. **Sample imaging and emission collection.** A telescope consisting of a spheric lens and the microscope objective scales the laser image down to micrometer size and projects it onto the sample inside the cryostat. Areas of high light intensity will produce high populations of polaritons, whose luminescence (purple) is collected by the microscope objective and directed to the detection setup.

3. **Spatial filtering of emission.** Some experiments require precise spatial control over the origin of the light to be analysed. With a pinhole placed at an intermediate real space image it is possible to select a small part of the emission, rather than the whole field of view of the microscope objective. This allows precise spatial study of the polariton flow dynamics.

4. **Phase measurements with an interferometer.** In order to study the coherence of the polariton population and to record full phase maps, the detection setup contains a Mach-Zehnder interferometer. The light field in the second arm in this interferometer is magnified to act as a flat phase reference for the interferogram.

5. **Direct and spectral imaging.** This integral part of the setup allows us to record 2D real space (near field) and k-space (far field) images by using the side entrance of the spectrometer (M4-M5-M6). The axial entrance (L9) of the spectrometer spectrally disperses the photoluminescence to record real space or k-space (dispersion curve) resolved spectra. Additional polarisation selectivity is obtained by placing a Wollaston prism between M6 and the CCD camera.

Tab. B.1 lists the important optical elements in the setup shown in Fig. 4.1. All optics are standard N-BK7 singlet lenses from Thorlabs with anti-reflection coating B for near-infrared light (650-1100 nm). Lens curvatures were chosen to minimise spherical aberration, e.g. using

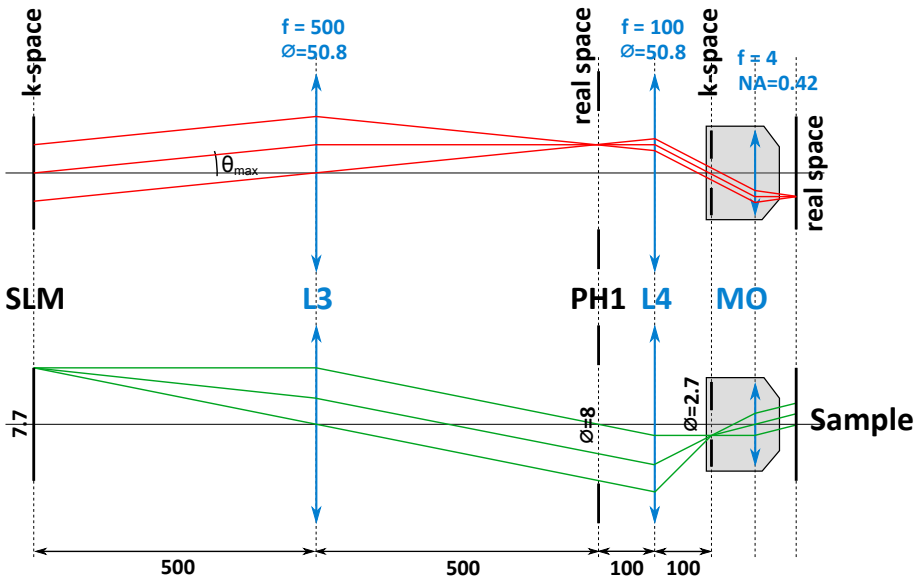

Figure 4.2: Sketch of the optical path from the SLM to the sample. Top: The imaging setup projects the modulated laser beam (k-space) to a real space laser image on the sample. An intermediate laser image is formed in the plane of PH1. Bottom: Ray path for k-space imaging. Distances are in millimetres.

a plano-convex lens with the flat facet facing the focus point of the beam path. The alignment procedures are collected in Appendix B.

4.1.1 Technical details of the experiment

The sample is excited using a 10 W green Nd:Yag **pump laser** (Coherent Verdi V10 or Laser Quantum Finesse Pure) which pumps a tuneable single mode CW Ti:sapphire (Coherent MBR) with a maximum output of 1.6 W at 750 nm. Reliable single mode operation is absolutely crucial to create stable polariton condensates of the type studied in our experiments, even though they are pumped non-resonantly. While both green pump lasers have comparable intensity noise, the Laser Quantum system in combination with the Coherent MBR showed a higher tendency for multi-mode lasing and mode hopping than the Coherent Verdi, which is why we chose the latter one, despite the slightly lower output power of generated NIR laser light.

The **acousto-optic modulator (AOM)** (NEOS Technologies, Model: 23080) in our experiment functions as a combined beam-chopper and intensity filter, to limit sample heating and control the pump power electronically. It is placed in a focus point and uses a plane sound wave in a crystal, travelling perpendicularly to the laser beam, to diffract a controlled amount of laser

light (up to 85%) into the first diffraction order. The AOM is driven by a computer-controlled function generator producing a rectangular waveform. Its amplitude controls the pump power and its duty cycle acts as a variable chopper producing μs pulses of light to reduce sample heating.

A **spatial light modulator (SLM)** can be any object that imposes a spatially varying modulation on a light beam, for example a Fresnel lens with concentric zone plates (amplitude modulation), a thin lens (phase shift modulation through different glass thickness) or a diffraction grating (spatially varying path length). Usually the term SLM describes an electro-optic device with an array of liquid-crystal-filled cells, each of which having its own electrode. Through a voltage applied to such a liquid crystal (LC) cell, the birefringent LC molecules can be aligned in a certain direction, thus changing the effective refractive index of the LC cell. Light passing through such a cell will experience a voltage-dependent phase shift. With a high resolution array of LC cells as in our SLM (BNS P512-0785, highly reflective LCOS device, 100% fill factor, 512×512 px á 15 μm), the wavefront of a laser beam can be phase-modulated arbitrarily, producing any kind of laser images (focussing lens, diffraction grating or complex 2D pictures) by employing a Fourier lens (Fig. 4.4).

Good SLM illumination (even intensity distribution, good collimation) is essential for the creation of good laser images. There is a trade-off between highly even illumination (large laser waist w_0) and high overall diffraction efficiency into the first order (small waist, all the beam's light hits the active area of the SLM). We chose a rather small waist by expanding the laser beam four-fold with a telescope (L1, L2) to get a full waist $w_0 = 7$ mm that matches the size of the SLM. Uneven radial illumination does not affect azimuthally symmetric phase patterns much and can be compensated for in software by tweaking the phase pattern of the SLM. Tests with a beam shaper projecting a square top-hat illumination on the SLM have not shown convincing improvements since the light phase is scrambled after this optical element.
A good trick to compensate for small illumination gradients on the SLM is to have a tip-tilt-mounted mirror M0 before the SLM. This mirror should be far from the SLM so that mostly the position of the laser beam on the SLM is changed, not its angular direction, which would require adjustment of the full optical path after the SLM. It is also helpful to place an iris diaphragm right in front of the SLM to restrict the illumination only to the active area of the SLM, otherwise scattered light affects the symmetry of the first order laser image. A reduction of the illuminated SLM area (the round iris shadows the corners) entails a loss in detail resolution in the laser image.

Projection optics. The SLM is set up to keep the angle between the incoming and the reflected modulated laser beam as small as possible, in our case 11°. The focal length of the

Fourier lens L3 is in principle arbitrary and was chosen to be $f = 500$ mm to form a 0.2× telescope in combination with L4 (Fig. 4.2). The telescope projects the modulated laser light in the SLM plane to the Fourier plane of the microscope objective, while reducing the size of the beam to fit the small back aperture ($\varnothing = 2.7$ mm) of the objective. The microscope objective acts as the final Fourier lens and projects the miniaturised laser image onto the sample. One can equally say that L3 creates an intermediate laser image, while L4 in combination with the microscope objective constitute a strongly de-magnifying telescope with M = 0.04 (rectangle nr 2 in Fig. 4.1).

The **beamsplitter BS1** (Thorlabs BS029 with R:T = 90:10) is necessary to separate the pump laser beam from the collected photoluminescence. This high-reflection-ratio beamsplitter is useful for two reasons: to direct most of the modulated light onto the sample, since the SLM diffraction efficiency is low for complicated laser images, and to collect the emission in transmission, thereby keeping scrambling of polarisation to a minimum. As a side note, we have used a pellicle beamsplitter before changing to the BS029; it worked well for diverting most of the light onto the sample but it terribly scrambles up the polarisation of the emitted light due to the dielectric coating. All beamsplitters in the setup are non-polarising cube beam splitters.

The **pinholes PH1 and PH2** are in fact iris diaphragms and they are used, respectively, to block out the $0^{th}, 2^{nd}$ and all higher diffraction orders and to spatially filter the emission in real space so as to analyse light stemming only from a small part of the polariton condensate. It is handy to be able to adjust the size of the iris for spatial filtering. At its smallest setting we obtain a $\varnothing \sim 0.5$ mm pinhole.

The **spatial tomography group** (rectangle nr 3 in Fig. 4.1) is a simple way to spatially filter the emitted light so as to study only the polaritons in a specific small part of the condensate ($\varnothing \sim 8\ \mu m$). The back aperture of the microscope objective is a k-space plane, which is transformed[1] into real space by L5 at the plane of the iris pinhole PH2. With this pinhole mounted on an x-y translation stage, a very specific part of the real space image can be transmitted and analysed. This technique is particularly useful to study local flow speeds and directions within the polariton condensate and to measure the local blueshift potential strength.

The **Mach-Zehnder interferometer** is used to check the spatial coherence of the polariton condensate and to record a full phasemap of it. It consist of the main beam path BS2-M2-BS3

[1]The lens L5 performs an optical Fourier transformation if the distances [back aperture of microscope objective to lens] and [lens to image plane] correspond to the focal length f. This is called a 2f-configuration.

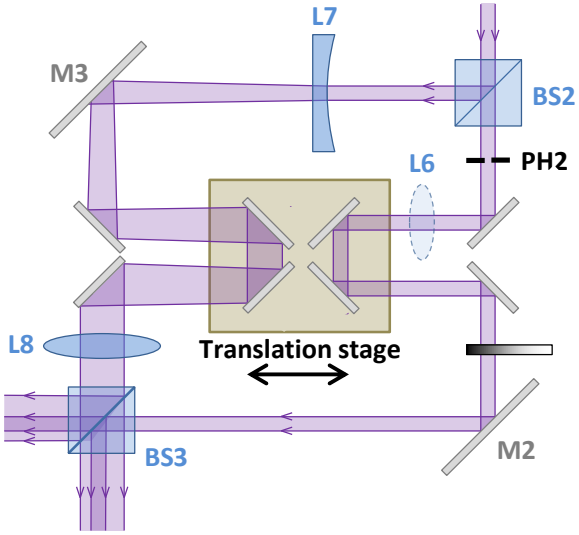

Figure 4.3: Mach-Zehnder interferometer with adjustable path difference.

($L \sim 600$ mm) and a highly magnified (3.75×) reference arm BS2-L7-M3-L8-BS3 (rectangle nr 4 in Fig. 4.1). The output image after BS3 (interferogram) consist of regular fringes as shown in Fig. 4.1. If a uniform part of the condensate (e.g. no "zero-crossings" between lobes) is selected for the phase reference, then the full phase of the condensate's wave function can be recovered with software routines (Sec. 4.5). For good results a properly aligned interferometer is imperative (Sec. B). In order to be able to match the path length in both arms, for maximum fringe contrast, we have used a retro-reflector on a translation stage setup as shown in Fig. 4.3. The path difference can be changed by up to 50 mm without beam misalignment.

The **imaging part** of the setup (rectangle nr 5 in Fig. 4.1) consists of a high spectral resolution 4f-spectrometer (Horiba Triax 550, $f = 550$ mm with 1200 grooves/mm grating) and a high resolution spectroscopy camera (Andor Newton DU940P-FI, front illuminated CCD with 2048×512 px á 13.5 μm). The interferometer offers two outputs, one of which is focussed by L9 onto the vertical spectrometer slit, projecting a real or k-space image on it. A slice of this image is dispersed in energy by the grating and FT-transformed back onto the CCD for real space or k-space (polariton dispersion curves) tomography. The plane for the spectral cut can be selected by moving L9 horizontally and a full spectral tomography $E(x, y)$ or $E(k_x, k_y)$ can by recorded by performing a scan of the L9 position from left to right. The second output of the interferometer is focussed by L10 directly onto the CCD via the flip mirror M6. In combination with the 50× microscope objective this allows for direct real space and k-space imaging. The

magnification is $M_{exp} \sim 88$ (6.6 px per μm) for real space and NA = 0.42, $k_{||,\max} = 3.5/\mu m$ (82.6 px per $1/\mu m$) for k-space.

Polarisation measurements can be performed easily by placing a Wollaston prism (Thorlabs WP10-B) 10-20 mm in front of the CCD camera, which splits the incoming light horizontally into the two orthogonal linear polarisations H (left part of image) and V (right part) with an angular divergence of about $\pm 10°$. Due to the birefringence of the calcite crystal there is horizontal distortion in the H and V images (one is stretched, the other one squeezed by a factor of 1.21), which can be easily compensated for in software.
By setting the waveplates WP1 ($\lambda/4$) and WP2 ($\lambda/2$) (see Fig. 4.1) to the angles as listed in Tab. 4.1 the sample is excited with either linearly (H orizontal or V ertical), circularly (R ight or L eft) or diagonally linear (D iagonal or A nti-diagonal) polarised light, provided the original polarisation of the pump laser is H. Similarly, by adjusting the angles of the waveplates WP3 ($\lambda/4$) and a WP4 ($\lambda/2$) one can measure polarisation directly in all three orthogonal bases H/V, L/R and D/A, whereby the Wollaston prism acts as the analyser[1].

The parameters S_i of the **Stokes vector** $\vec{S} = (S_0, S_1, S_2, S_3)$ can then be computed simply from the intensity differences of the left and right image in each basis [32]:

$$S_1 = \frac{I_H - I_V}{I_H + I_V} \qquad S_2 = \frac{I_R - I_L}{I_R + I_L} \qquad S_3 = \frac{I_D - I_A}{I_D + I_A} \tag{4.1}$$

where $S_0 = \sqrt{S_1^2 + S_2^2 + S_3^2} \leq 1$ is the total degree of polarisation. Our method for measuring the Stokes parameters was favoured over the one presented in [104] because it is much quicker to measure manually. The problem in our case is the slow temporal instability of the polariton condensate, which requires a "single shot" measurement technique, not a lengthy data acquisition for different angle setting with subsequent fit of the transmission data. In our case, 3 images (H/V, R/L, D/A) are sufficient to determine the Stokes parameter for a condensate. In our latest version of the setup all the full Stokes vector $\vec{S}$ is captured in a single shot on the same CCD by using a interferometer with three misaligned arms to separate all three polarisation bases.

[1] H-polarised light goes to the left part of the CCD image, V-polarised light to the right part.

Excitation polarisation	**WP1** $\lambda/4$	**WP2** $\lambda/2$
H	0°	0°
V	0°	45°
R	45°	0°
L	−45°	0°
D	0°	−22.5°
A	0°	22.5°

Projection basis	**WP3** $\lambda/4$	**WP4** $\lambda/2$
H/V	0°	0°
R/L	45°	0°
D/A	45°	22.5°

Table 4.1: List of optical elements in the setup. See Fig. 4.1.

4.1.2 Microcavity sample

The microcavity sample was carefully grown by molecular beam epitaxy (MBE) in an ultra-high vacuum chamber over 12 hours by our collaborators at the Department of Material Science and Technology at the University of Crete. It is made up of a stack of about 100 single-crystalline layers of 100 nm thick $Al_xGa_{1-x}As$ alloys. The well established growing technique for these alloys ensures high optical quality and the material choice (Al, Ga, As) allows to grow structures with large layer number without strain buildup due to lattice mismatch.
The optical resonator consists of two highly reflective Bragg mirrors with 32 (top) and 35 (bottom) alternating layer pairs of $Al_{0.15}Ga_{0.85}As$/AlAs of thickness 57.2/65.4 nm. The enclosed cavity layer has an effective optical length of $\frac{5}{2}\,\lambda_c$, where $\lambda_c = 805$ nm is the design wavelength for the microcavity. A set of three QWs (10 nm GaAs QW, 10 nm $Al_{0.3}Ga_{0.7}As$ spacers) is placed at each one of the four antinode positions of the electric field inside the cavity to guarantee strong coupling of the excitons to the photonic mode.
Experimental measurements reveal a microcavity quality factor exceeding $Q > 16,000$, corresponding to cavity-photon lifetimes $\tau_c > 7$ ps. The exciton-photon Rabi splitting is $\hbar\Omega_R = 9$ meV. All reported experiments were performed at sample positions where the cavity mode is detuned about 7 meV below the exciton energy. This rather negative detuning was chosen as the best compromise of long propagation distance of the condensate (even more negative detuning) and high PL emission but more sample disorder effects (more positive detuning).

4.2 Creating laser images

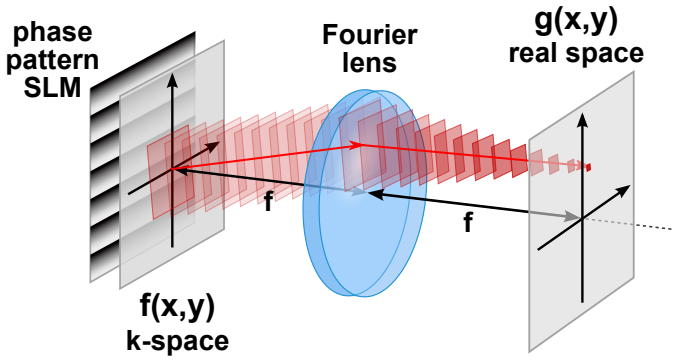

Figure 4.4: Generation of a laser image: A blazed grating phase pattern applied to the SLM tilts the wavefront of the light to deflect the laser beam away from the optical axis. The Fourier lens transforms the incidence angle of the beam into a focussed off-axis spot in the image plane $g(x, y)$.

One of the key features of the setup presented in this thesis is the ability to project laser images onto the sample, rather than just a single focussed spot. The principle for such a complex excitation geometry is depicted in Fig. 4.4. A phase pattern in the form of a blazed grating is applied to the SLM in the k-space plane $f(x, y)$. This tilts the wavefront of the light to deflect the laser beam from the optical axis according to the diffraction grating equation

$$d_g \left(\sin\theta_m + \sin\theta_i\right) = m\lambda \tag{4.2}$$

where d_g is the grating constant, θ_i, θ_m are the input and diffraction angles and m is the diffraction order. A Fourier lens transforms the incidence angle of the beam in the lens plane to a focussed off-axis spot in the image plane $g(x, y)$. The image $g(x, y)$ is then a depiction of all the diffraction angles present in the modulated laser beam $f(x, y)$, it is in fact its Fourier transform[1]:

$$g(x,y) = \mathcal{F}\{f\}(x,y) \equiv F(k_x,k_y)\Big|_{(k_x,k_y)=\frac{2\pi}{\lambda f}(x,y)} \tag{4.4}$$

A Fourier lens is a thin convex lens whose distance from both the k-space and the real space plane is identical to its focal length f. A thin lens of focal length f will analyse the light $f(x, y)$

[1] Capital letters like $F(k_x, k_y) \equiv \mathcal{F}\{f\}(k_x, k_y)$ denote the Fourier transform of the function $f(x, y)$

$$F(k_x,k_y) = \int_{\mathbb{R}^2} d^2x'\, f(x',y')\, \exp[+i\,(k_x x' + k_y y')] \tag{4.3}$$

in a plane located a distance $d = -f$ in front of the lens and image a Fourier transform of this light field $g(x, y)$ onto a plane at $d = +f$ after the lens (Fig. 4.4, Sec. C.2 and Eq. 4.4).
In order to create the intricate laser image, the SLM modulates a specific pre-calculated pattern onto the input laser beam. The latter is assumed to have Gaussian intensity distribution and flat phase profile: $A_{\text{ill}}(x, y) = \left[A_0 \exp\left(\frac{x^2+y^2}{2r_0^2}\right)\right] \exp(i\phi_0)$. For pure phase modulation, as employed in our experiment, the action of the SLM on the light beam can be written as

$$f(x, y) = A_{\text{ill}}(x, y) \xrightarrow{\text{SLM}} A_{\text{ill}}(x, y) \underbrace{\exp[i\,\phi_{\text{SLM}}(x, y)]}_{\text{phase modulation}} \tag{4.5}$$

with $\phi_{\text{SLM}}(x, y)$ being the phase pattern to generate the laser image. A more detailed description of this process is presented in Sec. A.1.

4.2.1 Phase pattern generation

Creating a laser image with a phase-modulating SLM first requires computing a suitable phase pattern (kinoform) from the target image. The phase-modulated laser beam will then produce the desired intensity distribution in the image plane, which is connected to the SLM plane via an optical Fourier transformation (FT). The difficulty of finding the right phase pattern for a desired laser image stems from the fact that the SLM modulates the phase only, while the Fourier transform requires a full complex light field, modulated both in amplitude and phase, to obtain the desired laser image (Fig. 4.5). Hence a simple IFT of the target image is not sufficient to yield a suitable phase pattern for the SLM, which lacks amplitude modulation capability.
The procedure to obtain a laser image from the phase pattern is a follows (see also Fig. 4.6):

1. **Select target image**, rescale it to SLM resolution or smaller and convert to grey scale.

2. **Create initial guess** for input light field.

3. **Calculate phase pattern** to be imprinted onto the SLM with grating formulas (Sec. 4.3.1) or iterative algorithms (Sec. 4.3.2).

4. **Add offset from 0^{th} order** by addition of an offset grating or a focussing lens phase pattern (Sec. 4.2.2), take modulo 2π of phase to restrict values to [0,1).

5. **Calibrate phase response** of SLM by restricting the maximum phase shift for the pump laser wavelength λ_l to $\phi_{\max} = 2\pi\lambda_l/\lambda_{\text{SLM}}$[1] and send phase pattern to SLM.

6. **Modulate resulting phase pattern** onto laser beam and perform an optical FT.

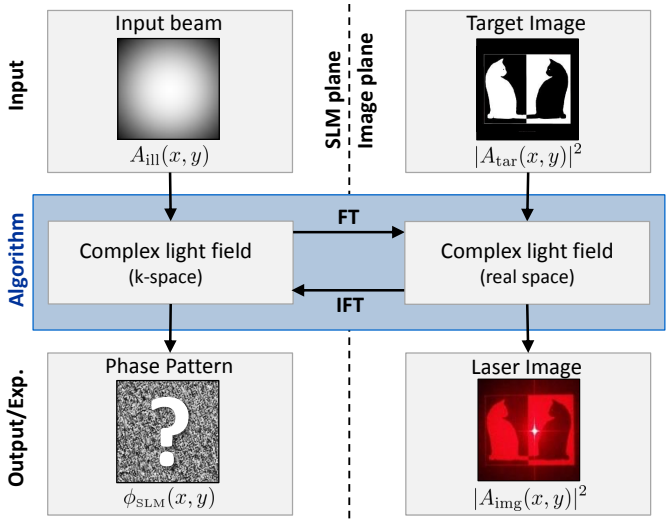

Figure 4.5: Principle of phase pattern generation: Given the target image and the amplitude and phase of the input beam, find the SLM phase pattern $\phi_{\mathrm{SLM}}(x,y)$ that generates the desired laser image after an optical Fourier transformation (FT).

The problem of finding the phase to a given complex field with added constraints is well known under the name "phase retrieval problem" [105, 106, 107]. It has important applications in various fields ranging from X-ray crystallography [108], transmission electron microscopy ([109]), coherent diffractive imaging (holography, laser images), optical wavefront correction in astronomy [110] and ptychographic microscopy [111, 112]. A multitude of methods have been developed to calculate good phase patterns for a given target image, some of which are presented in Sec. 4.3.

4.2.2 Separation from the 0^{th} order and higher order laser images

A fraction of the light hitting the SLM remains unmodulated due to several reasons: fill factor $< 100\%$, residual reflections from the active area of the SLM (despite the anti-reflection coating) and from illuminated non-modulating areas, non-perfect calibration of the 2π phase shift for the pump laser's wavelength, non-linear phase shift response, non-orthogonal angle of incidence of the pump laser and pixelation of the SLM modulation. This results in an unwanted bright and focussed laser spot at the origin of the laser image. Several methods to reduce the intensity of the 0^{th} diffraction order have been developed. One approach relies on producing a modulated light field that interferes destructively with the non-modulated zero-order spot in the laser image plane [113], thus reducing its intensity to a minimum. This approach is quite effective but is implemented only for direct phase pattern calculation algorithms.

[1] λ_{SLM} is the wavelength for which the SLM phase shift response has been calibrated.

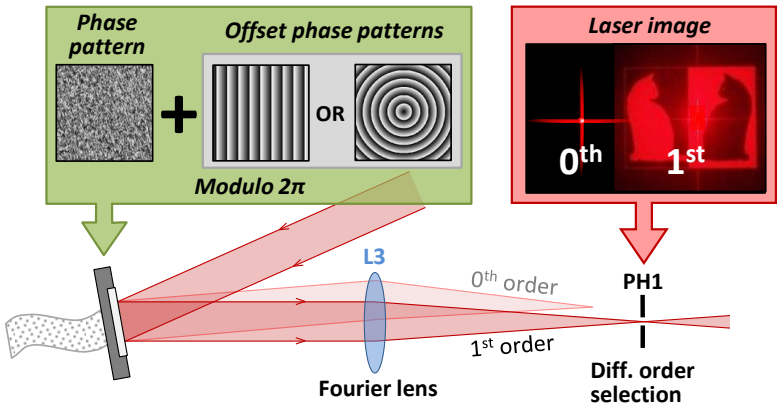

Figure 4.6: Separation from the unmodulated zero order. Adding a lens or offset grating phase pattern spatially separates the different diffraction orders of the laser image.

A more effective and general approach uses lateral or focus offset to separate the unmodulated 0^{th} order from the laser image in the 1^{st} order [114]. The separation is achieved by addition (modulo 2π) of a blazed offset grating, a focussing lens phase pattern or a combination of both (Eqs. 4.7, 4.8, 4.9) to the original phase pattern of the laser image, as shown in Fig. 4.6. As a bonus, this method spatially separates also the higher order diffraction modes, which is very useful to quickly check proper calibration of the SLM for the laser wavelength. If the 2^{nd} order laser image is unusually bright compared to the 1^{st} order, then $\phi_{\text{max}} > 2\pi$ for the used laser wavelength. In case the 1^{st} order and all higher diffraction orders are dark compared to the 0^{th} order, then $\phi_{\text{max}} < 2\pi$. Recalibration of the maximum phase shift can easily be done as described in Sec. A.3.

4.2.3 Kinoform? DOE? Hologram? CGH?

In the literature terms like kinoform, DOE (diffractive optical element), phase pattern, hologram and CGH (computer generated hologram) are sometimes used interchangeably to refer to the spatially varying phase modulation function $\phi_{\text{SLM}}(x, y)$ which is to be imprinted onto the SLM. There is however a clear distinction between these terms, based on whether the output light field is designed to produce an intensity target or a complex target.

Phase pattern, kinoform, DOE: A phase-only modulation of the laser beam optimised for high light efficiency and low background noise. In the image plane only the **intensity of the laser field** is relevant while the phase degree of freedom is used by some algorithms to further improve the DOE performance. Applications include creation of laser images, beam

shaping for industrial applications and beam multiplexing. The name kinoform originally referred to a Fresnel lens and is now used as a synonym for grating-type phase patterns. DOE refers to any optical element that alters the beam path by phase shift means (grating, glass beam shaper), whereas digital DOE stands for an SLM phase pattern only.

Hologram, CGH: A phase-only or complex modulation of the laser beam, optimised to produce a desired **complex light field** which, upon interference with a reference plane wave, will project a hologram. Applications are mainly 3D display technologies with real depth (as opposed to conventional 3D cinema technology with only shallow depth information [115, 116]). In the image plane both amplitude and phase are equally important, so complex modulation is more desirable, even though it is usually significantly less efficient than phase-only modulation.

Various algorithms to create phase patterns (phase modulation) or holograms (complex modulation on an amplitude-only or phase-only spatial modulator) are presented in the next section.

4.3 Algorithms for phase and complex beam modulation

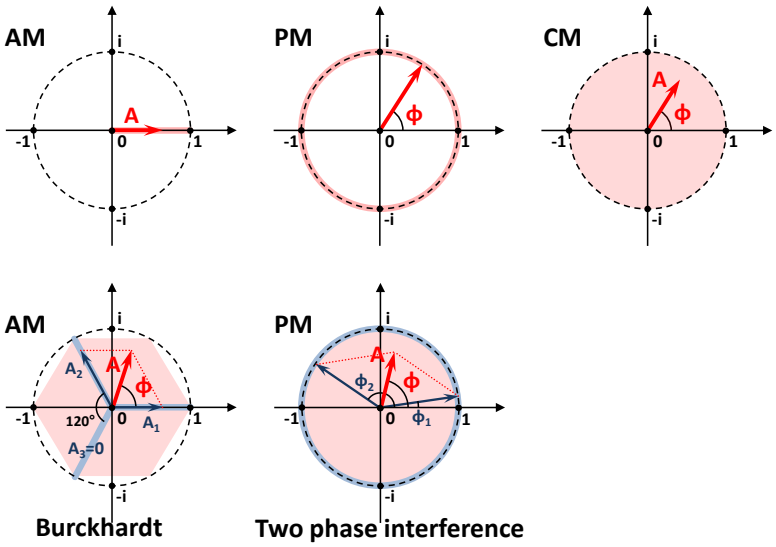

Figure 4.7: Modulation schemes for spatial light modulators: pure amplitude modulation (AM), pure phase modulation (PM), full complex modulation (CM). Bottom row: Schemes for achieving complex modulation using SLMs that can only do AM (Burckhardt method, left) and PM (two phase interference, middle). The shaded red area marks the possible modulation space.

SLMs come in three varieties: devices that modulate the amplitude of the beam only ("pro-

grammable beam masks", similar to a Fresnel zone plate or shadow mask), devices that modulate the phase only ("spatially configurable wave plates", similar to a Fresnel lens or a beam shaper) and mixed forms that modulate phase and amplitude simultaneously (mostly low-cost SLMs, hard to work with because phase and amplitude modulation is coupled). Given the right algorithm to compute the phase or amplitude pattern, any of these types of SLMs are capable of complex modulation (CM), that is combined amplitude (AM) and phase modulation (PM)

$$f(x,y) = A_{\text{ill}}(x,y) \xrightarrow{\text{SLM}} A_{\text{ill}}(x,y) \cdot \underbrace{\overbrace{A_{\text{SLM}}(x,y)}^{\text{AM}} \overbrace{\exp[i\,\phi_{\text{SLM}}(x,y)]}^{\text{PM}}}_{\text{CM}} \tag{4.6}$$

albeit the quality and efficiency of the laser image or hologram varies by orders of magnitude depending on the method.

Regarding the use for kinoforms/holograms, AM is rarely employed nowadays because of its very low light efficiency of typically a few percent or less. Despite this fact, an AM-SLM is capable of complex modulation using a clever scheme called Burckhardt encoding [117, 118] which is used in 3D hologram displays [116]. This algorithm works by creating a laser image offset from the optical axis, so that there is a net path difference of $\Delta d = \lambda/3$ to a point in the laser image between adjacent SLM pixels located in the direction of the offset. With the right offset and by combining three neighbouring AM pixels to one superpixel by vectorial addition of the three phasors spaced by 120°, complex modulation in 83% of the full modulation space (complex unit circle) can be achieved (Fig. 4.7, bottom left).

PM-SLMs are nowadays preferred for most applications because of their high diffraction efficiency and the simpler calculation of phase patterns from the target laser image. There are three approaches to calculate phase patterns (see also Fig. 4.11): analytical kinoforms (grating phase patterns, Sec. 4.3.1), global optimisation methods (find global maximum for a function with very large parameter space, using e.g. direct binary search [119], genetic search algorithms [120], simulated annealing [121] or optimal rotation angle [122]) and, the most popular one, iterative Fourier transform algorithms (IFTA, Sec. 4.3.2). As shown in Fig. 4.7 (bottom middle) it is possible to implement full complex modulation on a single PM-SLM through interfering pairs of pixels with complementary phases ϕ_1 and ϕ_2 [123]. The difficulty is then to interfere the complementary pixels, which was recently shown by [115] with a new monolithic type of phase modulating SLM capable of direct complex modulation. However the efficiency (8.5% in [116]) and resolution of this device is relatively low, which is why traditional phase modulation is still the preferred option. Grating algorithms can easily reach 60% efficiency even for compli-

cated spot/line images, while iterative algorithms typically reach 10-20% efficiency but can be optimised for higher light efficiency at the expense of laser image quality.

4.3.1 Phase patterns from grating formulas

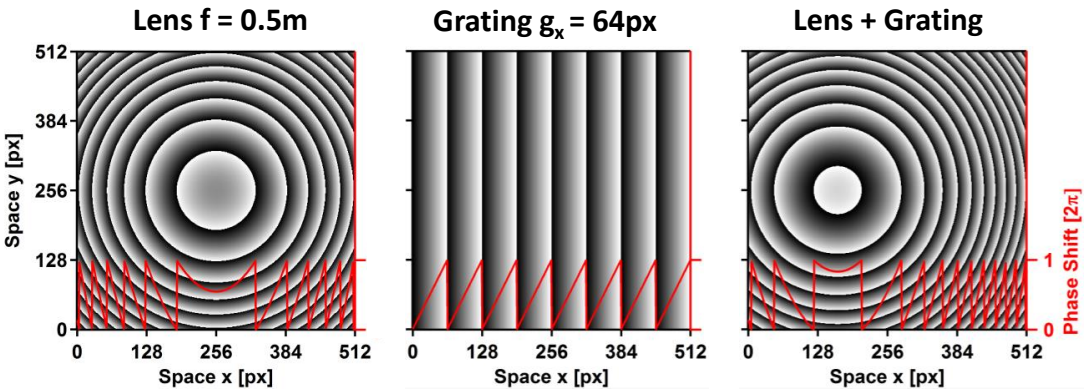

Figure 4.8: Simple phase patterns: focussing lens, blazed grating and a superposition of both. The red line is a horizontal cut through the centre of the pattern. Adding one of these patterns to a phase pattern spatially separates the different diffraction orders of the laser image.

A simple blazed diffraction grating with sawtooth profile (Fig. 4.8 centre) and grating constants g_x, g_y (unit: lines/mm or px for phase pattern) has the ability to efficiently diffract perpendicular light into a specific direction θ_m to the normal (Sec. 4.2 and Eq. 4.2). In combination with the Fourier lens with focal length f this angled plane wave is focussed to a small spot in the laser image plane with position $(x, y) = (f\lambda/g_x, f\lambda/g_y)$. Such diffraction grating phase patterns are very well suited for precise position and intensity control of one or more laser spots in the laser plane.

$$\phi_{\mathrm{SLM}}^{\mathrm{Grating}}(x,y) = A_{\mathrm{grating}} \bmod \left(\frac{x}{g_x} + \frac{y}{g_y} + \phi_0, 1 \right) \qquad \text{Grating} \qquad (4.7)$$

A_{grating} sets the power diverted from the zero order to the first diffraction order. Position control along the optical axis can be obtained with lens phase patterns (Fig. 4.8 left) that curves the wavefront of the laser beam to obtain a focal point at a distance f from the SLM plane – that is without a Fourier lens.

$$\phi_{\mathrm{SLM}}^{\mathrm{Lens}}(x,y) = \mathrm{mod} \left(\frac{\sqrt{x^2+y^2+f^2} - f}{\lambda}, 1 \right) \qquad \text{Lens} \qquad (4.8)$$

In the presence of a Fourier lens this phase pattern shifts the focal point of the laser image backwards and forwards with respect to the image plane of the lens and can be used to fine-tune the focus. With a combination of diffraction grating (x, y control) and lens (z control), 3D position control of multiple spots can be achieved (Fig. 4.8 right). The formula for such a focus/offset shift element is

$$\phi_{\mathrm{SLM}}(x,y) = \mathrm{mod}\left(\phi_{\mathrm{SLM}}^{\mathrm{Lens}}(x,y) + \phi_{\mathrm{SLM}}^{\mathrm{Grating}}(x,y), 1\right) \qquad \text{3D Beam Control} \qquad (4.9)$$

There are several ways to achieve multi-beam control with a single SLM. One option is to divide the SLM into sub-areas, each steering its own laser beam. Due to symmetry reasons (all laser spots should be aligned along a circle) we have chosen to divide the SLM in azimuthal direction as shown in Fig. 4.11(c). For instance, the function

$$\phi_{\mathrm{SLM}}(x,y) = A_n \,\mathrm{mod}\left(\frac{x\,\cos\left[\frac{2\pi}{N}(n+\frac{1}{2})+\alpha\right]}{g} + \frac{y\,\sin\left[\frac{2\pi}{N}(n+\frac{1}{2})+\alpha\right]}{g} + \phi_0, 1\right) \qquad (4.10)$$

$$\text{for segment } n \text{ with } \varphi = \mathrm{atan2}(y,x) \in \left[\frac{2\pi n}{N} + \alpha, \frac{2\pi(n+1)}{N} + \alpha\right) \qquad \text{Multi-Spot}$$

generates the n^{th} segment of a phase pattern with N spots and $n = 1, 2, ..., N$. Here g is controlling the radius of the circle on which the laser spots are located, A_n is the intensity of the n^{th} laser beam and α a rotation angle turning the orientation of the segment.
With an SLM it is surprisingly simple to shape a laser beam into a circle of light by employing a grating in the radial direction (a cone-shaped "Fresnel lens"). The radius of the circle is again set by the grating constant: $r = f\lambda/g_r$. The function for such a digital axicon ($g_x = g_y = g_r$, otherwise the laser image is an ellipse) is

$$\phi_{\mathrm{SLM}}^{\mathrm{Circle}}(x,y) = A_{\mathrm{grating}}\,\mathrm{mod}\left(\sqrt{\left(\frac{x}{g_x}\right)^2 + \left(\frac{y}{g_y}\right)^2} + \phi_0, 1\right) \qquad \text{Axicon} \qquad (4.11)$$

As a side note, subdivision of the SLM into a chequerboard, where each neighbouring pixel belongs to a different laser beam, is favourable when highly uniform intensity distribution in the beams is required (every laser beam gets light from every part of the SLM, as opposed to the pattern in Eq. 4.10). However this method suffers from a high fraction of scattered light and lower diffraction efficiency due to pixel cross-talk.

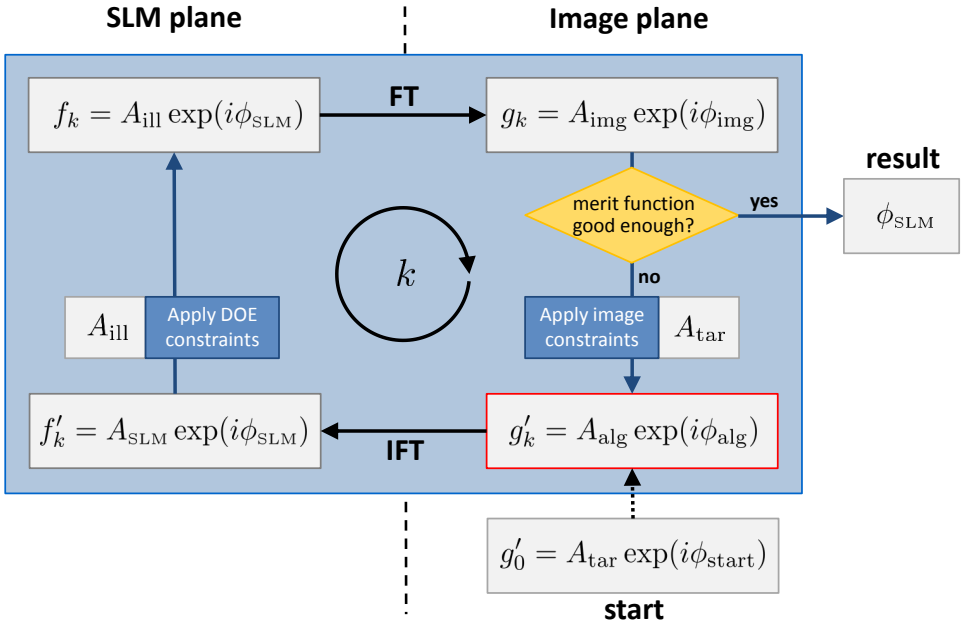

Figure 4.9: Scheme of iterative Fourier transform algorithms (IFTA). A complex field is Fourier-transformed back and forth between the direct and Fourier space, while simultaneously fulfilling constraints in both domains. Goal is optimisation of ϕ_{SLM} for a given target image $|A_{\text{tar}}|^2$.

4.3.2 Iterative Fourier transform algorithms

Iterative Fourier transform algorithms (IFTA) are a class of algorithms that Fourier-transform[1] a complex (light) field $A(x, y)\ \exp[i\,\phi(x, y)]$ back and forth between the real and the Fourier space, while fulfilling constraints in either domain (Fig. 4.9). The task is to find and optimise a phase pattern $\phi_{\text{SLM}}(x, y)$ to produce a good laser image $|A_{\text{img}}(x, y)|^2 \approx I_{\text{tar}}(x, y)$ that approximates the target image as closely as possible. For clarity the spatial dependencies (x, y) for the functions f, g, A, ϕ will be omitted in the following notation.

The starting point is the desired laser image amplitude A_{tar}, the given illumination distribution on the SLM A_{ill} (Eq. 4.5, Fig. 4.5) and an educated guess of the light field g'_0 in the image plane. An inverse Fourier transform (IFT) switches g'_k (with the iteration number $k = 0, 1, ...$) from the image plane to the SLM plane where f'_k is subjected to DOE constraints: its amplitude is set

[1] There is no restriction of IFTA-type algorithms to Fourier transform only, in fact any reversible transform, e.g. Fresnel transform, can be used [124, 125].

to the illumination distribution $A_{\mathrm{SLM}} \longrightarrow A_{\mathrm{ill}}$, while the phase ϕ_{SLM} can be freely modulated[1]. A subsequent FT brings the resulting field f_k back to the image plane to yield g_k, the complex amplitude of the laser image at iteration k. In the next step the value of the merit function MF is calculated from comparing the squared errorsfor each pixel between I_{img} and I_{tar}

$$\mathrm{MF} = \frac{\sum_{x,y} \left(|A_{\mathrm{img}}|^2 - |A_{\mathrm{tar}}|^2\right)^2}{\sum_{x,y} |A_{\mathrm{tar}}|^4} \qquad \text{merit function} \tag{4.12}$$

The MF decreases with the number of iterations k thus showing improved similarity of laser image and target image. If the value of the MF is still changes substantial compared to the previous iteration, then computation continues. The following image constraints are specific to the type of IFTA algorithm and affect both the amplitude and phase of the light field: $A_{\mathrm{img}} \exp(i\phi_{\mathrm{img}}) \longrightarrow A_{\mathrm{alg}} \exp(i\phi_{\mathrm{alg}})$. The underlying idea is to impose the target laser image amplitude $A_{\mathrm{tar}} = \sqrt{I_{\mathrm{img}}}$ while still retaining most of the phase and part of the amplitude information in g_k in a way that allows the algorithm to steadily converge to a global optimum without stagnating around a local minimum. Many IFTA algortihms have adjustable parameters in this part of the iteration to tweak the result for high efficiency or for low noise laser images, as will be explained in the next paragraph. Finally, when the MF changes tend to zero[2] the algorithm loop is exited and $\phi_{\mathrm{SLM}}(x, y)$, the phase pattern of the kinoform, is returned.

If the desired light distribution in the laser image has to be strictly enforced only in a smaller central signal region, then the outside or noise area can be used to improve image quality in the signal area. There are three types of design freedom for phase-only kinoform laser images: phase freedom, amplitude freedom in the noise area and a technique called over-tensing by which the intensity in the noise area is increased for improved signal fidelity. The latter technique (see Sec. 4.3.3) can be use to tune most algorithms between better signal quality and higher light efficiency in the signal region.

A few prominent IFTA algorithms are explained in the following list, based in parts on the excellent review by Ripoll et al. [126]. Specifically, the differences in finding a new starting point or constraint feedback (red box in Fig. 4.9) for the next iteration

$$g'_{k+1} \equiv A_{\mathrm{alg},k+1} \exp(i\phi_{\mathrm{alg},k+1}) = \mathrm{func}(g_k, g'_k, A_{\mathrm{tar}}) \tag{4.13}$$

[1] Provided the SLM has enough modulation levels. If the kinoform is only binary (phase levels 0 and π), 4 or 8 level then soft quantisation is imposed as an additional constraint (Sec. 4.3.3)

[2] The absolute value is no measure for the quality of the kinoform, since it strongly depends on the shape of the target laser image.

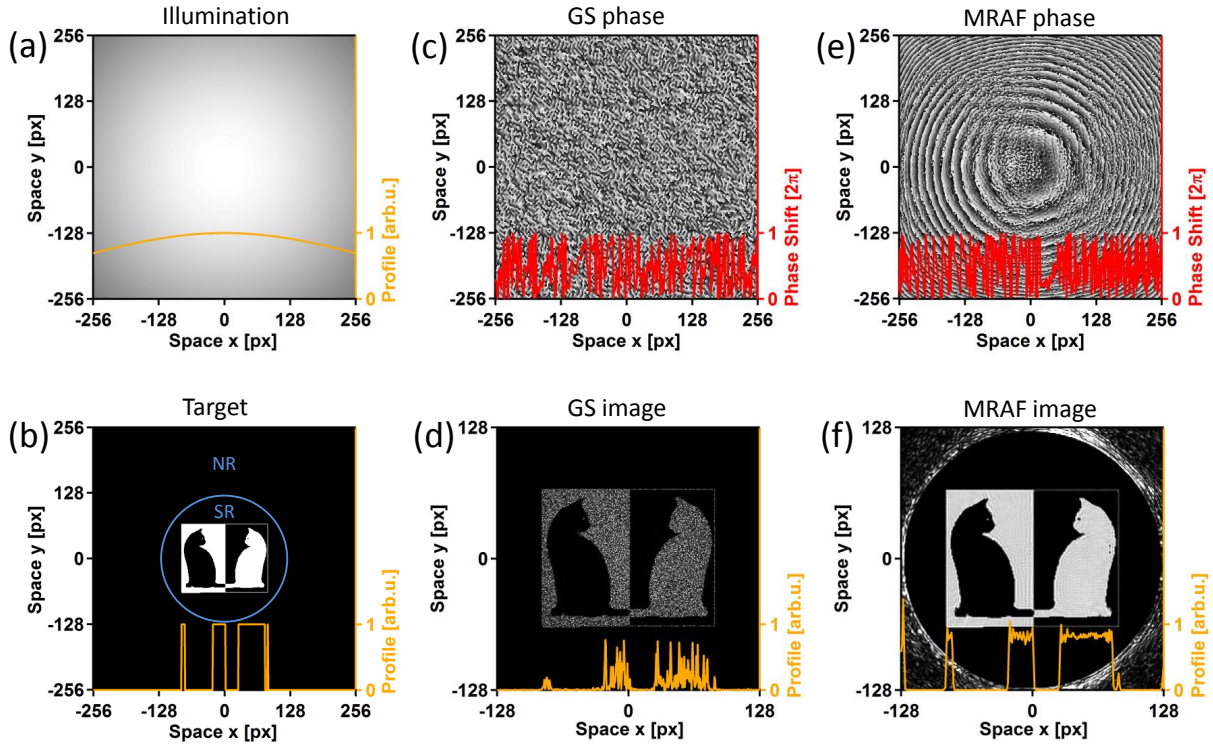

Figure 4.10: Comparison of phase patterns and simulated laser images (normalised) generated with the GS (c,d) and the MRAF algorithm (e,f) using a binary cat image as target (a) and Gaussian illumination (b). In contrast to the MRAF image, the GS picture quality is severely limited by speckle noise. The blue circle in (b) delimits the signal (SR) from the noise region (NR) for the MRAF calculation. Profiles are cuts through $y = 0$. Parameters: $N = 50$ iterations and (f) m = 0.3, $r_{\mathrm{SR}} = 125$ px. The SLM's resolution is 512×512 px.

are outlined and the performance figures in terms of light efficiency, noise and target shape are compared. More complex algorithms sometimes allow faster convergence, but mostly avoid stagnation at local minima at the expense of additional complexity to find the optimum feedback parameters.

Gerchberg Saxton (GS) algorithm: Adapted from phase retrieval techniques [127], this algorithm was the first IFTA to open up phase pattern calculation to non-mathematicians owing to its simple calculation and low computing effort. Due to its trivial constraint feedback $g'_{k+1} = A_{\mathrm{tar}} \exp(i\phi_{\mathrm{img},k})$ with no adjustable parameters (also known as error correction algorithm), convergence is slow and it can easily get trapped in local minima. It tends to produce laser images with strong speckle noise. Thanks to its simplicity many tweaks have been proposed for it, resulting in the variety of IFTA algorithms we use today.

Output-output (OO) algorithm: Based on the GS algorithm, this variant is the best performing one of the input-output algorithm class [106, 128] according to [126]. It offers a parameter β in the constraint feedback:

$$g'_{k+1} = g_k + \beta \left\{ A_{\text{tar}} \left[2 \exp(i\phi_{\text{img},k}) - \exp(i\phi_{\text{alg},k}) \right] - g_k \right\} \tag{4.14}$$

With the parameter choice $\beta \sim 1$ (tuning β has very little effect) the output-output algorithm gives, by design, better efficiency and faster convergence than the GS algorithm, albeit it cannot compete with more modern multi-stage algorithms like 3S.

Over-compensation (OC) algorithm: This algorithm [129] was proposed for highly efficient fan-out elements (beamsplitter) and is based on enhancement or suppression of values smaller or larger than the average target amplitude: $g'_{k+1} = A_{\text{alg},k} \frac{\langle A_{\text{tar}} \rangle}{A_{\text{img},k}} \exp(i\phi_{\text{img},k})$ with $\frac{\langle A_{\text{tar}} \rangle}{A_{\text{img},k}}$ the weighing factor for over-compensation, where $\langle A_{\text{tar}} \rangle$ is the average intensity of the target image. Because of its denominator, care has to be taken in areas where $A_{\text{img},k}$ tends to zero. Additionally, the total intensity has to be renormalised at each iteration. OC is a speciality algorithm that shows very good performance for tasks like beam shaping (top-hat) and beam splitting, where a non-zero, highly clean signal area is the target. It is not suited for laser images with zero regions or low intensity areas like a Gaussian profile. It is not tuneable since it is insensitive to over-tensing.

Three-step (3S) algorithm: The iteration process of this algorithm is a combination of three stages [126]. In the first one a kinoform for optimal efficiency is found using the GS or, preferentially, the OO algorithm (phase freedom). Most importantly, a good choice of starting phase by geometric phase initialisation (Sec. 4.3.3) is imperative to further improve the kinoform. In the second step the amplitude freedom of the noise area is switched on to improve the signal image quality. Third, soft quantisation is introduced to restrict the phases to a discrete set of values (e.g. $n = 4$ values: $0, \frac{\pi}{2}, \pi, \frac{3\pi}{2}$). Soft quantisation (see Sec. 4.3.3) is not needed for modern SLMs with 8-bit or 16-bit addressing, nevertheless it can introduce additional design freedom even for $n = 256$ to further avoid stagnation. Obviously, this algorithm is a good choice for binary or 4-level kinoforms, as used to produce monolithic beam shaping optical elements. The 3S algorithm is applicable to a wide range of designs (beam splitting and shaping, image generation). It is very flexible due to the soft quantisation step and highly tuneable due to the large number of parameters. Performance-wise it is better than GS and OO, whereas OC can show slighlty better results for specific designs (see above). Thanks to the amplitude freedom, it is particularly well suited to laser images that require a clean, low-noise zero window around the signal area.

Arrizón algorithm: This is an interesting and somewhat different algorithm [130] introduced for designing continuous profile laser images consisting of connected lines and spots, which present parageometric kinoforms without phase vortices (phase can be unwrapped). It implements an advanced geometric starting phase (Sec. 4.3.3) and decreases the overtensing parameter in the course of the optimisation process to yield a good compromise of efficiency and laser image quality.

MRAF algorithm: A very good algorithm called "mixed-region amplitude freedom" (MRAF) was proposed recently by Pasienski and Brian [131]. While the ideas behind it are not new, it is a very versatile and powerful yet simple algorithm that combines geometric phase initialisation, GS-IFTA calculation and extensive use of amplitude freedom outside the signal region. A single mixing parameter $\mathrm{m} \in (0, 1]$ controls the trade-off between efficiency ($\mathrm{m} = 1$) and signal quality ($\mathrm{m} \ll 1$). The advantages are manifold: fast and very simple to use, it produces neat clean laser images at the expense of light efficiency (typically an order of magnitude better in roughness and a factor 3 less efficient than the traditional GS or OC algorithms). Drawbacks of MRAF-computation are the low efficiency, which in practical terms goes down to 10-20% for $\mathrm{m} \sim 0.4$, and the occasional appearance of vortices in the phase of the light field in the image plane [131]. The feedback mechanism in the MRAF algorithm is:

$$g'_{k+1} = \left[\mathrm{m}\, A_{\mathrm{tar}}\big|_{\mathrm{SR}} + (1 - \mathrm{m})\, A_{\mathrm{img},k}\big|_{\mathrm{NR}}\right] \exp(i\phi_{\mathrm{img},k}) \tag{4.15}$$

If R is the full image plane matrix, then SR is the signal region around the desired laser image (e.g. a square or circle of radius r_{SR}, the second optimisation parameter) and NR=R\SR is the rest of the image plane matrix where amplitude freedom is allowed in addition to the global phase freedom [see Fig. 4.10(b)]. The algorithm enforces the target intensity only in a bounded signal region (SR) of the 2D laser image while the noise region (NR) is filled with speckles and has to be blocked in the image plane (PH1 in Fig. 4.6). Additionally, the complex light field is computed in a matrix 4 times the size of the SLM, which is imperative for good performance of any IFTA algorithm (see Sec. 4.3.3).
The MRAF algorithm is well suited for optical trapping in fields like atom optics [132] or polariton condensation [43, 73], where frequent and hassle-free recalculation of the hologram is as important as good optical smoothness and sharply defined boundaries. In terms of designs it is suited to shapes consisting of geometric lines and spots (Fig. 4.11) and to grey-scale images (Fig. A.1) and beam shaping applications (Fig. 4.10). It prefers lightly smoothed edges over step-like discontinuities and convincingly imposes zero intensity windows if necessary.

OMRAF algorithm: A recent evolution of MRAF algorithm which adds a background offset $\Delta \sim 0.1\,\max(\mathrm{A_{tar}})$ to the light amplitude of $A_{\mathrm{tar}} \longrightarrow \sqrt{A_{\mathrm{tar}}^2 + \Delta^2}$ of the signal area (O(ffset)MRAF, [132]). This removes a priori most of the optical vortices (reduction by factor ~ 10) from the signal area since they can form only in zero intensity regions. At the cost of halving the efficiency the RMS roughness in the laser image can be reduced to $\sim 7\%$ RMS for binary images (experimentally verified).

The second new feature of OMRAF is the modified propagation of the complex light field between the SLM and the image plane. Instead of using Fourier transformation (which already neglects the phase factor h_0 in Eq. C.19) it employs a Helmholtz propagation operator $\mathcal{P}$ isomorphic to the one given in Eq. C.14. This complex operator calculates the propagation from the SLM to the Fourier lens at $z = f$, followed by the lens' refraction action (Eq. C.13) and subsequent propagation to $z = 2f$ in the image plane. It uses the full expression of the free space propagation operator (Eq. C.6) without resorting to the commonly used paraxial approximation ($\xi = {}^1\!/_8\, kf\,\theta_{\mathrm{max}}^4 \approx 1$ is not much smaller than π, see Eq. C.7). According to [132] this leads to a further reduction of the RMS laser image roughness of 35% and gets rid of diffraction fringes at sharp edges. It has to be noted that, due to our longer focal length Fourier lens ($f = 500$ vs 200 mm) and the fact that mostly $\theta \ll \theta_{\mathrm{max}}$, this correction will not be as effective for our setup.

4.3.3 Techniques for IFTA algorithms

This section presents a list of useful general techniques to improve the kinoforms of IFTA algorithms for different target laser image requirements.

Geometric starting phase: Optimisation algorithms perform better with a starting guess that is already close to the final result. In IFTA algorithms a geometric start phase ϕ_{SLM} highly improves the output kinoform because it directs and pre-focusses the light field in such a way to the image plane that good overlap with the target image is achieved from the first iteration: $A_{\mathrm{img},k=0} \approx A_{\mathrm{tar}}$. The right form of initial phase distribution has to be used to avoid spontaneous creation of optical vortices in the image plane which can only rarely be removed by the algorithm [133]. The final result deteriorates considerably in the presence of vortices in the form of dark spots of 2×2 px with phase winding of 2π. Suitable phase functions are [131] gratings (lateral offsets), lenses (focus to target image dimension) and axicons (create holes in light field) [see Sec. 4.3.1], whose parameters f, g_x, g_y are adjusted manually to roughly match the outlines of the target image. In contrast to random or flat initial phase functions, geometric phases retain most of their initial shape because they are already a good estimate for the final kinoform. Such phase

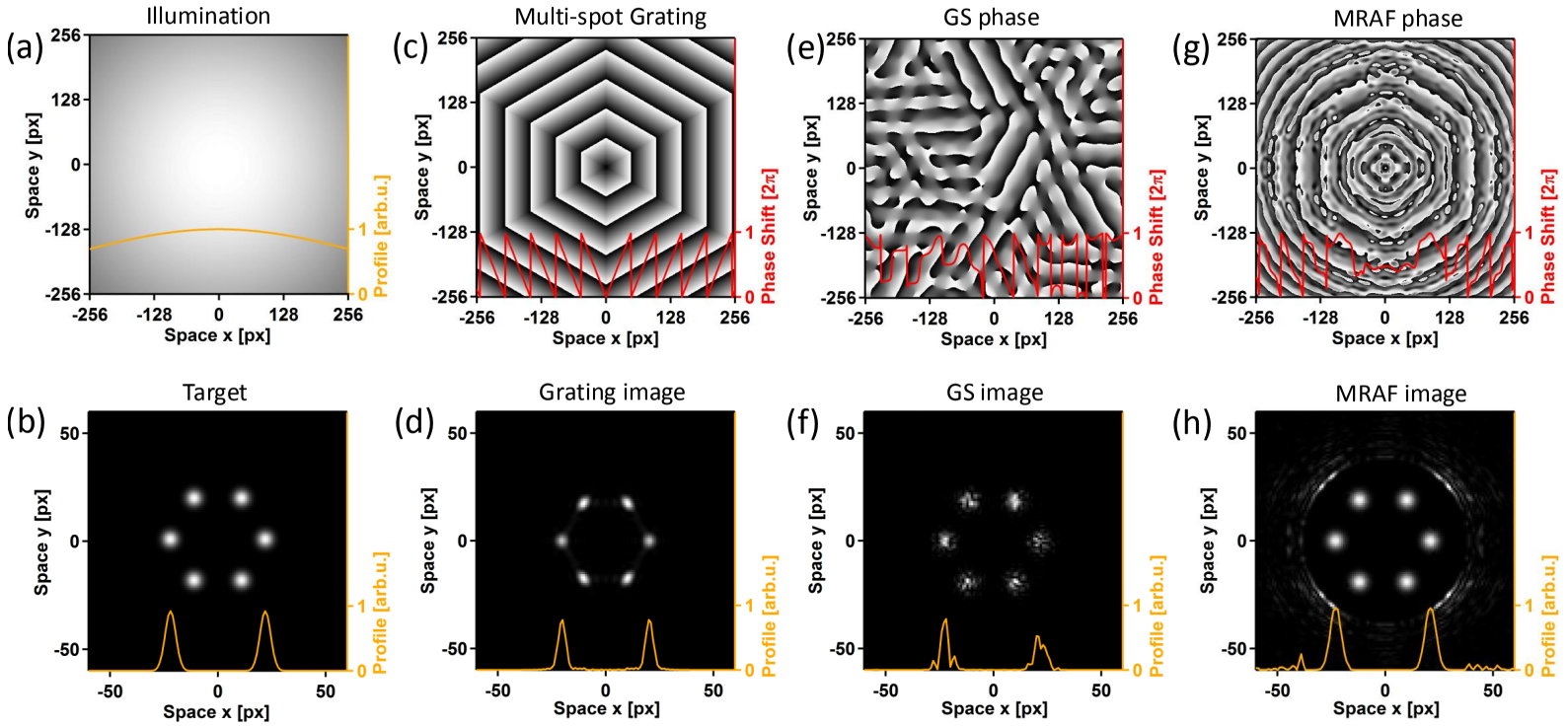

Figure 4.11: Comparison of phase patterns to produce the same laser image with 6 Gaussian spots arranged along a circle: (a,b) illumination and target image, (c,d) analytic grating phase patterns, (e,f) Gerchberg-Saxton (GS) algorithm and (g,h) MRAF algorithm. The simulated laser images are normalised, profiles are cuts along $y = 0$. Outstanding properties for each method: (d) highly efficient with clean background but spots slightly distorted, (f) rather good efficiency but strong speckle noise, (h) very good approximation of the target but rather low efficiency and removal of noise region needed.

Parameters: (b) Gaussian spots with 5 px FWHM and diametrically separated by 44 px, (c) grating constant $g = 25$ px, (e) $N = 50$ iterations, (g) $N = 50$ iterations, m = 0.5 and signal area radius $r_{\mathrm{SR}} = 38$ px.

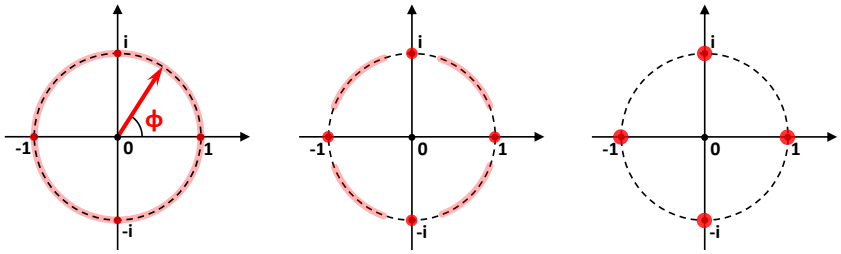

Figure 4.12: Soft Quantisation: permitted phase values (light red) are progressively projected onto quantised values (red dots).

patterns, as shown in Fig. 4.11(g), are called parageometric phase patterns and have the advantage that they can, due to the low number of vortices, be unwrapped in some cases.

Over-tensing: Is a simple technique to make many IFTA algorithms tuneable on the axis

$$\textbf{light efficiency} \xleftrightarrow{\gamma_o} \textbf{laser image quality}$$

$$g'_{k+1} \equiv A_{\mathrm{alg},k+1} \exp(i\phi_{\mathrm{alg},k+1}) = \gamma_o \,\mathrm{func}(g_k, g'_k, A_{\mathrm{tar}}) \tag{4.16}$$

that uses an enhanced ($\gamma_o > 1$, over-tensing, improve efficiency of phase pattern) or reduced feedback ($\gamma_o < 1$, under-tensing, results in cleaner, higher quality laser images) in Eq. 4.13. Over-tensing can, amongst others, easily be implemented with the GS and 3S algorithm. In this aspect, MRAF is also an over-tensing algorithm tuned towards better image quality ($\mathrm{m} < 1$).

Soft Quantisation: Some applications, like fabrication of monolithic optical elements for beam shaping, require kinoforms with a discrete number ($n = 2, 4, 8, ...$) of phase levels. The values of the phase ϕ_{SLM} between 0 and 2π have to be quantised accordingly. A good way to achieve this is by gradual, so called "soft" quantisation [134] to minimise the impact of quantisation on the laser image (ghost images, low efficiency, noise). As shown in Fig. 4.12, the phases in a narrow range are projected onto their nearest quantised value (in this case $0, \frac{\pi}{2}, \pi, \frac{3\pi}{2}$). With each iteration k this range is extended until all phase values are quantised.

Oversampling and laser image simulation: According to the Nyquist-Shannon sampling theorem a signal has to be discretised using a sampling rate $f_{\mathrm{S}} \geq 2\,(f_{\max} - f_{\min})$ or at least twice the bandwidth of the signal. In a $\mathrm{N} \times \mathrm{N}$ ($\mathrm{N} = 512$ px) image A_{tar} the highest-frequency pattern is a binary grating with period $\pm 2/\mathrm{N}$ and hence $f_{\mathrm{max,min}} = \pm \mathrm{N}/2$ which requires a sampling rate $f_{\mathrm{S}} \geq 2\mathrm{N}$. In order to represent such high frequencies in the FFT

(Fast Fourier Transform) spectrum in the SLM plane $A_{\mathrm{SLM}} \exp(i\phi_{\mathrm{SLM}})$ the computation matrix has to be at least 2N × 2N [131], otherwise aliasing problems occur and speckle noise appears in the laser image. The phase freedom of the SLM is allowed only in the central N × N part, the rest of the ϕ_{SLM} is padded with zeros.
More importantly, the same argument applies when simulating the output of given kinoform ϕ_{SLM} of resolution N×N. It is not sufficient to calculate $A_{\mathrm{img}} = \mathrm{FFT}\{A_{\mathrm{SLM}} \exp(i\phi_{\mathrm{SLM}})\}$ directly, instead the light field has to be padded with zeros to a resolution of 2N × 2N before Fourier transformation. This will accurately take care of the high frequencies in the phase pattern and simulate the speckle noise produced by them. Due to padding of the kinoform the simulated laser image will be double the pixel size compared to non-padded FFT calculation.

4.4 Which algorithm is best?

After delving in details of various approaches for kinoform calculation the big question is: Which algorithm is best? The answer is: it really depends on the shape of the phase pattern. A good and quick general purpose algorithm for beam shaping, grey-scale pictures, geometric shapes is certainly the (O)MRAF algorithm which we used extensively in the experiments. It is especially suited if the quality of the laser image is more important than the light efficiency of the kinoform (low efficiency of 10-20%, which the offset parameter further halves). It has to be stressed that the useful signal area and hence the target image has to be small (less than 25% of the SLM pixel area).
For simple shapes consisting of lines and a few focussed spots or for multi-beam steering, grating approaches and segmenting the SLM are recommended (Sec. 4.3.1). Positives are the simple computation and very high efficiency (> 60%) of the kinoforms, drawbacks are slight spot asymmetries due to the segmentation [see. Fig. 4.11(b)]. Due to the 3D focus positioning ability, this type of kinoform is the first choice for optical tweezers. Grating phase patterns are intuitively easy to understand, and a 4-spot grating pattern is immensely useful when aligning the optical setup.
Specifically for top beam shaping and multiplexing applications, OC, 3S, and Arrizón's algorithms have shown good performance [126]. The GS algorithm is, despite its inferior performance, still a simple and quick way to generate laser images, especially if enhanced with techniques presented in Sec. 4.3.3. Its randomized kinoforms offer the benefit to be insensitive to off-centre SLM illumination. Despite its strong speckle noise in the laser image it is still more efficient than the MRAF algorithm.

4.5 Phase retrieval from interferogram

A camera image records only the modulus squared of the complex light field $A_{\mathrm{img}} \exp(i\phi_{\mathrm{img}})$ while the phase information is completely lost. In order to measure phases in the experiment, interferograms are employed. By interfering a reference light wave $A_{\mathrm{ref}} \exp(i\phi_{\mathrm{ref}})$ with a flat phase front $\phi_{\mathrm{ref}} = \mathrm{const}$, the phase $\phi_{\mathrm{img}}(x, y)$ is encoded in an amplitude modulation process in the form of regular fringes in the interferogram

$$\mathrm{I} = A_{\mathrm{img}}^2 + A_{\mathrm{ref}}^2 + 2A_{\mathrm{img}}A_{\mathrm{ref}} \cos(\phi_{\mathrm{img}} - \phi_{\mathrm{ref}}) \qquad \mathrm{K} = \frac{2\,A_{\mathrm{img}}A_{\mathrm{ref}}}{A_{\mathrm{img}}^2 + A_{\mathrm{ref}}^2} \tag{4.17}$$

Requirements to ϕ_{ref} are: (i) coherence with the light field to be measured [i.e. use a magnified portion of this light field as the reference, as in Fig. 4.13(a)], (ii) featureless phase distribution (no vortices, best with no curvature) and (iii) matched amplitudes $A_{\mathrm{img,max}} \approx A_{\mathrm{ref,max}}$ for high fringe contrast K. The fringe spacing d_f should be chosen so that good spatial separation from the centre of the Fourier plane (i.e. background intensity in Fourier space) and the axes $f_x = 0$, $f_y = 0$ [the "cross" in Fig. 4.13(b)] can be achieved. Smaller fringe distances increase the phase resolution but one has to be careful to avoid aliasing problems. A good choice are fringes with spacing $d_f = 5$ to 10 px at 45°. The reference phase is adjusted with the adjustment screws on BS2 and BS3 in rectangle nr 4 in Fig. 4.1, magnification is obtained from the telescope L7-L8. In order to extract the phase from an interferogram four steps are necessary, as depicted in Fig 4.13:

(a) Carefully centre fringe image.

(b) Fast Fourier transform it.

(c) Select the rectangle with frequencies $f \sim 1/d_f \approx 0.15$ matching the fringe distance $d_f \approx 7$ px and centre this rectangle in the Fourier space, discard the rest of the matrix[1].

(d) Back-transform to real space, obtaining the full original light field $A_{\mathrm{img}} \exp(\phi_{\mathrm{img}})$.

The retrieved raw phase $\phi_{\mathrm{img,raw}}$ in Fig. 4.13(e) is warped due to the curvature of the reference phase[2] thus requiring phase correction to recover the original phase ϕ_{img} in Fig. 4.13(g). One has to manually fit a curved wavefront Fig. 4.13(f) that matches the spacing of the 2π ramps in the raw phase using the formulas for gratings, lenses and conical phase profiles presented in

[1] The choice of size for this rectangle is obvious from the image, it contains a replica of the real space image.

[2] Sources of the curved reference wave: arm length in the interferometer not equal, phase across one lobe changes from π (centre) to 0 (edge), spherical aberration in the magnifying telescope of the reference arm.

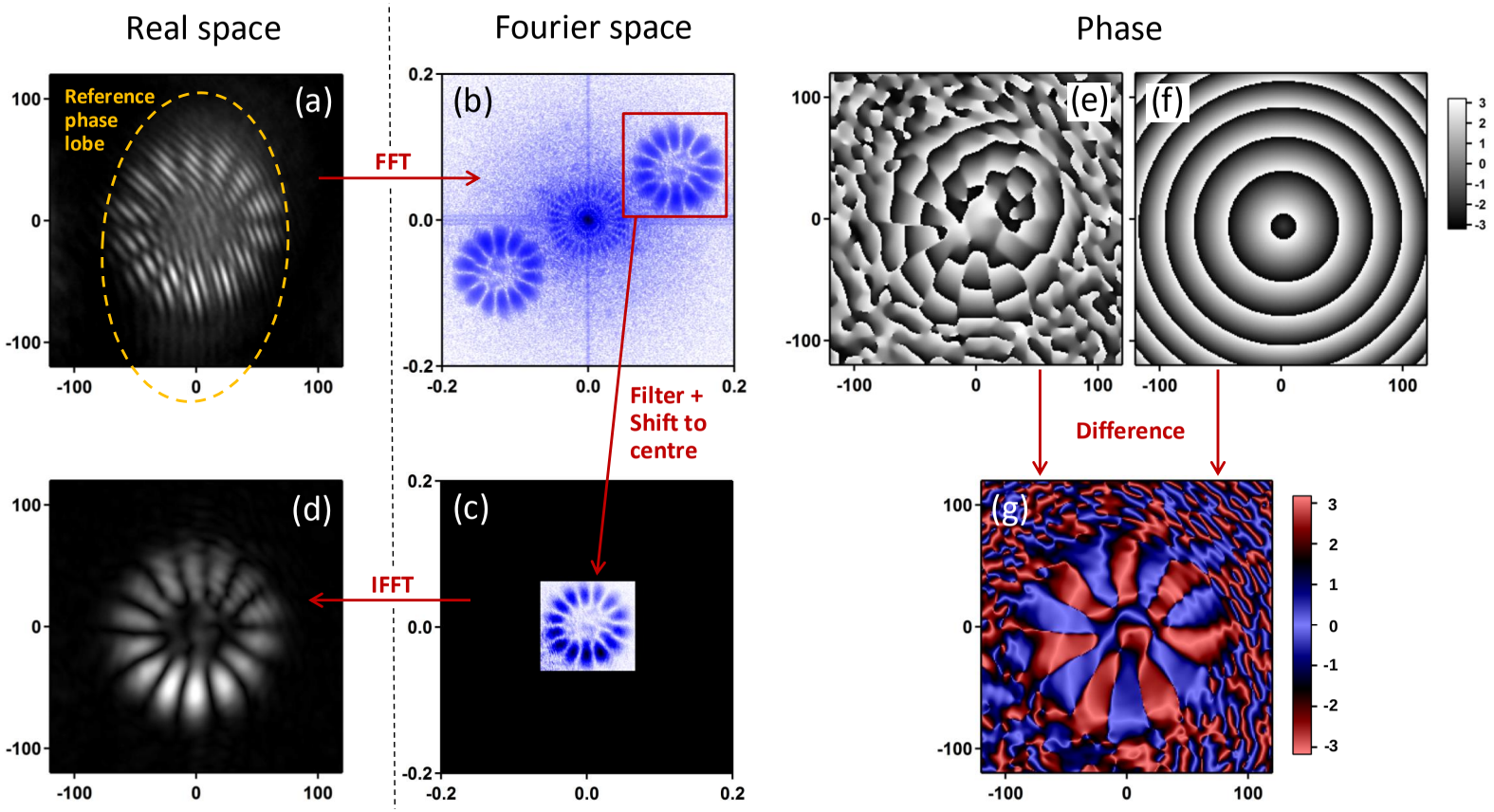

Figure 4.13: Phase extraction from interferogram. (a) Original interferogram (400 × 400 px) with size of magnified lobe for phase reference. (b) FFT of (a) in normalised frequency units $[-0.5, 0.5]$. (c) Filtered and shifted Fourier image. (d) Demodulated complex image, now containing phase information. (e) Raw phase of (d) which needs to be dewarped by subtraction of a fitted, curved and slightly off-centre reference phase (f) to yield the final phase map in a cycling colour scale (g).

Sec. 4.3.1. This correction phase ϕ_{corr} is subtracted from the raw phase to give[1]

$$\phi_{\text{img}} = \arg\left\{A_{\text{img}} \exp(\phi_{\text{img,raw}}) \cdot \exp(-i\phi_{\text{corr}})\right\} \equiv \phi_{\text{img,raw}} - \phi_{\text{corr}} \tag{4.18}$$

In the example presented here a mix of offset parabolic and conical wavefronts were used in the correction phase.

[1]The first term is easier to compute since it avoids modulo 2π problems.

Chapter 5

Phase-locked and trapped polariton condensates

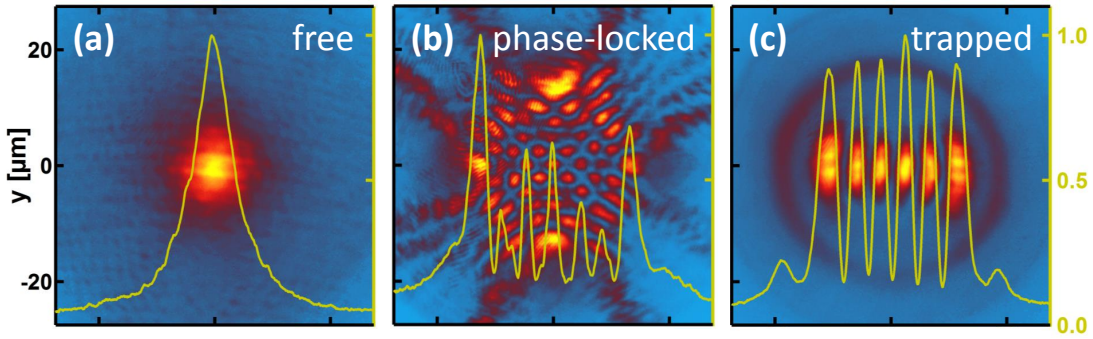

Figure 5.1: PL image of different types of polariton condensates: (a) freely expanding, (b) phase-locked and (c) trapped condensate. Profiles are cuts through the image centre.

5.1 Introduction

Polariton condensates are macroscopic quantum objects that show long-range coherence on 100 μm length scales. They are not static objects, unlike a true BEC at $T = 0$ K, so that constant pumping of the condensate is required to keep the occupation number above unity. Hence the behaviour of polaritons in a microcavity with negligible disorder is governed by the balance between creation and decay, and their strong long-range interactions.

In non-resonant optical pumping polaritons are created in the vicinity of the pump laser spots. The repulsion between these composite quasiparticles leads to expanding clouds of polariton quantum liquid, in which the flow is directed radially outwards from the pump spot [Figs. 5.1(a) and 2.13]. In continuous pumping, the condensate wavefunction reaches a steady state in which steady flows of polaritons exist within the condensed cloud, from areas of high net gain (around the pump spots) to places with higher loss rates (areas of low pump intensity, defects in the QWs, cracks in the DBR mirrors). These flows are associated with the spatial gradient of the condensate phase (Eq. 3.33).

5. PHASE-LOCKED AND TRAPPED POLARITON CONDENSATES

A polariton condensate forms in the valleys of the overall potential landscape inside the microcavity, as summarised in Sec. 2.3.6. An important role is also played by self-interactions, arising from the sum of all repulsive polariton-polariton and polariton-exciton scattering events and showing in a blueshift of the PL emission energy (Sec. 2.5.1). The balance of exciton reservoir mediated repulsion, used for pumping and trapping polaritons, and polariton related self-interaction, which leads to spreading of the wavefunction , stabilises the condensate in the steady state. A polariton condensate tends to fill out as much of the trap as possible while retaining good overlap with the pump and avoiding areas of high loss (defects).

The shape of the excitation laser determines the spatial distribution of the polariton condensate through the blueshift (or optical) potentials it forms in non-resonant pumping. Customised optical potentials can easily be implemented using an SLM to modulate the laser beam into a desired light pattern (Sec. 4.2). With this technique spatial variations of the gain and loss rates for polaritons are imprinted onto the sample. One of the simplest arrangements to study polariton condensation in optical potentials is with a set of $N = 1, 2, 3, 4, ...$ pump spots, regularly arranged along a ring of diameter d. As will be presented in this section, the symmetry of the pump geometry, as well as the separation and intensity of the pump spots determines if the resulting condensate is (a) radially expanding, (b) phase locked or (c) optically trapped, as shown in Fig. 5.1.

This chapter is organised in the same way as Fig. 5.1. The starting point is the dynamics of a single pump spot condensate in Sec. 5.2, followed by synchronisation (phase locking) of two independent condensates in Sec. 5.3. The surprising appearance of quantum harmonic oscillator wavefunctions in this dual pump configuration is presented in Sec. 5.3.2. Blueshift traps (Sec. 5.4), formed by placing N pump spots along a ring, play an important role to further control the polariton condensate. The transition from phase-locked to trapped condensates is studied in Secs. 5.5 and 5.5.1, followed by observations of which trap state wins the mode competition and becomes macroscopically populated (Sec. 5.5.2). Finally Sec. 5.6 presents cGLE simulations of this system which reproduce the observed transition with a change in pumping geometry. A discussion of the simulation and the advantages of trapped polariton condensates (Sec. 5.7) rounds off this chapter.

Work in Sec. 5.2 was performed by G. Christmann et al. [87], while G. Tosi et al. [44] conducted the work presented in Sec. 5.3.2. All other results were measured and analysed by myself in collaboration with the people stated in the declarations section.

5.2 Single spot condensates - radial flow with sunflower pattern

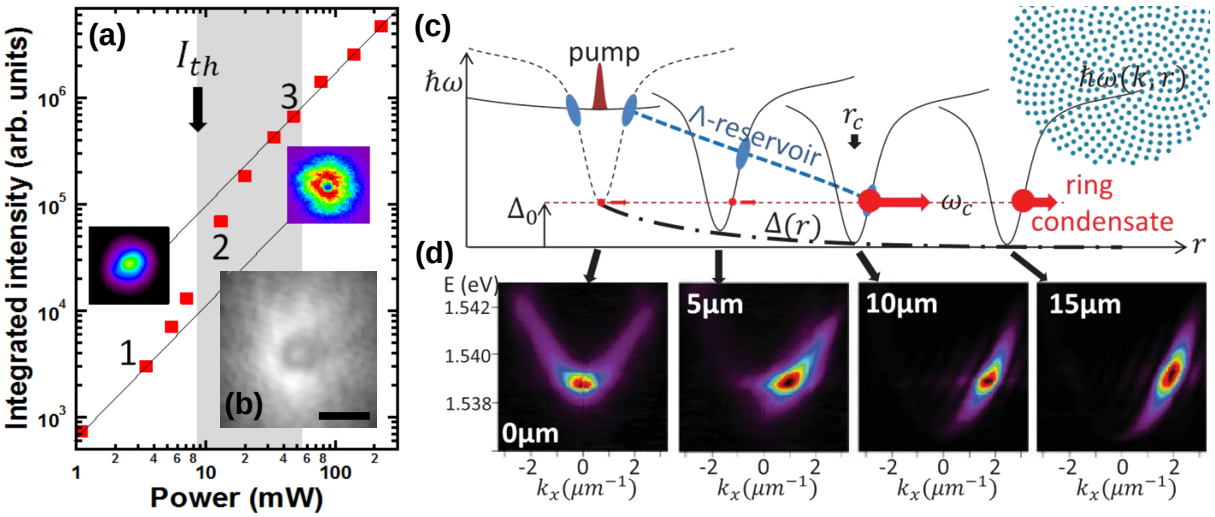

Figure 5.2: (a) Integrated polariton emission vs pump power for a single focussed pump spot, insets are real space PL emission images. Black lines are guides to the eye above/below the threshold which occurs at $P = 9$ mW. Grey region corresponds to the polariton condensate. (b) Real space image of the condensate showing sunflower ripples, scale bar is 10 μm. (c) Relaxation model for the condensate which is formed at the $k_{||} = 0$ blueshifted ground state at the laser spot and gains momentum (d) as it outflows to areas of smaller blueshift $\Delta(r)$. Gain is provided by a polariton reservoir higher up the dispersion curve [blue blob in (c)]. Adopted from [87].

Creating a single polariton condensate is as easy as focussing a laser beam (here: $\varnothing = 1.5$ μm) in the visible wavelength range onto a microcavity sample. As usual in polariton physics, one starts with studying the power dependence [Fig. 5.2(a)] of the photoluminescence $I_{\mathrm{PL}}(P)$. For pump powers below the condensation threshold $P < P_{\mathrm{thr}} = 9$ mW the PL emission is incoherent and shows a smooth, Gaussian-like spatial intensity profile (inset "1"). Relaxation to the lower energy states is limited with most polaritons not reaching the $k_{||} = 0$ ground state within their lifetime.

At $P > P_{\mathrm{thr}}$ an emission ring forms around the pump spot (inset "3") and ripples in a sunflower pattern appear [real space image in (b) and the right corner of (c)]. The emission intensity on the input-output curve becomes super-linear [grey rectangle in (a)] with strong blueshift (not shown). The important message is that momentum (d) is provided by the height of the blueshift potential [here $\Delta(r)$], while gain is acquired through stimulated scattering of reservoir polaritons [blue blob in (c)] into the condensate. This effect was first reported by Wertz et al. in [20]. We believe it happens predominantly when the reservoir, which relaxes monotonically

with radial distance r, reaches the condensate energy, whose energy remains constant at the maximum blueshift value Δ_0 at the centre of the pump spot.

As the condensate expands there is no energy relaxation (as a macroscopic quantum object individual local scattering events are suppressed [87]), while its momentum increases until it reaches a final velocity at a distance where the blueshift vanishes (compare Secs. 2.5.1 and 3.2.3). Continuous amplification by bottleneck polaritons allows the condensate to extend well over 50 μm and it is the reason why a photoluminescence image represents the condensate wavefunction. Multiple small scattering events with the rough sample surface lead to formation of a sunflower-like pattern of the condensate seen in (b). This is explained by interference of a spherical wave (the expanding condensate) with weaker Rayleigh-scattered plane waves in random directions, with random phases [87].

5.3 2-spot condensate - phase locking in a quantum harmonic oscillator

5.3.1 Phase and frequency locking

Two laser beams impinging on the same microcavity sample, separated by a distance d as in Fig. 5.3(a), will create two independent out-flowing condensates (assuming non-resonant excitation). As explained in Secs. 2.5.1 and 5.2, at distances where the blueshift potential is negligible, the condensates will have acquired a momentum $\hbar k_c = \sqrt{2m^* E_{\mathrm{BS}}}$. When the tails of two such condensates overlap, they interact and the feedback from one condensate to the other will lead to two outcomes in order to maximise the overall population in both condensates [44, 135]: phase-locking [(b), periodic peaking of the envelope amplitude as seen in a pulsed laser] or frequency locking [(c), i.e. their time evolution becomes synchronised].

Mode and frequency locking was reported already by Huygens in 1666, when he discovered that two pendulum clocks mounted on a common board synchronise their swing over time. This so called entrainment happens because the board transmits small vibrations that have a negative feedback on each pendulum and increase the overall loss of swing energy. The interactions transmitted by the board lead to a frequency equalisation over time. Huygens observed an "odd-sympathy" locking, i.e. the two pendulums prefer to lock out of phase with $\Delta\phi = \pi$, although in-phase locking is also possible.

For polariton condensates these locking mechanisms can be explained in a simplified picture

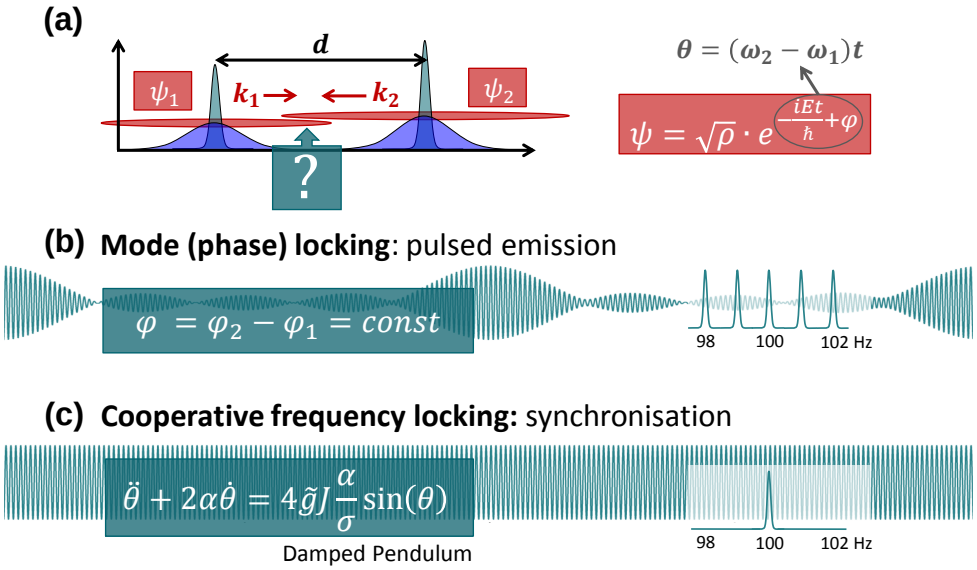

Figure 5.3: Interaction between two condensates Ψ_1 and Ψ_2 with initially different energy (a) leads to phase locking (b) with pulsed emission and frequency locking (c) which synchronises their time evolution completely. The equation in (c) describes the synchronisation dynamics (damped harmonic oscillation of the phase difference θ, see Sec. 5.6.1).

as follows. On the connection line between the pump spots the tails of the two condensates can be approximated by two monochromatic plane waves ψ_1 and ψ_2 with spatially decaying density (Eq. 3.34), separated by a distance d and travelling in opposite direction,

$$\psi_j(x,t) = \sqrt{\rho_j(x,t)}\,\exp[i\,\phi_j(x,t)] \qquad j = 1,2 \qquad (5.1)$$

$$\phi_j(x,t) = \pm\, k_j \cdot (x \pm d/2) + E_j\, t/\hbar + \varphi_j \qquad \text{phases} \qquad (5.2)$$

with $\rho_j, k_j, E_j, \varphi_j$ the density, momentum, energy and relative phase of each condensate. As observed experimentally [44, 135], interactions between the two condensates lead to combined frequency and phase locking: $E_1 = E_2 \equiv \hbar\omega$ and hence both condensate momenta $k_c = \sqrt{2m\omega/\hbar}$ are fixed too. A regular sequence of high-contrast and stationary fringes forms from the interfering condensates, similar to a standing wave of the form $|\Psi|^2 = |\psi_1(\vec{x},t) + \psi_2(\vec{x},t)|^2 \propto [1 + \cos(\vec{k}\cdot\vec{x} + \Delta\varphi)]$. The number of fringes is set by the momentum of the condensate k_c, however the symmetry – if there is a bright or dark fringe in the centre – depends only on the phase difference $\Delta\varphi$ of the two condensates, which can take on only the value 0 or π (the system has to be mirror symmetric around $x = 0$). Depending on the value of the product $k_c \cdot d$ either the "0" or "π" configuration is favoured for minimising in-plane outflow losses (see Sec. 5.3.3).

The appearing fringes are stable for minutes or longer, limited by the steadiness of the pumping laser. This is very remarkable given that the dynamics of the condensate happen on time scales of picoseconds, clocked by the relaxation time and lifetime of polaritons. It is also a strong hint that the non-equilibrium interactions in the condensate, $E_{\mathrm{BS}}(\vec{x}) = \hbar g\,|\Psi(\vec{x})|^2$, together with continuous pumping and decay, stabilise the system to the point where it reaches a stable quasi-equilibrium state.

5.3.2 Two interacting condensates form a quantum harmonic oscillator

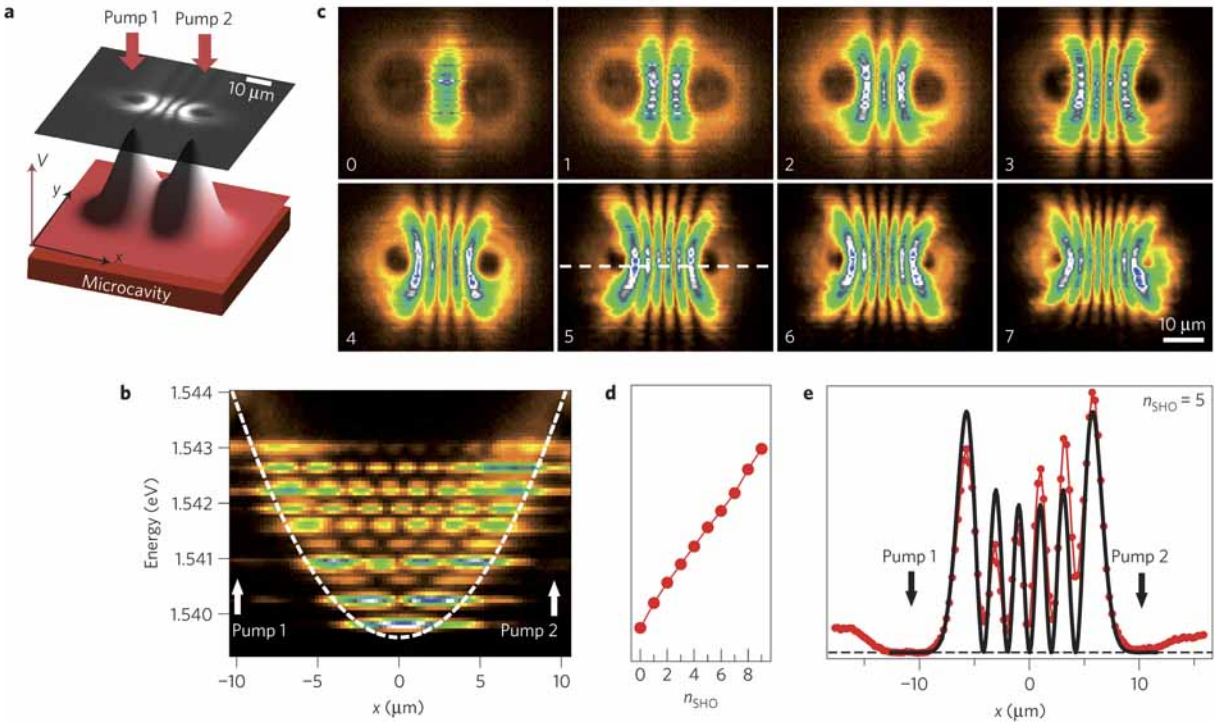

Figure 5.4: Spatially mapped polariton-condensate wavefunctions. (a) Experimental scheme with two pump spots, separated by 20 μm, focused on the planar microcavity. The blueshift potential (red) produces multiple condensates (grey image shows $n_{\mathrm{SHO}} = 3$ mode). (b) Real-space spectra along line between pump spots. (c) Tomographic images of polariton emission (repulsive potential seen as dark circles around pump spots). Labelled according to n_{SHO} assigned from (d). (d) Extracted mode energies versus quantum number. (e) Hermite-Gaussian fit of $\Psi^{n=5}_{\mathrm{SHO}}(x)$ to image cross-section, dashed in (c). Adopted from [44].

Pumping a microcavity with two tightly focussed laser spots, as shown in Fig. 5.4(a) creates a parabolic shaped blueshift potential between the two laser spots, as can be seen from an energy-resolved cut of the PL emission in (b). In this potential multiple condensates coexist, with their

energies spaced equidistantly (d): $E_n = \hbar\omega(n+\frac{1}{2})$. This is presumably a consequence of positive feedback from self-interaction (frequency pulling in Sec. 3.2.4), by which stimulated scattering into the condensates is maximised for equidistant energy levels – the polaritons and excitons in the system redistribute to form just such a parabolic blueshift potential.

As expected the energy spacing $\hbar\omega$ decreases with increasing d (tight confinement $\leftrightarrow$ large level spacing), while showing no pronounced dependence on the pump power. The wavefunctions of these condensates closely resemble Hermite-Gauss functions [Fig. 5.4(e)], just like the solutions of the textbook quantum harmonic oscillator problem. This reveals the very striking PL picture of evenly spaced harmonic oscillator states in Fig. 5.4(b,c) - visual quantum mechanics.

High pump powers and low spot separation d facilitate relaxation of polaritons, possibly due to more efficient stimulated scattering. While at threshold only one condensate is present, a larger number of polariton states condenses simultaneously for high pump powers. At large separation d the polariton population accumulates preferentially in the high energy condensates, with high fringe number, close to the maximum blueshift energy. Only for smaller d it becomes possible to populate the lowest energy states of the harmonic potential.

Phase locking[1] is also seen for two condensates A and B pumped with different pump power [44], as long as the difference $E_c^A - E_c^B > 0$ is not too large and both pump spots reach the condensation threshold (Eq. 3.43). In such a configuration the potential remains parabolic but its centre shifts towards the weaker laser spot B. In addition, only the lower energy levels in this potential are trapped, whereas all states $E > E_c^B$ are not confined. Nevertheless the blueshift barrier produced by spot B reflects a fraction of the escaping condensates – that is why weak fringes can still be seen for those states. For fringes to appear, a mechanisms equalising the energies (Sec. 5.3.3) of the two interacting condensates must exist, similar to injection locking in lasers, with interactions provided by polariton-polariton scattering (see also Sec. 5.6.1 and [135]).

Using time interferometry, another interesting property has been measured in this quantum oscillator. By superimposing the real space PL emission with a version of itself at a delayed time Δt, a strong return of the fringe visibility could be observed after a delay of $\Delta t = 13$ ps. This can be attributed to the *multiple condensates with equidistant energies*, as present in the parabolic potential, being phase-locked relative to each other: $\varphi_i - \varphi_j = \text{const}$. This fact allows us to create an analogy to a wavepacket that shuttles back and forth between the two pump

[1] Here I use the same term "phase locking" as in [44], although it is in reality frequency *and* phase locking, which constraints the whole time-dependent phase of both condensates.

spots every 13 ps, although it decays very fast, as seen by the strongly reduced fringe visibility after $2\Delta t$ or more.

Even though the two-spot condensate is not confined (it is bound in between the two pump spots, but not perpendicular to the imaginary line connecting them), the PL emission shows much stronger emission from the fringes of the phase-locked condensate compared to the regions behind one of the spots, where only radial outflow is expected. This can have many reasons: First, the imposed geometry, of lower symmetry and higher confinement, facilitates energy relaxation due to relaxed scattering conservation rules (for example in 0D micropillars, there are no selection rules, which greatly reduces condensation thresholds [77]). Fewer final states are available, so that the overall occupancy per quantum state increases. Second, the spatially stationary fringe pattern allows for more efficient stimulated scattering than the outflowing condensate, with the fringe itself increasing the density by a factor 2 compared to non-coherent addition[1], thus further reducing the spatial losses. Third, fringes will adjust so as to avoid particularly lossy spots on the sample, both by changing the number of fringes and shifting their position – lossy defect will sit at an antimode of the wavefunction.

5.3.3 Origin of phase locking

The number of fringes observed between the two pump spots is set by the distance d of the pump spots, and by the condensate momentum k_c, as studied in [135] for energy-degenerate condensates formed by laser pulses. The phase difference $\Delta\varphi$ can be either 0 (in-phase locking) or π (counter-phase locking), depending on which configuration maximises the overall population in both condensates. The effect of phase locking is attributed to **dissipative coupling** and **spontaneous global symmetry breaking**. During the formation process of the condensates the out-flowing polaritons can interfere constructively or destructively. The destructive configuration (at the centre where they meet first) results in lower losses of polaritons from the condensates and higher polariton occupation numbers, and is hence amplified further via stimulated scattering from the exciton reservoir. The overall polariton losses L due to in-plane outflow for the combined system can be approximated as [135]

$$L(k_c, d, \Delta\varphi) \propto [1 + \underbrace{\cos(\Delta\varphi)}_{\pm 1} J_0(k_c d)] \qquad \text{phase locking condition} \tag{5.3}$$

where $J_0(x)$ is the lowest order Bessel function, k_c momentum of the phase-locked condensates (acquired by the height of the blueshift potential), d is the pump spot separation and $\Delta\varphi$ is the

[1] Coherent addition $\max(|\Psi_1 + \Psi_2|^2) \propto 4|\Psi_1|^2$, whereas incoherent addition $\max(|\Psi_1|^2 + |\Psi_2|^2) \propto 2|\Psi_1|^2$

relative phase difference to which the condensate pair locks, either 0 or π. Since $J_0(k_c d)$ is a function oscillating around zero it is immediately clear that for a certain product $k_c d$ the system has to chose either $\Delta\varphi = 0$ or $\Delta\varphi = \pi$ to oppose the sign of $J_0(k_c d)$ for minimum losses. As the reservoir of a single laser pulse decays, the blueshift potential and condensate momentum k_c associated to it does too. Hence, for higher pump powers and longer observation times, a switching from a state with $\Delta\varphi = 0$ to $\Delta\varphi = \pi$ or vice-versa has been observed [135], again due to a diminishing product $k_c d$ in Eq. 5.3.

Interestingly, a recent study on the coherence of two polariton condensates [74], generated independently (non-resonant pulsed excitation) at widely separated positions in a mirror-symmetrical environment, has found that phase locking occurs before the wavefunctions of the two condensates start to overlap. Coherence is global and present at any time. The two condensates are described by one macroscopic order parameter and there is a fixed phase between then, which is imposed by the spatial symmetry of the excitation configuration and results in a symmetric order parameter both in real and reciprocal space.

Another theoretical mechanism to explain phase locking are pairwise Josephson oscillations between two neighbouring condensates (Sec. 5.6.1). Here the time-dependent phase difference θ between two condensates oscillates to zero like a damped harmonic oscillator [see Fig. 5.3(c)], so that in the steady state all phases become equal. Anti-phase locking is not explained by this mechanism, in contrast to dissipative phase locking presented above [135].

The reasons above, together with the fact that further separated pump spots incur higher polariton decay losses, might explain why the threshold for condensation is reduced for smaller optical traps, as presented in Sec. 5.5. Phase-locking of two condensates has been modelled theoretically for a double-well potential, mimicking the situation found in CdTe microcavities, where the strong disorder potential leads to localised condensates. Results show that Josephson currents can lock the two spatially separated condensates, provided the energy difference of the two wells is not too large [103] and the interaction strength (exciton-polariton and polariton-polariton scattering) is high enough.

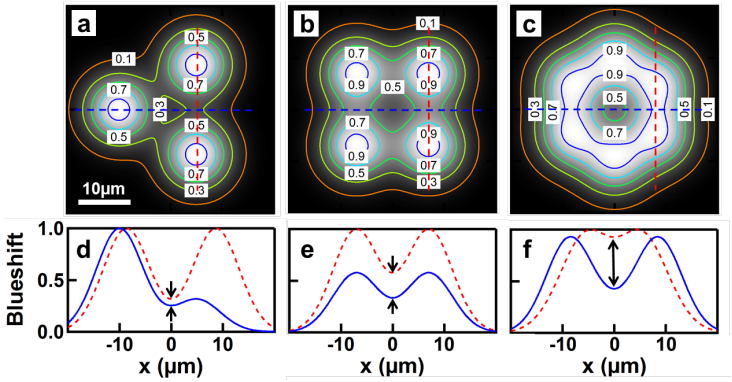

Figure 5.5: Gaps in the optically-induced polariton potential for multiple pump spots. (a-c) Real space images of the normalised polariton potential with 3,4,6 pump spots; contours to emphasise the trap shape. (d-f) Profiles of the blueshift potential, through the trap centre (trap depth, blue) and along two neighbouring pump spots (trap gaps, red). The black arrows mark the effective trap depth.

5.4 Blueshift trapping of polaritons with multiple pump spots

The blueshift potential attributed to each pump spot can be used to create all-optical traps for polariton condensates. By evenly spacing N laser spots on a small ring, their blueshift hills overlap and the enclosed area constitutes a trap for a polariton condensate, as shown in Fig. 5.5(a-c). The figure was obtained by adding $N = 3, 4, 6$ Gaussian blueshift hills at positions $\vec{x}_i$ on a circle of diameter $d = 20$ μm. The width of the blueshift hill is set by the microcavity parameters and was measured to be $w_{\mathrm{BS}} \sim 4$ μm.

$$V(\vec{x}) = E_{\mathrm{BS}}\, f(\vec{x}) \qquad f(\vec{x}) = \sum_{i=1}^{N} \exp\left[\frac{(\vec{x} - \vec{x}_i)^2}{2w_{\mathrm{BS}}^2}\right] \tag{5.4}$$

The colour map shows the strength of the blueshift (white is 1 meV, black is 0 meV) and the contour lines depict the shape of the formed potential: triangular in (a), square in (b) or hexagonal in (c). The depth of the trap can be read off the cross sections in (d-f): it is the energy difference between the inter-spot valley of the red profile (trap wall) and the valley of the blue cut across the trap centre (trap sink), as marked by the black arrows.

In the experiment we measure trap depths of ~ 1 meV for blueshift potentials $V_{\mathrm{BS}} = 2$ meV. For $N = 3$ the blueshifted potential landscape sustains only a very shallow trap, so that polaritons with even a small kinetic energy can readily escape through the inter-spot gaps. For $N \geq 4$ these gaps are effectively plugged [red line in (e,f)] and the potential becomes more circularly

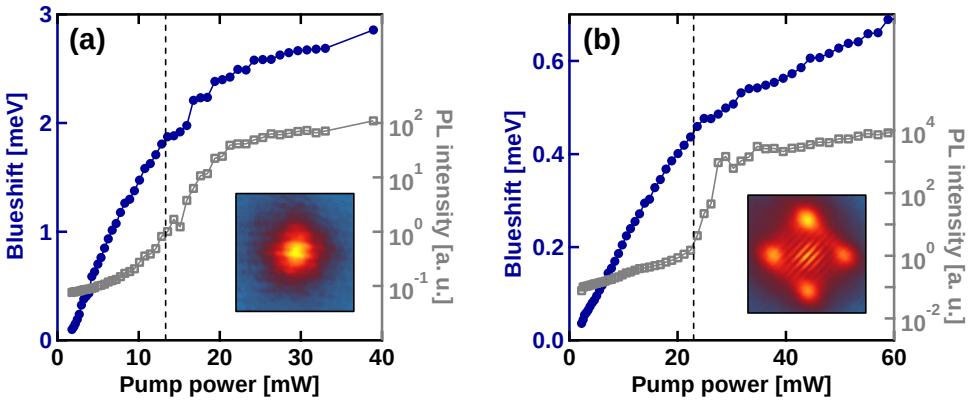

Figure 5.6: Blueshift and PL emission intensity for a single spot condensate (a) and a trapped condensate (b). Courtesy of Hamid Ohadi.

symmetric, with each added spot leading to a deep potential minimum (black arrows show trap depth) that supports trapped polariton condensates with lowered condensation threshold.

The blueshift experienced by a condensate in an optical trap is much smaller compared to a freely expanding condensate at the pump spot - the blueshift at the location of condensate formation determines the dynamics. This observation is plotted in Fig. 5.6 by recording the blueshift energy $E_{\mathrm{BS}}(P)$ and PL emission intensity $I_{\mathrm{PL}}(P)$ of a polariton population in free space (a) and in an optical trap (b) as a function of excitation power P. The single pump spot condensate in (a) shows a blueshift slope $\alpha = 0.15$ meV/mW around the condensation threshold, which decreases by a factor of 10 in the photon lasing regime.
In contrast the polariton energy for a condensate formed in a 4-spot trap blueshifts by only $\alpha = 0.02$ meV/mW below the condensation threshold. In the condensation regime the blueshift rate drops to $\alpha = 0.005$ meV/mW with a sharp kink which coincides with the onset of condensation at $P = 24$ mW. This data can be interpreted as follows: below threshold the pump light produces predominantly excitons at higher $k_{||}$ with small photonic fraction but large effect on the blueshift. This changes abruptly above threshold, where a large amount of the pump energy gets converted into condensate polaritons (drastic PL increase) which have a much lower impact on the rise of blueshift energy with P, hence also the much lower slope.

In summary one can say that in an optical trap the bulk of the blueshift energy stems from reservoir excitons and is present already below threshold. The contribution of condensed polaritons to the energy blueshift seems to be smaller by at least a factor 4 compared to reservoir excitons. This is a hint that the bulk of the trap potential is indeed formed by excitons, whereas

polaritons are created predominantly directly in the optical trap.

5.5 Trapped and non-trapped condensates

The geometry of optical excitation plays a critical role in selecting the stable polariton condensate formed. A sudden transition is seen, from a freely-flowing and phase-locked condensate to an optically trapped state, induced by a small change of the pump laser arrangement. The scope of this chapter is to study the effect of this transition on the condensation threshold, to find the relation between the pump geometry and the shape of the formed condensate and to highlight computer controlled optical trapping as a very useful tool to study polariton condensation in a cleaner environment, separated from the exciton reservoir.

We have studied phase locking and trapping of polariton condensates in a configuration where N pump spots are arranged along a circle of diameter d. The distance $d/2$ from the laser spots to the centre is computer controlled by a spatial light modulator with grating phase patterns, as explained in Sec. 4.3.1. It can be varied with sub-micrometer precision for each spot individually, along with the intensity in each pumping beam (non-resonant CW excitation at 755 nm). Three regimes can be distinguished for the polariton condensate created in a multi-spot pumping scheme [Fig. 5.7(c-e)], depending on the separation of the pump spots:

- **ballistic expansion regime (I)** at small $d \approx 0$
- **trapped condensate regime (II)** at intermediate $d < d_t$
- **phase-locked regime (III)** for large $d > d_t$

where $d_t(P, N)$ is the power and N-dependent distance below which trapped condensates are observed.

Each pump spot initially creates an independent, radially expanding condensate, accelerated by an exciton-induced blueshift potential. In the case $N = 2$, phase-locking is observed at all values of d (up to the field-of-view limit $d = 120$ μm), visualised by the set of time-stable and high contrast fringes in real space images, as shown in Fig. 5.7(a,b) for $d = 40$ μm and $d = 25$ μm. At the condensation threshold only a single quantum oscillator state is macroscopically populated. With increasing d the pump power for condensation rises along with the blueshift, and the fringe spacing is therefore reduced ($E_{\mathrm{BS}} \leftrightarrow k_c$, Sec. 5.3).

Phase locking of polariton condensates [(III), see Sec. 5.3] happens for any array of N pump spots, with the driving force being reduced overall polariton outflow loss [135] and hence lower condensation threshold. In order to maximise the state occupancy, the energies E_j and phase differences $\Delta\varphi_{i,j} = \varphi_i - \varphi_j$ with $i \neq j$ lock to a common value, so that all N single condensates

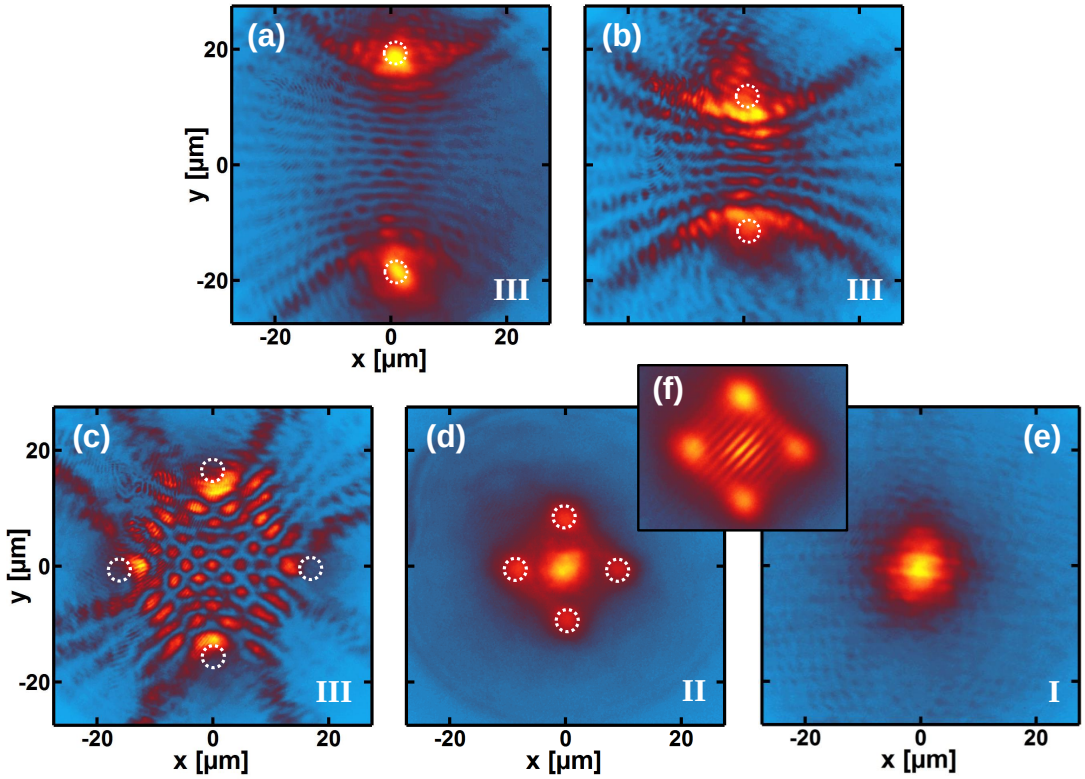

Figure 5.7: Transition from phase-locked to trapped condensates. Spatial images show condensates formed for 2 (a,b) and 4 (c-e) pump spots (white dotted circles) at decreasing separation d (left to right). Bottom row shows transition from a phase-locked multi-spot regime (III) to trapped condensate (II) to ballistic expansion regime (I), (f) shows coherence of (d).

become one big phase-locked condensate showing spatial coherence across its full extension. For a setup of $N = 3$ pump spots arranged in an equilateral triangle [Fig. 5.5(a)], a vortex lattice is seen, induced by the geometry of the pump arrangement [135, 136]. Apart from the trivial case where $\Delta\varphi_{i,j} = 0$ there are two degenerate configurations with stepwise phase gradient $\Delta\varphi_{i,j} = \pm 2\pi/3$, supporting six clockwise or anti-clockwise vortices in the centre with winding charge $\pm 1\hbar$ (see Sec. 3.1.3).

For three or more pumping spots arranged along a circle, intricate two-dimensional arrays of fringes form, which follow the symmetry of the pumping geometry. The wave function of such a phase-locked condensate is mostly restricted within the circle of diameter d, with some outflow between the pump spots beyond it [Figs. 5.7(c) and 5.8(a,b)].

For $N \geq 3$ optical traps can be formed if the diameter of the alignment circle is small enough:

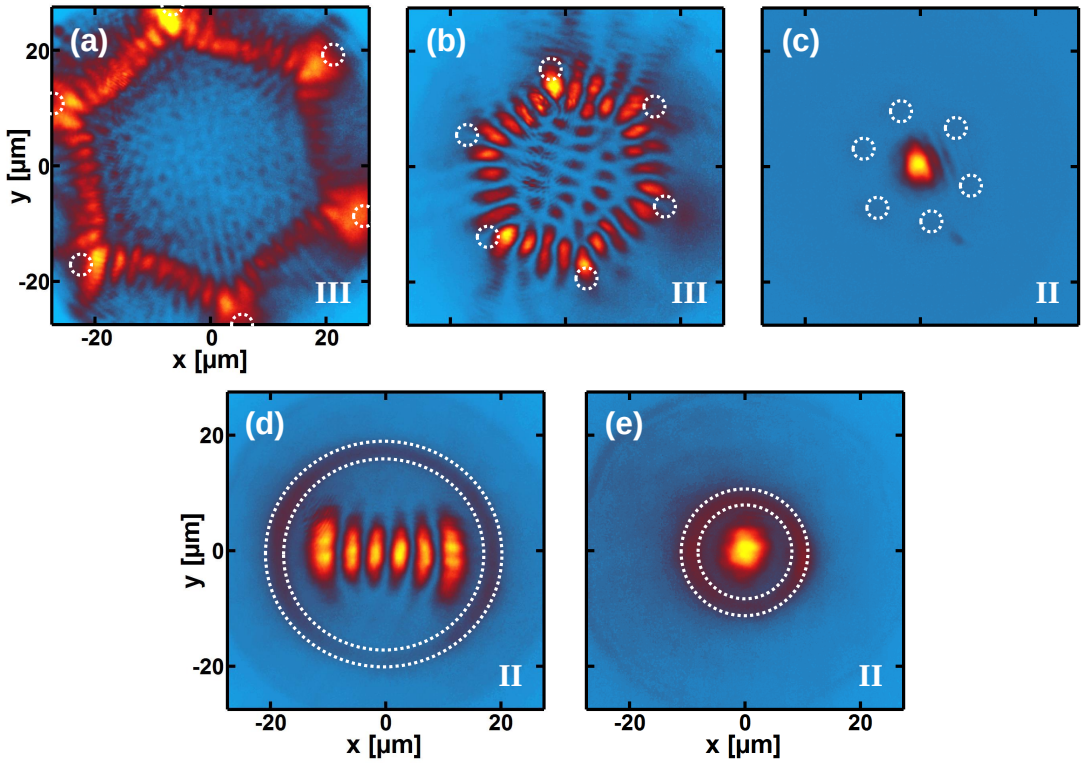

Figure 5.8: Phase-locked (regime III) and trapped (regime II) polariton condensates for 6 pump spots arranged in a hexagon (a-c) and for a circular pump (d,e), presented for reducing optical trap size (left to right). Pump laser indicated by white dotted lines.

$d < d_t(P, N)$. The case $N = 3$ forms only a shallow potential, while for $N \geq 4$ precisely controlled polariton traps can be created, in which trap dimensions, depth and symmetry can be varied with high precision (Sec. 5.4). Examples of trapped condensates (II) are shown in Figs. 5.7(d) and 5.8(c-e). Increasing the number of injection spots N raises the critical separation d_t and produces a greater variety of trapped wavefunctions. For example, for $N = 6$ in a hexagonal configuration, higher order states are seen at this transition [Fig. 5.8(b)].

In fact by making the potential deeper it is possible to excite selected higher order modes of the trapping potential. The shape of these states can be very well reproduced by solving the 2D Schrödinger equation for particles with mass m^* in a blueshift potential with trap depths of 1 meV or less, modelled according to the pump geometry. An interesting remark has to be made about the size of the trapped condensate: even in the state with the most shallow trap it does not extend past the boundaries of the trap, as shown by the strong fringes in the spatial autocorrelation image in Fig. 5.7(f). The background light stemming from the four pump spots

is of higher energy and incoherent. This is a further hint that the dynamics of the exciton reservoir and the polariton condensate are well separated spatially.

For increasingly azimuthal-symmetric situations such as a large diameter ring pump, already small asymmetries in shape or power distribution produce anisotropic combinations of the different higher-order near-degenerate wavefunctions for the trapped condensate state [Fig. 5.8(d)]. For such ring-shaped pumps, no phase-locked state is geometrically possible, and at the coherent threshold a trapped condensate is always formed [Fig. 5.8(d,e)]. In all cases, as the spacing between the pumps reduces, the trapped condensate collapses into a Gaussian-shaped ground state [Figs. 5.7(e) and 5.8(c,e)].

For $N = 6$ the trapped and the phase-locked condensate formed around $d = d_t$ shows a periodical hexagonal path reflected from each pump spot [Fig. 5.8(a,b)], similar to a whispering gallery modes in optical or acoustic resonators. The polariton is thus expelled from the centre and, due its the high momentum and the observed fringes, can be thought of circulating in this "waveguide" in both ways equally, as a form of persistent polariton current. Suggestively, they form only when the round trip time of a circulating polariton wavepacket becomes less than the polariton lifetime, so that coherence is preserved on one round trip. Some theoretical thought on this observation are presented in Sec. 5.7, although this observation is not fully understood.

As the pump spot separation d approaches zero, the individual blueshift potential hills overlap fully and the trap becomes so small in size and depth that no trapped condensate can be supported. This leads to the formation of a single ballistically expanding condensate (I) as explained in Sec. 5.2 with the corresponding sunflower pattern shown in Fig. 5.7(e).

5.5.1 Geometrically controlled trapping transition

To explore the phase transition between locked and trapped states in more detail, the power threshold for condensation is found for each spatial configuration and pump separation. This threshold is sharply defined by the appearance of fringes in the real space image interferogram (compare Figs. 5.7(d) and 5.7(f)). Three distinct regimes are seen as the separation d of the pump spots across the centre of the trap is reduced [Fig. 5.9(a)]. The trapping regime (II) is clearly marked by a lower condensation threshold between $d = 10 - 30$ μm. This is shown by the green area in Fig. 5.9(c), which flags the difference between the untrapped 2-spot configuration and the fully trapping circular pump. A phase diagram for the different geometries in (b), with the colour map coding the threshold pump power, shows how this trapped regime is more stable when the incident power is distributed more evenly around the trap.

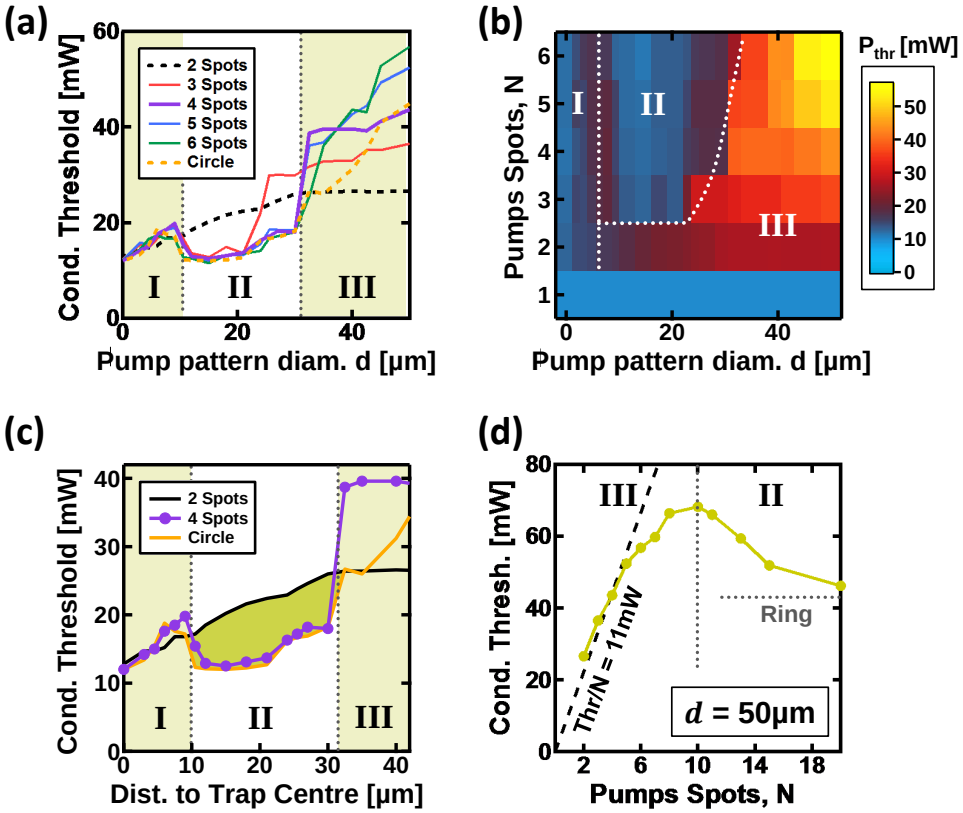

Figure 5.9: Geometry-controlled trapping transition. (a,b) Influence of pump spot distance and geometry on the condensation threshold, revealing transition from single (I) to trapped condensate (II), to phase-locked condensates (III) at large spot separation. (c) Reduction in condensation threshold achieved through trapping (green shaded area) compared to a phase locked two-spot condensate (black line). (d) Condensation threshold for multiple-spot (N) patterns of pumps around a ring of fixed diameter $d = 50$ μm, showing transition from phase-locked (III) condensates to trapped states (II).

At larger distances $d \approx 50$ μm the pump condensates phase-lock and form extended coherent structures many times the size of the polariton de Broglie wavelength $\lambda_{\mathrm{dB}} = h/\sqrt{2m^* E_{\mathrm{BS}}} \approx 8.7$ μm. Assuming ballistic propagation, a polariton can travel a distance $l = v_{\max}\tau \approx 30$ μm during their lifetime, with $v_{\max} = \sqrt{2E_{\mathrm{BS}}/m^*} \approx 4$ μm/ps. The distance l is considerably smaller than the phase locked condensates which can easily extend across 100 μm in size. Thus phase locking of N condensates (Sec. 5.3) helps to create extended single energy condensates. In addition it leads to a significant reduction in threshold, directly visible in the condensation thresholds per pump spot, as shown by the sublinear threshold increase in Fig. 5.9(d) in regime (III), below the value for a single pump spot $P_{\mathrm{thr}} = 11$ mW (dashed-dotted line).

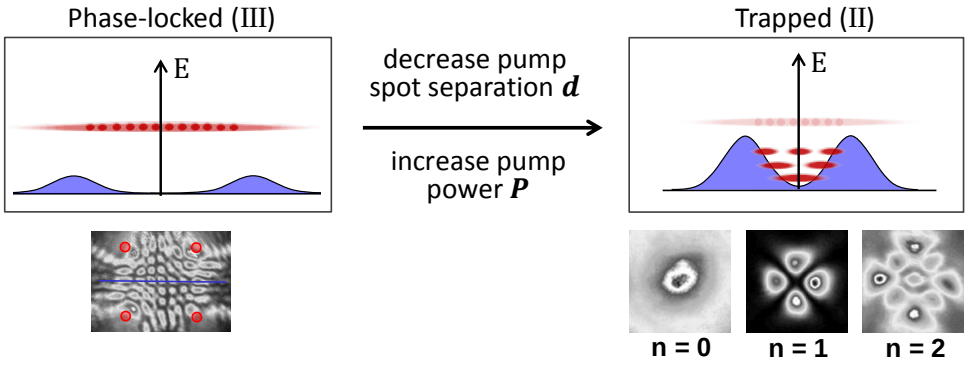

Figure 5.10: Sketch of a phase-locked and a trapped condensate (red) in an energy-space diagram. The blue curve represents the true trapping potential, i.e. a cut of the blueshift potential across the centre of the pump geometry, connecting two opposing saddle points (blue line in image, red circles are pump positions). In the trapped configuration multiple states can be present simultaneously, as shown in the grey scale real space images.

At smaller pump separations $d < d_t$ the polariton potential produces trapped condensates (region II), with an abrupt two-fold reduction in the condensation threshold at the transition which occurs below $d < 30$ μm [Fig. 5.9(a,c)]. The ring pumped condensate is always trapped (yellow line), experiencing increased thresholds for larger pump separations ($P_{\mathrm{thr}} \propto d$) due to the decreasing overlap of the pump reservoirs with the trapped state. Surprisingly, all trap geometries require more or less the same total pump fluence to reach condensation threshold, independent of the number of spots (plateau in Fig. 5.9(a), region II). This implies that condensation proceeds by combining polaritons harvested by stimulated scattering from all the reservoirs, and again shows that exciton reservoir and polariton condensate are well separated.

For distances $d < 12$ μm a second transition to a higher threshold condensate, regime (I), is seen. Here the overlapping blueshifts from the pump spots raise the potential in the central region, emptying the trap, and radially expelling the condensate. The spatial position of this transition to regime I is well predicted from the size w_{BS} of the blueshift hills: the threshold approaches that of a single pump as $d \to 0$, as expected for perfectly overlapped pumps.

5.5.2 State selection of the trapped polariton condensate

In a multi-spot pump geometry a reversible transition, induced by a change in either laser spot separation d or pump power P, switches the polariton condensate from phase-locked (III) to trapped (II). P changes the height of the blueshift potential hills while d controls their separation, so both affect their mutual overlap and hence set the trap depth. The phase-locked

state cannot be trapped by the shallow confinement from far-spaced laser spots (Fig. 5.10 left), so its wavefunction extends well beyond the pumping geometry due to in-plane outflow. The phase-locked condensate is fully coherent and spectrally appears at the maximum of the blueshift energy, the value at the pump spot.

The trapped state on the other hand forms for closely spaced laser spots $d < d_t$ which create a true blueshift confining potential. At the condensation threshold only a single state reaches macroscopic occupation, usually the highest energy one which is still trapped: $n_{\max}$. At fixed d, a further increase in P simultaneously excites more lower order states $n_{\max} - 1, n_{\max} - 2, \ldots$ of the optical trap, until eventually also the ground state $n = 0$ exceeds the threshold. This is shown on the right side of Fig. 5.10 for an $N = 4$ trap.

The reverse order with which trapped condensates reach threshold suggests that polariton relaxation plays a strong role, together with overlap of exciton reservoir and condensate. For large traps the Gaussian ground state cannot be excited, and only 3-4 high n states will light up in PL images. A simple calculation of the overlap of simple harmonic oscillator functions with oscillator length $a = \sqrt{\hbar/(2m^*\omega)}$, as seen in the experiment [73], has confirmed that for larger traps this overlap is maximum for high n trap states. As the trap size reduces, overlap to the lower energy states is favoured.

If one wants to selectively excite a specific trap condensate, say the $n = 1$ state in Fig. 5.10, the best way is to create a trap of size $d_1 \approx 25$ μm in which the highest trapped state is this $n = 1$ state. At $P = P_{\text{thr}}$ only the said state will reach threshold, while higher P will populate the ground state $n = 0$ as well. In large optical traps phase-locked and trapped condensates can coexist at higher P, whereas in smaller traps primarily confined states reach threshold (as sketched on the right side of Fig. **??**).

The requirements for a symmetric pump geometry rises quickly with d, especially for equal power in each pump spot. The $n = 0$ ground state condensate is the preferred choice for experiments requiring a stable condensate, since it is easy to realise in a small trap and it is independent of the pumping shape (always a Gaussian). Higher order states are more challenging to stabilise, they require fine adjustment of pump spot intensities, taking into account local disorder and coupling efficiency of the light into the microcavity. Often the excited condensates are (near-)degenerate and come in superpositions of trap eigenmodes, so that at the slightest change in pump power the PL emission fluctuates between these fundamental modes.

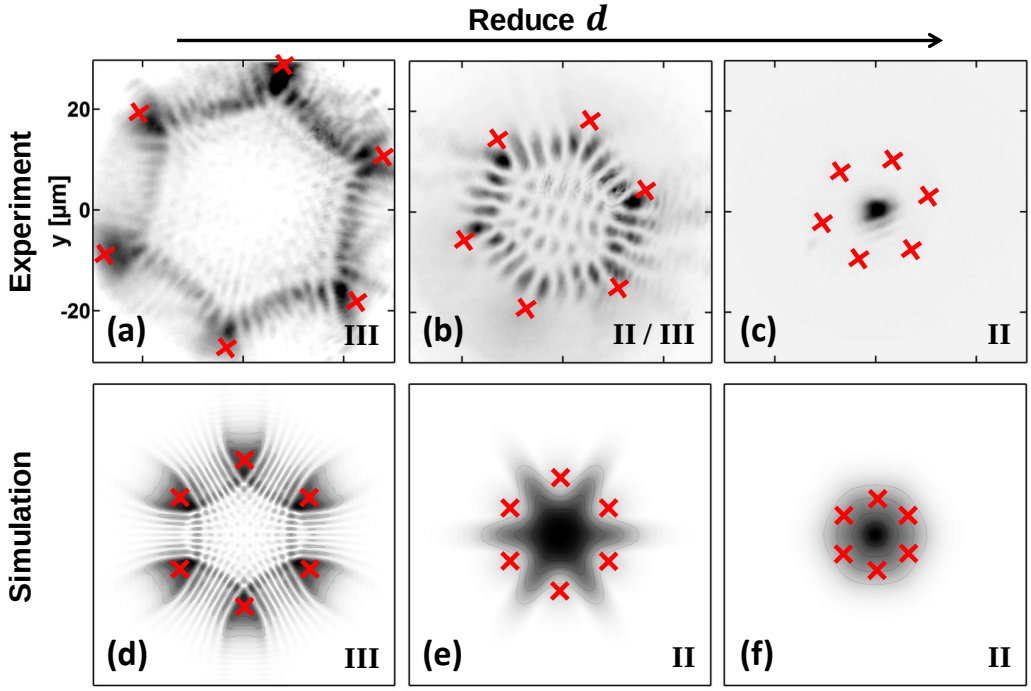

Figure 5.11: Transition from phase-locked to trapped condensate for $N = 6$ in experiment (a-c) and theory (d-f) for diminishing pump separation $d = 60, 40, 25$ μm. The white-to-black colour map codes the condensate density from low to high in linear scale, positions of pumping spots are marked by red crosses.

5.6 Theoretical simulation of N-spot condensates

Several factors influence the self-selected state of the condensate. Phase-locking is favoured by the stimulated scattering of bosons, emerging from the nonlinear complex Ginzburg-Landau (cGL) wave equation that describes the system [20, 44, 136]. Near-degenerate condensates are brought into degeneracy by the oscillatory exchange of coherent polaritons in Josephson coupling (Sec. 5.6.1 and Eq. 3.42). To understand the reason for the phase transition from locking to trapping, it is important to note that, as the pump approach each other more, the phase-locked polariton trajectories move to the inside of the pump ring, closer to the trap centre [Fig. 5.8(a,b)]. This might be because the polaritons radially emerging from each pump spot feel the combined flow of polaritons from all the other pump spots. On the inside towards the centre, these opposing flows at some point balance to produce a stationary flow velocity, $\vec{v} \propto \vec{\nabla}\phi = 0$ (for wavefunction $\Psi = \sqrt{\rho}\exp(i\phi)$) at which the polariton density ρ is then higher.

Our collaborators Guido Franchetti and Natasha Berloff have modelled this system with the

normalised complex Ginzburg Landau equation [94, 136],

$$-i\,\frac{d}{dt}\Psi(\vec{x}) = \left\{\left[1 - i\eta(\vec{x})\right]\nabla^2 - g|\Psi(\vec{x})|^2 - V(\vec{x}) - i\left[\alpha(\vec{x}) - \sigma(\vec{x})|\Psi(\vec{x})|^2\right]\right\}\,\Psi(\vec{x}) \tag{5.5}$$

where $\alpha(\vec{x})$ is the effective gain that incorporates non-equilibrium pumping and decay, $\eta(\vec{x})$ is a polariton diffusion constant arising from energy relaxation, $\sigma(\vec{x})$ is the gain saturation to avoid infinite growth of the condensate population with time (Eq. 3.31) and g is the polariton-polariton interaction constant, which can be set to 1 without loss of generality due to the used renormalisation $\Psi \rightarrow \Psi/\sqrt{g}$. The blueshifted potential $V(\vec{x}) = E_{\mathrm{BS}}\, f(\vec{x})$ from the combined pump reservoirs is the sum $f(\vec{x})$ of N Gaussian of width $w_{\mathrm{BS}} = 4\ \mu$m (see Eq. 5.4), while gain, saturation coefficient and diffusion are assigned a similar spatial dependence: $\alpha(\vec{x}) = f(\vec{x})$, $\sigma(\vec{x}) = 0.3\, f(\vec{x})$ and $\eta(\vec{x}) = 0.1\, f(\vec{x})$. The cGL simulation is performed on a discretised grid by calculating the time evolution of the wavefuntion in small time steps Δt, starting from a uniform distribution, until a steady state solution is reached: this is the final condensate Ψ.

This model qualitatively reproduces the transition described previously, as shown for $N = 6$ by the good match of PL images (a-c) and simulation (d-f) in Fig. 5.11. The phase-locking state (III) in (a,d) is reproduced with high fidelity and shows the same arrow-like features around the pump spots, arched connections of fringes between them and a regular hexagonal lattice of ripples with considerably smaller amplitude in the centre (condensate is prevented from reaching the centre). For reduced pump spot separation $d < d_t$ below the critical value for trapping, a clear transition to a condensate confined within the pump spots (II) is seen (c,e,f), with repulsion of the wavefunction from the blueshift potential around the pump spots.

It has to be mentioned however that the confinement to the trap is weaker than observed experimentally and that higher-mode trapped condensates, stationary in time as in (b), could not be reproduced convincingly in the simulation. Additionally, the trapped state's corners in (e) do not face the pump spots as seen in the experiment (b), but rather take up the potential valley in between them. A possible reason for this discrepancy is the simplified incorporation of non-resonant pumping. In our model gain is described by a single scattering rate $\alpha(\vec{x})$ into the condensate state and thus neglecting the full energy relaxation dynamics from non-condensed higher energy polariton states and some effects of exciton diffusion. Both factors enter only partially in the energy diffusion term $\eta(\vec{x})$.

5.6.1 Phase locking of condensates

To indicate how two condensates lock together, the cGL equations are written for interactions between two condensates Ψ_1 and Ψ_2 forming at different pump spots. In the Josephson limit (weakly coupled condensates) and in dimensionless units this gives

$$i\frac{d}{dt}\Psi_1 = [-\nabla^2 + |\Psi_1|^2 + (1-u)|\Psi_2|^2 + i(\alpha - \sigma|\Psi_1|^2)]\Psi_1 + J\Psi_2 \tag{5.6}$$

and similarly for Ψ_2, with $(1-u)$ explicitly describing the strength of the repulsive interaction between polaritons generated at different pump spots (i.e. effect of the blueshift of Ψ_2 on Ψ_1). To discuss the dynamics it is convenient to neglect the spatial dynamics and reparametrise using

$$\psi_{1,2} = \sqrt{\rho_{1,2}}\,\exp[i(\phi \pm \theta/2)] \qquad R = \frac{\rho_1 + \rho_2}{2} \qquad z = \frac{\rho_1 - \rho_2}{2} \tag{5.7}$$

and write coupled equations for θ, R, z (the global phase ϕ does not affect the dynamics). In visualizing the dynamics, one may consider a Bloch vector, defined by $\{x = \sqrt{\rho_1\rho_2}\cos\theta, y = \sqrt{\rho_1\rho_2}\sin\theta, z\}$ in terms of the above variables. Since there is pumping and decay, the length of the Bloch vector is not conserved, hence there is a dynamical equation for $R = \sqrt{x^2+y^2+z^2}$. The coupled equations have the form:

$$\frac{d\theta}{dt} = -2uz + \frac{2Jz\cos\theta}{\sqrt{R^2 - z^2}} \tag{5.8}$$

$$\frac{dz}{dt} = 2(\alpha - 2\sigma R)z - 2J\sqrt{R^2 - z^2}\sin\theta \tag{5.9}$$

$$\frac{dR}{dt} = 2\sigma\left(\frac{\alpha}{\sigma}R - R^2 - z^2\right) \tag{5.10}$$

The choice of parameters puts the system in the "Josephson regime" of the Josephson equation, i.e. $uR \gg J$, and that in addition $z \ll R$. In this case and by assuming the steady state solution $\frac{dR}{dt} = 0$, Eq. 5.10 simply reduces to $R = \alpha/\sigma$. Then one finds $z \approx -\frac{1}{2u}\frac{d\theta}{dt}$ from Eq. 5.8, which is substituted into Eq. 5.9 to yield:

$$\frac{d^2\theta}{dt^2} + 2\alpha\frac{d\theta}{dt} = 4uJ\frac{\alpha}{\sigma}\sin\theta \tag{5.11}$$

This equation describes a damped pendulum with α, which in rescaled units is proportional to the effective polariton gain, providing the rate of damping. This shows how two condensates which both experience gain and are weakly coupled will lock together to zero phase difference at a rate given by the gain coefficient α.

5.6.2 Analysis of the governing equation and simulations

Derivation by Natasha Berloff. The starting point is the non-dimensional form of the cGLE

$$-i\frac{d\Psi}{dt} = \left[(1-i\eta)\vec{\nabla}^2 - |\Psi|^2 - V - i(\alpha - \sigma|\Psi|^2)\right]\Psi \tag{5.12}$$

By using the Madelung transformation $\Psi = \sqrt{\rho}\exp(i\phi)$, where the velocity is $\vec{v} = \vec{\nabla}\phi$, we obtain the continuity equation

$$\frac{1}{2}\frac{d\phi}{dt} + \vec{\nabla}\cdot(\rho\vec{v}) = (\alpha - \sigma\rho)\rho \tag{5.13}$$

and the integrated form of the Bernoulli equation

$$\frac{d\phi}{dt} + v^2 + V + \rho - \frac{\nabla^2\sqrt{\rho}}{\sqrt{\rho}} - \frac{\eta}{\rho}\vec{\nabla}\cdot(\rho\vec{v}) = 0 \tag{5.14}$$

where only the leading order terms in η are kept. The last two terms are responsible for the difference between the usual Bernoulli equation of classical inviscid hydrodynamics and the Ginzburg-Landau equation in Eg. 5.12. The last term of Eq. 5.14 describes the friction between condensate particles and non-condensed particles and corresponds to the term introduced by Khalatnikov [137] into the equation of superfluid motion. In this formulation the coefficient η corresponds to the second kinematic viscosity ζ_3.
The term $-\nabla^2\sqrt{\rho}/\sqrt{\rho}$ of Eq. 5.14 is called the quantum pressure term. It is important at places where the density varies on distances comparable to the healing length given by $\xi = \hbar/\sqrt{2\mu}$, where μ is the chemical potential. For the steady state of Eqs. 5.13 and 5.14 we have

$$\vec{\nabla}\cdot(\rho\vec{v}) = (\alpha - \sigma\rho)\rho \tag{5.15}$$

$$\mu = v^2 + V + \rho - \frac{\nabla^2\sqrt{\rho}}{\sqrt{\rho}} - \frac{\eta}{\rho}\vec{\nabla}\cdot(\rho\vec{v}) \tag{5.16}$$

Combining the two equations we get the following expression for μ:

$$\mu = v^2 + V + \rho - \eta(\alpha + \sigma\rho) - \frac{\nabla^2\sqrt{\rho}}{\sqrt{\rho}} \tag{5.17}$$

where the terms quadratic in η are neglected. Note that in our full simulations we find that the terms $\eta\sigma$ and $\eta\alpha$ are indeed small compared to all the others because the second kinematic viscosity η is small. However the quantum pressure is a significant contribution to this chemical potential, and is the reason that potential energy from the blueshifts at the pump spots cannot be simply transferred into kinetic energy, as previously assumed for polariton condensates.

5.7 Discussion

Under certain aspects one can view the transition from a phase-locked state of N pump condensates to a trapped polariton condensate, which is separated from the reservoir, as a second order phase transition. By definition such a phase transition occurs at finite temperature $T > 0$ and changes the physical properties of a system upon variation of an external control parameter [138], such as pressure, magnetic field or chemical composition. This classification requires the presence of an order parameter which has to be zero in one phase and non-zero in the other, ordered, phase. In our case this order parameter is simply the wavefunction Ψ of the *trapped polariton condensate* and the control parameter is the trap depth related to d and P. For a second order transition, the increase of Ψ has to be marked by a kink right from the point when the threshold is crossed, i.e. the derivative of the order parameter with respect to the control parameter has to be discontinuous, which is clearly the case in our system.

The symmetry of the pumping geometry and hence the superfluid flow can be used to seek an intuitive explanation for the observed phase transition. The chemical potential [139] derived for this system in the limit of negligible diffusion constant $\eta \approx 0$ (see 5.6.2) is

$$\mu \approx \frac{m^* v^2}{2} + V + \hbar g \rho - \frac{\hbar^2}{2m^*} \frac{\vec{\nabla}^2 \sqrt{\rho}}{\sqrt{\rho}} \tag{5.18}$$

where $\rho = |\Psi|^2$. The four terms that make up the chemical potential are, respectively, the kinetic energy (KE), the exciton and polariton blueshift repulsion, and the quantum pressure (QP) energy. While the first three terms are in general positive, the QP contribution $-\vec{\nabla}^2\sqrt{\rho}/\sqrt{\rho}$ to μ is positive or negative, depending on the curvature or ρ in a specific location. This can reduce (condensate trough) or increase (condensate hill) μ, i.e. the free energy of the condensate.

In general the simulations show that for well separated pump spots the QP term in Eq. 5.18 dominates the polariton flow as it is important wherever the density varies on distances comparable to the healing length $\xi = \hbar/\sqrt{2m^*\mu} \sim 1$ μm. For a uniform quantum fluid with uniform pumping this term is significant at a vortex core and at the boundaries. It is also this term that gives the quantisation of the vortex circulation. In the bulk of the fluid, away from vortices and boundaries, the quantum pressure term is insignificant. When pumping is non-uniform the superposition of out-flowing waves creates a lattice of ripples as in Fig. 5.12(a). The ripple size is inversely proportional to the flow velocity, which for large velocities can become as small as the healing length and generate high values of the quantum pressure.

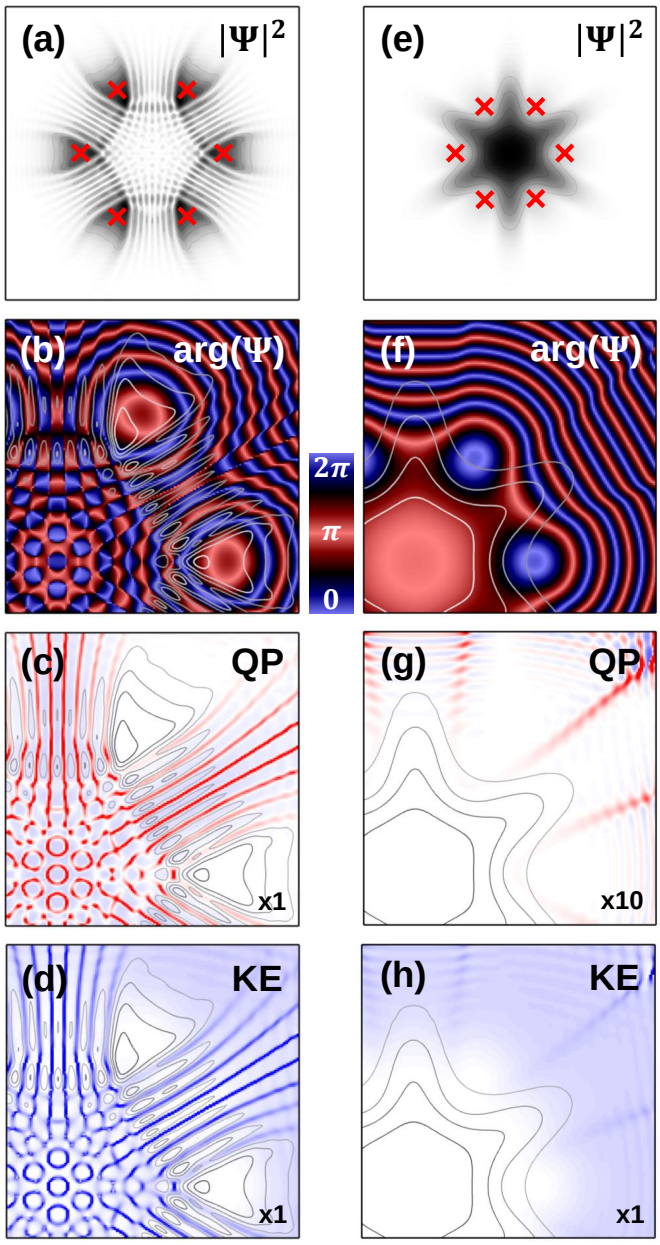

Figure 5.12: Details of the cGL simulation for the steady state condensate wavefunction Ψ in the phase-locked regime (a) and in the trapped regime (e). 2× magnified plots show the phase $\phi = \arg(\Psi)$ (b,f), the quantum pressure QP (c,g) and the kinetic energy KE (d,h) for these two regimes. Grey contour lines trace the wavefunction density $|\Psi|^2$ depicted in (a,e). For the QP and KE plots, positive contributions to the chemical potential μ are shown in red, negative contributions in blue; colour map scaling factors are shown in the bottom right corner, in order to compare energies directly in (c,g) and (d,h).

The phase-locked regime (III) in Fig. 5.12(a) is characterised by a very fragmented phase (b) in the centre between the pump spots, leading to very high negative QP energies in the troughs of the wavefunction, marked red in (c). In comparison, the positive contributions on the hills of $|\Psi|^2$ in blue are small. Because the chemical potential μ has to be the same everywhere in space, the kinetic energy in (d) balances the negative QP energy in (c) with an equally strong positive contribution, due to rapid changes in the phase ϕ. In the case of a trapped condensate (II) in (e) no fringes are present and the phase changes smoothly in space (f), signifying loss for the condensate in form of radial outflow. The QP energy is two orders of magnitude smaller (g) and now completely absent inside the condensate. The same observation is true for the kinetic energy.

In regime (III) the repulsive potential hills centred at each pump spot cause the velocity of outflow to increase with distance from the pumping spots, thus reducing the fringe spacing $\lambda_f = \pi/k_{||}^{\mathrm{BS}} = h/\sqrt{8m^* E_{\mathrm{BS}}}$ of the standing waves formed by the counter-propagating polariton currents between neighbouring pump spots. The fringe width is as small as the healing length, $\lambda_f \approx \xi$, with the QP term erecting a large energy barrier that strongly retards the flow of polaritons from each pump spot directly into the trap centre, thus preventing the locked state from collapsing.

Increasing the power or decreasing d destabilizes this situation. When the pumps approach close enough, then $\lambda_f > \xi$, the quantum pressure decreases, and the system becomes turbulent with vortices appearing, interacting, and disappearing, unconstrained by the quantum pressure barrier. In this domain the simulations show time-varying behaviour that never settles down even at long times. At even smaller separations the system again stabilizes to a trapped condensate in regime (II), the quantum pressure term reduces drastically, and all the vortices are expelled from the condensate, which is now trapped in the centre. While the quantum pressure controls the transition, it arises as a by-product of the initial phase locking rather than causing it directly.

On the theory front, energy relaxation of polaritons, from the exciton reservoir into the condensate state and also polariton relaxation among condensates at different energies, is not yet fully understood and implemented in our simulations. However, recently new and very promising theoretical tools [139, 140, 141] have being developed to shed light on this crucial topic for non-resonantly pumped condensates, which are non-equilibrium by nature.

In conclusion, the work presented here shows how a polariton condensate can transit from a phase-locked (III) to a trapped (II) configuration with a simple reduction in pump spot separation or an increase in pump power. Below a critical pump separation $d < d_t$, found both

experimentally and theoretically, the polariton superflow completely reorganizes into a trapped state in the centre of the pumping geometry. In regime (III) the dynamics are exciton-blueshift dominated, leading to accelerated expansion and in-plane diffusion of the polariton population. In contrast, in regime (II) the condensate is selectively excited and efficiently trapped in the desired state, well separated from unwanted interactions with the exciton reservoir. This very stable and clean condensate, amenable to further manipulation, is very important for high precision experiments such as extended cascaded polariton logic circuits [82], the envisaged polariton gyroscope [142] or a practical condensate spin switch similar to [143], which is the ongoing project of this experiment. In the latter effect, the spin of a non-resonantly pumped condensate in an optical trap can be flipped by a small change of voltage applied across the microcavity in growth direction.

Chapter 6

Flow properties and coherence of optically guided polariton condensates

6.1 Introduction

Polaritons interact strongly with each other and with laser-induced excitons, which leads to non-linear self-interaction and linear blueshift of the dispersion curve for rising pump power. For polaritons created at the peaks of the blueshift potential (on top of the pump laser) the excess potential energy is converted into kinetic energy as they flow away from gain regions towards dark, un-blueshifted areas of the sample. The gained momentum $\hbar k_{||}$ can be tracked by recording the k-space distribution of the PL, filtered with a pinhole transmitting light only from a small area of the sample plane.

The spatial shape of an extended non-resonant pump configuration plays an important role for the cloud of polaritons it creates. For trapped condensates presented in chapter 5 the condensate shape is determined by the competition between repulsive polariton interactions and the pursuit of high net gain, i.e. good overlap with the exciton reservoir. This leads to the formation of polariton condensates not at the pump line, but next to it, in wells of the blueshift potential. The influence of extended and structured optical excitation is a very recent development [144, 145] and has consequently been studied much less.

Commonly either tightly focussed pump spots or uniform illumination are used in polariton experiments. In this chapter the happy medium between these two extremes is examined, a geometry involving a single and two parallel laser pump lines (Sec. 6.2). The emission properties of the resulting polariton cloud are studied in power dependence both below and above the condensation threshold in Sec. 6.3. For the dual pump lines the polaritons are semi-trapped, i.e. free flowing in one direction and trapped in the orthogonal one, with constant gain provided over a 50 μm distance. In this configuration the polariton emission shows a wave-guiding effect with a bell-shaped polariton distribution. Spatially resolved analysis of the PL in k-space in

Sec. 6.3.2 reveals linear acceleration of the polariton flow. As shown in Sec. 6.4, the spatial coherence in the polariton cloud appears well below the condensation threshold and builds up gradually until a single energy condensate is formed. This continuous onset of condensation is further affirmed in Sec. 6.5 by analysing the power dependence of the dispersion curve, yielding information about cloud temperature and chemical potential. An interesting theoretical side note is presented in Sec. 6.6: a strong and spatially localised gain distribution inherently supports stationary wavefunctions that are analogous to those found in a finite box potential. Finally the implications of the experimental findings are discussed in Sec. 6.7.

6.2 Experimental setup and methods

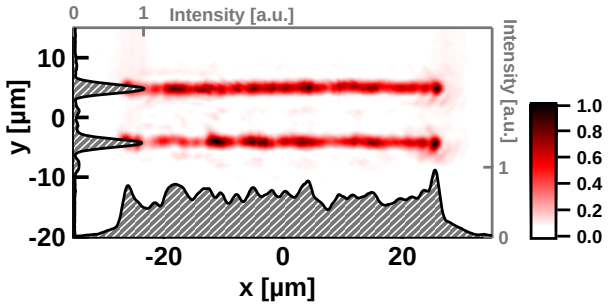

Figure 6.1: Excitation profile of two parallel laser lines.

The experimental setup, is identical with Fig. 4.1, with the exception of the pinhole interferometer described in the top sketch of Fig. 6.5. In this case a double pinhole replaces the element PH2. The pump laser is modulated into a single or two parallel lines with the SLM using the MRAF algorithm of Sec. 4.3.2. Separation of the phase-modulated laser beam from the unmodulated zero order is achieved by adding a blazed grating phase pattern ($g_x = 5$ px) on the SLM. The resulting laser image, recorded as reflected image off the sample surface in Fig. 6.1, presents two 50 μm long laser lines which are separated by 9 μm and have a FWHM of 1.6 μm. The profile across the line is a smooth Airy function, limited by the physical size of the SLM. Despite the considerable intensity variation in the horizontal cut (standard deviation of 18% around the mean), the low power PL images in Fig. 6.2(d) demonstrate that these spatial pump strength variations do not coincide with the ripples seen in the polariton condensate in Fig. 6.2(j), and are most likely due to dust flatness imperfections on the sample (laser image projected into the sample is much cleaner than the recorded reflection from it).

Optical diffraction is seen for spatially resolved data due to the small pinhole size ($\varnothing = 8$ μm for good spatial resolution). This inevitably washes out the k_x, k_y information, making it difficult

to asses the correct value for the polariton momentum in dispersion curves at low PL intensities and close to the apex at $k_x = k_y = 0$. To overcome this problem the $I(E, k_y)$ data is fitted with a parabola following the polariton dispersion curve [e.g. dashed parabola in Fig. 6.7(a1)]. A line profile with small averaging width *along* a path following this parabola is then calculated. From the projections of this line profile onto the k_y and the E axis it is easy to assess with high accuracy the local energy and momentum of the polariton population selected by the pinhole.

6.3 Polariton condensation with single and double line pumps

Polariton condensates rely on constant pumping due to their finite lifetime on the order of 10 ps. Hence spatially shaping the pump laser, and therefore the gain distribution, strongly affects the shape of the forming polariton condensate. Fig. 6.2 presents a comparison of the polariton luminescence (PL) below and above condensation threshold for pump geometries using a single (a-c, g-i) and two parallel (d-f, j-l) laser lines separated by $d_{\mathrm{sep}} = 9$ μm, marked by the white bars in (a,d,g,j). The PL images for **low excitation power** look similar for both pump geometries (left two columns), showing maximum emission on the pump line in real space (a,d). In k-space a suppression by one order of magnitude of polaritons with momenta directed along the laser line is seen [lack of luminescence in (b,e) with $k_y \gg k_x$]. With increasing pump power the luminescence distribution $I(k_x, k_y)$ narrows in width and is pushed to higher k_x momenta which lie on the un-blueshifted dispersion curve (c,f).

This observation is consistent with the picture of polaritons being created at the laser line, on top of a blueshift potential "hill" $E_{\mathrm{BS}}(\vec{x})$, and converting their potential energy into kinetic energy as they flow away in the direction of the potential gradient (Sec. 2.5.1). Far away from the laser line $E_{\mathrm{BS}}(\vec{x}) = 0$ and the polariton flow reaches its maximum momentum,

$$\hbar k_{\mathrm{max}} = \sqrt{2m^* \max[E_{\mathrm{BS}}(P)]} \tag{6.1}$$

set by the highest blueshift energy E_{BS} found within the polariton cloud for a certain pump power P. As shown in Fig. 6.4(d) E_{BS} increases linearly with pump power.

A departure from this simple picture is seen for two parallel pump lines in the form of two peaked, high-k_y lobes appearing at either side of the origin in the momentum distribution $I(k_x, k_y)$, marked "WG" (waveguided) in Fig. 6.2(e). Their energy [central blob in (f)] is slightly higher than the lowest energy polaritons on the outer dispersion curve. Already at low pump power these lobes represent fast flowing polaritons, ejected at each end of the waveguide formed by the two pump laser lines (j). **At the critical density** for polariton condensation ($P_{\mathrm{thr}} \sim 16$ mW

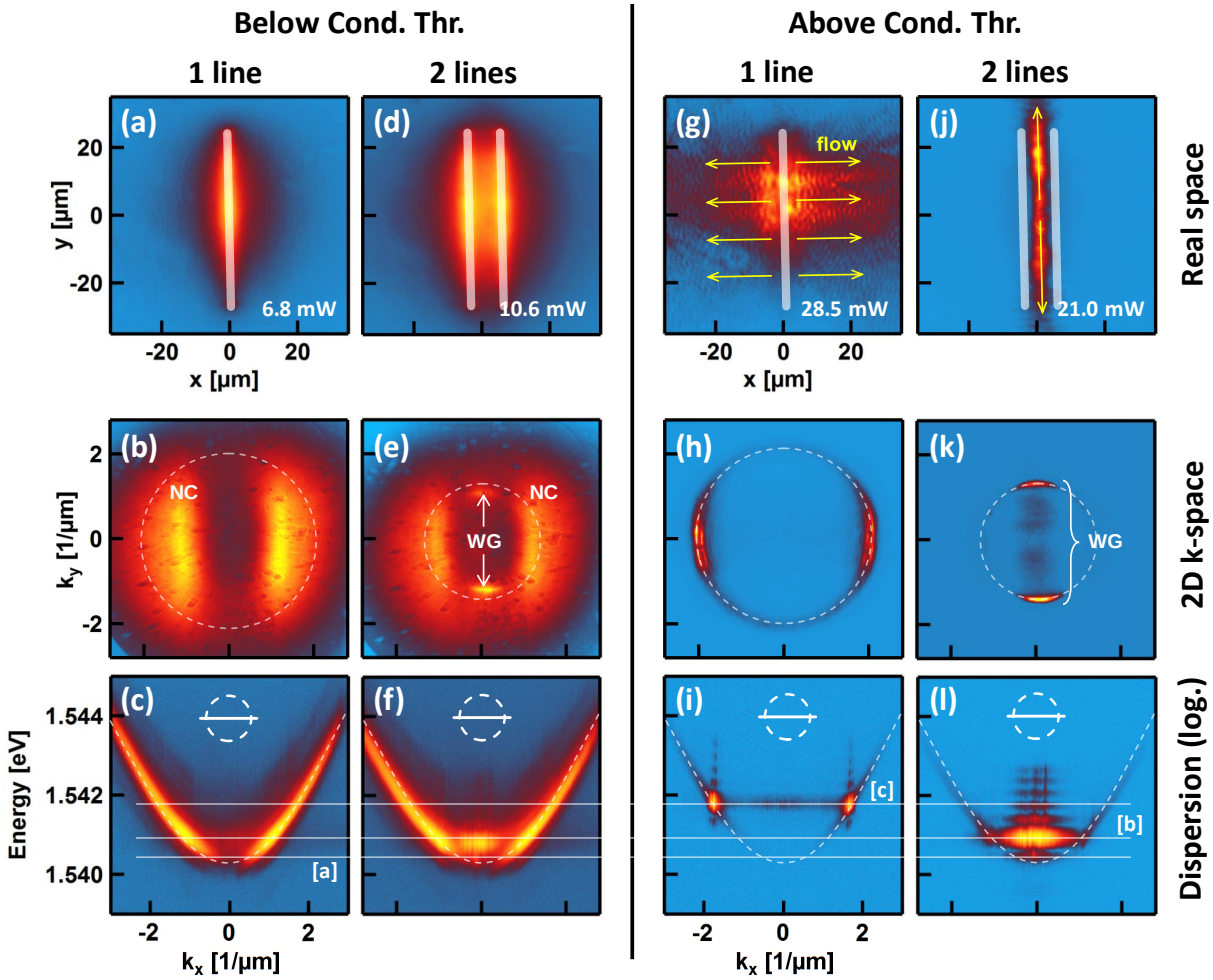

Figure 6.2: Polariton luminescence for a single (a-c, g-i) and two parallel (d-f, j-l) laser pump lines [translucent white bars in (a,d,g,j)], below and above the condensation threshold. Top row: real space PL images with added polariton flow direction (yellow arrows) and respective pump powers. Middle row: corresponding 2D k-space showing main flow directions. Bottom row: energy-resolved cuts along $k_y = 0$ of the 2D k-space images with dashed lines to emphasize the energy difference of the formed polariton condensates. Labels WG (wave-guided polaritons) and NC (non-condensed polaritons) are used later for the dual line pump configuration.

for the dual line pump) the difference between the single line and the double line pump becomes very pronounced, with polaritons flowing exclusively in orthogonally opposite directions, as shown in (g,j) [yellow arrows show flow direction] and confirmed by the k-space images in (h,k). Interestingly, the blueshift of the condensate in the double line case is only a third of the value for a comparable single line condensate (i,l) at roughly equal excitation power. This suggests that condensed polaritons are not formed on top of the laser line but rather directly inside the waveguide. This is because polaritons are not point-like objects but extended wave-like bosons, described by a wavefunction $\Psi(\vec{x})$ of size $\lambda_{\mathrm{dB}} = h/p$.

Another remarkable feature is the complete absence of polaritons in states with energy lower than the condensate in the two-line case in Fig. 6.2(l), compared to a single pump line in (i) [see also Fig. D.3(m-o)]. This hints to a very efficient harvesting mechanism, presumably stimulated bosonic scattering. In this way, the condensate collects the overwhelming share of the higher energy polaritons from the dispersion curve, leaving no gain to states with energies lower than its own. A possible explanation for this could be the quasi-1D environment created by the two pump lines, restricting motion in k_x direction and hence lifting momentum conservation for k_x altogether (only energy and k_y have to be conserved). In summary, the incoherent and non-resonant double line pump profile in Fig. 6.2(i) shows that polariton emission can efficiently be channelled in a semi-confined geometry (weakly already below threshold), creating a high-gain polariton jet with well-defined energy, which is controlled by the pump power.

6.3.1 Spatial profiles in power dependence

A power dependence of the spatial emission profiles (normalised for easy comparison) along the x and y directions (Fig. 6.3, full dataset in Figs. D.2 and D.3) reveals an even clearer distinction between the two geometries. For a **single pump line** (a,b) the peak emission centre coincides with the laser line (grey hatched curve) for all pump powers. The FWHM of the profile in (a) increases linearly with pump power from 6 μm to 17 μm, consistent with the faster outflow seen in k-space. The onset of condensation is accompanied by appearance of fairly regular ripples spaced by 1.5 μm in the outflow (orange and yellow profile in (a)) as observed in [87], which is comparable to the expected condensate healing length ξ.
Beyond $x = \pm 15$ μm the profile shows a constant intensity level for more than 30 μm of free space propagation (aperture limited field of view). Here the polaritons have reached the edge of the blueshift potential and travel at constant momentum of $k_x = \pm 1.8/\mu$m away from the laser [Fig. 6.2(g)]. Propagation over such long distances with little decay is unusual, since the fraction of non-decaying polaritons in this stretch should be very small, $\exp(-\frac{m^* x}{\hbar k_x \tau}) = 4\%$. A defect represents an obstacle for the outflow and is clearly visible as a jump in the profile (dashed line

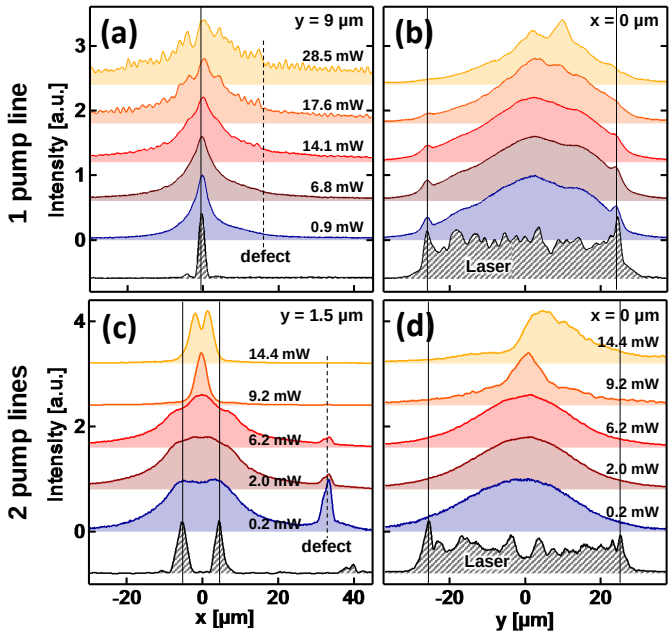

Figure 6.3: Spatial profiles of the polariton emission for different pump powers for a single (a,b) and a double (c,d) pump laser line. The hatched profile belongs to the pump laser projected onto the sample, solid lines are guides to the eye and the dashed line in (a) marks the position of the defect in Fig. 6.2(g).

in Fig. 6.3(a)). In the y direction [(b), along the laser line] the PL emission becomes localised above threshold, with intensity peaks appearing in the otherwise smooth profile.

For **two pump lines** the behaviour is radically different. In the x direction (c) the emission is located on the two pump lines at first and moves in between them with increasing P. Above condensation threshold a sharp peak (FWHM = 3.8 μm) arises *in between* the lines, well confined to the narrow waveguide (orange profile in (c)). In contrast to a single pump line at similar pump power, the profile is completely smooth with no substantial perpendicular outflow – all the light is guided along the channel imposed by the laser lines.
Both observations support the argument that the x degree of freedom is frozen out due to strong gain along the channel (Sec. 6.6) and due to tight confinement: $\lambda_{\mathrm{dB}} \gtrsim d_{\mathrm{sep}}$ (Eq. 3.6). In the y direction and below the condensation threshold the profile is very well fitted by a Gaussian with half width $\sigma_x = 20$ μm ($\chi^2 = 0.08$), while above threshold the profile shows some localisation of the emission attributed to local disorder and spatial fluctuation of the pump laser intensity along the pump line. A further Increase of P leads to simultaneous appearance of higher order wavefunctions with two or more lobes in the tightly confined x direction [yellow profile in (c,d)],

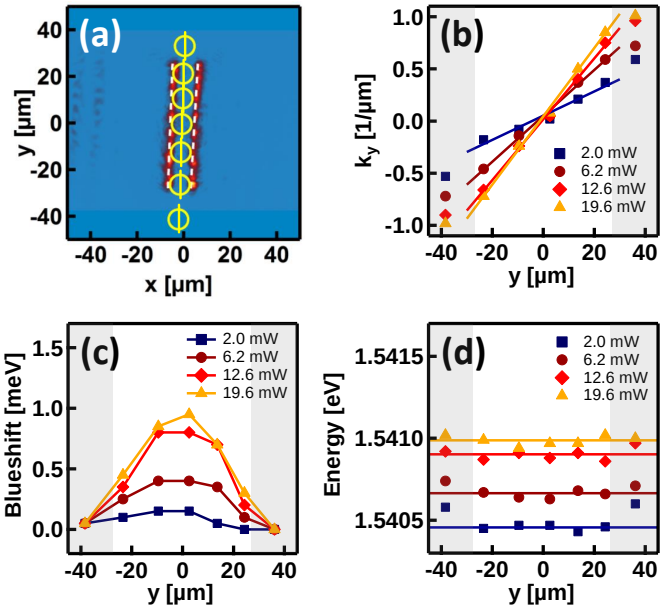

Figure 6.4: Polariton dynamics from spatially and energy resolved PL for the laser waveguide. (a) Image of the pump laser with yellow symbols marking pinhole positions. (b-d) Polariton momentum, local blueshift energy and absolute energy for the positions marked in (a). Grey shaded areas are outside the pump region.

while sample disorder again leads to peaking of emission along y.

In summary the analysis of the spatial emission profiles shows strong ripple formation and perpendicular outflow for a single pump line above threshold. For two pump lines the emission is fully waveguided by the laser lines, with the orthogonal cross-section demonstrating that this system behaves essentially as a 1D semi-confined system with strong gain all along the area enclosed by the laser line. As will be outlined in Sec. 6.6, the Schrödinger equation supports stationary states that resemble closely the low pump power profiles in Fig. 6.3(d).

6.3.2 Flow analysis in k-space inside the waveguide

Insight into the polariton dynamics can be obtained from spatially resolving the PL for several positions, with a pinhole PH2 in an intermediate real space plane in the detection path (Fig. 4.1). Recording the dispersion curve in such a way for different pinhole positions and pump powers in between the two laser lines (Figs. 6.4 and D.1) yields information about the local flow direction, speed, blueshift potential and energy relaxation of the waveguided polaritons. The yellow symbols in (a) mark the pinhole position and size, while the lines encode the direction of the momentum cut imaged by the spectrometer (data analysis described in Sec. 6.2). The extracted

momenta at these positions are plotted in (b) for a series pump powers, from very low powers to $P > P_{\mathrm{thr}} = 16$ mW. It is evident that the waveguided outflow momentum k_y increases linearly with y, for all pump powers within the area enclosed by the pump lines (white region), $k_y \propto y$. This implies that polaritons accelerate linearly with distance from the centre over a stretch of 50 μm, until they reach the end velocity set by the blueshift in the grey shaded area.

The spatially resolved blueshift profile in Fig. 6.4(c) is found to have a bell shaped curve whose amplitude increases linearly with pump power up to the condensation threshold. It is obtained from the energy shift of the local polariton dispersion parabola (PH in real space plane) compared to the low power un-blueshifted curve. However the absolute energy of the polariton population in (d) (simply the mean polariton energy measured at a PH position) remains at a constant value for all pump powers and along all the way from the centre to the edge of the line pump [compare also Fig. D.1(d,i)]. In the grey shaded area, outside the pumped region, a slight increase of the polariton energy is found at low P. An interesting observation is the difference by a factor ~ 2 between the maximum local blueshift in (c) and the global condensate energy in (d) with rising pump power, hinting at a possible pair creation mechanism: two polaritons share half of the blueshift energy and travel in opposite directions $\pm y$ with momenta $\pm k_y$, respectively.

6.4 Below threshold coherence

As shown in Fig. 6.4(a,b) polaritons inside the waveguide are accelerated in a linear fashion from the centre towards both ends of the laser lines. For all measured pump powers they retain constant total energy throughout their travel, with no measurable energy relaxation. Since there is no abrupt change of dynamics at the condensation threshold, this poses the question whether coherence is established already below the condensation point. Similar observations of macroscopic coherence below threshold have been reported for a single exciton state in an individual ordered conjugated polymer chain [146] and to some extent in a 1D polariton wire [20]. In 2D geometries however, coherence seems to be present only above the condensation threshold [147].

In the experiment presented here this point is addressed by performing Young's-slit-type interferometry on the PL emitted in between the two laser lines [Fig. 6.5(a)]. Similar to [146] we are using two pinholes with variable separation d placed in an intermediate real space plane to select light from two distant regions and interfere it in the far field through diffraction (Fig. 6.5 top). Each pinhole filters out a circular region of 3.8 μm diameter from the PL light. The presence of spatial coherence between the two selected regions shows up in k-space as interference fringes [Fig. 6.5(b)]. The fringe contrast is a measure of the degree of coherence [20] as seen from

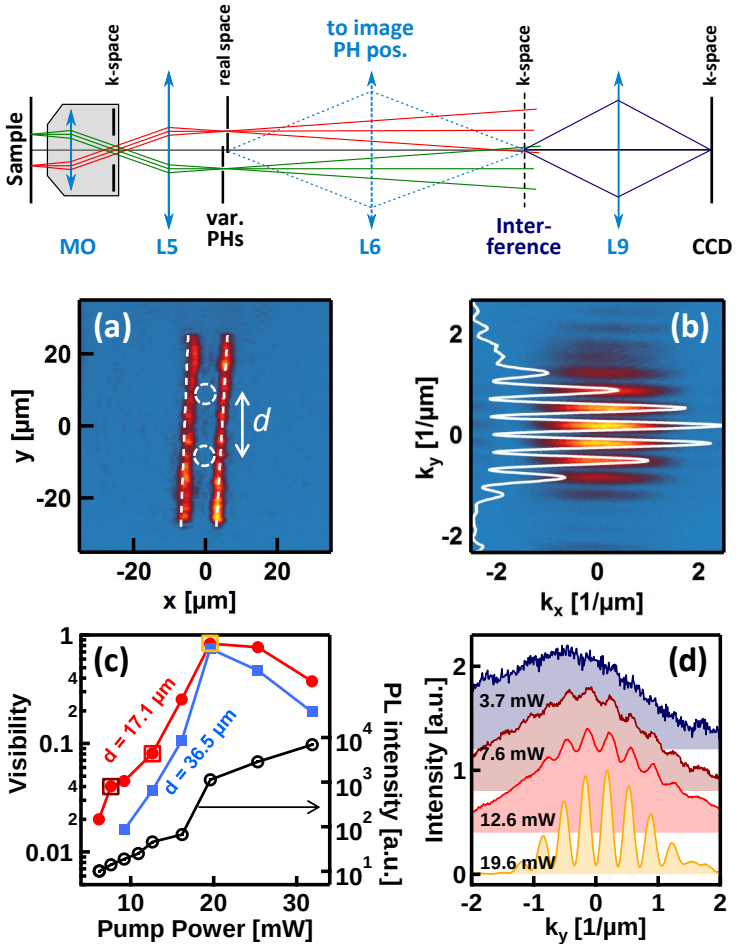

Figure 6.5: Coherence of the waveguided polaritons as a function of pump power. Top: optical setup consisting of two pinholes in a real space plane with variable separation d. The resulting interference fringes in k-space are imaged by the lens L9 directly onto the CCD camera. The removable lens L6 is used to image the pinhole position (compare to Fig. 4.1).
(a) Laser image with location of pinholes. (b) Double pinhole interference pattern formed in the far field for a condensate. (c) Pump power dependence of the fringe visibility for two pinhole separations d with corresponding integrated photoluminescence intensity (black curve). (d) Fringe cross section for $d = 17.1$ μm for selected pump powers which are highlighted by the coloured squares in (c).

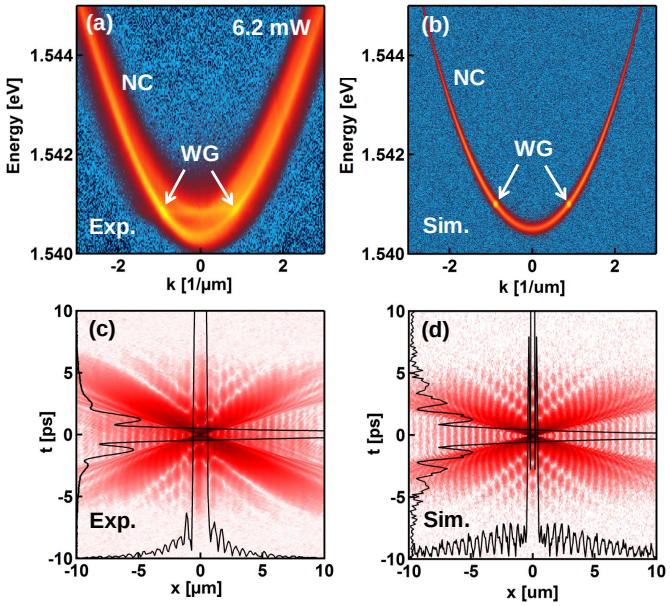

Figure 6.6: Estimation of the coherence from the dispersion curve by Fourier transformation. (a,b) Experimental and simulated polariton distributions $I(k_y, E)$ along the dispersion curve. (c,d) Coherence function $g^{(1)}(\Delta y, t)$ obtained from a Fourier transformation of (a,b).

the power dependence in Fig. 6.5(d), performed at a pinhole separation $d = 17.1$ μm. Finally the plot in (c) presents the fringe contrast for two pinhole separations $d = 17.1$ μm (red curve) and $d = 36.5$ μm (blue line) as a function of pump power P. These separations correspond to about 2 and 4 times the assumed de Broglie wavelength $\lambda_{\mathrm{dB}} = 9$ μm. In both cases the rise of coherence with pump power is exponential, rather than zero below threshold with an abrupt onset.

Remarkably, long-range spatial coherence can be tracked down to pump powers as low as 0.3 P_{thr} (5 mW). The threshold is estimated to be at $P_{\mathrm{thr}} = 16$ mW, where the fringe contrast peaks and the total PL emission [black curve in (c)] shows a strong kink from linear to superlinear dependence on the pump power. Past the condensation point the visibility diminishes again due to formation of multiple condensates at different energies. The range d_{coh} of the coherence increases with pump power, since fringes appear for narrow spaced pinholes first in a pump power ramp-up. As a side note, the black input-output curve in (c) seems to show only a very narrow power window of superlinear PL emission. The negative kink at $P = 20$ mW is attributed to the population of higher energy modes of the waveguide which have considerably larger loss rates due to weaker confinement.

A remarkable property of the dispersion curve is that temporal and spatial coherence can be

studied from its intensity spectrum $I(k_y, E)$. In fact, $I(k_y, E)$ is linked to the first order coherence function $g^{(1)}(\Delta y, t)$ by a simple 2D Fourier transformation [147]. Despite the limited resolution of the setup (energy resolution 0.1 meV for the spectrometer, momentum resolution $\sim 0.04/\mu$m from optical setup), this method is useful to test the presence of spatial coherence, signalled by vertical stripes in Fig. 6.6(c,d). As explained above, coherence is established by the waveguided polariton population which will be denoted as WG from here on, as opposed to the non-condensed polariton population NC found mainly outside the waveguide (Fig. 6.2(e,k)).

By creating a dummy power spectrum as shown in Fig. 6.6(b) it is possible to selectively switch on or off the contribution of WG or NC polaritons in the coherence function $g^{(1)}(\Delta y, t)$. Polaritons smoothly distributed along the dispersion curve (NC) produce all diagonal features in Fig. 6.6(c,d), while vertical fringes stem exclusively from WG polaritons (see Fig. D.4). The fringe spacing is very sensitive on the momentum separation of the two WG polariton lobes, hence this method can accurately measure the maximum WG momentum, by adjusting the dummy WG position in $k_{||}$ to obtain fringes identical to the experimental data, e.g. $k_{\mathrm{WG}} = 0.89/\mu$m in Fig. 6.6(a). As a side note, if one distributes WG polaritons with width tangential to the dispersion curve (i.e. a macroscopic population of a range of adjacent states on the dispersion curve) one cannot reproduce the features seen in (c) [compare also Fig. D.4]. This implies that WG polaritons are indeed condensed and populate a single state, whose spread in E and k is completely unrelated to the dispersion curve. Temporal coherence is seen to slightly increase with pump power but the width of the time feature in (c,d) is essentially resolution limited. The spatial coherence can be estimated from $\Delta s = c \cdot \Delta t = 120$ μm, where $\Delta t = 0.4$ ps is the width of the main temporal feature in Fig. 6.6(c,d). This result agrees with interferometric results.

6.5 Secrets of the dispersion curve: temperature and chemical potential

The most important relation in polariton research is arguably the dispersion curve. All the important properties of polaritons can be extracted from it, the effective mass, the quantum number and population of the polariton state, its composition and the coupling strength of the system. Hence it is important to study the process of condensation on the dispersion curve. The PL distribution for waveguided polaritons[1] as a function of energy is plotted in Fig. 6.7(a) for a set of different pump powers on algorithmic scale: the black curves are obtained from integrating the dispersion curve [e.g. in (a1-a3)] along the k_y-coordinate. Two peaks are visible in each profile, the lower energy one belongs to the non-condensed (NC) population (blue shaded area)

[1]The spectrometer slit selects only PL along the line $k_x = 0$ between the two pump laser stripes.

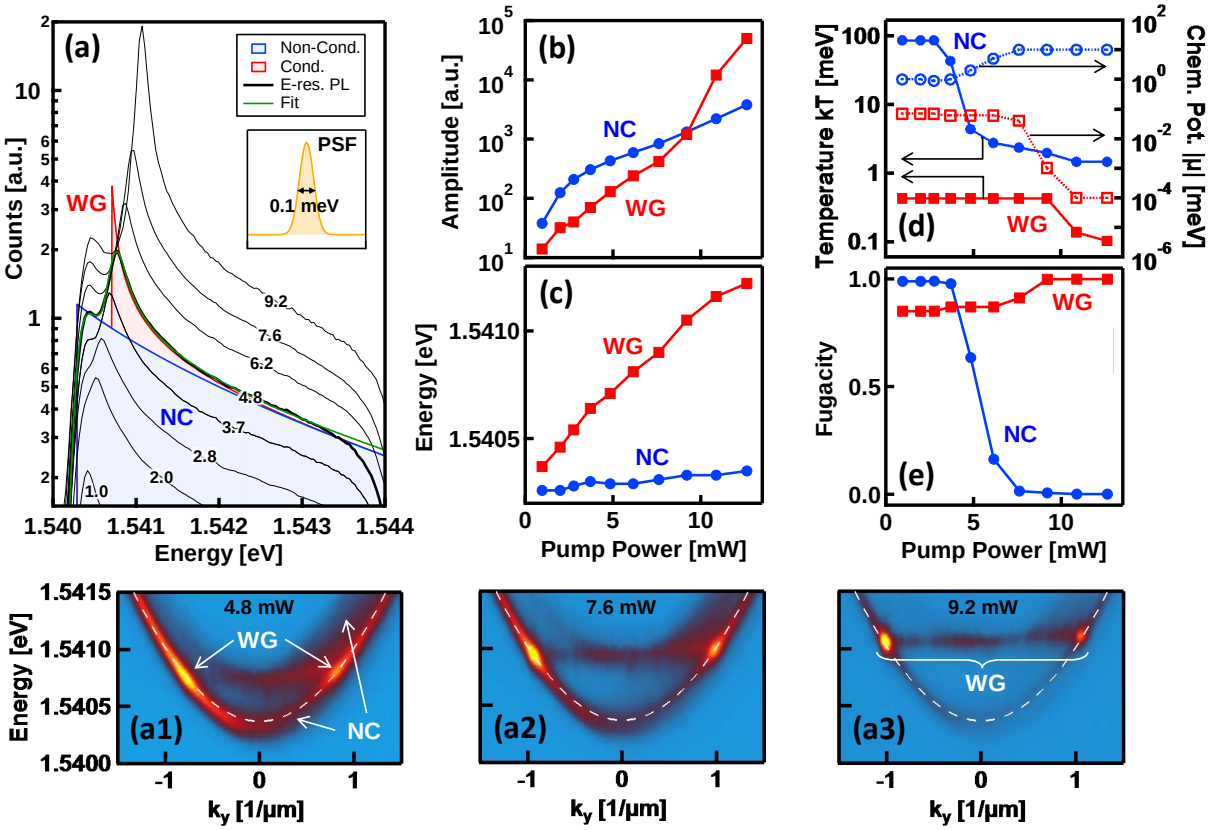

Figure 6.7: Fitting of the condensed part of the waveguided polariton population. (a) Energy-resolved PL intensity (black) for different pump powers (numbers in mW) in logarithmic scale. Black curves are integrated PL from the dispersion curves (a1-a3) along k_y. Two Bose functions (green, Eq. 6.2) are fitted, one for the non-condensed cloud (blue, NC: not condensed) and one for the condensed population (red, WG: wave-guided). Fit parameters are plotted as a function of pump power for WG and NC polariton population: relative occupation (b), blueshift energy (c), temperature and chemical potential (d) and fugacity (e).

and the blueshifted peak to the right refers to the waveguided (WG) portion of the luminescence, which condenses (peaked red shaded region). The cut-off of the PL at the high energy end of the spectrum is due to the band pass filter used to remove featureless high energy PL from the polariton reservoirs around the laser.

Very good fit results, matching the data for all pump powers, are obtained by fitting two Bose functions[1] for the NC and WG polaritons (green curve), convolved with a Gaussian point spread function (PSF) of FWHM = 0.1 meV [inset in (a), yellow] to account for the limited energy

[1]Can Bose functions validly fit non-equilibrium systems? I don't know, however the PL data in Fig. 6.7(a) fits extraordinarily well with Bose functions, for all measure pump powers.

resolution of the spectrometer

$$f(E) = \left[\frac{A_{\mathrm{NC}}}{\exp\left(\frac{E-E_{\mathrm{NC}}-\mu_{\mathrm{NC}}}{k_{\mathrm{B}}T_{\mathrm{NC}}}\right)-1} + \frac{A_{\mathrm{WG}}}{\exp\left(\frac{E-E_{\mathrm{WG}}-\mu_{\mathrm{WG}}}{k_{\mathrm{B}}T_{\mathrm{WG}}}\right)-1} + \mathrm{BG} \right] * \mathrm{PSF} \tag{6.2}$$

BG is simply the noise background of the image and the Bose functions for NC and WG polaritons are normalised so that the amplitudes $A_{\mathrm{NC}}, A_{\mathrm{WG}}$ represent the respective populations. The resulting fit parameters as a function of pump power are presented in Fig. 6.7(b-e) for both populations, NC in blue and WG in red. The amplitude data $A_{\mathrm{NC}}, A_{\mathrm{WG}}$ in (b) reveals that the WG population increases at much higher rate than the NC population (logarithmic plot). WG polaritons are blueshifted linearly and much more than NC polaritons (c), as expected.

For this measurement it is not easy to define a sharp condensation threshold for WG polaritons. Already at 4.8 mW a sizeable population accumulates in the WG state [Fig. 6.7(a1) and red area in (a)], while its amplitude is half an order of magnitude smaller than for NC polaritons (b). The point at $P_{\mathrm{thr}} = 9.2$ mW in (b), where $A_{\mathrm{NC}} = A_{\mathrm{WG}}$, will be used as a conservative estimate of the condensation threshold in this measurement. A remarkable observation is that the temperature of WG polaritons [solid red squares in (d)] remains constant at $T_{\mathrm{WG}} = 5$ K (with $k_{\mathrm{B}} \cdot 1\ \mathrm{K} \approx 0.1$ meV), from low pump power all the way into the condensation regime. In order to fit the NC population [blue "line" in (a), nearly a Boltzmann distribution] a high temperature of $T_{\mathrm{NC}} \sim 1000$ K has to be used, which reflects the non-equilibrium nature of the system. Above P_{thr} the NC population cools to 17 K, which might correlate with improved polariton relaxation or better feeding of the WG population at high pump power.

The chemical potential for WG polaritons [open red squares in (d)] decreases by three orders of magnitude around the condensation threshold as a consequence of the peaking in the energy distribution. For NC polaritons the chemical potential is four orders of magnitude higher at the condensation threshold and seems to increase only slightly, compared to the big drop seen for WG polaritons. From the fugacity plot $z = \exp(\mu/k_{\mathrm{B}}T) \in [0, 1]$ in (e), which describes if the Bose gas is in the quantum limit [148] ($z = 1$, condensate) or not ($z \sim 0$, classical gas), one can see that the WG polaritons are very close to a condensate already from low pump powers. The "condensed" regime $z = 1$ of NC polaritons for low pump power is likely an artefact of a too small estimation of $|\mu_{\mathrm{NC}}|$ in conjunction with the high temperature T_{NC}.

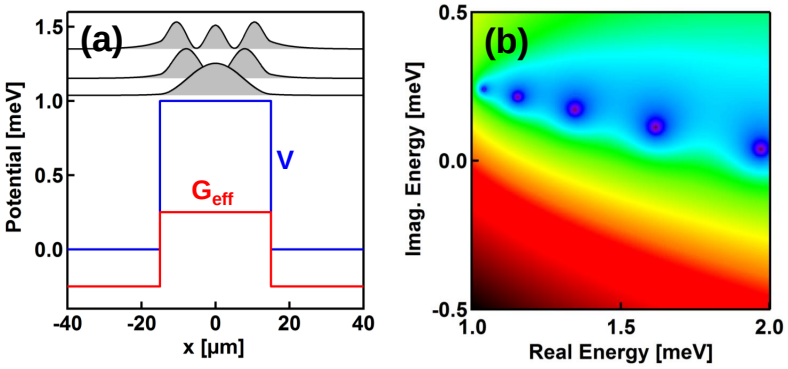

Figure 6.8: (a) "Bound" states in a repulsive potential (blue) with effective gain (red). Grey shaded curves show the first three quantum states plotted at the respective eigenenergies real(E). (b) Corresponding poles in the complex energy plane.

6.6 Simulation with 1D Schrödinger equation

It is well known that polariton physics and non-linear optics share many similarities (the strong $\xi^{(3)}$ non-linearity is $\hbar g|\Psi|^2$ in the case of polaritons). In fact, classical light has been shown recently to form a coherent state with all relavant signatures of a BEC [149]. Furthermore, numerical simulations have shown that the Schrdinger equation in the presence of gain[1] is equivalent to a non-linear electromagnetic wave equation and that a system with sufficient gain becomes insensitive to time-dependent perturbations [150] – the strong gain stabilises the system to a stationary state. This can be seen from studying the eigensolutions of the 1D time-independent Schrödinger equation[2] in the presence of a complex potential $\tilde{V}(x) = V(x) + iG_{\text{eff}}(x)$:

$$\left\{ \frac{d^2}{dx^2} + \frac{2m^*}{\hbar^2} \left[E - \tilde{V}(x) \right] \right\} \Psi(x) = 0 \tag{6.3}$$

This problem is mathematicaly identical to a single particle in a finite box, but instead of the box potential $V(x)$ the effective gain $G_{\text{eff}}(x)$ dominates the system properties. Bound states exist if the energy poles are in the upper half of the complex plane. This happens if there is net gain $G_{\text{eff}} > 0$ in some region (accounting for gain and loss), independently of the values of $V(x)$ (it can be repulsive too), so that the imaginary part of the eigenvalues E of Eq. 6.3 are positive.

[1] Which is the generalised GPE equation in the limit of negligible non-linearity
[2] Confinement in second dimension is tighter than λ_{dB}

Fig. 6.8(a) shows a transfer matrix simulation for a complex potential

$$\tilde{V}(x) = \begin{cases} (1 + 0.25\,i) \text{ meV} & |x| < 15\ \mu\text{m} \\ -0.25\,i \text{ meV} & |x| > 15\ \mu\text{m} \end{cases} \tag{6.4}$$

Despite the strong repulsive potential (simulating the blueshift potential) bound states are supported in this system (grey curves, plotted at their respective eigenenergies). Note that the first state looks remarkably similar to the low-pump-power PL profile in the Fig. 6.3(d). This shows that a system with effective gain can express stationary states localised to the gain area, analogous to those found in a finite potential well.

The plot in (b) shows the corresponding energy poles, which lie in the upper half of the complex plane and are short lived ($\text{imag}(E) \approx G_{\text{eff}}(0)$). In order to develop coherence in this system the lifetime of the state, deduced from the imaginary energy in (b), has to be larger than the polariton lifetime $\tau_s = \hbar/\text{imag}(E) > \tau_{\text{pol}}$. In our case this imposes a lower limit to the effective gain, $G_{\text{eff}}(0) > \hbar/\tau_{\text{pol}} = 0.1$ meV, above which the system supports bound-state wavefunctions for a spatially localised gain distribution.

6.7 Discussion

Optical traps have been used successfully to create polariton condensates with clear spatial separation of condensate and pump geometry, showing good coherence properties and reduced condensation threshold. In this chapter the related geometry of two parallel pump lines is studied. For a single pump line the observations are congruent with those from a focused pump spot, except for the strong suppression of polariton population with small k_x momentum. In contrast the dual line pump creates a 1D waveguide which channels the flow and speed of polaritons already below threshold. Spatial coherence and linear momentum gain are both found already at $0.3\,P_{\text{thr}}$. Above threshold the waveguided flow becomes highly dominant: polaritons are accelerated from the centre to the edges of the waveguide, where they are expelled with high end velocity, set by the blueshift potential.

Experimental results show that polaritons formed in between these two pump lines are extended matter waves with wavelength $\lambda_{\text{dB}} \sim 9\ \mu$m that tend to behave like a single 1D quantum object right from very low pump powers. The bell-shaped wavefunction profile seen in our experiment suggests that a collection of polaritons reacts to its environment as a single unit even below threshold. By progressively assimilating their momenta and gaining coherence, the condensate simultaneously screens out the disorder potential and gain imbalances. Such profiles

are stationary states of the 1D Schrödinger equation for the case of a positive imaginary gain potential, which mathematically is equivalent to a trapped state inside a finite potential well. It is not clear why no signature of the double-lobe states, as in Fig. 6.8(a), has been seen in the experiments. Presumably it is energetically not favourable to populate this state even though it is only 0.15 meV higher in energy (smaller than $k_{\mathrm{B}}T_{\mathrm{WG}} = 0.4$ meV) in this system due to non-linear feedback from continuous pumping.

The hypothesis of very early onset of condensation is supported experimentally by fits to the energy distribution along the dispersion curve, which suggest a constant cloud temperature of waveguided polaritons of $T_{\mathrm{WG}} = 5$ K or lower for all investigated pump powers. Furthermore the data shows a linear increase of the polariton momentum with distance from the line centre. Spatial correlations are visible already at a fraction of the condensation power and over distances of several λ_{dB}. The exponential rise of fringe visibility suggests that coherence is intrinsic to the population of waveguided polaritons. A possible model explaining these observations could be based on pair scattering, creating two polaritons with opposite momentum while preserving spatial correlation. With this mechanism two polaritons from the gain reservoir at $k_y \approx 0$ are scattered into two polaritons moving apart from each other in $\pm y$ direction with constant acceleration up to the blueshift limited end velocity $\pm\hbar k_c/m^*$. In contrast to a trapped condensate, here the maximum momentum is equal to the free polariton momentum at the blueshift energy (Eq. 6.1) as can be seen from Fig. D.3(k-o).

In summary the dual line pump configuration offers a very interesting quasi-1D environment in which many properties related to condensation and coherence dynamics can be studied. In this geometry polaritons are efficiently waveguided along the channel and then ejected as a jet of well controlled direction and flow speed. These properties could become useful for all-optical polariton circuits requiring a defined polariton flow from a source offering much better control than the simple focussed single pump spot. From the theoretical point of view this system has not been explored yet but could reveal interesting insights into a quasi-1D condensate, with the main blueshift gradient well separated from the flow direction.

Chapter 7

Polaritons with an electric dipole moment

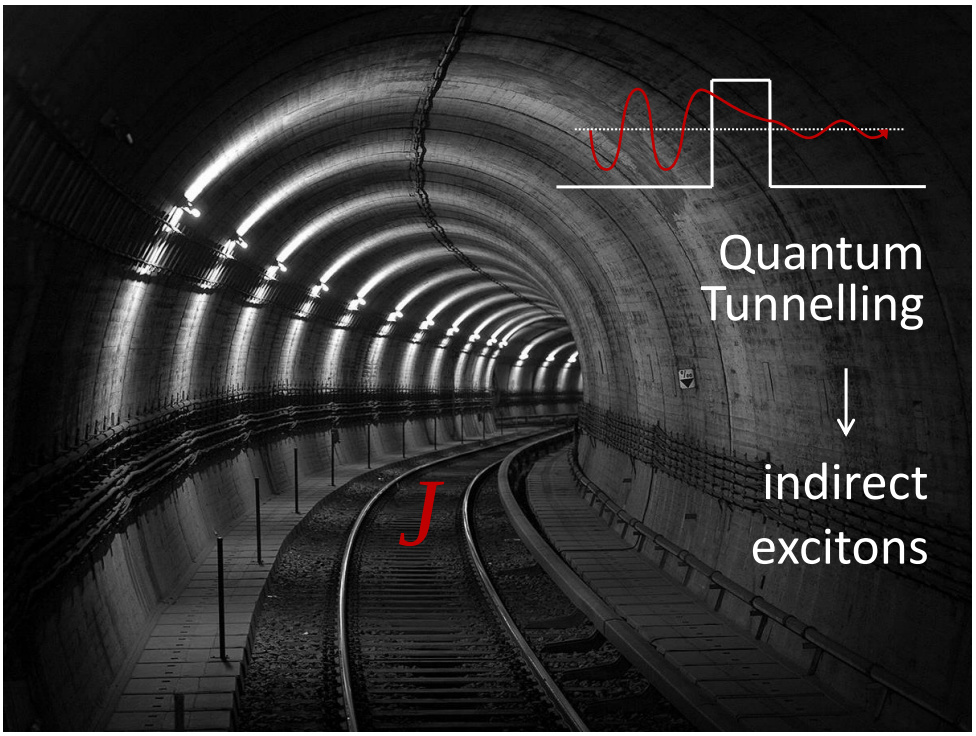

Figure 7.1: Electron tunnelling through a thin potential barrier between two adjacent quantum wells leads to the formation of indirect excitons.

This chapter is dedicated to a slightly different topic: polaritons in a microcavity containing sets of *coupled* QWs at the antinodes of the cavity light field. Each pair of QWs is separated by a nanometre thin spacer layer which constitutes a potential barrier separating the electron level in the two QWs. An electric field can be applied to this microcavity, allowing electrons to tunnel through this barrier, as sketched above. The concept of a "dipolariton" will be introduced here, the result of a microcavity with three interacting excitations – direct exciton, indirect exciton and cavity photon – coupled by two interactions: strong tunnelling coupling (direct to indirect exciton) and strong optical light-matter coupling (direct exciton to polariton, Sec. 2.3).

The starting point are electron energy levels in coupled QWs and how they couple with tunnelling interaction. The formation of mixed direct-indirect excitons is explained in Sec. 7.2 using the same coupled oscillator model as for polaritons (Eq. 2.1). In Sec. 7.3 strong optical coupling is added to this model and the system's three "dipolariton" eigenmodes are analysed with respect to tuning possibilities and composition properties. The sample and experimental characterisation techniques are outlined in Sec. 7.4. Experimental results of bias-dependent PL emission follow in Sec. 7.5, together with a study of the effect of tunnelling barriers of different thickness (Sec. 7.5.1) and list of the sample limitations (Sec. 7.5.3). Finally, Sec. 7.6 discusses implications of the experimental findings and Sec. 7.7 presents a summary and outlook to future experiments.

7.1 Introduction

Tunnelling of electrons through a potential barrier is fundamental to chemical reactions, electronic transport in semiconductors and superconductors, magnetism, and devices such as THz oscillators. In engineered devices the rate of electron tunnelling between two energy levels, separated by a thin tunnelling barrier, is typically controlled by electric fields. Two QWs stacked next to each other, separated by a thin layer of semiconductor material, form a coupled quantum well system. The coupling is mediated by quantum tunnelling of electrons or holes through the thin spacer layer. When such an active region is embedded in a microcavity, selective electron tunnelling can be combined with strong coupling to the microcavity mode, leading to the formation of "dipolaritons" [8].

Dipolaritons are hybrid direct-indirect excitons that couple to the cavity mode. They inherit a number of interesting properties from the indirect exciton: a large tuneable static dipole moment, sufficiently long lifetimes for thermalization [151], better transport properties, high susceptibility to electric fields and stronger long-range interactions. For this reason dipolaritons are expected to favour room temperature solid-state condensation [152]. In analogy to atomic systems [153, 154] or optical waveguides [155], they could offer new possibilities for electromagnetically-induced transparency and adiabatic population transfer from light to the well studied [156, 157, 158] matter state of indirect excitons, which are very long-lived compared to polaritons, easily controlled and trapped with electrical fields [159, 160] and have shown strong spin-sensitive interactions [161]. Dipolariton systems have recently been proposed as a promising laser source emitting continuous THz radiation [162]; however experimental realisation of such a device is yet to be shown.

7.2 Exciton mixing in coupled quantum wells

Excitons are charge-neutral excitations of a semiconductor, a bound electron-hole pair, created either by absorption of a photon with energy larger than the bandgap or by pairing of electrons and holes injected through a diode structure. In contrast to direct excitons, the centre of mass of electron and hole does not coincide for indirect excitons and hence they possess a static electric dipole moment oriented perpendicular to the microcavity plane [Fig. 7.3(d)]. In this section coupling of QW electron levels will be introduced, which is then extended to exciton states in tunnel-coupled QWs.

7.2.1 Energy levels in tunnel-coupled QWs

QWs are narrow two-dimensional traps for excitons, they constitute a square potential well in the growth direction for the electron in the conduction band and for the hole in the valence band. The in-plane wavefunction $\phi_{e,h}(x,y)$ is usually assumed to be spherically symmetric and exponentially decaying with some characteristic radius $r_{e,h}$ in the QW plane. The energy levels $E_{e,h}$ of electron and hole in a potential are calculated by solving the Schrödinger equation using the separation ansatz $\Psi(x,y,z) = \phi(x,y)\,\psi(z)$, which yields

$$\left[-\frac{\hbar^2}{2m_{e,h}}\frac{d^2}{dz^2} + V(z) \mp eFz\right]\psi_{e,h}(z) = E_{e,h}\,\psi_{e,h}(z) \tag{7.1}$$

for the z component in each domain **I,II,III,IV,V** in Fig. 7.2(c). $V(z)$ is the QW potential (the conduction/valence band in z direction) and F is the applied DC electric field amplitude in growth direction. The electron and hole eigenvalues $E_{e,h}$ and eigenfunctions $\psi_{e,h}(z)$ in a uniform electric field $F = \text{const}$, as in our case, can be calculated analytically [163] and are presented in Fig. 7.2. Eigensolutions are found using boundary conditions[1] and complex Airy functions $\mathrm{Ai}(z)$, $\mathrm{Bi}(z)$ with material parameters from [164].

In square potentials, $\psi_{e,h}(z)$ are the well known oscillator wavefunctions with exponential decay in the potential walls, as is Fig. 7.3(a). In the presence of an electric field the band structure tilts and electrons can tunnel through the triangular tunnelling barrier on the right side of the right quantum well (RQW) in Fig. 7.2(c). This is reflected by the non-vanishing wavefuntion density[2] at the far edge of this barrier at $z > 20$ nm in Fig. 7.2[e1].

[1] The wavefunction and its derivative have to be continuous at each interface and the wavefunction has to vanish towards infinity to be normalisable.

[2] Wavefunctions which tunnel through the barrier are not confined in space and but still have to be normalised for the calculation, in this case from $z = -\infty$ up to z_{edge} where the far edge to the triangular barrier meets the wavefunction's energy (curved feature on the right side Fig. 7.2[e1-e3].

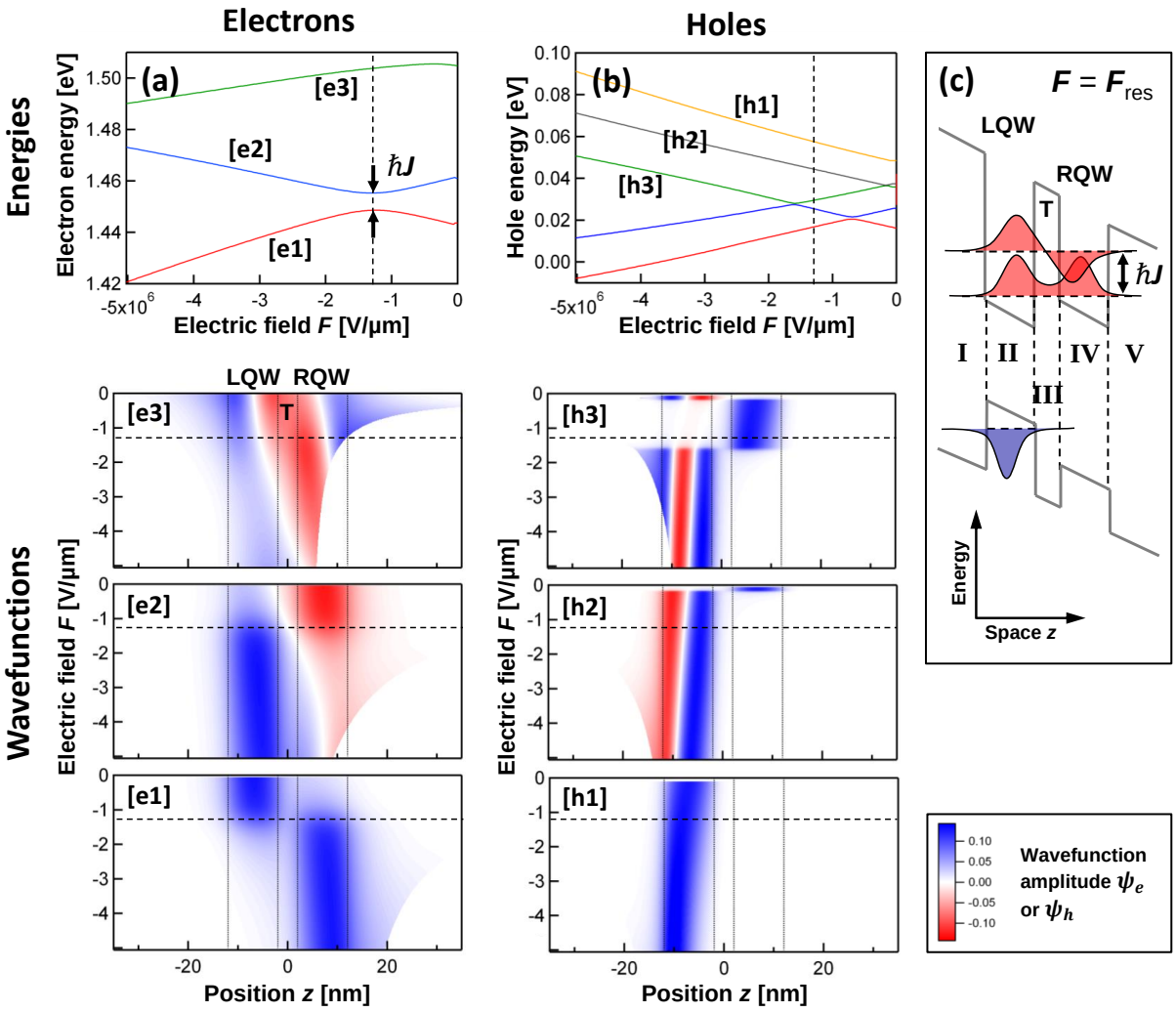

Figure 7.2: Simulation of electron and hole wavefunctions in a coupled asymmetric double quantum well as a function of electric field F (reverse bias). (a,b) Energy levels for electrons and holes vs electric field F. The corresponding wavefunctions for the lowest three energy levels for electrons [e1,e2,e3] and holes [h1,h2,h3] are plotted below, opposite parity is show by red and blue colour. (c) Sketch of energy bands and wavefunctions at the resonance electric field $F_{\mathrm{res}} = -1.3$ V/μm, marked by the dashed line in (a,b). Abbreviations: RQW – right quantum well, LQW – left quantum well, T – tunnelling barrier.

At the resonance electric field (dashed lines, $F_textres = -1.3$ V/μm) the electron levels are split by the tunnelling energy $\hbar J = 6$ meV in (a) and the corresponding wavefunctions have even [e1] or odd [e2] parity and are both localised in the QWs. Higher order electron wavefunctions [e3] are essentially unconfined and can hence have high probability amplitude inside the tunnelling barrier T. The situation is different for holes, which are much better confined. The lowest energy hole wavefunction [h1] firmly resides in the left quantum well and shifts slightly to the outer edge with increasing field F. For the physics presented in this chapter only the states [e1,e2,h1] are of interest, all other states are either unbound or too far off the cavity resonance to play a role in the optical spectra. From graphs (a,b) one can estimate the exciton transition energy vs F as the difference of the lines [e1] and [h1], although here the exciton binding energy of ~ 10 meV is neglected (compare to Eq. 2.2).

7.2.2 Direct and Indirect Exciton

Neighbouring QWs in a microcavity are usually spaced far enough from each other to avoid coupling between them, which leads to N independent QWs that contribute to the Rabi splitting of the cavity as $\sqrt{N}$ (Sec. 2.2). However in coupled quantum well (CQW) systems two identical QWs, 1 and 2, are spaced only by a thin material layer so that the electron can tunnel through this potential barrier. The quantum tunnelling rate J leads to a normal mode splitting of the two degenerate electron states $E_1 = E_2 \equiv E \rightarrow E \pm \hbar J$, with the low (high) energy state supporting a symmetric (antisymmetric) wavefunction $\psi_1 + \psi_2$ ($\psi_1 - \psi_2$), as shown in red in the insets of Fig. 7.3(e).

The samples in our experiments contain asymmetric double QWs (ADQW), in which the composition (or thickness) of the two coupled QWs is slightly different. This arrangement entails an intrinsic energy difference in the electron and hole levels of the two QWs. In the absence of an electric field, direct excitons (DX) in the left QW couple to the photonic mode to form ordinary polaritons [Fig. 7.3(a)], like in a conventional microcavity. This is because of the slightly different semiconductor alloy composition chosen for the two QWs, which makes the band gap of the left QW smaller than the right QW. An electric field can bring the electron levels in these two QWs into resonance so that the tunnelling interaction J couples them as described above [Fig. 7.3(c)]. In this system four exciton transitions are allowed. The two relevant ones are of lower energy, the direct exciton (DX) transition in the left QW and the indirect exciton (IX) transition between the left QW valence band and the right QW conduction band [Fig. 7.3(a)]. In the latter the electron and the hole of the exciton are spatially separated by around 14 nm.

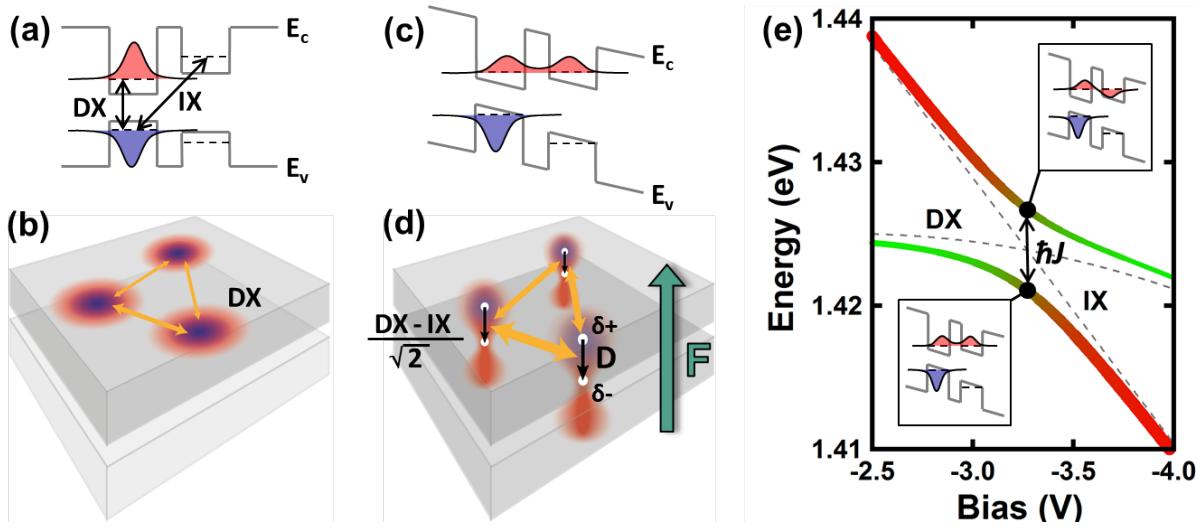

Figure 7.3: Band structure of asymmetrically coupled QWs for electrons (red) and holes (blue). Off resonance, direct excitons live in the left QW (a) and resemble disc-like two-dimensional positronium atoms (b). An electric field F brings the two conduction band levels into resonance so that the electron occupies both QWs through quantum tunnelling (c). These mixed direct-indirect excitons acquire a static dipole moment D (d). (e) Simulation of bias tuning of the direct (DX) and indirect exciton (IX) levels with electric field strength for our microcavity mesa. Line colour represents the mixing of the excitons (green is for DX and red is for IX), thickness codes the linewidth. Insets show symmetric and antisymmetric mixed state, split in energy by the tunnelling coupling $\hbar J$.

7.2.3 Electron tunnelling in asymmetric double quantum wells

The quantum tunnelling rate $\hbar J$ between two adjacent QWs depends on the energy spacing of the levels in the two QWs (resonance condition) and the design of the structure: height and width of the QWs and thickness of the tunnelling barrier. In this coupled system quantum interference of matter occurs. With an electric field F, a bias voltage applied perpendicular to the QW plane, the energy levels in our sample can be shifted with respect to each other, as drawn in Fig. 7.3(a,c,e), so that tunnelling can be switched on smoothly when they come into resonance. The direct exciton DX tunes approximately quadratically with the electric field F: $E_{\mathsf{DX}} = a + bF + cF^2$ (Stark effect), the indirect exciton IX dependence is linear to first order: $E_{\mathsf{IX}} = d + eF$ (band bending in electric field); a, b, c, d, e are fit parameters.

The coupled QW system can be described as coupled oscillators in the basis $\{|\mathsf{IX}\rangle, |\mathsf{DX}\rangle\}$:

$$H = \hbar \begin{pmatrix} \omega_{\mathsf{IX}} - i\gamma_{\mathsf{IX}} & -J/2 \\ -J/2 & \omega_{\mathsf{DX}} - i\gamma_{\mathsf{DX}} \end{pmatrix} \tag{7.2}$$

where J is the tunnelling coupling constant[1] between the two QWs, $\omega_{\mathsf{IX}}, \omega_{\mathsf{DX}}$ are the IX and DX resonance frequencies and $\gamma_{\mathsf{IX}}, \gamma_{\mathsf{DX}}$ are their linewidths. At zero electric field, when the electron levels are far apart, the low energy exciton mode has both electron and hole firmly located in the left QW [Fig. 7.3(a,b)]. Due to the strong confinement by the QW these **direct excitons (DX)** resemble disk-like two-dimensional positronium atoms. The Coulomb interaction between them is mostly screened and the residual interaction is weakly repulsive, so that they can be regarded as a weakly interacting 2D bosonic gas. DXs have the advantage of large oscillator strength and hence strong coupling to the cavity mode, and a relatively small linewidth of 1meV. On the downside the DX lifetime is short (about 20 ps in a single GaAs QW but still 3 times longer than microcavity polaritons [157]) and their tuning possibilities with electric or magnetic fields are limited.

When an electric field is applied to reach the resonance point $E_{\mathsf{IX}} = E_{\mathsf{DX}} \equiv E_{\mathrm{res}}$ [Fig. 7.3(c,d)], electron tunnelling reaches its maximum and the coupled **symmetric and antisymmetric exciton modes** become split by $\hbar J$ [Fig. 7.3(e)] , where J is the bare tunnelling rate (fixed by sample design):

$$E_{\substack{A \\ S}} = E_{\mathrm{res}} \pm \tfrac{J}{2} \qquad |{}^{\mathsf{X}_A}_{\mathsf{X}_S}\rangle = \tfrac{1}{\sqrt{2}} \left(|\mathsf{DX}\rangle \mp |\mathsf{IX}\rangle\right) \tag{7.3}$$

Here the linewidths were neglected, they would lead to a slightly reduced splitting (Sec. 2.3.4). With the electron extending over both QWs, the charge centres of electron and hole separate. Consequently this mixed exciton acquires a large static dipole moment of $D \approx 300$ Debye in our sample, 10 times higher than the dipole moment of a diatomic molecule but two orders of magnitude lower than Rydberg atoms. Tunnelling for the holes is inefficient in our sample because of the increased energy difference of the hole levels with rising electric field [Fig.7.3(c)]. Additionally, the confinement for holes inside the QW is higher than for electrons because of their larger effective mass.

At higher fields F, past the resonance point, the ground state consists of **indirect excitons (IX)** only, with electrons located in the right QW and holes in the left QW. The advantages of

[1] The tunnelling interaction lowers the energy for the symmetric electron state $\Psi_1 + \Psi_2$, hence the off-diagonal terms in H are negative.

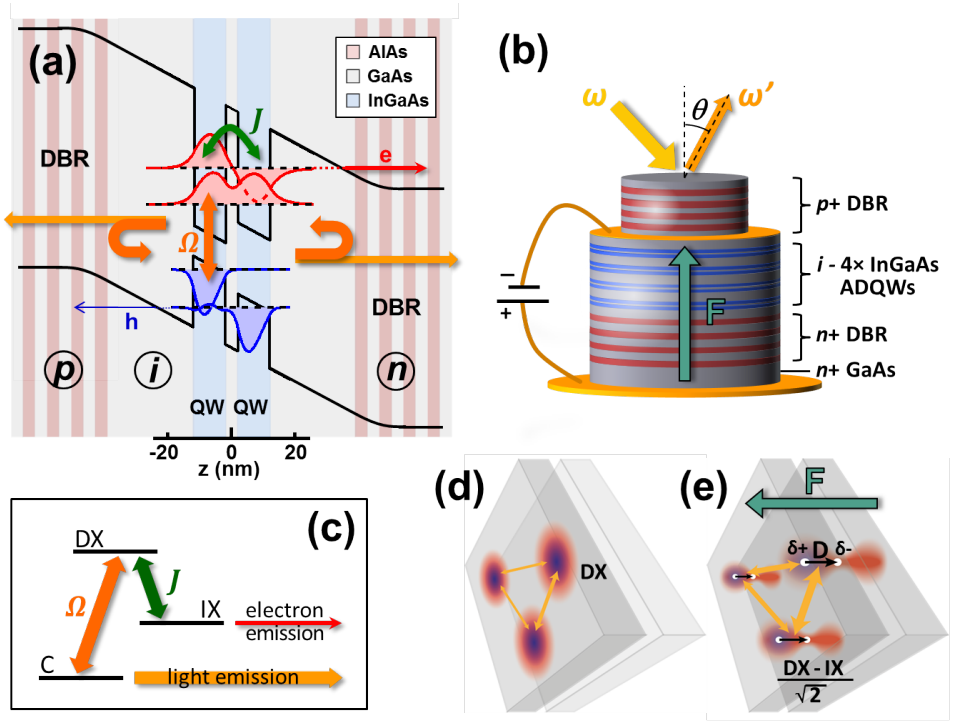

Figure 7.4: (a) Schematic band structure at tunnelling resonance, surrounded by doped mirrors (DBRs). The exciton extends over both wells giving rise to dipolaritons. (b) Structure of electrically-contacted mesa. The bias voltage controls the tunnelling properties via the alignment of the QW levels. (c) Three-level Λ-scheme coupling cavity (C), direct (DX) and indirect (IX) modes by classical intense laser pump Ω_R and quantum tunnelling J. (d,e) Difference between direct (d) and hybrid excitons (e) at resonance electric field F, forming polaritons with dipole moment $\vec{D}$ in the strong coupling regime.

indirect excitons are manifold: much longer lifetime (up to μs [157, 165]), a large static dipole moment and tunable effective mass [156]. The dipole repulsion between them screens out part of the QW disorder potential [157], thus helping to achieve condensation. On the negative side the IX has negligible coupling to the cavity mode (little e-h overlap → small oscillator strength) and is very sensitive to thickness fluctuation of the tunnelling layer.

The strength of the coupled QW system is the possibility to easily tune the exciton properties between the two regimes of DX and IX, combining advantages of the strong coupling to the cavity mode with the long lifetime and the large static dipole moment.

7.3 Dipolaritons

In a microcavity with asymmetric double quantum wells (ADQW) hybrid direct-indirect excitons [Fig. 7.4(e)] form at the resonance bias voltage. In combination with strong optical coupling to the cavity mode C, dipolaritons are created which combine the large oscillator strength of the DX with the large static dipole moment of the IX. In order to understand the mixing of these three modes, we combine the oscillator model for conventional polaritons from Eq. 2.1, coupled by Ω_{R}, with the tunnelling interaction between DX and IX in Eq. 7.2, described by the tunnelling rate J, as depicted in Fig. 7.4(a). Similar to [28] the (non-Hermitian) Hamiltonian H in the basis $\{|\mathsf{IX}\rangle, |\mathsf{DX}\rangle, |\mathsf{C}\rangle\}$ is:

$$H = \hbar \begin{pmatrix} \omega_{\mathsf{IX}} - i\gamma_{\mathsf{IX}} & -J/2 & 0 \\ -J/2 & \omega_{\mathsf{DX}} - i\gamma_{\mathsf{DX}} & -\Omega_{\mathrm{R}}/2 \\ 0 & -\Omega_{\mathrm{R}}/2 & \omega_{\mathsf{C}} - i\gamma_{\mathsf{C}} \end{pmatrix} \tag{7.4}$$

where $|\mathsf{DX}\rangle$ couples to both $|\mathsf{IX}\rangle$ and $|\mathsf{C}\rangle$, while there is negligible[1] interaction between $|\mathsf{IX}\rangle$ and $|\mathsf{C}\rangle$ [Fig. 7.4(c)]. Independent control over all parameters in this model is possible: angle-tuning shifts the cavity frequency, bias voltage tunes both the IX (directly) and DX levels (weakly due to the quantum confined Stark effect), the barrier width sets the intrinsic tunnelling rate J, and Ω_{R} is set by the microcavity design and geometry. The bias dependence of DX and IX is obtained from fitting this 3-mode model to the voltage scan of the PL spectra with dependencies as explained in Sec. 7.2.3.

Diagonalisation of H yields the three dipolaritons modes $|\mathsf{LP}\rangle$, $|\mathsf{MP}\rangle$ and $|\mathsf{UP}\rangle$, as shown in the simulation in Fig. 7.5 as a function of bias. The line colour describes the composition in terms of the uncoupled modes (red $\rightarrow$ IX, green $\rightarrow$ DX, blue $\rightarrow$ C) and the thickness codes the linewidth of the polariton modes. As explained in the legend, the dual strong coupling leads to three types of quasiparticles, the conventional polariton (DX & C, Sec. 2.3.1), the hybrid exciton (DX & IX, Sec. 7.2.3) and the "dark state" polariton (IX & C, more on this below). The LP, for example, changes from being half DX half C to being dominantly an indirect exciton as the two exciton modes redshift with bias.

For the general case, eigenenergies and eigenvectors of Eq. 7.4 are best computed numerically since the analytical solution is inconveniently long. There is however a simplified case that gives considerable insight into the system. Assuming the IX to be resonant with the cavity (the DX

[1] The IX has very little oscillator strength due to minimal overlap of its electron and hole wavefuctions.

can be detuned from the two modes by an arbitrary value δ)

$$\omega_{\mathsf{C}} = \omega_{\mathsf{IX}} = \omega_{\mathsf{DX}} + \delta, \tag{7.5}$$

and further neglecting the linewidths[1] of the modes ($\gamma_{\mathsf{C}} = \gamma_{\mathsf{IX}} = \gamma_{\mathsf{DX}} = 0$) and setting the resonance energy as the zero point for simplicity leads to the matrix

$$H = \hbar \begin{pmatrix} 0 & -J/2 & 0 \\ -J/2 & \delta & -\Omega_{\mathrm{R}}/2 \\ 0 & -\Omega_{\mathrm{R}}/2 & 0 \end{pmatrix} \tag{7.6}$$

whose eigenenergies are given by

$$E_{\mathsf{MP}} = 0 \tag{7.7}$$

$$E_{\substack{\mathsf{UP} \\ \mathsf{LP}}} = \tfrac{1}{2}(\delta \pm S) \tag{7.8}$$

and its eigenvectors are the three dipolariton modes

$$|\mathsf{MP}\rangle = \frac{\Omega_{\mathrm{R}}|\mathsf{IX}\rangle - J|\mathsf{C}\rangle}{\sqrt{\Omega_{\mathrm{R}}^2 + J^2}} \tag{7.9}$$

$$|^{\mathsf{UP}}_{\mathsf{LP}}\rangle = \frac{J|\mathsf{IX}\rangle + \Omega_{\mathrm{R}}|\mathsf{C}\rangle - (\delta \pm S)|\mathsf{DX}\rangle}{\sqrt{2S(S \pm \delta)}} \tag{7.10}$$

where $S = \sqrt{\Omega_{\mathrm{R}}^2 + J^2 + \delta^2}$ is the total splitting between LP and UP at the resonance point of Eq. 7.5.

One interesting fact to note is the absence of the DX mode in $|\mathsf{MP}\rangle$, independently of the detuning δ of the DX. This observation is intrinsic to 3-mode-systems with two couplings as shown in Fig. 7.4(c), where there is no interaction between the modes C and IX ($H_{13} = H_{31} = 0$) while the third mode, DX, couples to both via Ω_{R} and J. In atomic physics such system is known as a Λ-scheme and the analogy of the $|\mathsf{MP}\rangle$ is the "dark state", a superposition of the two ground states that does not couple to light. Interference of the transition amplitudes between the states in a Λ-system in a dilute atomic gas has shown many fascinating phenomena, e.g. electromagnetically induced transparency (EIT) and coherent adiabatic population transfer [166]. Analogies between our system and EIT and possible implications for the properties of the $|\mathsf{MP}\rangle$ state are discussed in more detail in Sec. 7.6.3.

[1] This approximation is acceptable since the linewidths γ affect the splitting S between the polaritons and hence the relative mode position as $\mathcal{O}[\frac{1}{4}(\gamma/\Omega_{\mathrm{R}})^2]$. Estimating $h\gamma_{\mathsf{C}} = 0.5$ meV, $h\gamma_{\mathsf{DX}} = 1$ meV, $h\gamma_{\mathsf{IX}} = 3$ meV, the mean linewidth for dipolaritons is $h\gamma \sim 1.5$ meV. With $\Omega_{\mathrm{R}} = 6$meV the error is $< 5\%$.

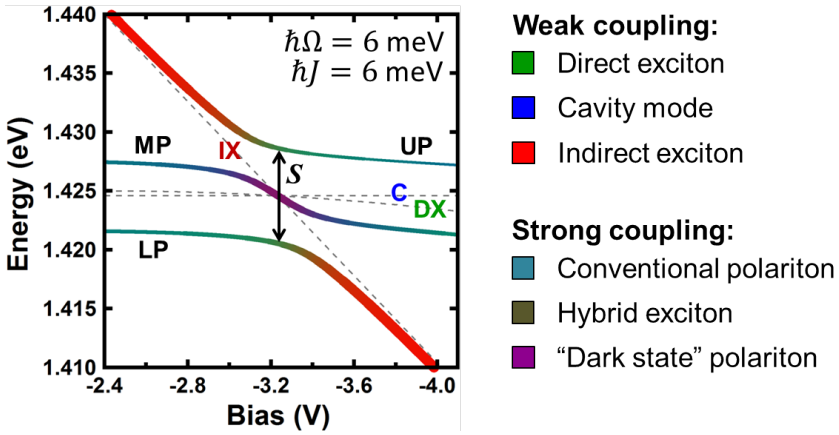

Figure 7.5: Simulation of the bias tuning of the lower LP, middle MP and upper UP dipolariton mode from Eq. 7.4 resulting from a common resonance point at $-3.2\ V$. Dashed lines are the uncoupled modes DX, IX and C, colours in the legend explain the composition and linewidths are represented by the thickness of the coupled modes.

7.4 Sample fabrication and experiment details

ADQW Polariton diode: design and principle

The microcavities used in these experiments are contacted mesa structures [SEM image in Fig. 7.6(b)] and consist of a negatively doped bottom DBR and a positively doped top DBR, separated by an undoped cavity layer, as shown in Fig. 7.4(b). This *p-i-n* structure is referred to as a polariton diode [9, 37, 167] and resembles a vertical-cavity surface emitting laser (VCSEL) [168]. The active region is made up of 4 pairs of ADQWs [Fig. 7.4(a)] spaced by a thin tunnelling barrier of a few nanometers in width. The InGaAs QWs in each pair have slightly different indium content so that at flatband condition[1] [Fig. 7.3(a)] the energy levels in both QWs separate, activating only the DX transition in the left QW (conventional microcavity). The right QW exciton transition is much higher in energy than the cavity mode and is hence inaccessible at flatband condition. However a reverse bias voltage, applied through the electrical ring contact evaporated onto the diode, brings the two levels into resonance [Fig. 7.3(b)] so that tunnelling of the electron from the left QW to the right one and vice versa becomes possible. This couples the IXs to the polariton mode and forms dipolaritons with static out-of-plane dipole moment.

[1]When the energy band diagram of the structure is flat, so that no charge is present. Due to doping and the work function difference of the microcavity material a built-in electric field is always present and an external counteracting voltage has to be applied to reach flatband condition.

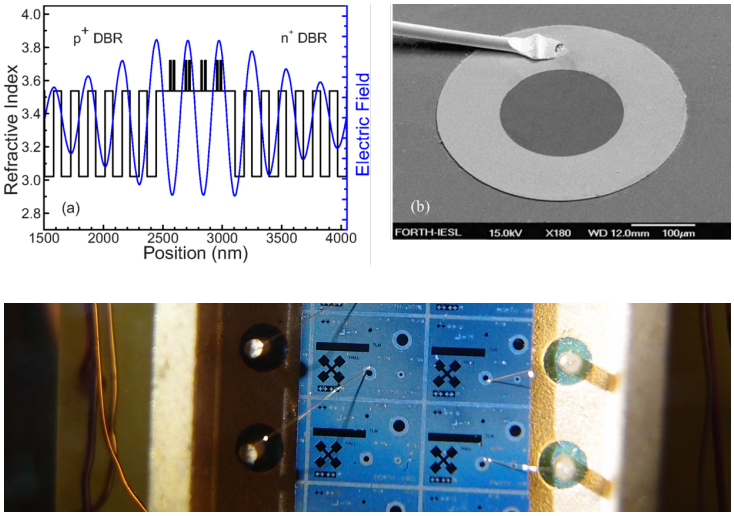

Figure 7.6: (a) Refractive index profile of the structure and internal light field. The QWs are positioned at the maxima of the electric field to increase light-matter coupling. (b) SEM image of polariton LED showing the ring electrode on top of the polariton VCSEL structure, from [167]. Bottom: Photo of the sample piece in the cryostat. Thin gold wires connect electrically contacted mesas to the copper wiring in the background. (a,b): courtesy of Pavlos Savvidis.

Fabrication Details

The samples are grown by molecular beam epitaxy (MBE) on highly n-doped GaAs (001) substrates. The optical resonator consists of a highly n-doped lower distributed Bragg reflector (DBR) (21 periods of GaAs/AlAs) and a highly p-doped upper DBR (17 periods of GaAs/AlAs). Doping densities are $n_n = 2{\cdot}10^{18}$ cm^{-3} (silicon) and $n_p = 4{\cdot}10^{18}$ cm^{-3} (beryllium). The $\frac{5}{2}\lambda$ cavity is designed for $\lambda = 880$ nm and contains 4 sets of asymmetric double quantum wells [ADQWs, Fig. 7.3] positioned at the antinodes of the optical field. The QWs in each ADQW ensemble are 10 nm wide, have different depths with $In_xGa_{1-x}As$ of $x = 0.10$ (left) and $x = 0.08$ (right), and are separated by a GaAs barrier [Fig. 7.4(a)]. Figures for the microcavity are: linewidth $h\gamma_c = 1$ meV, finesse $F = 250$, Q-factor $Q = 1400$ and effective cavity length $L_{\text{eff}} = 1.49$ μm.

Three sample wafers with barrier widths L_B of 4 nm, 7 nm, and 20 nm are fabricated to access different tunnelling coupling strengths $\hbar J$. Cylindrical mesas of 350 μm diameter are processed into the samples using BCl_3/Cl_2 reactive ion etching [Fig. 7.6(b)]. A constant electric field can be applied across the microcavity through electric contacts evaporated on the back side (Au/Ge ohmic contact) of the substrate and on top of the cavity layer (using a ring-shaped electrode, Ti/Pt ohmic contact) in reverse bias to avoid electrical injection of charge carriers and electroluminescence. In order to avoid injection losses in forward bias due to the high re-

sistivity of the p-type top DBR, the GaAs layer on the inside of the DBRs is kept undoped and the ring-shaped electrode on top is recessed so as to be closer to the cavity layer [Fig. 7.4(b)]. Further information on the sample can be found in [9, 167].

Optical Characterization

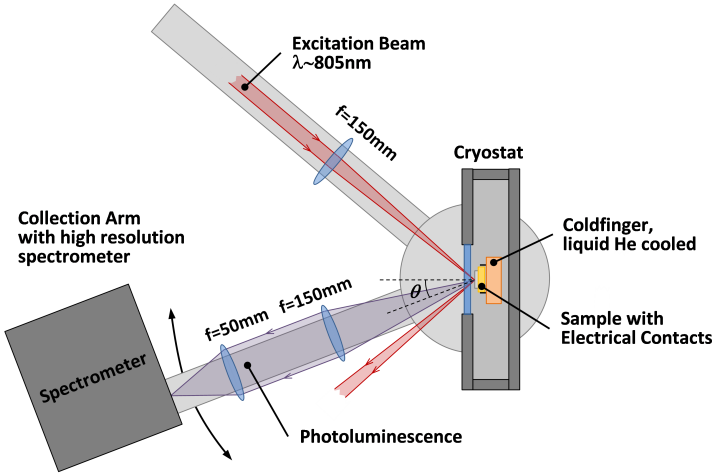

Figure 7.7: Goniometer setup for angle-resolved photoluminescence with high angle non-resonant excitation beam. The PL is collected with a high resolution spectrometer mounted directly on the goniometer arm.

Optical measurements are performed in a temperature-stabilised continuous-flow liquid helium cryostat at $\sim$ 10 K. Each mesa is excited non-resonantly at the first high-energy minimum of the DBR stopband at high angle by a Ti-sapphire laser (cw-operation at 805 nm) with up to 200 μW of laser power, focussed to a 100 μm diameter spot. The angle and bias dependence of the photoluminescence are measured using a 150 mm focal length collection lens and a high resolution spectrometer mounted directly on the second goniometer arm, whose angle θ is variable (Fig. 7.7). For polarisation dependent measurements a polariser is inserted in the collection path. Spectra are measured using a computer program recording a spectrum for each bias value set by a computerised source measuring unit (SMU). Changes of the collection angle θ are performed manually. Integration time is chosen automatically by the measurement program to ensure smooth data collection in a wide range of exposure times from 10 ms to 100 s. When necessary, the spectra are background corrected by subtracting the spectrum recorded at highest bias voltage, where all dipolariton modes have disappeared in the background noise.

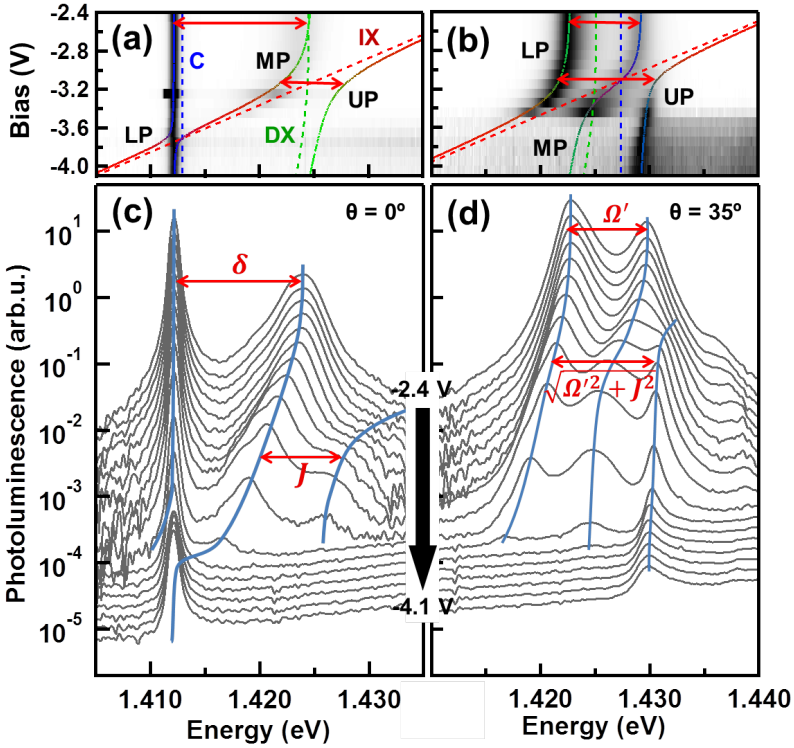

Figure 7.8: Dependence of the PL spectra on the bias voltage for off-resonant cavity (a,c) and close to resonance (b,d) for a mesa with $L_B = 4$ nm. Polariton lines LP, MP and UP in (a,c) are fits to the coupled oscillator model Eq. 7.4, dashed lines show the uncoupled modes: cavity (C, blue), direct (DX, green) and indirect (IX, red) excitons. In (c,d) the spectra are plotted in logarithmic scale and shifted for clarity, blue lines are guides to the eye. Spectra in (a,b) are normalised to the maximum value to better reveal the modes.

7.5 Experiment Results: Dipolariton Modes in PL

Our microcavity mesas mix direct (DX) and indirect (IX) excitons through electron tunnelling $\hbar J$, controlled by a static bias voltage, while the optical microcavity ensures coupling $\hbar\Omega_R$ of the DX to the light field C. In the dual strong coupling regime, when J is larger than the carrier escape rate from the coupled QWs and Ω_R is faster than the photon decay rate, the system displays three distinct eigenmodes: the lower (LP), middle (MP), and upper (UP) dipolariton.

The bias dependence of the photoluminescence of a mesa with tunnelling barrier width $L_B = 4$ nm (Fig. 7.8) clearly reveals these three dipolariton modes. At normal incidence (a,c) the narrow cavity mode is detuned 10 meV below the excitons and hence is effectively decoupled from the excitons. The weak exciton PL nonetheless directly resolves their tunnel splitting $\hbar J$

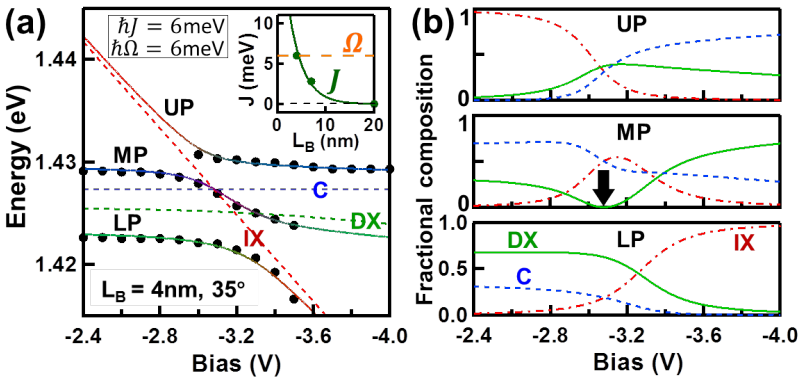

Figure 7.9: Bias-dependent polariton modes observed in photoluminescence for $L_B = 4$ nm with fits to the coupled oscillator model Eq. 7.4. (b) Bias dependence of the polariton composition as computed from the fit to (a); black arrow for MP marks position of the pure dipolariton of Eq. 7.11.

at the anti-crossing bias $U = -3.2$ V. Through this transition, the low energy exciton (here the MP) transforms from DX to IX, tracking the electron's location from the left QW to the right QW at more negative bias. The minimal splitting between LP and MP illustrates the absence of direct coupling between the IX and C, justifying $H_{13} = H_{31} = 0$ in Eq. 7.4.

This situation changes at high collection angle $\theta = 35°$ (b,d) where the cavity mode is blueshifted to be resonant with the indirect exciton at $U = -3.0$ V. For low bias voltage the IX is far detuned and the system behaves as a single-QW microcavity with conventional DX-polaritons only and a detuned splitting[1] $\hbar\Omega' = \hbar\sqrt{\Omega_R^2 + \delta^2}$. Simultaneous resonance of DX, IX and C is reached at $U = -3.2$ V and appears as three clearly distinct polariton branches spanned by an anti-crossing of width $\hbar S = \hbar\sqrt{\Omega'^2 + J^2}$. The eigenvectors at resonance are (copied from Sec. 7.3)

$$|\mathsf{MP}\rangle = \frac{\Omega_R|\mathsf{IX}\rangle - J|\mathsf{C}\rangle}{\sqrt{\Omega_R^2 + J^2}} \tag{7.11}$$

$$|{}^{\mathsf{UP}}_{\mathsf{LP}}\rangle = \frac{J|\mathsf{IX}\rangle + \Omega_R|\mathsf{C}\rangle - (\delta \pm S)|\mathsf{DX}\rangle}{\sqrt{2S(S \pm \delta)}} \tag{7.12}$$

Remarkably, while the central MP has no DX admixture at resonance (independent of the detuning δ) it is clearly visible in emission through the tunnelling interaction with the cavity photon and almost as strong as the other polaritons, however the exact reason is currently not understood. The absence of DX in the MP arises from the destructive interference of transition

[1] $\delta(U, \theta)$ is the detuning of DX below C at each bias and angle value.

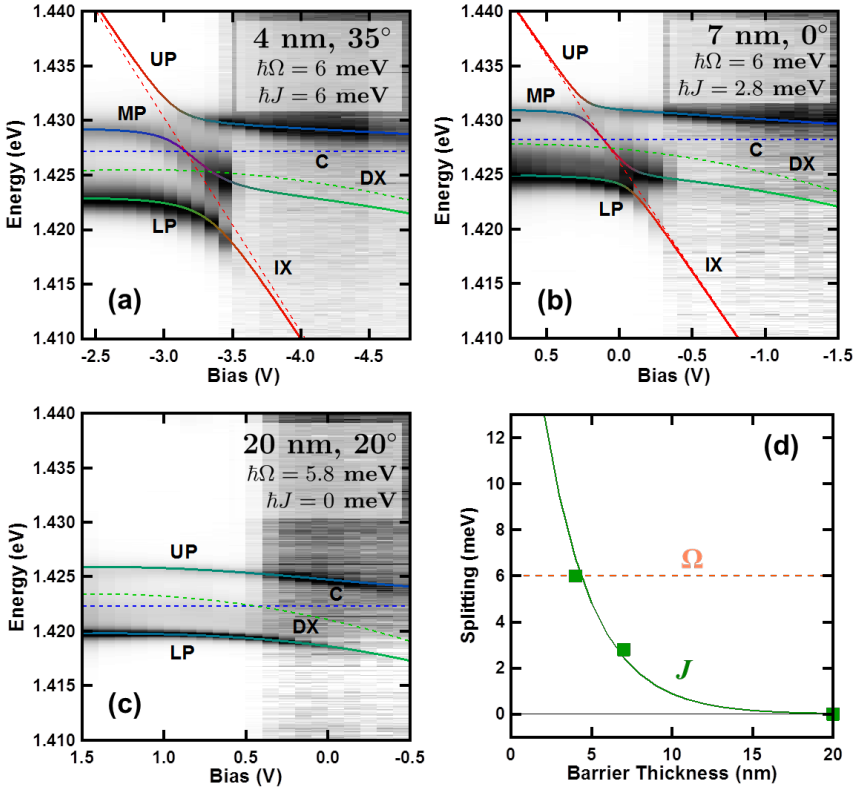

Figure 7.10: Bias-dependent polariton modes observed in photoluminescence (logarithmic intensity scale) for samples with L_B of (a) 4 nm, (b) 7 nm and (c) 20 nm. Solid coloured lines are fits to the coupled oscillator model Eq. 7.4 with line colour reflecting the composition (red: IX, green: DX, blue: C). (d) Tunnel splitting $\hbar J$ versus barrier thickness L_B, showing match between theoretical calculation (solid line) and $\hbar J$ extracted from data (squares). Dashed orange line is the measured Rabi splitting $\hbar\Omega_{\mathrm{R}}$.

amplitudes, as seen in Fig. 7.9(b), which shows the composition of each of the polariton modes versus bias, as extracted from the fit of the coupled oscillator model to Fig. 7.9(a). With increasing field the MP turns from an ordinary DX-polariton to a pure dipolariton at resonance (black arrow), consisting only of $|\mathsf{IX}\rangle$ and $|\mathsf{C}\rangle$ (Eq. 7.11), with the electron and hole located in different QWs and possessing a static dipole moment oriented perpendicularly to the QW plane [Fig. 7.4(d)]. The LP branch could be of particular interest for condensation experiments because of the extensive tuning possibilities of the dipolaritons with cavity detuning and bias voltage, as the bottom graph in Fig. 7.9(b) demonstrates. Condensation of dipolaritons has not been reported to date (see also Sec. 7.5.3).

7.5.1 Influence of the Tunnelling Barrier Width

The bare tunnelling rate J controls the coupling between the two exciton modes and is set by the width and height of the barrier between the QWs. To test the tunnel control of dipolaritons, devices with barrier widths of 4 nm, 7 nm, and 20 nm were fabricated. Fits of the coupled dispersion curves LP, MP, UP to the emission PL measurements (Fig. 7.10) describe the PL data well (a-c) and confirm the dependence of strong coupling dipolariton modes on the tunnelling rate J. Extraction of the polariton Rabi splitting for each sample gives $\hbar\Omega_{\mathrm{R}} = 6.0$ meV, whereas the tunnel splitting varies from $\hbar J = 0$ to 6 meV (a-c), which proves that small tunnelling barriers L_B are required to see dipolaritons. The data points for J (green squares) match with the tunnelling splitting calculated from a parameter-free solution of the Schrödinger equation[1] for this asymmetric double QW system with electric field [40], showing the expected exponential decrease in splitting with increased barrier width.

The spectrum for each bia value in Fig. 7.10 is normalised to its maximum value to allow the polariton mode dispersion to be seen. Different bias voltages were required for different mesas to bring DX and IX into resonance, stemming from intrinsic *p-i-n* electric field and the fact that mesas with larger tunnelling barrier require higher fields to make the electron levels of the two QWs degenerate. For voltage tuning the diode is used in reverse bias operation to apply an electric field, rather than induce charge carriers into the depletion region. Hence the resonance voltage U is negative, except for when the intrinsic potential of the structure shows a large positive value as in Fig. 7.10(c).

Furthermore the energy of the cavity mode C varies slightly from mesa to mesa, hence data is collected at the appropriate angles to bring it close to resonance with the excitons. A slightly positive detuning of the cavity was chosen to improve the PL signal from the high energy polariton modes due to increased photonic fraction (compare Eqs. 2.21 and 2.9). It is worth noting that the DX shows a faint anticrossing [LP in Fig. 7.10(b) and MP in Fig. 7.8(c)] that could be attributed the QWs having slightly different widths which affects their energies.

In all three samples the PL signal disappears rapidly beyond a critical negative bias voltage. We believe this critical electric field value is found where the triangular barrier on the right side of the ADQW becomes small enough so that the electrons can tunnel out of the system [red arrow in Fig. 7.4(a)] within the 10-100 ps radiative lifetime [169] of reservoir excitons (as seen previously in reflectivity [40]). Furthermore the binding energy of excitons reduces as they become more like an indirect exciton, meaning that strong coupling is lost either due to exciton

[1] Using tabulated material parameters for arsenide alloys [164].

dissociation ($T \sim 10$ K is high for indirect exciton experiments) or due to loss of the strong coupling regime (reduced oscillator strength and a low $Q = 1400$ of the microcavity mesa due to doped mirrors).

The results in Fig. 7.10(a-c) clearly show that a large tunnelling rate is necessary to optically couple the IX to the cavity mode. For wide barriers $L_B \geq 20$nm the system behaves like an ordinary DX-polariton microcavity with weak electrical tuning, and the dipolariton modes disappear. In fact the optimum condition for pure dipolaritons $\frac{1}{\sqrt{2}}(|\mathsf{IX}\rangle - |\mathsf{C}\rangle)$ is $\Omega = J$, which is the case in our 4 nm barrier sample.

7.5.2 Tunnelling Control with Angle and Bias

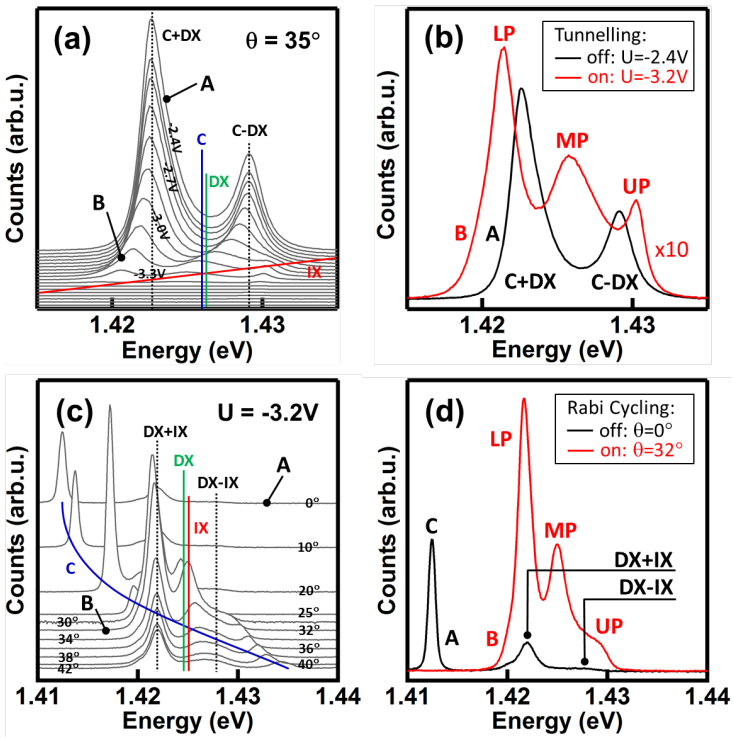

Figure 7.11: Tunnelling control with bias voltage and angle in linear scale. (a) Bias dependence of photoluminescence at 35°, shifting predominantly the indirect exciton mode in energy. (b) At low voltage $U = -2.4$ V the microcavity produces standard DX-polaritons (A) while at the resonance $U = -3.2$ V tunnelling is switched on and three equidistant peaks appear (B). Composition of these modes in Fig. 7.9(b). (c) Angle dependence of the tunnelling coupling, with cavity mode shifting quadratically (blue). (d) Spectrum with off-resonant cavity, when the tunnelling coupling splits the excitons into a symmetric and antisymmetric state (A) and when tunnelling couples all three modes to form dipolaritons (B).

The $L_B = 4$ nm polariton diode mesa with $\hbar J = \hbar\Omega_{\mathrm{R}} = 6$ meV constitutes a sensitive tunnelling switch (Fig. 7.11), toggling between the regime of conventional polaritons and the regime of strongly tunnel-coupled dipolaritons with a small change in bias voltage U (a,b) or cavity angle θ (c,d). In the case of bias-switching (a,b), the DX and C modes are always in resonance and the microcavity is populated by LP and UP polaritons in the strong optical coupling regime sitting in the left QW, as shown by the black double-peaked curve A in Fig. 7.11(b). With increasing bias voltage the IX shoots in from the high energy side [Fig. 7.8(b)] to switch on gradually the tunnelling interaction. At the resonance voltage, $U = -3.2$ V, electron tunnelling is switched on and three dipolariton peaks appear in the red PL spectrum B in Fig. 7.11(b), albeit with $10\times$ smaller intensity.

In the optical-controlled mode of switching, the two exciton modes are in resonance, producing coupled excitons $|{}^{\mathsf{X}_A}_{\mathsf{X}_S}\rangle = \frac{1}{\sqrt{2}}|\mathsf{DX}\rangle \mp |\mathsf{IX}\rangle$. This can be seen in Fig. 7.11(c) by the black dotted lines which are spaced by the tunnelling interaction $\hbar J = 6$ meV (tunnelling "on" all time) and in the spectrum A in Fig. 7.11(d) for off-resonant cavity mode $\theta = 0°$, hence the system is in the strong tunnelling regime but with only weak optical coupling. When the cavity mode (blue curve C in Fig. 7.11(c)) is angle-tuned into resonance with the exciton energy, $\theta = 32°$, the familiar dipolariton spectrum reappears (red curve B in Fig. 7.11(d)), this time with much increased intensity due to the much better optical outcoupling. This shows that simple and independent control of optical and electrical coupling strength in dipolaritons is possible with bias voltage and cavity angle tuning.

7.5.3 Limitations of the Sample

Over the course of many PL-measurements performed on different mesas, several limitations of such samples have become apparent. Most significantly the PL signal from two of the dipolariton modes vanishes at bias voltages slightly higher than resonance ($\omega_{\mathsf{IX}} = \omega_{\mathsf{C}}$), leaving only weak emission from the most cavity-like mode. This observation is linked to the electron being able to tunnel through the triangular barrier on the right side of the ADQW system at a rate faster than the exciton reservoir lifetime [41] [Fig. 7.4(a)]. This loss of PL signal depends strongly on the excitation power [Fig. 7.12(a)] but only insignificantly on the tunnelling barrier width L_B [Fig. 7.10(a,b)] and matches with the onset of photocurrent, as seen from resonant excitation experiments on these samples [170]. As Fig. 7.12(a) shows, with increasing pump power the resonance point shifts exponentially to higher voltages at a rate of 0.65 V/decade. This suggests a reduced electric field inside the cavity which we attribute to charging of the DBRs [41] with free electrons and holes that screen part of the applied voltage.

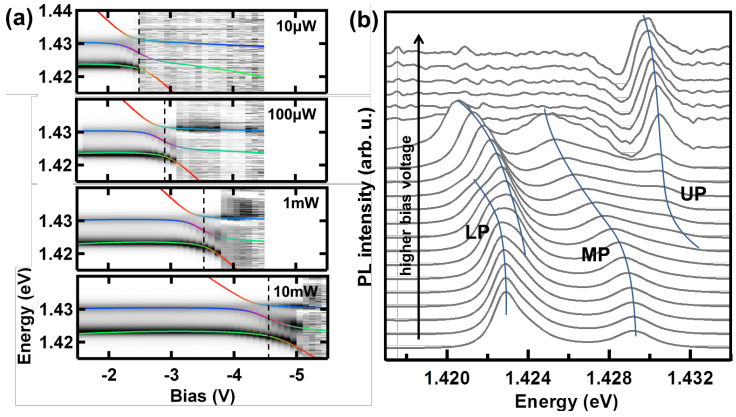

Figure 7.12: (a) Power dependence of the PL under bias tuning and non-resonant optical excitation. Dashed line marks resonance point, which shifts to higher bias values for increasing pump power. (b) Level crossing of the DX as seen in PL from some mesas in bias tuning on the LP, blue lines are guides to the eye. All spectra are normalised to unity.

Furthermore the bias tuning response of the excitons becomes weaker with rising pump power, as seen from the diminishing slope of the IX mode in Fig. 7.12(a), which could stem from a series resistance in the DBRs. Moreover, we found that different mesas on the same sample start tuning at different bias voltage, possibly attributed to spatially changing growth conditions that result in varying charging rates of different mesas. For all the above mentioned reasons, it is not possible to relate the applied bias voltage directly to the intra-cavity electric field strength F and one has to resort to the bias tuning dependence of the IX level to extract F. Another effect, seen in some PL measurements more pronounced than in others, is the faint level crossing of the DX in Fig. 7.12(b), which could hint to the presence of QWs with slightly different widths that tune marginally different in an electric field.

There are several ideas to improve the current sample design, the most obvious one being the introduction of a 8 nm wide AlAs potential barrier to both sides of the ADQW pair [see. Fig.7.4(a)] to prevent the electron from escaping the coupled QW system. The reasons why we see essentially no luminescence from the IX mode[1] coupled to the cavity, as opposed to the experiments performed on coupled QWs without microcavity [171, 172, 173], are the elevated temperature in our cryostat (10 K vs 0.05 K or 0.4 K [172]) and the lower quality of our QWs. The microcavity growth introduces disorder and prevents near-perfect QW interfaces. Our sample uses $In_xGa_{1-x}As$ QWs that are known to show broader linewidth than the high quality GaAs QWs. For these reasons a more radical change of the sample design (higher quality QWs,

[1]Due to the small overlap of the electron and the hole wavefunction the PL signal from an IX-polariton is expected to be much weaker than that of DX-polaritons.

better microcavity) and a better cryostat is probably needed in order to show condensation of dipolaritons.

7.6 Discussion

7.6.1 Static Dipole Moment of Dipolaritons

Interactions between dipolaritons with vertically-aligned dipole moments are expected to be stronger than for induced dipole-dipole scattering between in-plane excitons and could be an interesting addition to the rich scattering phenomena observed in polariton systems (relaxation bottleneck [71], polariton amplifier [4], parametric scattering [3, 34]). Neither the PL measurements presented here, nor the pump-probe experiments performed on these samples [40, 41] have shown direct evidence of the static dipole moment of the dipolaritons. The dipole moment should be on the order of 300 Debye (1 Debye = 10^{-27}C·m), 100 times larger than in a diatomic molecule but much weaker than in Rydberg atoms in an electric field.

Since dipole-dipole interaction should affect light coupling through reduced electron-hole overlap, it should be visible in polarisation-resolved PL measurements (TE/TM) in Fig. 7.13(a), recorded for non-resonant pumping. The reason is that for TM polarisation the electric field vector of the light has a substantial projection of the dipolariton dipole moment at incidence angles $\theta > 0°$, while for TE polarised light the two vectors remain always orthogonal: this effect should hence be visible in the PL emission. The extracted peak positions from the PL at $\theta = 35°$ in Fig. 7.13(b) show indeed a spectral splitting[1], whereby the amount of splitting is proportional to the photonic fraction of the respective dipolariton branch. This is, however, due to the effect of polarisation splitting of the cavity mode[2], as the fit with two different cavity energies confirms. The surprising effect in this data is the larger amplitude of the UP peak in TM polarisation just before resonance voltage (when the UP is still highly IX-like), best visible in intensity polarisation $P_I = (I_{\mathrm{TM}} - I_{\mathrm{TE}})/(I_{\mathrm{TM}} + I_{\mathrm{TE}})$ in Fig. 7.13(c) (blue curve). We have no explanation for this anomaly so far and but it is probably not attributed to the dipole moment, as in this case the effect should occur also on the MP which possesses a 50% IX fraction. In other words, should there be an effect on the PL polarisation for our sample then it is too weak to be discriminated against the polarisation splitting of the cavity mode.

The presence of static dipole interaction between dipolaritons could however leave its trace

[1] The data was corrected for spectrometer efficiency and transmission losses related to high angle reflection off the cryostat window and at the interface sample-vacuum (Fresnel formulas).

[2] Polarisation- or TE-TM-splitting: a naturally occurring asymmetry in the microcavity that separates the energies of the cavity mode for the two orthogonal polarisations TM and TM [28]

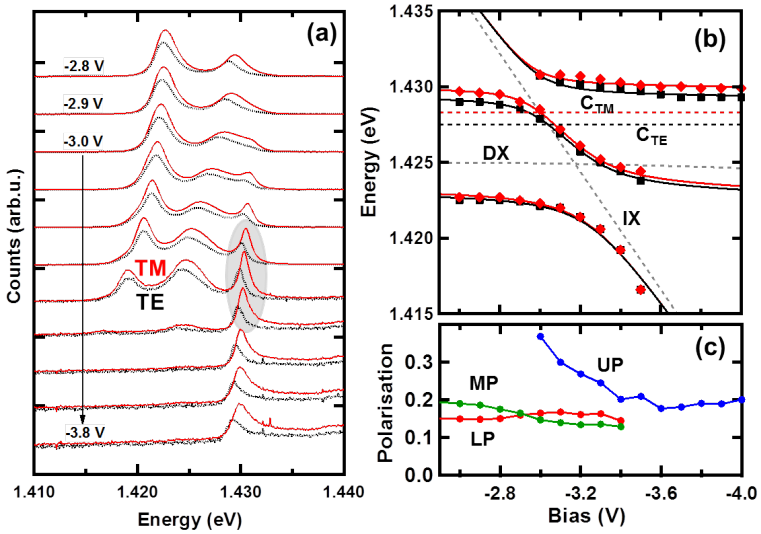

Figure 7.13: Polarisation resolved PL of dipolaritons. (a) TE and TM spectra for various bias voltages, shifted for clarity. Grey oval: region of high amplitude polarisation. (b) Extracted peak position and coupled oscillator fit with two polarisation-split cavity modes C_{TE} and C_{TM}. (c) Intensity polarisation P_I versus bias voltage for all three branches.

in a modified polariton scattering rate at resonance. Pulsed pump-probe experiments [4] in a sample improved for higher electric fields (see Sec. 7.5.3) could show changes in the stimulated scattering rate, and even significant reduction of the relaxation bottleneck [5, 71], which would become visible as a population redistribution along the dispersion curve. Another possibility would be a careful study of the polariton blueshifts with electron tunnelling on and off, which should also be more pronounced on resonance compared to the case of large detuning, owing to the stronger repulsion between dipolaritons.

7.6.2 Dipolar Strength – C-IX Coupling

The pure dipolariton DP, the MP at resonance $\omega_{\mathsf{IX}} = \omega_{\mathsf{C}}$ in Eq. 7.11 with $\Omega_{\mathrm{R}} = J$, is half C and half IX, and possesses the highest dipole moment per dipolariton. Interesting for condensation is however not only the dipole moment but also an efficient coupling to light. A measure for both is the light-dipole coupling strength $V_{\mathsf{LD}} = |C_{\mathsf{IX}}|^2 \cdot |C_{\mathsf{C}}|^2$ which we define as the product of the IX and C fractions. V_{LD} can be calculated using Eq. 7.4 for each polariton branch, as a function of detunings δ_{C} and δ_{DX} from the IX energy and is shown in Fig. 7.14(a) for $\hbar\Omega_{\mathrm{R}} = \hbar J = 6$ meV. The maximum coupling strength value is $V_{\mathrm{LD}} = 0.25$ per polariton mode and is only reached for the pure dipolariton DP. For positive DX detuning $\delta_{\mathsf{DX}} = 6$ meV large coupling strength can be reached also on the LP branch, which is particularly interesting for condensation.

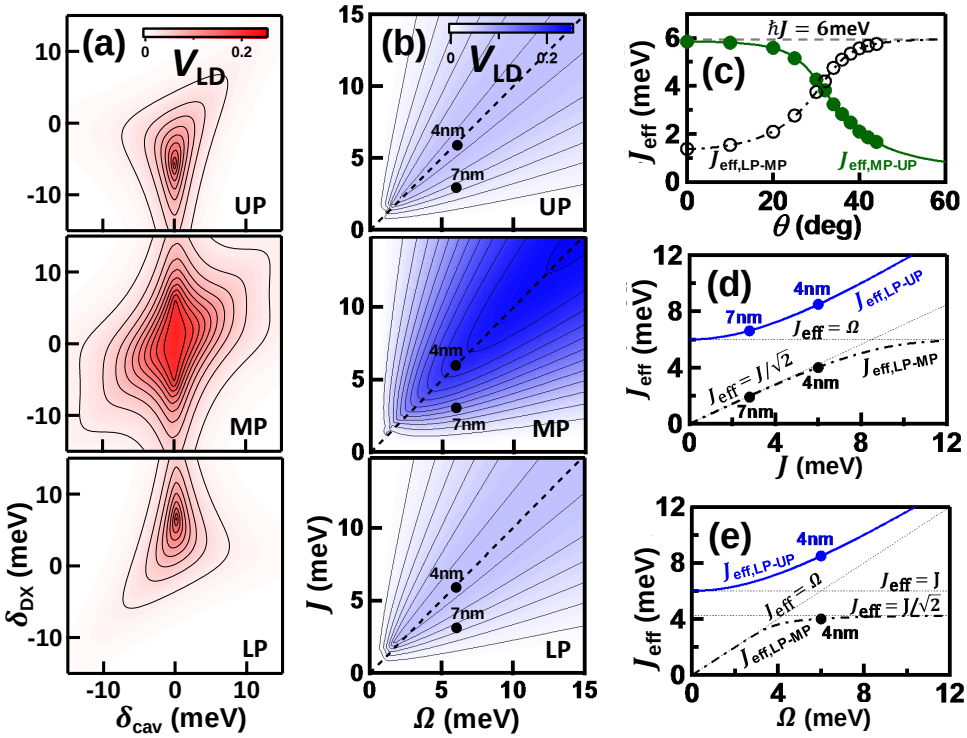

Figure 7.14: (a,b) Analysis of the optical-dipole coupling strength V_{LD} for the $L_B = 4$ nm sample as a function of (a) detuning of C and DX mode from the IX energy for $\hbar\Omega_{\mathrm{R}} = \hbar J = 6$ meV and (b) as a function of $\hbar\Omega_{\mathrm{R}}$ and $\hbar J$ at resonance $\delta_{\mathsf{DX}} = \delta_{\mathsf{C}}$. Black dots in (b) indicate the points that are accessible with our samples. (c) Effective tunnelling splitting J_{eff} between the LP and MP branch (black; dash-dotted) and between the MP and UP branch (blue or green; solid line), as a function of (c) cavity detuning (angle θ), (d) bare tunnelling coupling constant J and (e) Rabi coupling constant Ω_{R}.

Fig. 7.14(b) displays the light-dipole coupling strength as a function of the Rabi frequency Ω_{R} and the tunnelling rate J at the resonance point $\delta_{\mathsf{DX}} = \delta_{\mathsf{C}}$. Unsurprisingly, the highest value for V_{LD} is reached for $\Omega_{\mathrm{R}} = J$ for all dipolaritons (compare to Eq. 7.11). The black dots indicate the points that are accessible in the experiment with our samples. The conclusion from this graph is that a smaller barrier width $L_B < 4$ nm, which is linked to the tunnelling rate J, does not significantly increase the light-dipole coupling, but it causes a reduction in the dipole moment due to smaller charge separation.

Since the detuning reduces the coupling interaction, the anticrossing splittings in the energy dispersion of LP-MP and MP-UP [Fig. 7.9(a)], i.e. the minimum energy separation between two neighbouring dipolariton branches, quantify the effective tunnelling rate J_{eff}, depending on J, Ω and detunings between the modes. Extracting the anticrossings $J_{\mathsf{eff,LP\text{-}MP}}$ and $J_{\mathsf{eff,MP\text{-}UP}}$

with increasing angle of the cavity photon shows the strong detuning and angle-dependence of J_{eff} in Fig. 7.14(c). For the LP it can be suppressed by more than 300% by tuning the cavity mode far to the blue at high θ. In a simplified way one could say that the far detuned cavity mode, entailing minimal optical coupling, provides only little IX population on the LP branch to shuttle between the left and right QW, hence the effective tunnelling rate is small too.

Using the Eq. 7.4, the dependence of the smallest energy splittings LP-UP (blue, solid) and LP-MP (black, dash-dotted) can be computed [Fig. 7.9(d,e)] as a function of J or Ω_{R}. Here all detunings and linewidths have been set to zero, with $\Omega_{\mathrm{R}} = 6$ meV in (d), and $J = 6$ meV in (e) while the filled circles indicate the splittings measured for our samples. The effective splitting $J_{\mathsf{eff,LP\text{-}MP}}$ increases linearly for small J and Ω and it either saturates at the value $J_{\mathsf{eff,LP\text{-}MP}} = \Omega_{\mathrm{R}}$ (behaving as a DX-polariton with no tunnelling) for $J > \Omega \gg 0$, or it saturates at $J_{\mathsf{eff,LP\text{-}MP}} = J/\sqrt{2}$ (behaving as a dipolariton with reduced tunnelling) for $0 \ll J < \Omega$.

7.6.3 $|\mathsf{MP}\rangle$ - the "Dark" Polariton?

In atomic physics, a three-level excitation schemes arranged in a Λ, as in the Λ-scheme shown in Fig. 7.15(a), is a popular system to study and manipulate coherent optical nonlinearities of a medium, usually in a diluted atomic gas. It is important to note that the two ground states, $|1\rangle$ and $|3\rangle$, should at least be meta-stable and that no transitions occur between them. The basic idea is that a strong pump laser alters the optical properties of the medium (produces dressed states via AC-Stark splitting) so that a weak resonant probe laser experiences strongly modified propagation in this medium. The probe laser leads to destructive interference between the transition amplitudes to these two dressed states. In this context electromagnetically induced transparency (EIT) has been shown [174] two decades ago, where an optically thick medium is rendered transparent for the probe laser. Another interesting phenomenon possible in Λ-systems is the creation of slow light. Due to the extremely steep dispersion that can be created with a pump laser, the group velocity for the perpendicular probe laser can become as low as 17 m/s [175], thus enabling reversible optical storage.

A third very useful effect is coherent *adiabatic* population transfer [166, 176] (Fig.7.15), also known as STImulated Raman Adiabatic Passage (STIRAP). With this technique it becomes possible to transfer an electronic population from one ground state of the Λ-system, $|1\rangle$, to the other one, $|3\rangle$, without ever populating the excited state $|2\rangle$, thus efficiently preventing losses and dephasing [(g) and dashed arrow in Fig. 7.15(b)]. For this population transfer to be efficient, the coupling lasers have to be switched on and off in a counter-intuitive sequence [laser amplitude vs time in Fig. 7.15(d)]. First the signal laser S creates an atomic coherence between the states

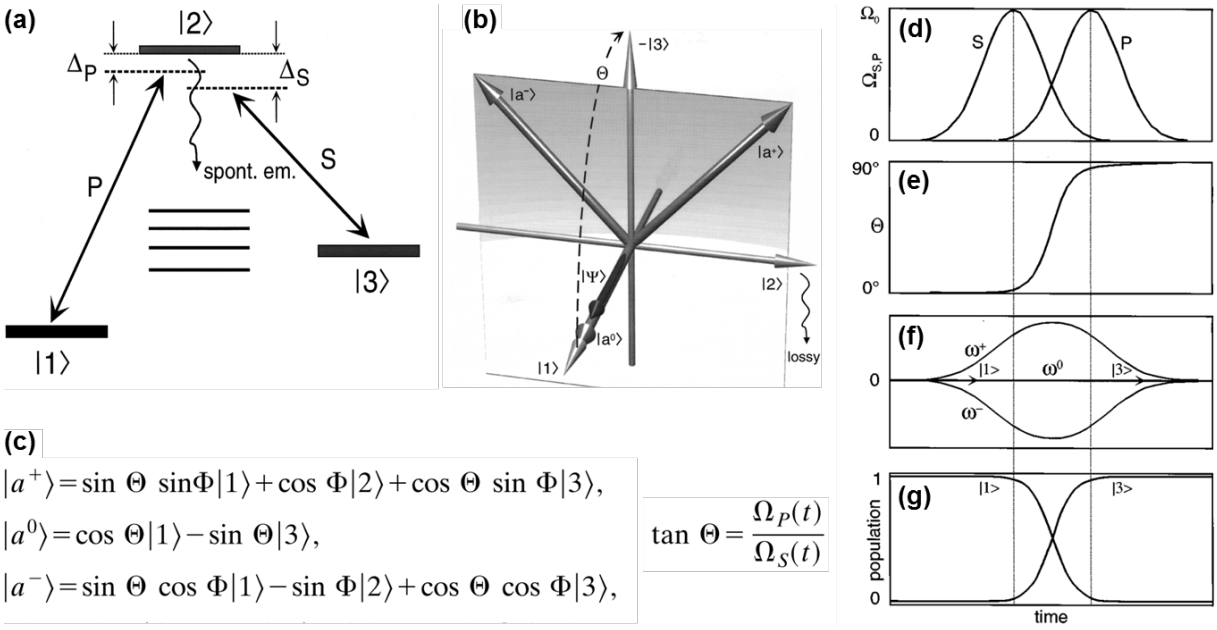

Figure 7.15: (a) Λ excitation scheme in atomic physics. The initially populated state $|1\rangle$ and the final state $|3\rangle$ are coupled by Stokes laser $\{S, \Omega_S(t)\}$ and pump laser $\{P, \Omega_P(t)\}$ via an intermediate state $|2\rangle$, which may decay by spontaneous emission to other levels. Δ_P, Δ_S are detunings. (b) Graphic representation of the Hilbert space for the bare states $|1\rangle$,$|2\rangle$,$|3\rangle$ and in the basis of the dressed states $|a^0\rangle$,$|a^+\rangle$,$|a^-\rangle$. Adiabatic population transfer (dashed arrow) makes the dark state $|a^0\rangle$ evolve in time so that the population is channelled from the initial state $|1\rangle$ to the final state $|3\rangle$ without mixing with the lossy states $|a^-\rangle$,$|a^+\rangle$. (c) Eigenstates of the coupled Hamiltonian [analogous to Eq. 7.4, just with time-dependent coupling constants $\Omega_S(t), \Omega_P(t)$]. Time evolution of (d) the Rabi frequencies of the pump and Stokes laser; (e) the mixing angle; (f) the dressed-state eigenvalues; (g) the population of the initial level $|1\rangle$ (starting at unity) and the final level $|3\rangle$ (reaching unity). All images taken from [166].

$|2\rangle$ and $|3\rangle$ [dressed states split in energy $\omega^{\pm}$ in Fig.7.15(f)], then the pump laser P transfers the population adiabatically from ground states $|1\rangle$ to $|3\rangle$ if the coupling lasers S and P are switched as shown in Fig. 7.15(d). The temporal shape of the laser pulses is irrelevant as long as they are smooth and overlap in the right way [166]. The 3×3 Hamiltonian describing this system is identical to Eq. 7.4 and produces the eigenstates shown in Fig. 7.15(c), whereby the state $|a^0\rangle$ is the so called dark state, a superposition of the two ground states that does not couple to light.

The MP is formally identical to the dark state $|a^0\rangle$ in atomic physics except that it doesn't couple to the DX mode. Introducing the mixing angle θ_{DP} defined by $\tan\theta_{\mathsf{DP}} = \Omega_{\mathrm{R}}/J$, the MP $|\mathsf{DP}\rangle$ can be expressed as (compare analogous treatment for atomic physics in the review by

Bergmann [166])

$$|\mathsf{DP}\rangle = \cos\theta_{\mathsf{DP}}|\mathsf{C}\rangle - \sin\theta_{\mathsf{DP}}|\mathsf{IX}\rangle \tag{7.13}$$

It can easily be checked that this state reduces to $|\mathsf{C}\rangle$ for $\Omega_{\mathrm{R}} \to 0$ and to $-|\mathsf{IX}\rangle$ for $J \to 0$. Assuming the excitation is initially in the cavity mode C, then an adiabatic sweep of the mixing angle from $\theta_{\mathsf{DP}} = 0$ to $\theta_{\mathsf{DP}} = \pi/2$ could map the photon state directly to the long-living IX state, thus bypassing the DX state. This process could be used for optical storage or for optical gates harnessing electrically controlled exciton interactions in addition to optical spin control [69].
To which extent the MP will show atomic physics properties like EIT is a question that can only be answered with further experiments. Whether or not this system is suitable for STIRAP with dipolaritons depends on how well it fulfils the adiabaticity condition[1] and if the dephasing time of the two ground states is long enough compared to the lifetime of dipolaritons to allow coherent transfer. The equivalent to the control lasers P and S in Fig. 7.15(a) is turning on the strong optical and tunnelling coupling. Therefore an important requirement is independent control of Ω_{R} and J, which could be achieved by electric-field tuning for J and by changing the mirror reflectivity for Ω_{R}. It could well be that a condensate of dipolaritons is necessary to provide coherence to show STIRAP-type control in dipolaritons systems.

7.7 Conclusion

Indirect excitons are excitations with sufficiently long lifetimes for thermalization and a large static dipole moment [151]. These properties enable efficient in-plane electrostatic traps [160] and the coherent control of electron spins. On the negative side, the binding energy of an indirect exciton is lower and its coupling to the cavity mode is minimal, so that strong coupling in the dipolariton is weakened. By embedding tunnel-coupled quantum wells inside a microcavity in the strong coupling regime, the concepts of indirect excitons and microcavity polaritons can be united to produce dipolaritons. These optically active quasiparticles have a large dipole moment and several advantages they inherit from their hybrid nature: longer lifetime, tuneable dipole moment, stronger long-range interactions, large de Broglie wavelength and strong optical coupling. Most interestingly, electrical control over these properties may allows us to study the BEC-BCS crossover by changing the quasiparticle density (pump power P) and tunnelling coupling (electric field F) [177]: at low P and F a polariton BEC is seen, while high values of

[1] Following [166], the adiabaticity criterion at resonance is

$$\left|\tfrac{d}{dt}\theta\right| = \left|\frac{\frac{dJ}{dt}\Omega_{\mathrm{R}} - J\frac{d\Omega_{\mathrm{R}}}{dt}}{\Omega_{\mathrm{R}}^2 + J^2}\right| \ll \tfrac{1}{2}\sqrt{\Omega_{\mathrm{R}}^2 + J^2} = \frac{S}{2} \qquad \text{for all times } t \tag{7.14}$$

parameters lead into the BCS regime, where fermionic interactions dominates and a metallic condensate is predicted, a new state showing coherence and metallic conductivity.

Previous work, upon which the results of this chapter are based, include the first experimental observation of dipolaritons[1] [40, 41] which showed sensitive and strong optical gain control with bias voltage, and the mapping of the dipolariton dispersion curves in electrical tuning, revealing a bias-controlled bistability due to intrinsic charge trapping in the ADQW structure [170]. In this chapter strong coupling of mixed direct-indirect excitons with the cavity mode was demonstrated, leading to three clearly separated dipolariton modes in the PL spectrum [Fig. 7.8(b)]. The simple coupled oscillator model Eq. 7.4 has proven to be very useful for understanding the composition (Fig. 7.9) and the bias and angle dependence of the dipolariton modes. In Fig. 7.11 independent control of optical and tunnelling coupling via detuning of the C and IX mode was demonstrated. For efficient coupling of the IX to the light field a small tunnelling barrier of 4 nm or less is necessary, otherwise the dipolaritons make way to conventional DX-polaritons with an optically inaccessible IX state [$L_B = 20$ nm sample in Fig. 7.10(c)].

Of particular interest is the $|\mathsf{MP}\rangle = \alpha|\mathsf{IX}\rangle - \beta|\mathsf{C}\rangle$ state at resonance, which is a pure mixture of the indirect exciton and the cavity photon and whose mixing ratio $\alpha/\beta = \Omega_\mathrm{R}/J$ is controlled purely by the coupling constants. According to the 3-mode coupled oscillator model the MP arises from destructive interference of transition amplitudes which cancels out the DX part. In atomic physics this state is known as a dark polariton [153] and is employed for electromagnetically induced transparency (EIT) [178] in atomic media or waveguides [155], to drastically slow down light [179] and for light storage [154, 180]. The MP dipolariton differs from atomic dark polaritons in that the role of the first pump laser in the Λ-scheme is taken by the cavity-exciton Rabi coupling, while the second probe laser is substitutes by the bias-controlled electron tunnelling transition. Applying EIT to a condensed dipolariton population could thus map photonic states onto electron tunnelling states that can be read out in charge transport. This suggests new strategies for quantum readout and optical interconnects, for example as a variable pulse delay element in dipolariton signal processing.

Furthermore, interactions between dipolaritons with vertically-aligned dipole moments are much stronger (by a factor 100) than for typical dipole-dipole scattering between in-plane excitons [152], and resemble an ensemble of Rydberg atoms in an electric field [181]. The stronger repulsion of dipolaritons over conventional polaritons leads to increased stimulated scattering rates, and hence lower condensation thresholds [152]. In this sense dipolaritons could be interesting

[1] Then called oriented polaritons.

for the creation of condensates with long-range dipole interactions that can be tuned both electrically and optically. The electrical control properties are of particular interest, with static dipole moment being a handle to transport dipolaritons in the microcavity plane with electric fields. If successfully implemented, this ability could be beneficial for transistors [82, 83], which could possibly also be operated in combination with electrical pumping. A bit futuristic is the realisation of optical polariton memories, where the information of a photon is stored in an IX with longer lifetime and good manipulation capabilities, benefiting from the spin-sensitive optical bistability of polaritons [182, 183].

Whether these ideas work in tunnel-coupled polariton systems or not can only be proven with further experiments. Direct effects of the static dipole moment have not been shown yet (Sec. 7.6.1), possibly due to our sample losing the strong optical coupling for electric fields past the resonance point, where we see a drastic drop in the PL emission (Sec. 7.5.3). In my view a new sample which shows condensation from the DX-polariton regime all the way *past the tunnelling resonance* is required to study effects of the dipole and phenomena related to EIT and coherent population transfer in more detail. Such a sample would probably also be suited to show indirect exciton condensation and might have to be operated at temperatures below 4 K.

On the other hand recent theoretical work [177] suggests that for strong enough photon coupling constant Ω_{R} coherence of dipolaritons develops even if an exciton condensate cannot be formed for $\Omega_{\mathrm{R}} = 0$, in the absence of light-matter coupling. At large bias, in the indirect-exciton state, coupling to light is expected to still be surprisingly persistent because of the tunnel coupling between the exciton states. Further theoretical work has investigated the possibilities of the dipolariton system to study BEC-BCS crossover [177] and for new applications like THz lasers [162, 184] and single photon sources [185]. In this respect, the future of dipolaritons remains interesting.

Chapter 8

Conclusion and outlook

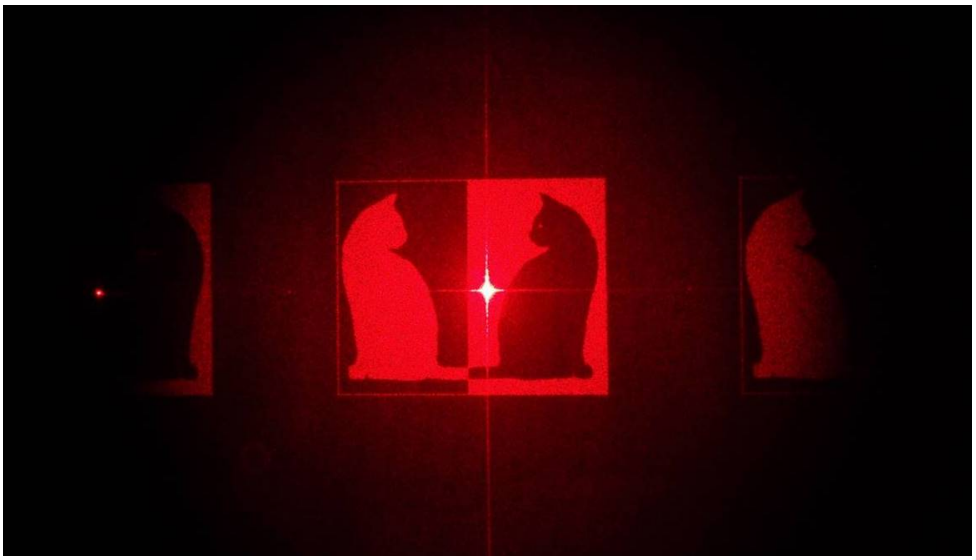

For me studying polaritons has been an interesting and challenging experience, sometimes fun, sometimes frustrating. For sure I have learned a lot about academic research, physics and optics, semiconductors, algorithms and Fourier transformation, programming and image analysis in the process of it. All the time spent in the lab and reading scientific literature has widely broadened my knowledge of polaritons, but on the other hand one also realises how much more is not fully understood on this topic – and that scientific theories are just what the word implies – theories waiting to be falsified and replaced by a better fitting model.

8.1 Optical control of polariton condensates

Microcavity **polaritons** are lightweight quasi-particles resulting from the coherent superposition of a trapped photon and a QW exciton in a semiconductor microcavity. The combination of bosonic character, two dimensional nature (in-plane momentum conservation and hence direct state readout) and a tiny effective mass $m^* = 5.4 \cdot 10^{-35}$ kg have made polaritons a much studied system for matter coherence phenomena in the last decade. Polaritons are short-lived with lifetimes of typically 10 ps, thus requiring constant pumping. Therefore condensation occurs in a steady-state equilibrium of creation and decay of polaritons, rather than in full thermal equilibrium of an isolated system. Non-resonant pumping creates an exciton reservoir which provides condensate gain and kinetic energy via the blueshift potential. Both of these properties determine the flow of polaritons within the condensate and the shape it assumes for a given pump configuration.

The flexibility of a **spatial light modulator** to phase-modulate the pump laser beam into any shape (chapter 4) makes it possible to study optically trapped polariton condensates for the first time in more detail. A simple change in the pumping configuration, like a reduction of the spacing for N pump spots arranged along a circle, as presented in chapter 5, induces a transition from a **phase-locked condensate** to a **trapped condensate**. In the former an array of multiple out-flowing condensates, which originate at the respective laser spots, synchronise to a common energy in order to increase the condensate's population, thus creating a regular network of condensate fringes. Simulations of this system suggest that quantum pressure plays the leading role to stabilise the phase-locked state. A trapped condensate on the other hand has a smoother wavefunction, hence quantum pressure plays a negligible role. It is stationary, optically trapped and well separated from the exciton reservoir. Benefits of the trapped condensate over the phase-locked condensate include better coherence properties and a reduced condensation threshold. Optically trapped condensates are very stable and "clean", which could prove to be very useful in future experiments requiring high precision control of the condensate's population, size and shape, for example in extended cascaded polariton logic circuits.

The SLM allows to explore a variety of more complex excitation shapes. The geometry presented in chapter 6 comprises **two parallel pump lines** with small separation, which creates an effective **1D waveguide** that channels the flow and speed of polaritons already below threshold. Above threshold the waveguided flow becomes dominant and polaritons are expelled at both ends of the channel with high speed. Acceleration of polaritons is linear inside the waveguide, starting from its centre, up to a blueshift-limited end velocity. These properties could become

useful for polariton circuits requiring a defined polariton flow from a precisely controllable source. Interestingly this geometry shows strong indications of a continuous onset of coherence at pump powers far lower than the condensation threshold. The waveguided polaritons are found to be mono-energetic and at a low temperature of 5 K already at a fraction of the condensation power. They accelerate linearly, starting from the centre of the waveguide. The envelope function of the polariton cloud remains identical for all pump powers up to the condensation threshold and could be related to a stationary state of the gain distribution. The understanding of the condensation and acceleration processes in this geometry would definitely benefit from further theoretical investigation, accompanied by cGLE simulations.

In the study time of this thesis the **advantages and limitations of all-optical control** of polariton condensation have become quite clear. On the positive side this technique is very flexible and allows in principle generation of any desired excitation shape. Real-time reconfiguration of the laser image with kHz refresh rates are possible. Grating or iterative FT algorithms can be chosen depending on the desired laser shape and performance requirements (smoothness, diffraction efficiency, complexity of the pattern, computation time). Blueshift potentials are very effective to confine and guide the polariton flow, albeit the additional gain they provide can lead to unpredicted condensate shapes, especially for complex pump patterns.

Laser images are fundamentally limited by the $\varnothing \sim 1$ μm spot size which the microscope objective can produce. Furthermore the polariton condensate cannot support features smaller than its healing length ξ. In general small structures in a condensate wavefunction, like the ripples of a phase-locked condensate array, require high polariton momenta k_c to form, making features of 1-2 μm hard to achieve for trapped condensates; an exception herefrom are ring condensates [43]. Practical restrictions we have found in the experiments are related to the pumping laser. It absolutely has to operate in a stable single-mode regime for formation of single energy condensates. Particularly detrimental for condensate stability is gain competition between two laser modes, which leads to fast intensity fluctuations of the pump laser image and results in multiple condensates being excited simultaneously. The condensate's energy fluctuates so fast in time that PL images show a continuum of excited states in this case. Furthermore, one has to ensure that enough pump laser power is at disposal to create a laser image with the precise but inefficient MRAF algorithm. Grating-based algorithms fare much better in this respect but can be used only for simple geometries consisting if lines and dots.

8.2 Dipolaritons

Dipolaritons are the synthesis of indirect excitons with polaritons in the **strong optical and strong tunnelling coupling** regime. They were observed for the first time with great clarity in the experiments presented in chapter 7. Dipolaritons feature improved properties over conventional polaritons which include longer lifetime, tuneable dipole moment, stronger long-range interactions, large de Broglie wavelength and controlled electron tunnelling, at the cost of reduced optical coupling $\hbar\Omega_{\mathrm{R}}$. Most interestingly, electrical control over these properties is predicted to allow for studying the BEC-BCS crossover by changing the quasiparticle density (pump power P) and tunnelling coupling $\hbar J$. The simple coupled oscillator model (Eq. 7.4) has proven to be very useful for understanding the composition as well as the bias and angle dependence of the three dipolariton modes. Independent control of optical and tunnelling coupling via detuning of the C and IX mode could be demonstrated in angle and bias resolved PL measurements. Furthermore results for different tunnelling structures show that efficient coupling of the IX to the light field needs a thin GaAs tunnelling barrier of 4 nm or less. Direct effects of the strong static dipole moment remain to be proven experimentally.

Of particular interest for future experiments could be the MP mode at resonance, a state consisting solely of an indirect exciton and a cavity photon. The coupled oscillator model predicts analogies of this state to the dark state in atomic physics and hence it could allow phenomena like electromagnetically induced transparency (EIT) and stimulated Raman adiabtic passage (STIRAP) to be studied in conjunction with polaritons. There are however still some **limitations of the current sample** which have to be overcome. First and foremost the loss of strong optical coupling at higher electric field has to be solved, so that dipolaritons can condense in such a future microcavity. The loss of the strong tunnelling regime at large bias seems to be under control nowadays through additional barrier layers, positioned at either side of the coupled quantum well region, which prevent electron escape.

8.3 Outlook

The future of the work presented in this thesis goes in two directions, which might eventually be joined. On the one side the **spatial shaping of the pumping laser** beam has proven to be a very useful manipulation tool for polariton condensates and it will definitely continue to be used in forthcoming experiments. It is envisaged to use lattices of optically controlled polariton condensates to study tuneable spin interactions of polaritons under non-resonant pumping [186]. In addition, polaritons have a high susceptibility to magnetic fields, making them very interesting for optical spin sensing and spin manipulation of the polariton condensate. This route towards polariton sensors is currently being pursued on the setup developed in my PhD time.

All-optical control of polaritons has unavoidable problems: separation of blueshift potential from the optical gain and high in-plane dissipation of polaritons. Building on the work in [91], simple logic circuits based on etched structures for confinement in combination with optical control for switching and directing polaritons at flow splitters are certainly within reach in the next 1-2 years and worth further study. Single polariton circuits as future devices or metrology systems are a bit of a dead end in my opinion, because polaritons are too volatile as single units, and instead a condensate is needed for reliable operation. Since polaritons are quasiparticles, their number is not conserved as for electrons.

Any future practical application would greatly benefit if the inefficient optical pumping was replaced by electrical injection, with the use of light pulses to control and manipulate the formed condensates. Electrical polariton lasing at room temperature, shown very recently in GaN [21] thanks to a new in-plane pumping scheme, has to be adapted to GaAs systems. However, to also move to organic or nitride-based materials would allow working in the strong coupling regime at room temperature. For both materials the respective problems of photo bleaching and difficult fabrication seem to be solvable with current progress rates in the near future.

In my view real-world applications of polaritons in the form of commercial light sources, sensors or logic processing devices are rather limited due to the very same properties that makes them an interesting study object in the first place: they are too volatile for computing and memories due to their short lifetime (up to 200 ps is possible [187]), dense packing of polariton transistors is not possible due to the limits of optical addressing, and polariton lasing, despite being energy-efficient, is suited only for low emission powers, above which the strong coupling regime is lost. For metrology purposes atomic condensates or SQUID devices are better suited for precision measurements due to their much higher stability and reliability.

On the other side **dipolaritons** have not reached full maturity yet due to sample limitations. New samples have to improve on two fronts: the regime of strong tunnelling coupling has to be retained also past the resonance condition and a considerably stronger optical coupling is necessary to allow formation of dipolariton condensates in this sample. The future of this work is to couple high quality microcavities, in which condensation can easily be achieved, with the versatility of electrical control offered from electrically pumped dipolariton mesas. The prospect of producing electrically tuneable dipolariton condensates on-demand is very exciting for studying new physics. In combination with the optical excitation control described above this would open up completely new possibilities to study condensates with long-range dipole interactions that can be tuned both electrically and optically, and which can transit smoothly between being bosonic (low bias and high density) and fermionic (high bias and high density) – the BEC-BCS crossover proposed in [177].

In the last decade it seemed a few times already as if polariton research is past its peak. This has been disproved by the large number of interesting publications which appear every year in top scientific journals. While my outlook on commercial polariton devices may seem a bit pessimistic, I am quite positive about the future of polaritons for studying new physics, because it is such a rich system where many processes are still not properly studied and understood, even two decades after the first microcavity polariton was excited. And finally, why not finish this thesis with a typo found while correcting the introduction section:

"Polaritons are god candidates for matter wave phenomena."

Appendix A

Additional SLM topics

A.1 Phase modulation using a real SLM

The phase modulation of a real SLM with $N \times N$ pixels is pixelated. Assuming a fill factor of $\sim 100\%$ and pixel size a it can be written in mathematical form[1] as [188]

$$f(x,y) = \text{rect}\left(\frac{x}{Na}, \frac{y}{Na}\right) \left\{ \sum_{m=-\frac{N}{2}}^{\frac{N}{2}-1} \sum_{n=-\frac{N}{2}}^{\frac{N}{2}-1} A_{mn} \exp(i\,2\pi\phi_{mn}) \cdot \frac{1}{a^2} \text{rect}\left(\frac{x-ma}{a}, \frac{y-na}{a}\right) \right\} \tag{A.1}$$

which becomes

$$g(k_x,k_y) = (Na)^2 \,\text{sinc}\left(\frac{k_x Na}{2}, \frac{k_y Na}{2}\right) * \left\{ \sum_{m=-\frac{N}{2}}^{\frac{N}{2}-1} \sum_{n=-\frac{N}{2}}^{\frac{N}{2}-1} A_{mn} \exp(i\,2\pi\phi_{mn}) \cdot \ldots \right.$$
$$\left. \exp[i\,(k_x m + k_y n)a] \,\text{sinc}\left(\frac{k_x a}{2}, \frac{k_y a}{2}\right) \right\} \tag{A.2}$$

in the image plane after Fourier transformation. Eq. A.2 describes how the light of each pixel (m,n) on the SLM, together with a position dependent phase shift $\exp[i\,2\pi(m+n)a]$, contributes to the total intensity in a point (k_x, k_y) of the laser image (addition of phasors). The first term in Eq. A.2 is a fast varying envelope function stemming from the physical aperture of the active area $Na \times Na$ of the SLM[2]. It is responsible for the resolution limit of features in the laser images. The first root of the sinc function is at $k_x Na/2 = \pi$. With $k_x = 2\pi x/(\lambda_l f)$ (Eq. C.12), $f = 500$ mm and $M = 25$ (Sec. A.2) the size of the smallest achievable features in the laser image on the sample becomes:

$$\Delta x = \frac{\lambda_l f}{MNa} = 2.0\ \mu m \qquad \text{Resolution limit of our laser image} \tag{A.3}$$

[1] The rectangular window function is $\text{rect}(x,y) = 1$ if $-a/2 < x, y < a/2$ and $\text{sinc}(x,y) = \sin(x)\sin(y)/(xy)$ describes diffraction effects.

[2] The second sinc function in Eq. A.2 is not important because it is a very slow modulation (first zero at $x = N\Delta x = 1000\ \mu m$) compared to the maximum extension of the laser image of $\pm 530\ \mu m$.

This value coincides with the minimum feature seen in the experiment and compares quite well with the diffraction limited spot size $\Delta x = \lambda/(2\,\mathrm{NA}) = 0.9\ \mu m$ of the microscope objective. The same result for Δx can be obtained with simple geometric arguments, as shown in the next section.

A.2 Resolution limit and size of laser images

The maximum [minimum] deflection angle $\theta_{\max}\,[\theta_{\min}]$ that the SLM can produce for a 2 px binary [512 px blazed] diffraction grating are small according to Eq. 4.2

$$\sin\theta_{\max} = \frac{\lambda}{d_g} = \frac{0.8\,\mu m}{2\cdot 15\,\mu m} = 0.027 \qquad \longrightarrow \qquad \theta_{\max} = \pm 1.53^\circ \tag{A.4}$$

$$\sin\theta_{\min} = \frac{0.8\,\mu m}{512\cdot 15\,\mu m} = 1.04\cdot 10^{-4} \qquad \longrightarrow \qquad \Delta\theta_{\min} = 0.006^\circ \tag{A.5}$$

Finer angle variations are however possible because each pixel of the SLM is addressed with 8bit (256 values), hence smaller grating slopes can be realised at the expense of diffraction efficiency. From these numbers the size of the laser image $x_{\max}$ in the sample plane [and at the intermediate image plane at PH1] can be readily computed (see Fig. 4.1)

$$x_{\max} = f\,M\,\sin\theta_{\max} = \pm 530\ \mu m \qquad [\pm 13.4\ \mathrm{mm}] \tag{A.6}$$

where $M = 25$ is the magnification of the telescope L4 with the microscope objective and $f = 500$ mm is the focal length of the Fourier lens L3. The SLM is capable of producing laser images of 1×1 mm, however the small back aperture of the microscope objective limits the effective size of laser images in the sample plane to about $100 \times 100\ \mu m$. The resolution limit of our setup is not set by the minimum deflection angle but rather by the active area of the SLM, relating to Airy disk of radius $\Delta x = 2.0\ \mu m$ in the sample laser image (see Eq. A.3).

A.3 Working with SLMs

A few remarks learned from working with SLMs:

- They are not very efficient: the bare reflectivity of a good device is $> 90\%$ and grating phase patterns have an efficiency (power in 1^{st} order divided by incident power) of $\eta > 65\%$. However, for complicated laser images that require advanced algorithms (as in Sec. 4.3.2) the efficiency drops significantly to $\eta = 10 - 25\%$, depending on the parameters used.
- Grating-based phase patterns work for simple shapes and are really good for clear laser

images and high efficiency, since they are an *analytic solution*, but also very sensitive to even SLM illumination. Iterative algorithms like Gerchberg-Saxton are more universal and less prone to SLM illumination gradients but lead to speckled laser images, which can be corrected for at the expense of a further reduction in diffraction efficiency.

- Pulsed lasers result in much cleaner laser images without speckles, since the light is not as monochromatic.

- SLMs generally modulate only one linear polarisation of light. Putting a polariser after the SLM that rejects the unmodulated polarisation greatly helps to get clean laser images with very little light in the unwanted diffraction orders.

- Calibration of the SLM for the used laser wavelength is essential! This is best done by putting a simple grating pattern (grating constant $g > 10$ px) on the SLM, whose amplitude is decreased from 1 (maximum possible phase shift) to 0 (no extra phase shift) in small steps of 0.02 until the power in the 1^{st} diffraction order is highest. For our SLM, which is built for $\lambda = 785$ nm, a value of 0.94 leads to good results. The degeneration of the SNR with phase modulation errors is calculated in [116].

- In principle the effects of the Fourier lens can be incorporated into the phase pattern directly by adding an extra hyperbolic phase profile of the form [189] $\phi(r) = \frac{2\pi}{\lambda}(\sqrt{r^2 + f^2} - f)$. While this leads to a more compact setup and theoretically higher resolution laser images, it considerably increases the computational complexity of phase patterns and makes them less intuitive (convolution with Fresnel kernel instead of simple Fourier transformation, see Sec. C). In my experience the resulting laser image is cleaner when formed by a dedicated physical lens for the Fourier transformation into far field, because it eases alignment and leaves the full 2π modulation depth for the phase pattern instead of the focussing function curvature, thus making the phase patterns much flatter (less $0 - 2\pi$ jumps).

- Phase modulation applied by an SLM is digital: due to the inertia of the LC the voltage applied to the LC cell is a very fast pulse width modulation rectangle signal. The LC molecules thus retain a certain orientation but can show a slight trembling motion that translates into weak fluctuation in the modulated phase shift. This fact, know as phase flicker, translates to a temporal intensity noise in the pump laser image. Fortunately, it turns out that this noise (300 Hz for the Holoeye Pluto, 4 kHz for the BNS) has no detrimental effects on the stability of the polariton condensate.

A.4 High fidelity grey-scale laser images using MRAF algorithm

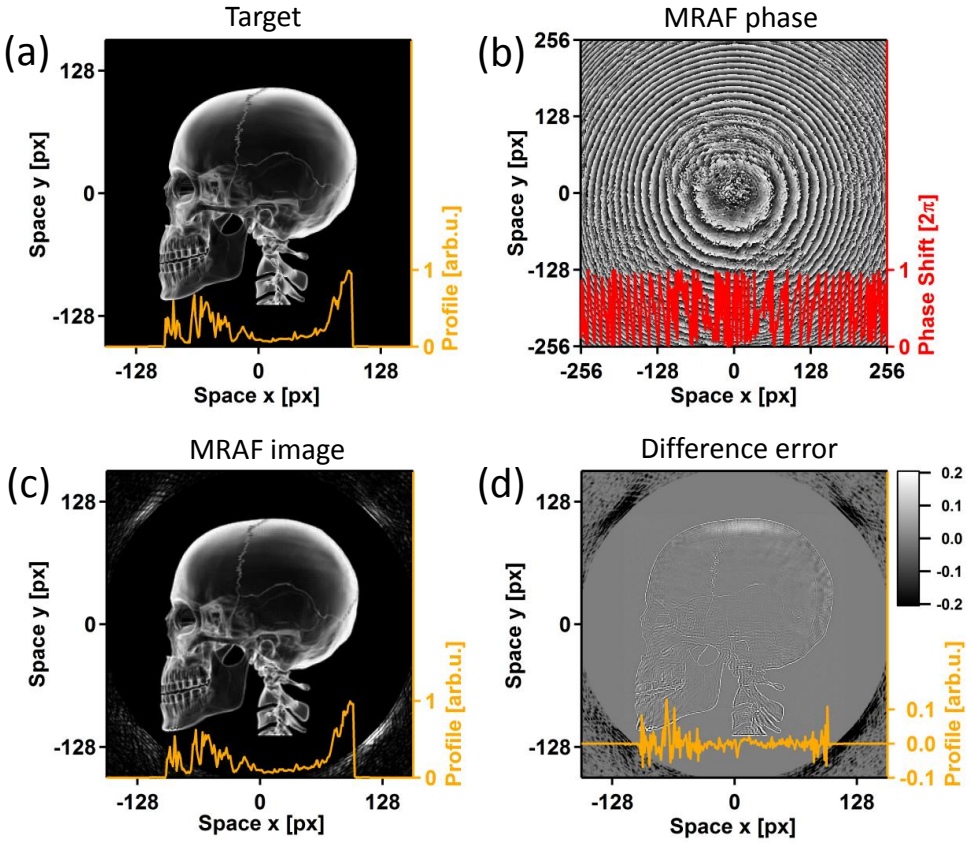

Figure A.1: The MRAF algorithm is particularly well suited to generate high fidelity grey-scale laser images with little computing time. The small differences (d) between the target (a) and the simulated laser image (c) of less than $\pm 10\%$ occur mostly at sharp edges and are usually only one pixel wide. The phase pattern (b) is of parageometric form. Profiles (cuts along $y = 0$) in (a,c) show how small the discrepancies are. Parameters: $N = 100$, m $= 0.4$, $r_{\mathrm{SR}} = 162$ px.

Appendix B

Alignment Procedure

Opt. Element	Details	f [mm]	size [mm]	Transl./Rot.
L1, L2	4× beam expander	300, 75	⌀ 25.4	–
L3	Fourier lens	500	⌀ 50.8	flip
L4	collimation lens	400	⌀ 50.8	x,y,z, flip
MO	microscope objective	4	⌀ 2.7	–
L5	k-space lens, flip mount	150	⌀ 25.4	x,y,z, flip
L6	real space lens	200	⌀ 25.4	flip
L7, L8	3.75× beam expander	-200, 750	⌀ 25.4	–
L9	spectrometer lens	250	⌀ 50.8	x,y,z
L10	imaging lens	400	⌀ 50.8	z
BS1	beamsplitter R:T=90:10	–	25.4×25.4	–
BS2	beamsplitter R:T=50:50	–	25.4×25.4	θ_x, θ_y
BS3	beamsplitter R:T=50:50	–	25.4×25.4	θ_x, θ_y
WP1,WP3	$\lambda/4$ waveplate	–	⌀ 25.4	θ_z
WP2,WP4	$\lambda/2$ waveplate	–	⌀ 25.4	θ_z
M0	Ag mirror R>98%	–	⌀ 25.4	θ_x, θ_y
M1-M5	Ag mirrors R>98%	–	⌀ 50.8	θ_x, θ_y
M6	PC-steered Ag flip mirror	–	40×40	flip
PH1	iris diaphragm as pinhole	–	⌀ 0.8-12	x,y
PH2	iris diaphragm as pinhole	–	⌀ 0.8-12	x,y, flip
SLM	spatial light modulator	–	7.7×7.7	θ_x, θ_y
AOM	acousto-optic modulator	–	–	–
CCD	spectroscopy camera	–	27.6×6.9	–

Table B.1: List of optical elements in the setup. See Fig. 4.1.

Tab. B.1 lists the important optical elements[1] in the setup shown in Fig. 4.1. The "size" column refers to the usable optical aperture of the element and the "Transl./Rot." column specifies the degrees of freedom of the element's mount: translation in x,y (perpendicular to beam) or z (axial) directions, rotations θ_x, θ_y for tilting the element (yaw, pitch) and if the element resides on a flip mount to quickly remove it from the optical path. All optics are standard N-BK7 singlet lenses from Thorlabs with anti-reflection coating B for near-infrared light (650-1100 nm). Lens curvatures were chosen to minimise spherical aberration, e.g. using a plano-convex lens with the flat facet facing the focus point of the beam path.

[1]For the microscope objective MO, f is the effective focal length, ⌀ is the clear entrance aperture at the back focal plane.

B. ALIGNMENT PROCEDURE

Proper alignment of the optical setup is imperative to obtain symmetric and stable trapped polariton condensates. The most critical parts are the SLM illumination, the light path from the SLM to the sample and the Mach-Zehnder-interferometer for phase measurements. Very important: **Cool down the cryostat before doing any serious alignment!** Since our laser source is far away from the SLM, even small misalignment in the laser path means we have to align most of the setup on a daily bases.
Good optical alignment is important for two reasons. First, the DBR mirror of the microcavity is a very sensitive angle filter at the 1st minimum of the stopband, so a beam coming in at a different angle will be transmitted much less/more. Second, the condensate is exponentially sensitive on intensity differences and any asymmetry will switch the condensate into a different shape state. Here is the alignment procedure for the setup (see Fig. 4.1):

1. **Excitation part:**

   (a) Optimise pump laser alignment into MBR laser by monitoring the output power on a power meter.

   (b) Send laser centred onto SLM using mirror M0 and put a 4-spot grating pattern on SLM ($g \sim 50$ px, offset grating $g_x = 5$ px, angle of 45°, so that spots are left/right, top/bottom). Roughly focus the laser light on the sample by using the z translation stage of the cryostat.

   (c) Insert SLM adjustable iris, reduce its diameter to minimum and centre illumination so that laser image of the 4 spots look symmetric at the intermediate image at PH1.

   (d) Flip L3 and L4 out of the optical path. Centre the modulated laser beam (still 4 spots) on the microscope objective's back aperture **and** make sure the real space camera image looks symmetric by beam-walking with the SLM adjustment screws and M1. To check alignment, place a cross-hair on the camera image and move the cryostat focussing translation stage back and forth to move the laser image in and out of focus. If properly aligned, the centre of the laser image should not move laterally when the sample focus is changed, ensuring perfectly vertical excitation. If this is not the case yet, beam-walk until perfect.

   (e) Flip lens L3 into the optical path and adjust the (x,y) position of the lens mount to minimise the lateral movement of the laser image on the camera, as before. Flip in L4 and repeat this procedure once more.

   (f) Focus the sample z stage. If the camera image moves laterally when going in and out of focus, adjust micrometers on L4.

   (g) With sufficient pump power there should be dark circles at the positions of the laser beams surrounded by bright PL rings. If the four laser spots reflected from the sample do not coincide with the spots in PL then the focus of L4 is wrong. In this case adjust the focus of the microscope objective first, using white light illumination and maximising the contrast of a defect on the sample surface by looking at the camera image. Then switch back to the laser and shift L4 along the optical axis until the camera laser spot positions matches with the PL image.

(h) Usually a few iterations of the steps above are necessary for alignment from scratch, however on a daily bases checking M0 for SLM illumination, turning the SLM for best symmetry laser image, shifting the (x,y) position of L4 to compensate left/right or top/bottom asymmetries in the laser image and checking M0 again for maximum condensate symmetry are sufficient.

2. **Detection part:**

   (a) Laser and PL emission do not necessarily coincide on the camera. First centre the laser (course alignment), then the PL (fine adjustment), through the detection setup: flip out L5 and send laser straight into spectrometer by beam walking with M2 (position on spectrometer slit) and L9 (position on CCD).

   (b) Adjust k-space lens L5 so that real-space image and k-space image have the same centre (otherwise spectra have wrong cut through image). Then adjust the L5 focus on the microscope objective back aperture by looking at the 2D k-space image of a single spot condensate in PL. When the focus is correct, a thin circle should appear at high k, if badly focussed it is washed out.

   (c) Check that the spectrum cut through the 2D real or k-space plane is well centred. To do this, open the slit of the spectrometer completely and centre the PL from a 4-spot trapped clover-leaf condensate (see below) by gradually closing the slit and adjusting with L9.

   (d) Align interferometer (see below).

   (e) Fine-tune the image on the CCD coming from the side port using M4 and L10 (beam-walk).

3. **Mach-Zehnder-interferometer** (Fig. 4.3):

   (a) Remove L7 and L8 and align BS2 and BS3 so that the interferometer is perfectly square, otherwise strong fringes will appear due to the anti-reflection coatings of the beam splitters. Start with a single or 4-spot laser beam and block the path via M2. Make sure that BS2 is absolutely perpendicular to the laser beam – no fringes should be seen in PL.

   (b) Use the screws on BS3 and M3 to adjust the other interferometer arm until very wide fringes appear. This involves beam walking, whereby M2 is used to ensure beam overlap of the two arms right after BS3 and M3 is used to overlap the beams on the camera image. Now the interferometer is aligned for perfect co-linear beam output.

   (c) Insert L7 and align it in (x,y) to get back co-linear output.

   (d) Using M3 and the last mirror before L8 (Fig. 4.3), misalign the magnified reference arm to get nice fringes at 45° (to avoid Moiré effects from pixel array). A good fringe space for phase measurements is 6 camera pixels.

   (e) Insert L8 in the right distance from L7 (550 mm) and align (x,y).

   (f) Use the translation stage of the interferometer to adjust the path difference to $\Delta s = 0$. This is done by maximising the fringe contrast of the interferometer image of a single energy trapped or phase-locked condensate while moving the translation stage.

   (g) Align optical paths from interferometer exits to camera once more.

4. **Adjust condensate symmetry:**

   (a) Adjust pump laser wavelength to get maximum PL intensity (find first DBR minimum on high energy side of the stopband).

   (b) Put a 4-spot phase pattern with $g = 30$ px on the SLM and adjust the SLM illumination with mirror M0 so that all four spots are equally bright, both in laser reflection off the sample and in PL emission. Sometimes this is not possible for both, in this case optimise the PL intensities.

   (c) Use L4 to adjust illumination symmetry (left-right, up-down), first with the laser reflection off the sample, then with the PL from a phase locked polariton state or trapped condensate. Adjustment is done with a 4 spot phase pattern ($g = 30$ px for locked state, $g = 50$ px for trapped condensate, both with 45° angle). Fine tuning is best done with a trapped condensate with four lobes in a cloverleaf shape. This condensate needs pump power just above the condensation threshold, the right grating constant (too large and it will be higher order or phase-locked, too low and it will be only a single central blob) and a well adjusted light path from SLM to the sample (improve symmetry of condensate with L4 position).

   (d) Reducing the opening of the iris before the SLM to avoid scattered light from areas that the SLM cannot modulate makes for cleaner, although slightly lower resolution laser images. It helps to improve the stability of the condensates. When looking at the laser reflected off the sample the iris is closed until the four spots look round and clean and the elongated light trails from the spots to the centre disappear.

   (e) Points 4(b,c) might have to be performed iteratively until satisfactory results are obtained.

Appendix C

Optical Fourier transform

C.1 Fourier transform property of free space propagation

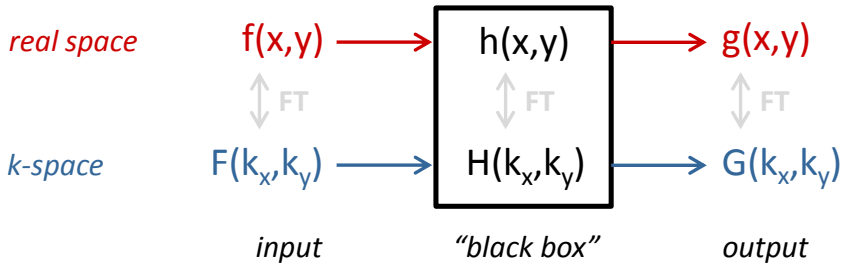

Figure C.1: Scheme of a linear system, a "black box" fully described by the impulse response function $h(x, y)$, which allows to calculate the output $g(x, y)$ for a given input $f(x, y)$ via convolution. The spectral response is calculated with the transfer function $H(k_x, k_y)$.

Fourier optics is a powerful way to describe light phenomena such as diffraction, image formation by a lens, optical filtering and holography. It focusses on the wave aspects of light and relies on two fundamental mathematical principles: analysis of the light as harmonics (Fourier transform) and description as a linear system (light waves satisfies the linear Helmholtz equation, thus the superposition principle holds). A linear system consist of a linear operator $h(x, y)$ that maps an input field[1] $f(x, y)$ to an output field $g(x, y)$ as follows:

$$g(x, y) = h(x, y) * f(x, y) \qquad \text{real space domain} \qquad \text{(C.1)}$$

$$G(k_x, k_y) = H(k_x, k_y) \cdot F(k_x, k_y) \qquad \text{k-space domain} \qquad \text{(C.2)}$$

The first equation states that the output in real space $g(x, y)$ of a linear system can be calculated from a convolution $(*)$ of the impulse response function[2] $h(x, y)$ with the input $g(x, y)$. Equally, the output spectrum $G(k_x, k_y)$ can be computed from a multiplication of the input spectrum $F(k_x, k_y)$ with the transfer function $H(k_x, k_y)$.

[1] For an explanation of $f(x, y)$, $g(x, y)$, $F(k_x, k_y)$ and $G(k_x, k_y)$ see Sec. 4.2.
[2] $h(x, y)$ is the output of the system for a Dirac delta as input: $f(x, y) = \delta(x - x_0, y - y_0)$.

C. OPTICAL FOURIER TRANSFORM

Fourier optics decomposes an arbitrary monochromatic wave of light $u(x, y, z)$ with wavelength λ into a superposition of plane waves with spatial frequencies $\nu_x = k_x/2\pi$, $\nu_y = k_y/2\pi$ and amplitudes $A(k_x, k_y)$ using the 2D Fourier transform. The wave vector component k_z is fixed by $k^2 = k_x^2 + k_y^2 + k_z^2 = (2\pi/\lambda^2)$. This Fourier transform property of free space can be shown as follows (parts based on the chapter "Fourier Optics" in [190]):

$$u(\vec{x}) = \int_{\mathbb{R}^3} \frac{d^3k}{(2\pi)^3}\, U(\vec{k})\, \exp(-i\vec{k}\cdot\vec{x})\, \delta(|k| = 2\pi/\lambda) \qquad \text{3D IFT} \tag{C.3}$$

$$= \int_{\mathbb{R}^2} \frac{d^2k}{(2\pi)^2}\, U(k_x, k_y)\, \exp\left[-i\,(k_x x + k_y y)\right] \exp(-i\,k_z z) \tag{C.4}$$

$$U(k_x, k_y) = \int_{\mathbb{R}^2} d^2x'\, u(x', y', z)\, \exp[+i\,(k_x x' + k_y y')] \qquad \text{2D FT} \tag{C.5}$$

In Eq. C.4 one can recognise the free space transfer function $H(k_x, k_y)$, which can be expanded in terms of the angle $\theta = \frac{\lambda}{2\pi}\sqrt{k_x^2 + k_y^2} \equiv k_\perp/k$ between the wave's k-vector and the optical z-axis (paraxial wave approximation, $\theta \ll \pi$)

$$H(k_x, k_y) = \exp(-i\,k_z z) = \exp\left[-i\,\frac{2\pi z}{\lambda}\sqrt{1 - \frac{\lambda^2}{4\pi^2}(k_x^2 + k_y^2)}\right] \tag{C.6}$$

$$\approx \exp\left[-i\,kz\,\left(1 - \frac{\theta^2}{2} - \frac{\theta^4}{8} + \mathcal{O}(\theta^6)\right)\right] \tag{C.7}$$

Under Fresnel conditions the third expansion term can be neglected $\xi = {}^1\!/_8\, kz\,\theta^4 \ll \pi$, which holds as shown in Eq. A.4 with $z \approx 1$ m ($\xi = 0.5$). The second term $\propto \theta^2$ however cannot be neglected ($\xi = 700$). This means that under free space diffraction of $z \approx 1$ m the laser image is described by Fresnel diffraction, and by combining Eqs. C.4, C.7 and C.5 one obtains after integration $\int d^2k\,(...)$:

$$g(x, y) = \frac{\exp(-i\,kz)}{i\lambda z}\int_{\mathbb{R}^2} d^2x'\, \exp\left(-i\,\frac{\pi}{\lambda z}\left[(x - x')^2 + (y - y')^2\right]\right)\, f(x', y') \tag{C.8}$$

$$g(x, y) = h(x, y) * f(x, y) \qquad \textbf{Fresnel diffraction} \longrightarrow \textbf{convolution!} \tag{C.9}$$

Eqs. C.8 and A.4 prove that free space propagation of a light field $g(x, y) \equiv u(x, y, z)$ over a typical distance $z \approx 1$ m happens in the Fresnel limit in our experiment and is mathematically described by a 2D convolution of the input field $f(x, y) = u(x, y, 0)$ with the impulse response

function (convolution kernel for Fresnel diffraction)

$$h(x,y) = h_0 \exp\left[-i\frac{\pi}{\lambda z}(x^2+y^2)\right] \qquad h_0 = \frac{\exp(-i\,kz)}{i\lambda z} \tag{C.10}$$

The exponential in the integral of Eq. C.8 can be further simplified for large distances z. The small size of the SLM limits the coordinates to $|x', y'| \leq 3.75$ mm, whereas the coordinates in the image plane can reach values of $|x| \leq x' + z\sin\theta_{\max}$, $|y| \leq y' + z\sin\theta_{\max}$. So for the far field $z \gg (x'^2 + y'^2)/\lambda \approx 15$ m we enter the Fraunhofer diffraction regime and can approximate $(x-x')^2 \approx x^2 - 2xx'$ and $k_x = k\sin\theta_x \approx 2\pi x/\lambda z$, resulting in (compare to Eq. C.5)

$$g(x,y) = \frac{\exp\left[-i\,kz - ik(x^2+y^2)/2\right]}{i\lambda z}\int_{\mathbb{R}^2} d^2x'\, f(x',y')\,\exp\left[i\,(k_x x' + k_y y')\right] \tag{C.11}$$

$$g(x,y) = g_0\,F(k_x,k_y) \equiv g_0\,\mathcal{F}\{f\}\left(\frac{2\pi x}{\lambda z}, \frac{2\pi y}{\lambda z}\right) \tag{C.12}$$

Fraunhofer diffraction $\longrightarrow$ Fourier transform!

The interpretation of Eq. C.11 is that, apart from an irrelevant phase shift and amplitude factor in g_0, the far field $g(x,y)$ of a light field corresponds to the Fourier transform of its near field (complex) wavefront $f(x,y)$. Unfortunately in our experiment we never reach the far field condition, therefore a dedicated Fourier lens has to be employed to transform the phase-modulated laser beam to the real space plane in which the laser image forms.

C.2 Fourier transform with a thin lens

A thin spherical lens, set up in the way shown in Fig. 4.4, can perform an optical Fourier transform on the input light field: Fresnel propagation of $z = f$ from the SLM to the lens surface, phase shift of the lens element, propagation of $z = f$ from the second lens surface to the image plane. Using the expression for phase shift acquired after transmission through the thin lens of focal length f and central thickness d_0 ([190] p.54) the lens transmission function becomes

$$l(x,y) = \exp(-i\phi_0)\exp\left[i\,\frac{k}{2f}(x^2+y^2)\right] \qquad \phi_0 = (n-1)kd_0 \tag{C.13}$$

and the output light field can be written as

$$g(x,y) = \Big[\mathcal{F}\{F(k_x,k_y)\cdot H(k_x,k_y)\}\cdot l(x,y)\Big] * h(x,y) \tag{C.14}$$

with $h(x, y, z = f)$ and $H(k_x, k_y, z = f)$ as defined in Eqs. C.7 and C.10 and $F(k_x, k_y) = \mathcal{F}^{-1}\{f(x, y)\}$. Putting all the expressions together one gets

$$g(x,y) = \int_{\mathbb{R}^2} d^2x' \int_{\mathbb{R}^2} \frac{d^2k}{(2\pi)^2} \exp\left[-i\left(k_x x' + k_y y'\right)\right] F(k_x, k_y) \cdot \exp(-i\,kf) \exp\left[i\,\frac{f}{2k}(k_x^2 + k_y^2)\right] \cdot \ldots$$
$$\cdot \exp(-i\phi_0) \exp\left[i\,\frac{k}{2f}(x'^2 + y'^2)\right] \cdot \frac{\exp(-i\,kf)}{i\lambda f} \exp\left\{-i\,\frac{k}{2f}\left[(x - x')^2 + (y - y')^2\right]\right\} \tag{C.15}$$

where the exponents with x' can be grouped as (identical for y')

$$\exp\left[-ik_x x' + i\frac{kx'^2}{2f} - i\,\frac{k(x - x')^2}{2f}\right] = \exp\left[-i\frac{k}{2f}x^2 + ix'\left(k_x - \frac{kx}{f}\right)\right] \tag{C.16}$$

Using the property of the delta function and $k = 2\pi/\lambda$

$$\int_{-\infty}^{\infty} dx' \exp\left[ix'\left(k_x - \frac{kx}{f}\right)\right] = 2\pi\,\delta\left(k_x - \frac{2\pi x}{\lambda f}\right) \tag{C.17}$$

expression Eq. C.15 simplifies to

$$g(x,y) = \frac{\exp[-i(2kf + \phi_0)]}{i\lambda f} \int_{\mathbb{R}^2} d^2k\ \delta\left(k_x - \frac{2\pi x}{\lambda f}\right) \delta\left(k_y - \frac{2\pi y}{\lambda f}\right) \cdot \ldots$$
$$\cdot F(k_x, k_y) \exp\left[i\,\frac{f}{2k}(k_x^2 + k_y^2)\right] \exp\left[-i\,\frac{k}{2f}(x^2 + y^2)\right] \tag{C.18}$$

$$g(x,y) = h_0\, F\left(\frac{2\pi x}{\lambda f}, \frac{2\pi y}{\lambda f}\right) \qquad\qquad h_0 = \frac{\exp[-i(2kf + \phi_0)]}{i\lambda f} \tag{C.19}$$

Interestingly the action of the two delta functions cancels the two exponential terms in the integral, stemming from the two propagation terms $z = f$. This leaves the neat simple Fourier transformation of the input field $F(\frac{2\pi x}{\lambda f}, \frac{2\pi y}{\lambda f})$, matching with result for the far field limit in Eq. C.12.

Appendix D

Additional graphs for line pumps

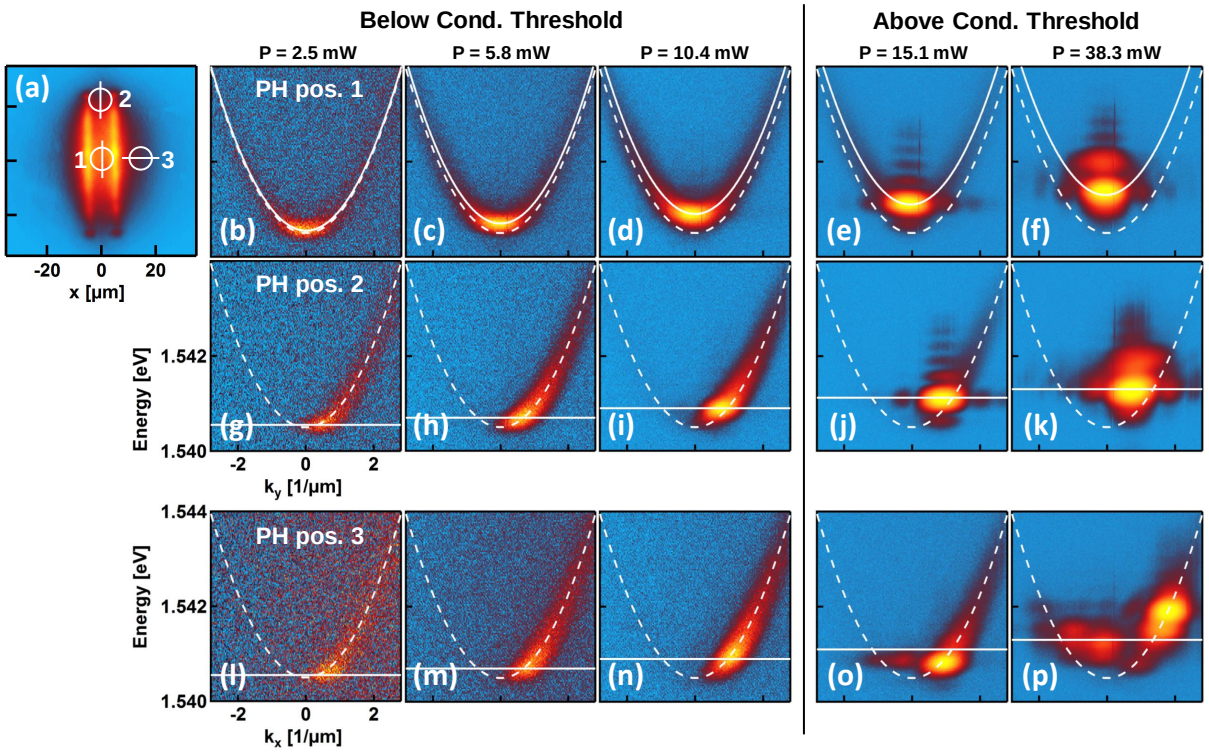

Figure D.1: Flow analysis for a dual line pump below and above condensation threshold. (a) A $\varnothing = 8$ μm pinhole in a real space plane of the detection setup allows to spatially resolve the PL emission as a function of pump power P and energy E in positions 1,2,3. The plots show the blueshifted disperion curve in k_y direction at the centre (b-f) and at the edge (g-k) of the forming condensate. The condensate has clearly the same energy in both positions, as symbolised by the solid blueshifted parabola and line. There is no change in k-vector and the blueshift is linear, as shown by the equidistant solid lines in (g-k). There is only little blueshift with increasing power, and hence also a small change in momentum. Dashed parabolas are the same everywhere, $m^* = 5.4 \cdot 10^{-34}$ kg and apex at $E_0 = 1.5405$ eV.

D. ADDITIONAL GRAPHS FOR LINE PUMPS

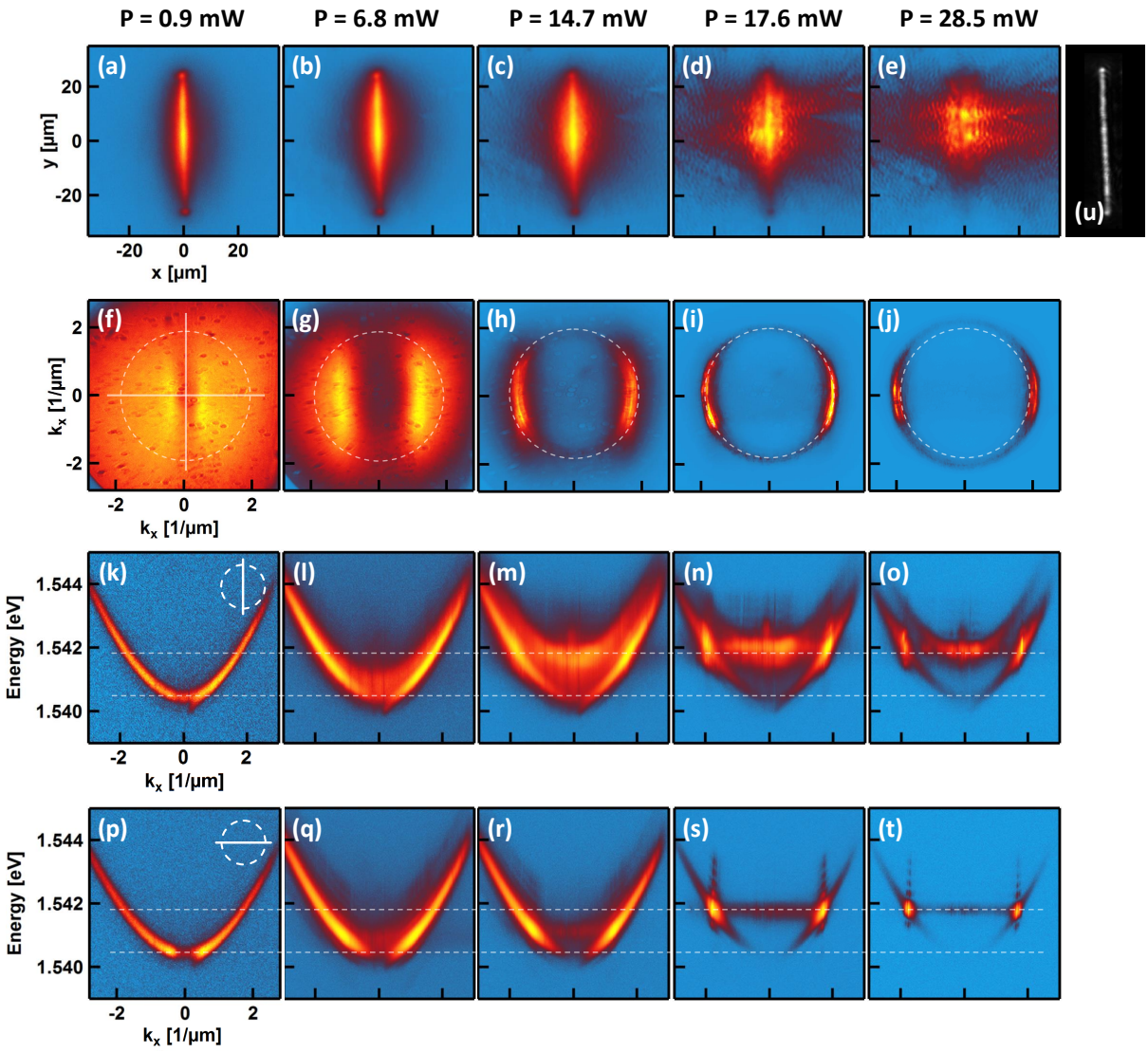

Figure D.2: Power dependence of the PL emission from a single line pump (u) in real space (a-e) and in k-space (f-j). (p-o) Energy-resolved cuts in logarithmic scale in form of dispersion curves along the k_x-axis (k-o) and k_y axis (p-t). The symbol in the top right corner of (k,p) marks the cut direction.

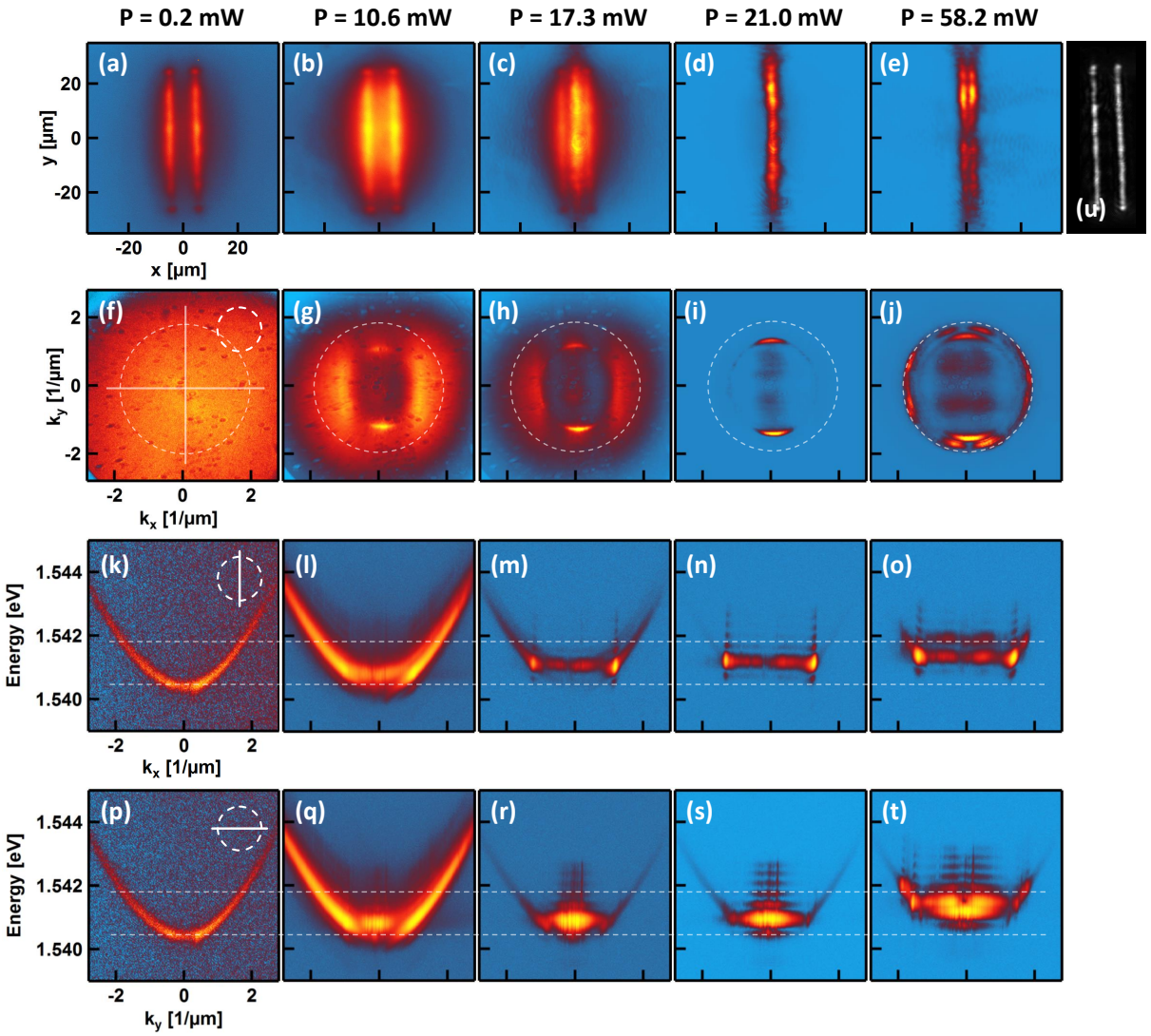

Figure D.3: Power dependence of the PL emission from two parallel pump lines (u) in real space (a-e) and in k-space (f-j). (p-o) Energy-resolved cuts in logarithmic scale in form of dispersion curves along the k_x-axis (k-o) and k_y axis (p-t). The symbol in the top right corner of (k,p) marks the cut direction.

D. ADDITIONAL GRAPHS FOR LINE PUMPS

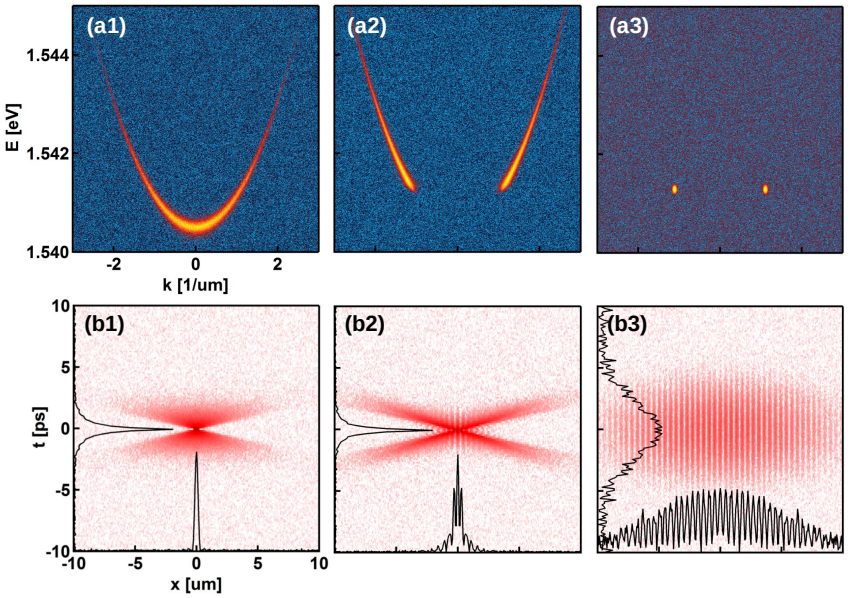

Figure D.4: Simulation of the coherence function $g^{(1)}(\Delta x, t)$ (b1-b3) obtained from Fourier transformation of the dispersion curve (a1-a3). Different occupations of polariton states are investigated: thermalised distribution with $k_{\mathrm{B}}T = 2$ meV (a1), truncated thermal distribution (a2) and condensed distribution with $\sigma_E = 60$ μeV and $\sigma_k = 0.04/\mu$m (a3).

Nomenclature

CONSTANTS

ε_0	dielectric constant of vacuum, $\varepsilon_0 = 8.854 \cdot 10^{-12}$ A·s/V·m
c	speed of light in vacuum, $c = 2.998 \cdot 10^{8}$ m/s
e	electron charge, $e = 1.602 \cdot 10^{-19}$ C
$h, \hbar$	Planck's constant $h = 6.626 \cdot 10^{-34}$ J·s and the reduced version $\hbar = \frac{h}{2\pi}$
i	imaginary unit, $i^2 = -1$
k_B	Boltzmann constant, $k_B = 1.381 \cdot 10^{-23}$ J/K
m_e	electron mass, $m_e = 9.109 \cdot 10^{-31}$ kg

GREEK SYMBOLS

δ_c	detuning of the cavity mode with respect to the exciton line [meV]
γ_o	over-tensing parameter, controls whether phase pattern is optimised for high efficiency or high laser image quality
$\hbar\gamma_\mathsf{x}, \hbar\gamma_\mathsf{c}$	exciton and photon linewidth [meV]
$\hbar\Omega_\mathrm{R}$	full vacuum Rabi splitting [meV]
λ_dB	matter wavelength [μm]
λ_0, λ	wavelength of light in vacuum [nm] and in a medium, $\lambda = n\lambda_0$
λ_c	microcavity design/resonance wavelength [nm]
λ_l	pump laser wavelenght [nm]
μ	chemical potential [meV]
ν_x, ν_y	spatial frequency [1/m] or [lines/mm]
ϕ_0	additional phase shift [rad]
ϕ_{mn}	phaseshift imposed by the SLM for pixel with coordinates (m,n), 65536 values in the range [0,1] (16bit addressing)
$\phi(\vec{x})$	phase of the complex order paramenter $\Psi(\vec{x})$ [rad]
$\Psi(\vec{x})$	order parameter, condensate wavefunction, $\Psi(\vec{x}) = N\,\psi(\vec{x}) = \sqrt{\rho(\vec{x})}\,\exp[i\phi(\vec{x})]$

NOMENCLATURE

$\psi(\vec{x})$	complex probability amplitude of single particle wavefunction [$1/\mu$m]
$\rho(\vec{x})$	probability density [$1/\mu\text{m}^2$], $\rho(\vec{x}) = \Psi^*(\vec{x})\Psi(\vec{x})$
$\tau_{\mathsf{x}}, \tau_{\mathsf{c}}$	exciton and photon lifetime [ps]
θ_i, θ_m	angle of incident/diffracted light with respect to optical axis [rad]
ε	dielectric constant of a medium, $\varepsilon = n^2\varepsilon_0$
ξ	healing length of the condensate [μm]

ROMAN SYMBOLS

$\hbar g$	polariton-polariton interaction constant [meV$\cdot\mu m^2$]
$\hbar J$	tunnelling splitting [meV]
$\hbar R$	exciton reservoir relaxation rate [meV$\cdot\mu$m^2]
$\vec{\text{J}}(\vec{x})$	quantum current density [$1/(\text{kg}\cdot\mu\text{m}^3)$]
$\vec{j}(\vec{x})$	matter flux $\vec{j}(\vec{x}) = \frac{\hbar}{m}\rho(\vec{x})\vec{\nabla}\phi(\vec{x})$, [$1/(\mu\text{m}\cdot\text{ps})$]
A	area on the sample [μm^2]
a	SLM pixel pitch and pixel size [μm]
a_0	s-wave scattering length [μm]
a_{x}	exciton Bohr radius [nm]
c_s	sound velocity in the superfluid [μm/ps]
D	in-plane diffusion constant [μm^2/s]
D	static dipole moment [C·m]
d	diametrical distance of pumping spots in optical trap [μm]
d_g	distance of grooves on diffraction grating [μm] of [px]
E_{BS}	blueshift potential [meV]
F	electric field [V/μm]
f	lens focal length [mm]
g, g_x, g_y, g_r	grating constants of SLM patterns [px]
k	wave vector $k = \pm\sqrt{k_x^2 + k_y^2 + k_z^2} = \pm\, 2\pi/\lambda$ im [$1/\mu m$]

$k_{\parallel}, k_{\perp}$	in-plane and perpendicular momentum component of the photon or polariton
L_{eff}	effective length of a microcavity [nm]
L_B	tunnelling barrier thickness [nm]
m	diffraction order
m^*, m_{c}^*	effective mass of the polariton or cavity photon [kg]
N	integer number, e.g. number of pixels of SLM in x direction
n	refractive index of a medium
P	pump laser power [mW]
Q	microcavity quality factor
r	radial coordinate [m]
r_0	radius of pump laser beam before SLM [mm]
r_{SR}	radius of the signal region for MRAF-IFTA calculation [px]
S	full anticrossing with between dipolariton modes LP and UP at resonance
s	polariton spin [$\hbar$]
S_0, S_1, S_2, S_3	Stokes parameters
U	bias voltage [V]
v	polariton flow speed
x, y, z	space coordinates in [μm]
F	free energy $E - \mu N$ [meV]
g_i	degeneracy of single particle state i
m	tuning parameter for MRAF, algorithm trades off efficiency for laser image quality, m $\in (0, 1]$
n_i	mean occupation number of single particle state i

ACRONYMS

DX, IX	direct or indirect polariton
LP, MP, UP	lower, middle or upper polariton branch
AM, PM, CM	amplitude, phase or complex modulation of phase

NOMENCLATURE

BE, BEC	Bose-Einstein (condensate)
BS	beam splitter
CCD	charge coupled device
CGH, DOE	computer generated hologram, diffractive optical element
CW	continuous wave
DBR	distributed Bragg reflector
FT, IFT	(inverse) Fourier transformation
FWHM	full width at half maximum
GS	Gerchberg-Saxton [SLM algorithm]
IFTA	iterative Fourier transformation algorithm
KE	kinetic energy
LC, LCOS	liquid crystal (on silicon)
MBE	molecular beam epitaxy
MF	merit function
MO	microscope objective
MRAF	mixed region amplitude freedom [SLM algotithm]
NA	numerical aperture of microscope objective
NC	non-condensed
NR, SR	noise or signal region
PH	pinhole
PL	photoluminescence
QP	quantum pressure
QW, RQW	(right) quantum well
SLM	spatial light modulator
WG	waveguided
WP	waveplate

References

[1] B. Deveaud-Plédran. On the condensation of polaritons. *Journal of the Optical Society of America B: Optical Physics*. **29** 2 (2012) pp. A138–A145. doi:10.1364/JOSAB.29.00A138.
URL http://josab.osa.org/abstract.cfm?URI=josab-29-2-A138 2, 20, 25, 29, 31, 33

[2] M. Skolnick, R. Stevenson, A. Tartakovskii, R. Butt, M. Emam-Ismail, D. Whittaker, P. Savvidis, J. Baumberg, A. Lemaître, V. Astratov and J. Roberts. Polariton-polariton interactions and stimulated scattering in semiconductor microcavities. *Materials Science and Engineering: C*. **19** 12 (2002) pp. 407 – 416. doi:http://dx.doi.org/10.1016/S0928-4931(01)00433-7.
URL http://www.sciencedirect.com/science/article/pii/S0928493101004337 5

[3] C. Ciuti, P. Schwendimann and A. Quattropani. Theory of polariton parametric interactions in semiconductor microcavities. *Semiconductor Science and Technology*. **18** 10 (2003) pp. 279–293. doi:10.1088/0268-1242/18/10/301.
URL http://iopscience.iop.org/0268-1242/18/10/301 5, 13, 15, 37, 155

[4] P. G. Savvidis, J. J. Baumberg, R. Stevenson, M. S. Skolnick, D. M. Whittaker and J. S. Roberts. Angle-resonant stimulated polariton amplifier. *Physical review letters*. **84** 7 (2000) pp. 1547–50.
URL http://www.ncbi.nlm.nih.gov/pubmed/11017564 5, 20, 155, 156

[5] F. Tassone and P. Schwendimann. Bottleneck effects in the relaxation and photoluminescence of microcavity polaritons. *Physical Review B*. **56** 12 (1997) pp. 7554–7563. doi:10.1103/PhysRevB.56.7554.
URL http://link.aps.org/doi/10.1103/PhysRevB.56.7554 5, 20, 31, 156

[6] G. Cassabois, A. L. C. Triques, F. Bogani, C. Delalande and C. Piermarocchi. Polariton - acoustic-phonon interaction in a semiconductor microcavity. *Physical Review B*. **61** 3 (2000) pp. 1696–1699. doi:10.1103/PhysRevB.61.1696.
URL http://link.aps.org/doi/10.1103/PhysRevB.61.1696 5

[7] A. Amo, J. Lefrère, S. Pigeon, C. Adrados, C. Ciuti, I. Carusotto, R. Houdré, E. Giacobino and A. Bramati. Superfluidity of polaritons in semiconductor microcavities. *Nature Physics*. **5** 11 (2009) pp. 805–810. doi:10.1038/nphys1364.
URL http://www.nature.com/doifinder/10.1038/nphys1364 5, 9, 22, 29, 30, 35

[8] P. Cristofolini, G. Christmann, S. I. Tsintzos, G. Deligeorgis, G. Konstantinidis, Z. Hatzopoulos, P. G. Savvidis and J. J. Baumberg. Coupling quantum tunneling with cavity photons. *Science*. **336** 6082 (2012) pp. 704–707. doi:10.1126/science.1219010.
URL http://dx.doi.org/10.1126/science.1219010 5, 9, 24, 136

[9] S. I. Tsintzos, N. T. Pelekanos, G. Konstantinidis, Z. Hatzopoulos and P. G. Savvidis. A GaAs polariton light-emitting diode operating near room temperature.. *Nature*. **453** 7193 (2008) pp. 372–375. doi:10.1038/nature06979.
URL http://dx.doi.org/10.1038/nature06979 5, 21, 24, 145, 147

[10] T. A. Fisher, A. M. Afshar, M. S. Skolnick, D. M. Whittaker and J. S. Roberts. Vacuum rabi coupling enhancement and zeeman splitting in semiconductor quantum microcavity structures in a high magnetic field. *Phys. Rev. B*. **53** (1996) pp. R10469–R10472. doi:10.1103/PhysRevB.53.R10469.
URL http://link.aps.org/doi/10.1103/PhysRevB.53.R10469 5

[11] J. D. Berger, O. Lyngnes, H. M. Gibbs, G. Khitrova, T. R. Nelson, E. K. Lindmark, A. V. Kavokin, M. A. Kaliteevski and V. V. Zapasskii. Magnetic-field enhancement of the exciton-polariton splitting in a semiconductor quantum-well microcavity: The strong coupling threshold. *Phys. Rev. B*. **54** (1996) pp. 1975–1981. doi:10.1103/PhysRevB.54.1975.
URL http://link.aps.org/doi/10.1103/PhysRevB.54.1975 5

REFERENCES

[12] V. Savona. Quantum well excitons in semiconductor microcavities: Unified treatment of weak and strong coupling regimes. *Solid State Communications*. **93** 9 (1995) pp. 733–739. doi:10.1016/0038-1098(94)00865-5.
URL http://linkinghub.elsevier.com/retrieve/pii/0038109894008655 7, 19

[13] G. Khitrova, H. M. Gibbs, M. Kira, S. W. Koch and A. Scherer. Vacuum rabi splitting in semiconductors. *Nature Physics*. **2** 2 (2006) pp. 81–90. doi:10.1038/nphys227.
URL http://www.nature.com/doifinder/10.1038/nphys227 7, 19

[14] J. Jacobson, S. Pau, H. Cao, G. Björk and Y. Yamamoto. Observation of exciton-polariton oscillating emission in a single-quantum-well semiconductor microcavity. *Physical Review A*. **51** 3 (1995) pp. 2542–2544. doi:10.1103/PhysRevA.51.2542.
URL http://link.aps.org/doi/10.1103/PhysRevA.51.2542 7

[15] V. Savona. The Physics of Semiconductor Microcavities - Chapter: Fifteen years of microcavity polaritons, Wiley2007. doi:10.1002/9783527610150.ch1.
URL http://dx.doi.org/10.1002/9783527610150.ch1 7

[16] J. Kasprzak, M. Richard, S. Kundermann, A. Baas, P. Jeambrun, J. M. J. Keeling, F. M. Marchetti, M. H. Szymańska, R. André, J. L. Staehli, V. Savona, P. B. Littlewood, B. Deveaud-Plédran and L. S. Dang. Bose-einstein condensation of exciton polaritons. *Nature*. **443** 7110 (2006) pp. 409–14. doi:10.1038/nature05131.
URL http://dx.doi.org/10.1038/nature05131 9, 20, 21, 29

[17] R. Balili, V. Hartwell, D. Snoke, L. Pfeiffer and K. West. Bose-einstein condensation of microcavity polaritons in a trap. *Science*. **316** 5827 (2007) pp. 1007–1010. doi:10.1126/science.1140990. http://www.sciencemag.org/content/316/5827/1007.full.pdf.
URL http://www.sciencemag.org/content/316/5827/1007.abstract 9, 24, 29, 39

[18] E. Cerda-Méndez, D. N. Krizhanovskii, M. Wouters, R. A. Bradley, K. Biermann, K. Guda, R. Hey, P. V. Santos, D. Sarkar and M. S. Skolnick. Polariton condensation in dynamic acoustic lattices. *Physical Review Letters*. **105** 11 (2010) pp. 1–4. doi:10.1103/PhysRevLett.105.116402.
URL http://link.aps.org/doi/10.1103/PhysRevLett.105.116402 9, 24, 39

[19] A. Amo, D. Sanvitto, F. P. Laussy, D. Ballarini, E. del Valle, M. D. Martin, A. Lemaître, J. Bloch, D. N. Krizhanovskii, M. S. Skolnick, C. Tejedor and L. Viña. Collective fluid dynamics of a polariton condensate in a semiconductor microcavity. *Nature*. **457** 7227 (2009) pp. 291–5. doi:10.1038/nature07640.
URL http://dx.doi.org/10.1038/nature07640 9, 35, 38

[20] E. Wertz, L. Ferrier, D. D. Solnyshkov, R. Johne, D. Sanvitto, a. Lemaître, I. Sagnes, R. Grousson, a. V. Kavokin, P. Senellart, G. Malpuech and J. Bloch. Spontaneous formation and optical manipulation of extended polariton condensates. *Nature Physics*. **6** 11 (2010) pp. 860–864. doi:10.1038/nphys1750.
URL http://www.nature.com/doifinder/10.1038/nphys1750 9, 29, 30, 37, 38, 39, 93, 110, 126

[21] P. Bhattacharya, T. Frost, S. Deshpande, M. Z. Baten, A. Hazari and A. Das. Room temperature electrically injected polariton laser. *Physical Review Letters*. **112** (2014) p. 236802. doi:10.1103/PhysRevLett.112.236802.
URL http://link.aps.org/doi/10.1103/PhysRevLett.112.236802 9, 21, 24, 167

[22] P. Savvidis. Optoelectronics: A practical polariton laser. *Nat Photon*. **8** 8 (2014) pp. 588–589. doi:10.1038/nphoton.2014.176.
URL http://dx.doi.org/10.1038/nphoton.2014.176 9, 21, 24, 33

[23] K. G. Lagoudakis, M. Wouters, M. Richard, A. Baas, I. Carusotto, R. André, L. S. Dang and B. Deveaud-Plédran. Quantized vortices in an exciton-polariton condensate. *Nature Physics*. **4** 9 (2008) pp. 706–710. doi:10.1038/nphys1051.
URL http://www.nature.com/doifinder/10.1038/nphys1051 9, 35

[24] D. Sanvitto, F. M. Marchetti, M. H. Szymańska, G. Tosi, M. Baudisch, F. P. Laussy, D. N. Krizhanovskii, M. S. Skolnick, L. Marrucci, A. Lemaître, J. Bloch, C. Tejedor and L. Viña. Persistent currents and quantized vortices in a polariton superfluid. *Nature Physics*. **6** July (2010) pp. 527–533. doi:10.1038/nphys1668.
URL http://www.nature.com/doifinder/10.1038/nphys1668 9, 22, 35

[25] A. Amo, S. Pigeon, D. Sanvitto, V. G. Sala, R. Hivet, I. Carusotto, F. Pisanello, G. Lemnager, R. Houdr, E. Giacobino, C. Ciuti and A. Bramati. Polariton superfluids reveal quantum hydrodynamic solitons. *Science*. **332** 6034 (2011) pp. 1167–1170. doi:10.1126/science.1202307. http://www.sciencemag.org/content/332/6034/1167.full.pdf.
URL http://www.sciencemag.org/content/332/6034/1167.abstract 9

[26] F. Jahnke, M. Kira and S. Koch. Linear and nonlinear optical properties of excitons in semiconductor quantum wells and microcavities. *Zeitschrift für Physik B Condensed Matter*. **104** 3 (1997) pp. 559–572. doi:10.1007/s002570050490.
URL http://dx.doi.org/10.1007/s002570050490 10

[27] A. K. Cousins and S. C. Gottschalk. Application of the impedance formalism to diffraction gratings with multiple coating layers. *Applied Optics*. **29** 28 (1990) pp. 4268–4271. doi:10.1364/AO.29.004268.
URL http://ao.osa.org/abstract.cfm?URI=ao-29-28-4268 10

[28] G. Panzarini, L. C. Andreani, A. Armitage, D. Baxter, M. S. Skolnick, V. N. Astratov, J. S. Roberts, A. V. Kavokin, M. R. Vladimirova and M. A. Kaliteevski. Exciton-light coupling in single and coupled semiconductor microcavities: Polariton dispersion and polarization splitting. *Physical Review B*. **59** 7 (1999) pp. 5082–5089. doi:10.1103/PhysRevB.59.5082.
URL http://link.aps.org/doi/10.1103/PhysRevB.59.5082 11, 13, 15, 143, 155

[29] R. Houdré, C. Weisbuch, R. Stanley, U. Oesterle, P. Pellandini and M. Ilegems. Measurement of cavity-polariton dispersion curve from angle-resolved photoluminescence experiments. *Physical Review Letters*. **73** 15 (1994) pp. 2043–2046. doi:10.1103/PhysRevLett.73.2043.
URL http://link.aps.org/doi/10.1103/PhysRevLett.73.2043 11, 15

[30] J. C. Maan, G. Belle, A. Fasolino, M. Altarelli and K. Ploog. Magneto-optical determination of exciton binding energy in GaAs-$Ga_{1-x}Al_xAs$ quantum wells. *Phys. Rev. B*. **30** (1984) pp. 2253–2256. doi:10.1103/PhysRevB.30.2253.
URL http://link.aps.org/doi/10.1103/PhysRevB.30.2253 12

[31] L. C. Andreani and A. Pasquarello. Accurate theory of excitons in GaAs-$Ga_{1-x}Al_xAs$ quantum wells. *Phys. Rev. B*. **42** (1990) pp. 8928–8938. doi:10.1103/PhysRevB.42.8928.
URL http://link.aps.org/doi/10.1103/PhysRevB.42.8928 14

[32] H. Deng, H. H. and Y. Yamamoto. Exciton-polariton bose-einstein condensation. *Reviews of Modern Physics*. **82** 2 (2010) pp. 1489–1537. doi:10.1103/RevModPhys.82.1489.
URL http://link.aps.org/doi/10.1103/RevModPhys.82.1489 15, 18, 20, 28, 29, 30, 68

[33] B. Sermage, S. Long, I. Abram and J. Y. Marzin. Time-resolved spontaneous emission of excitons in a microcavity: Behavior of the individual exciton-photon mixed states. *Physical Review B*. **53** 24 (1996) pp. 16516–16523. doi:10.1103/PhysRevB.53.16516.
URL http://link.aps.org/doi/10.1103/PhysRevB.53.16516 17

[34] J. J. Baumberg, P. G. Savvidis, R. M. Stevenson, A. I. Tartakovskii, M. S. Skolnick, D. M. Whittaker and J. S. Roberts. Parametric oscillation in a vertical microcavity: A polariton condensate or micro-optical parametric oscillation. *Phys. Rev. B*. **62** (2000) pp. R16247–R16250. doi:10.1103/PhysRevB.62.R16247.
URL http://link.aps.org/doi/10.1103/PhysRevB.62.R16247 20, 155

[35] H. Deng, G. Weihs, D. Snoke, J. Bloch and Y. Yamamoto. Polariton lasing vs. photon lasing in a semiconductor microcavity. *Proceedings of the National Academy of Sciences of the United States of America*. **100** 26 (2003) pp.

15318–23. doi:10.1073/pnas.2634328100.
URL http://www.pnas.org/content/100/26/15318.abstract 20, 31

[36] A. Vinattieri, J. Shah, T. C. Damen, D. S. Kim, L. N. Pfeiffer, M. Z. Maialle and L. J. Sham. Exciton dynamics in GaAs quantum wells under resonant excitation. *Phys. Rev. B*. **50** (1994) pp. 10868–10879. doi:10.1103/PhysRevB.50.10868.
URL http://link.aps.org/doi/10.1103/PhysRevB.50.10868 21

[37] D. Bajoni, E. Semenova, A. Lemaître, S. Bouchoule, E. Wertz, P. Senellart and J. Bloch. Polariton light-emitting diode in a GaAs-based microcavity. *Phys. Rev. B*. **77** (2008) p. 113303. doi:10.1103/PhysRevB.77.113303.
URL http://link.aps.org/doi/10.1103/PhysRevB.77.113303 21, 23, 24, 145

[38] R. Houdré, R. P. Stanley and M. Ilegems. Vacuum-field rabi splitting in the presence of inhomogeneous broadening: Resolution of a homogeneous linewidth in an inhomogeneously broadened system. *Physical Review A*. **53** 4 (1996) pp. 2711–2715. doi:10.1103/PhysRevA.53.2711.
URL http://link.aps.org/doi/10.1103/PhysRevA.53.2711 21

[39] R. P. Stanley, R. Houdré, C. Weisbuch, U. Oesterle and M. Ilegems. Cavity-polariton photoluminescence in semiconductor microcavities: Experimental evidence.. *Physical review. B, Condensed matter*. **53** 16 (1996) pp. 10995–11007.
URL http://www.ncbi.nlm.nih.gov/pubmed/9982672 21

[40] G. Christmann, A. Askitopoulos, G. Deligeorgis, Z. Hatzopoulos, S. I. Tsintzos, P. G. Savvidis and J. J. Baumberg. Oriented polaritons in strongly-coupled asymmetric double quantum well microcavities. *Applied Physics Letters*. **98** 8 (2011) p. 081111. doi:10.1063/1.3559909.
URL http://link.aip.org/link/APPLAB/v98/i8/p081111/s1&Agg=doi 22, 151, 155, 161

[41] G. Christmann, C. Coulson, J. J. Baumberg, N. T. Pelekanos, Z. Hatzopoulos, S. I. Tsintzos and P. G. Savvidis. Control of polariton scattering in resonant-tunneling double-quantum-well semiconductor microcavities. *Physical Review B*. **82** 11 (2010) pp. 2–5. doi:10.1103/PhysRevB.82.113308.
URL http://link.aps.org/doi/10.1103/PhysRevB.82.113308 22, 153, 155, 161

[42] M. Assmann, J.-S. Tempel, F. Veit, M. Bayer, A. Rahimi-Iman, A. Lffler, S. Hfling, S. Reitzenstein, L. Worschech and A. Forchel. From polariton condensates to highly photonic quantum degenerate states of bosonic matter. *Proceedings of the National Academy of Sciences*. **108** 5 (2011) pp. 1804–1809. doi:10.1073/pnas.1009847108. http://www.pnas.org/content/108/5/1804.full.pdf+html.
URL http://www.pnas.org/content/108/5/1804.abstract 22, 33

[43] A. Dreismann, P. Cristofolini, R. Balili, G. Christmann, F. Pinsker, N. G. Berloff, Z. Hatzopoulos, P. G. Savvidis and J. J. Baumberg. Coupled counterrotating polariton condensates in optically defined annular potentials. *Proceedings of the National Academy of Sciences*. **111** 24 (2014) pp. 8770–8775. doi:10.1073/pnas.1401988111. http://www.pnas.org/content/111/24/8770.full.pdf+html.
URL http://www.pnas.org/content/111/24/8770.abstract 22, 38, 82, 165

[44] G. Tosi, G. Christmann, N. G. Berloff, P. Tsotsis, T. Gao, Z. Hatzopoulos, P. G. Savvidis and J. J. Baumberg. Sculpting oscillators with light within a nonlinear quantum fluid. *Nat Phys*. **8** 3 (2012) pp. 190–194. doi:10.1038/nphys2182.
URL http://dx.doi.org/10.1038/NPHYS2182 22, 23, 29, 30, 31, 92, 94, 95, 96, 97, 110

[45] I. Carusotto and C. Ciuti. Quantum fluids of light. *Rev. Mod. Phys.*. **85** (2013) pp. 299–366. doi:10.1103/RevModPhys.85.299.
URL http://link.aps.org/doi/10.1103/RevModPhys.85.299 22, 49, 51, 52, 53

[46] N. Takemura, S. Trebaol, M. Wouters, M. T. Portella-Oberli and B. Deveaud. Polaritonic feshbach resonance. *Nat Phys*. **10** 7 (2014) pp. 500–504. doi:10.1038/nphys2999.
URL http://dx.doi.org/10.1038/nphys2999 24, 50

[47] N. Y. Kim, K. Kusudo, C. Wu, N. Masumoto, A. Löffler, S. Höfling, N. Kumada, L. Worschech, A. Forchel and Y. Yamamoto. Dynamical d-wave condensation of exciton-polaritons in a two-dimensional square-lattice potential. *Nat Phys*. **7** 9 (2012) pp. 681 – 686. doi:10.1038/nphys2012.
URL http://dx.doi.org/10.1038/nphys2012 24, 39

[48] B. Zhang, Z. Wang, S. Brodbeck, C. Schneider, M. Kamp, S. Hofling and H. Deng. Zero-dimensional polariton laser in a subwavelength grating-based vertical microcavity. *Light Sci Appl*. **3** (2014) p. e135. doi:10.1038/lsa.2014.16.
URL http://dx.doi.org/10.1038/lsa.2014.16 24, 38, 39

[49] D. Bajoni, P. Senellart, A. Lemaître and J. Bloch. Photon lasing in GaAs microcavity: Similarities with a polariton condensate. *Phys. Rev. B*. **76** (2007) p. 201305. doi:10.1103/PhysRevB.76.201305.
URL http://link.aps.org/doi/10.1103/PhysRevB.76.201305 24, 29, 32, 38

[50] A. Armitage, T. A. Fisher, M. S. Skolnick, D. M. Whittaker, P. Kinsler and J. S. Roberts. Exciton polaritons in semiconductor quantum microcavities in a high magnetic field. *Phys. Rev. B*. **55** (1997) pp. 16395–16403. doi:10.1103/PhysRevB.55.16395.
URL http://link.aps.org/doi/10.1103/PhysRevB.55.16395 24

[51] F. J. Duarte. Tunable laser applications, CRC, New York 2009. 25

[52] K. Sugioka and Y. Cheng. Ultrafast lasers – reliable tools for advanced materials processing. *Light Sci Appl*. **3** (2013) p. 143. doi:10.1038/lsa.2014.30.
URL http://dx.doi.org/10.1038/lsa.2014.30 25

[53] A. Einstein. Albert Einstein: Akademie-Vorträge. chapter Quantentheorie des einatomigen idealen Gases, pp. 237–244, Wiley-VCH Verlag GmbH & Co. KGaA2006. ISBN 9783527608959. doi:10.1002/3527608958.ch27.
URL http://dx.doi.org/10.1002/3527608958.ch27 26, 28

[54] K. Bongs and K. Sengstock. Physics with coherent matter waves. *Reports on Progress in Physics*. **67** 6 (2004) p. 907.
URL http://stacks.iop.org/0034-4885/67/i=6/a=R03 26

[55] F. London. The λ-phenomenon of liquid helium and bose-einstein degeneracy. *Nature*. **141** (1938) pp. 643–644 & 913. 28

[56] K. B. Davis, M. O. Mewes, M. R. Andrews, N. J. van Druten, D. S. Durfee, D. M. Kurn and W. Ketterle. Bose-einstein condensation in a gas of sodium atoms. *Physical Review Letters*. **75** (1995) pp. 3969–3973. doi:10.1103/PhysRevLett.75.3969.
URL http://link.aps.org/doi/10.1103/PhysRevLett.75.3969 28

[57] M. H. Anderson, J. R. Ensher, M. R. Matthews, C. E. Wieman and E. A. Cornell. Observation of bose-einstein condensation in a dilute atomic vapor. *Science*. **269** 5221 (1995) pp. 198–201. doi:10.1126/science.269.5221.198. http://www.sciencemag.org/content/269/5221/198.full.pdf.
URL http://www.sciencemag.org/content/269/5221/198.abstract 28

[58] H. Stolz, R. Schwartz, F. Kieseling, S. Som, M. Kaupsch, S. Sobkowiak, D. S., N. Naka, T. Koch and H. Fehske. Condensation of excitons in Cu_2O at ultracold temperatures: experiment and theory. *New Journal of Physics*. **14** 10 (2012) p. 105007.
URL http://stacks.iop.org/1367-2630/14/i=10/a=105007 28

[59] L. V. Butov, A. Zrenner, G. Abstreiter, G. Böhm and G. Weimann. Condensation of indirect excitons in coupled AlAs/GaAs quantum wells. *Physical Review Letters*. **73** 2 (1994) pp. 304–307. doi:10.1103/PhysRevLett.73.304.
URL http://link.aps.org/doi/10.1103/PhysRevLett.73.304 28

[60] M. Richard, J. Kasprzak, R. Romestain, R. André and L. S. Dang. Spontaneous coherent phase transition of polaritons in cdte microcavities. *Physical Review Letters*. **94** (2005) p. 187401. doi:10.1103/PhysRevLett.94.187401.
URL http://link.aps.org/doi/10.1103/PhysRevLett.94.187401 29, 37, 55

[61] J. Kasprzak, D. D. Solnyshkov, R. André, L. S. Dang and G. Malpuech. Formation of an exciton polariton condensate: Thermodynamic versus kinetic regimes. *Physical Review Letters*. **101** (2008) p. 146404. doi:10.1103/PhysRevLett.101.146404.
URL http://link.aps.org/doi/10.1103/PhysRevLett.101.146404 29

[62] G. Christmann, R. Butté, E. Feltin, J. F. Carlin and N. Grandjean. Room temperature polariton lasing in a GaN-AlGaN multiple quantum well microcavity. *Applied Physics Letters*. **93** 5 051102. doi:http://dx.doi.org/10.1063/1.2966369.
URL http://scitation.aip.org/content/aip/journal/apl/93/5/10.1063/1.2966369 29

[63] J. J. Baumberg, A. V. Kavokin, S. Christopoulos, A. J. D. Grundy, R. Butté, G. Christmann, D. D. Solnyshkov, G. Malpuech, G. Baldassarri Höger von Högersthal, E. Feltin, J.-F. Carlin and N. Grandjean. Spontaneous polarization buildup in a room-temperature polariton laser. *Physical Review Letters*. **101** (2008) p. 136409. doi:10.1103/PhysRevLett.101.136409.
URL http://link.aps.org/doi/10.1103/PhysRevLett.101.136409 29

[64] E. Wertz, L. Ferrier, D. D. Solnyshkov, P. Senellart, D. Bajoni, A. Miard, A. Lemaître, G. Malpuech and J. Bloch. Spontaneous formation of a polariton condensate in a planar GaAs microcavity. *Applied Physics L.* **95** 5 (2009) p. 051108. doi:10.1063/1.3192408.
URL http://dx.doi.org/10.1063/1.3192408 29

[65] H. Deng, G. S. Solomon, R. Hey, K. H. Ploog and Y. Yamamoto. Spatial coherence of a polariton condensate. *Physical Review Letters*. **99** (2007) p. 126403. doi:10.1103/PhysRevLett.99.126403.
URL http://link.aps.org/doi/10.1103/PhysRevLett.99.126403 29

[66] K. S. Daskalakis, S. A. Maier, R. Murray and S. Kèna-Cohen. Nonlinear interactions in an organic polariton condensate. *Mater, Nat*. **13** 3 (2014) pp. 271–278. doi:10.1038/nmat3874.
URL http://dx.doi.org/10.1038/nmat3874 30, 38

[67] J. D. Plumhof, T. Stöferle, L. Mai, U. Scherf and R. F. Mahrt. Room-temperature bose-einstein condensation of cavity exciton-polaritons in a polymer. *Nature Materrials*. **13** 3 (2014) pp. 247–252. doi:10.1038/nmat3825.
URL http://dx.doi.org/10.1038/nmat3825 30

[68] A. P. D. Love, D. N. Krizhanovskii, D. M. Whittaker, R. Bouchekioua, D. Sanvitto, S. A. Rizeiqi, R. Bradley, M. S. Skolnick, P. R. Eastham, R. André and L. S. Dang. Intrinsic decoherence mechanisms in the microcavity polariton condensate. *Physical Review Letters*. **101** (2008) p. 067404. doi:10.1103/PhysRevLett.101.067404.
URL http://link.aps.org/doi/10.1103/PhysRevLett.101.067404 30

[69] T. K. Paraïso, M. Wouters, Y. Léger, F. Morier-Genoud and B. Deveaud-Plédran. Multistability of a coherent spin ensemble in a semiconductor microcavity.. *Nature materials*. **9** 8 (2010) pp. 655–60. doi:10.1038/nmat2787.
URL http://www.ncbi.nlm.nih.gov/pubmed/20601942 30, 160

[70] R. Houdré, J. L. Gibernon, P. Pellandini, R. P. Stanley, U. Oesterle, C. Weisbuch, J. O'Gorman, B. Roycroft and M. Ilegems. Saturation of the strong-coupling regime in a semiconductor microcavity: Free-carrier bleaching of cavity polaritons. *Phys. Rev. B*. **52** (1995) pp. 7810–7813. doi:10.1103/PhysRevB.52.7810.
URL http://link.aps.org/doi/10.1103/PhysRevB.52.7810 30

[71] A. I. Tartakovskii, M. Emam-Ismail, R. M. Stevenson, M. S. Skolnick, V. N. Astratov, D. M. Whittaker, J. J. Baumberg and J. S. Roberts. Relaxation bottleneck and its suppression in semiconductor microcavities. *Phys. Rev. B*. **62** (2000) pp. R2283–R2286. doi:10.1103/PhysRevB.62.R2283.
URL http://link.aps.org/doi/10.1103/PhysRevB.62.R2283 31, 155, 156

[72] T. Lecomte, V. Ardizzone, M. Abbarchi, C. Diederichs, A. Miard, A. Lemaître, I. Sagnes, P. Senellart, J. Bloch, C. Delalande, J. Tignon and P. Roussignol. Optical parametric oscillation in one-dimensional microcavities. *Phys. Rev. B*. **87** (2013) p. 155302. doi:10.1103/PhysRevB.87.155302.
URL http://link.aps.org/doi/10.1103/PhysRevB.87.155302 31

[73] P. Cristofolini, A. Dreismann, G. Christmann, G. Franchetti, N. G. Berloff, P. Tsotsis, Z. Hatzopoulos, P. G. Savvidis and J. J. Baumberg. Optical superfluid phase transitions and trapping of polariton condensates. *Physical Review Letters*. **110** 18 (2013) p. 186403. doi:10.1103/PhysRevLett.110.186403.
URL http://link.aps.org/doi/10.1103/PhysRevLett.110.186403 31, 38, 39, 82, 109

[74] C. Antón, G. Tosi, M. D. Martín, Z. Hatzopoulos, G. Konstantinidis, P. S. Eldridge, P. G. Savvidis, C. Tejedor and L. Viña. Quantum coherence in momentum space of light-matter condensates. *Phys. Rev. B*. **90** (2014) p. 081407. doi:10.1103/PhysRevB.90.081407.
URL http://link.aps.org/doi/10.1103/PhysRevB.90.081407 31, 99

[75] P. R. Eastham. Mode locking and mode competition in a nonequilibrium solid-state condensate. *Phys. Rev. B*. **78** (2008) p. 035319. doi:10.1103/PhysRevB.78.035319.
URL http://link.aps.org/doi/10.1103/PhysRevB.78.035319 31, 56, 57, 58, 59

[76] D. Racine and P. R. Eastham. Quantum theory of multimode polariton condensation. *Phys. Rev. B*. **90** (2014) p. 085308. doi:10.1103/PhysRevB.90.085308.
URL http://link.aps.org/doi/10.1103/PhysRevB.90.085308 31

[77] D. Bajoni, P. Senellart, E. Wertz, I. Sagnes, A. Miard, A. Lemaître and J. Bloch. Polariton laser using single micropillar GaAs-GaAlAs semiconductor cavities. *Physical Review Letters*. **100** (2008) p. 047401. doi:10.1103/PhysRevLett.100.047401.
URL http://link.aps.org/doi/10.1103/PhysRevLett.100.047401 32, 39, 98

[78] P. Cilibrizzi, H. Ohadi, T. Ostatnicky, A. Askitopoulos, W. Langbein and P. Lagoudakis. Linear wave dynamics explains observations attributed to dark solitons in a polariton quantum fluid. *Physical Review Letters*. **113** (2014) p. 103901. doi:10.1103/PhysRevLett.113.103901.
URL http://link.aps.org/doi/10.1103/PhysRevLett.113.103901 33

[79] C. J. Pethick and H. Smith. Bose - Einstein Condensation in Dilute Gases, Cambridge University Press 2008. iSBN: 9780521846516. 35, 44, 45, 47, 49

[80] D. N. Krizhanovskii, D. M. Whittaker, R. A. Bradley, K. Guda, D. Sarkar, D. Sanvitto, L. Viña, E. Cerda, P. V. Santos, K. Biermann, R. Hey and M. S. Skolnick. Effect of interactions on vortices in a nonequilibrium polariton condensate. *Physical Review Letters*. **104** 12 (2010) pp. 1–4. doi:10.1103/PhysRevLett.104.126402.
URL http://link.aps.org/doi/10.1103/PhysRevLett.104.126402 35

[81] K. G. Lagoudakis, T. Ostatnick, A. V. Kavokin, Y. G. Rubo, R. Andr and B. Deveaud-Pldran. Observation of half-quantum vortices in an exciton-polariton condensate. *Science*. **326** 5955 (2009) pp. 974–976. doi:10.1126/science.1177980. http://www.sciencemag.org/content/326/5955/974.full.pdf.
URL http://www.sciencemag.org/content/326/5955/974.abstract 35

[82] D. Ballarini, M. De Giorgi, E. Cancellieri, R. Houdré, E. Giacobino, R. Cingolani, A. Bramati, G. Gigli and D. Sanvitto. All-optical polariton transistor. *Nature Communications*. **4** 1778. doi:10.1038/ncomms2734.
URL http://dx.doi.org/10.1038/ncomms2734 35, 36, 117, 162

REFERENCES

[83] T. Gao, P. S. Eldridge, T. C. H. Liew, S. I. Tsintzos, G. Stavrinidis, G. Deligeorgis, Z. Hatzopoulos and P. G. Savvidis. Polariton condensate transistor switch. *Phys. Rev. B*. **85** (2012) p. 235102. doi:10.1103/PhysRevB.85.235102.
URL http://link.aps.org/doi/10.1103/PhysRevB.85.235102 35, 36, 38, 39, 40, 162

[84] V. D. Kulakovskii, A. I. Tartakovskii, D. N. Krizhanovskii, N. A. Gippius, M. S. Skolnick and J. S. Roberts. Nonlinear effects in a dense two-dimensional exciton-polariton system in semiconductor microcavities. *Nanotechnology*. **12** 4 (2001) p. 475.
URL http://stacks.iop.org/0957-4484/12/i=4/a=319 37

[85] S. Zaitsev, V. Kulakovskii, A. Maksimov, D. Pronin, I. Tartakovskii, N. Gippius, M. Litz, F. Fisher, A. Waag, D. Yakovlev, W. Ossau and G. Landwehr. Giant blue shift of photoluminescence in strongly excited type-ii znse/bete superlattices. *Journal of Experimental and Theoretical Physics Letters*. **66** 5 (1997) pp. 376–381. doi:10.1134/1.567525.
URL http://dx.doi.org/10.1134/1.567525 37

[86] S. Okumura and T. Ogawa. Boson representation of two-exciton correlations: An exact treatment of composite-particle effects. *Phys. Rev. B*. **65** (2001) p. 035105. doi:10.1103/PhysRevB.65.035105.
URL http://link.aps.org/doi/10.1103/PhysRevB.65.035105 37

[87] G. Christmann, G. Tosi, N. G. Berloff, P. Tsotsis, P. S. Eldridge, Z. Hatzopoulos, P. G. Savvidis and J. J. Baumberg. Polariton ring condensates and sunflower ripples in an expanding quantum liquid. *Phys. Rev. B*. **85** (2012) p. 235303. doi:10.1103/PhysRevB.85.235303.
URL http://link.aps.org/doi/10.1103/PhysRevB.85.235303 37, 38, 55, 92, 93, 94, 123

[88] M. Wouters, I. Carusotto and C. Ciuti. Spatial and spectral shape of inhomogeneous nonequilibrium exciton-polariton condensates. *Phys. Rev. B*. **77** (2008) p. 115340. doi:10.1103/PhysRevB.77.115340.
URL http://link.aps.org/doi/10.1103/PhysRevB.77.115340 37, 54, 55, 56

[89] L. Ferrier, E. Wertz, R. Johne, D. D. Solnyshkov, P. Senellart, I. Sagnes, . Lemaître, G. Malpuech and J. Bloch. Interactions in confined polariton condensates. *Physical Review Letters*. **106** (2011) p. 126401. doi:10.1103/PhysRevLett.106.126401.
URL http://link.aps.org/doi/10.1103/PhysRevLett.106.126401 38, 39

[90] N. Peyghambarian, H. M. Gibbs, J. L. Jewell, A. Antonetti, A. Migus, D. Hulin and A. Mysyrowicz. Blue shift of the exciton resonance due to exciton-exciton interactions in a multiple-quantum-well structure. *Physical Review Letters*. **53** (1984) pp. 2433–2436. doi:10.1103/PhysRevLett.53.2433.
URL http://link.aps.org/doi/10.1103/PhysRevLett.53.2433 38

[91] C. Sturm, D. Tanese, H. Nguyen, H. Flayac, E. Galopin, A. Lemaître, I. Sagnes, D. Solnyshkov, A. Amo, G. Malpuech and J. Bloch. All-optical phase modulation in a cavity-polariton machzehnder interferometer. *Nat Commun*. **5**. doi:10.1038/ncomms4278.
URL http://dx.doi.org/10.1038/ncomms4278 38, 40, 167

[92] E. Cerda-Méndez, D. Krizhanovskii, K. Biermann, K. Guda, R. A. Bradley, R. Hey, P. Santos and M. Skolnick. One dimensional confinement of microcavity polaritons using non-piezoelectric surface acoustic waves. *Physica E: Low-dimensional Systems and Nanostructures*. **42** (2010) pp. 2548–2551. doi:10.1016/j.physe.2010.02.004.
URL http://linkinghub.elsevier.com/retrieve/pii/S1386947710000883 39

[93] Z. Hadzibabic and J. Dalibard. Two-dimensional bose fluids: An atomic physics perspective. *Rivista del Nuovo Cimento*. **34** 389. doi:10.1393/ncr/i2011-10066-3.
URL http://arxiv.org/abs/0912.1490 47, 48

[94] I. S. Aranson and L. Kramer. The world of the complex ginzburg-landau equation. *Rev. Mod. Phys.*. **74** (2002) pp. 99–143. doi:10.1103/RevModPhys.74.99.
URL http://link.aps.org/doi/10.1103/RevModPhys.74.99 48, 51, 111

[95] C. R. Doering, J. D. Gibbon, D. D. Holm and B. Nicolaenko. Low-dimensional behaviour in the complex ginzburg-landau equation. *Nonlinearity*. **1** 2 (1988) p. 279.
URL http://stacks.iop.org/0951-7715/1/i=2/a=001 48, 51

[96] D. S. Petrov, D. M. Gangardt and G. V. Shlyapnikov. Low-dimensional trapped gases. *J. Phys. IV France*. **116** (2004) pp. 5–44. doi:10.1051/jp4:2004116001.
URL http://dx.doi.org/10.1051/jp4:2004116001 50

[97] L. P. Pitaevskii and S. Stringari. Bose Einstein condensation, Clarendon Press, Oxford 2004. 50

[98] M. Wouters and I. Carusotto. Excitations in a nonequilibrium bose-einstein condensate of exciton polaritons. *Physical Review Letters*. **99** (2007) p. 140402. doi:10.1103/PhysRevLett.99.140402.
URL http://link.aps.org/doi/10.1103/PhysRevLett.99.140402 51

[99] H. Ohadi, E. Kammann, T. C. H. Liew, K. G. Lagoudakis, A. V. Kavokin and P. G. Lagoudakis. Spontaneous symmetry breaking in a polariton and photon laser. *Physical Review Letters*. **109** (2012) p. 016404. doi:10.1103/PhysRevLett.109.016404.
URL http://link.aps.org/doi/10.1103/PhysRevLett.109.016404 53

[100] M. Wouters and I. Carusotto. Excitations and superfluidity in non-equilibrium bose-einstein condensates of exciton-polaritons. *Superlattices and Microstructures*. **43** 56 (2008) pp. 524 – 527. doi:http://dx.doi.org/10.1016/j.spmi.2007.07.024.
URL http://www.sciencedirect.com/science/article/pii/S0749603607002303 53

[101] M. Richard, J. Kasprzak, R. André, R. Romestain, L. S. Dang, G. Malpuech and A. Kavokin. Experimental evidence for nonequilibrium bose condensation of exciton polaritons. *Phys. Rev. B*. **72** (2005) p. 201301. doi:10.1103/PhysRevB.72.201301.
URL http://link.aps.org/doi/10.1103/PhysRevB.72.201301 55

[102] M. Wouters and V. Savona. Stochastic classical field model for polariton condensates. *Phys. Rev. B*. **79** (2009) p. 165302. doi:10.1103/PhysRevB.79.165302.
URL http://link.aps.org/doi/10.1103/PhysRevB.79.165302 56

[103] M. Wouters. Synchronized and desynchronized phases of coupled nonequilibrium exciton-polariton condensates. *Phys. Rev. B*. **77** (2008) p. 121302. doi:10.1103/PhysRevB.77.121302.
URL http://link.aps.org/doi/10.1103/PhysRevB.77.121302 57, 99

[104] B. Schaefer, E. Collett, R. Smyth, D. Barrett and B. Fraher. Measuring the Stokes polarization parameters. *Am. J. Phys.*. **75** (2007) pp. 163–168. doi:10.1119/1.2386162.
URL http://dx.doi.org/10.1119/1.2386162 68

[105] J. R. Fienup. Reconstruction of an object from the modulus of its fourier transform. *Optics Letters*. **3** 1 (1978) pp. 27–29. doi:10.1364/OL.3.000027.
URL http://ol.osa.org/abstract.cfm?URI=ol-3-1-27 72

[106] J. R. Fienup. Phase retrieval algorithms: a comparison. *Applied Optics*. **21** 15 (1982) pp. 2758–2769. doi:10.1364/AO.21.002758.
URL http://ao.osa.org/abstract.cfm?URI=ao-21-15-2758 72, 81

[107] V. Elser. Phase retrieval by iterated projections. *Journal of the Optical Society of America A, Optics and Image Science*. **20** 1 (2003) pp. 40–55. doi:10.1364/JOSAA.20.000040.
URL http://josaa.osa.org/abstract.cfm?URI=josaa-20-1-40 72

[108] F. Pfeiffer, T. Weitkamp, O. Bunk and C. David. Phase retrieval and differential phase-contrast imaging with low-brilliance x-ray sources. *Nat Phys*. **4** 2 (2006) pp. 258 – 261. doi:10.1038/nphys265.
URL http://dx.doi.org/10.1038/nphys265 72

[109] W. Coene, G. Janssen, M. Op de Beeck and D. Van Dyck. Phase retrieval through focus variation for ultra-resolution in field-emission transmission electron microscopy. *Physical Review Letters*. **69** (1992) pp. 3743–3746. doi:10.1103/PhysRevLett.69.3743.
URL http://link.aps.org/doi/10.1103/PhysRevLett.69.3743 72

[110] R. A. Gonsalves. Phase retrieval and diversity in adaptive optics. *Optical Engineering*. **21** 5 (1982) pp. 215829–215829–. doi:10.1117/12.7972989.
URL http://dx.doi.org/10.1117/12.7972989 72

[111] A. M. Maiden and J. M. Rodenburg. An improved ptychographical phase retrieval algorithm for diffractive imaging. *Ultramicroscopy*. **109** 10 (2009) pp. 1256 – 1262. doi:http://dx.doi.org/10.1016/j.ultramic.2009.05.012.
URL http://www.sciencedirect.com/science/article/pii/S0304399109001284 72

[112] G. Zheng, R. Horstmeyer and C. Yang. Wide-field, high-resolution fourier ptychographic microscopy. *Nature Photon*. **7** 9 (2013) p. 739745. doi:10.1038/nphoton.2013.187.
URL http://dx.doi.org/10.1038/NPHOTON.2013.187 72

[113] G. Milewski, E. D. and B. J.. Diffractive optical elements designed for highly precise far-field generation in the presence of artifacts typical for pixelated spatial light modulators. *Applied Optics*. **46** 1 (2007) pp. 95–105. doi:http://dx.doi.org/10.1364/AO.46.000095.
URL http://www.opticsinfobase.org/ao/abstract.cfm?uri=ao-46-1-95 72

[114] H. Zhang, J. Xie, J. Liu and Y. Wang. Elimination of a zero-order beam induced by a pixelated spatial light modulator. *Applied Optics*. **48** 30 (2009) pp. 5834 – 5841.
URL http://dx.doi.org/10.1364/AO.48.005834 73

[115] S. Reichelt, R. Häussler, G. Fütterer, N. Leister, H. Kato, N. Usukura and Y. Kanbayashi. Full-range, complex spatial light modulator for real-time holography. *Optics Letters*. **37** 11 (2012) pp. 1955–1957. doi:10.1364/OL.37.001955.
URL http://ol.osa.org/abstract.cfm?URI=ol-37-11-1955 74, 75

[116] S. Reichelt and N. Leister. Computational hologram synthesis and representation on spatial light modulators for real-time 3d holographic imaging. *Journal of Physics: Conference Series*. **415** 1 (2013) p. 012038.
URL http://stacks.iop.org/1742-6596/415/i=1/a=012038 74, 75, 171

[117] W. H. Lee. Sampled fourier transform hologram generated by computer. *Applied Optics*. **9** 3 (1970) pp. 639–643. doi:10.1364/AO.9.000639.
URL http://ao.osa.org/abstract.cfm?URI=ao-9-3-639 75

[118] C. B. Burckhardt. A simplification of lee's method of generating holograms by computer. *Applied Optics*. **9** 8 (1970) pp. 1949–1949. doi:10.1364/AO.9.001949.
URL http://ao.osa.org/abstract.cfm?URI=ao-9-8-1949 75

[119] M. A. Seldowitz, J. P. Allebach and D. W. Sweeney. Synthesis of digital holograms by direct binary search. *Applied Optics*. **26** 14 (1987) pp. 2788–2798. doi:10.1364/AO.26.002788.
URL http://ao.osa.org/abstract.cfm?URI=ao-26-14-2788 75

[120] G. Zhou, Y. Chen, Z. Wang and H. Song. Genetic local search algorithm for optimization design of diffractive optical elements. *Applied Optics*. **38** 20 (1999) pp. 4281–4290. doi:10.1364/AO.38.004281.
URL http://ao.osa.org/abstract.cfm?URI=ao-38-20-4281 75

[121] N. Yoshikawa and T. Yatagai. Phase optimization of a kinoform by simulated annealing. *Applied Optics*. **33** 5 (1994) pp. 863–868. doi:10.1364/AO.33.000863.
URL http://ao.osa.org/abstract.cfm?URI=ao-33-5-863 75

[122] J. Bengtsson. Kinoform design with an optimal-rotation-angle method. *Applied Optics*. **33** 29 (1994) pp. 6879–6884. doi:10.1364/AO.33.006879.
URL http://ao.osa.org/abstract.cfm?URI=ao-33-29-6879 75

[123] C. K. Hsueh and A. A. Sawchuk. Computer-generated double-phase holograms. *Applied Optics*. **17** 24 (1978) pp. 3874–3883. doi:10.1364/AO.17.003874.
URL http://ao.osa.org/abstract.cfm?URI=ao-17-24-3874 75

[124] G. Situ and J. Zhang. A lensless optical security system based on computer-generated phase only masks. *Optics Communications*. **232** 16 (2004) pp. 115 – 122. doi:http://dx.doi.org/10.1016/j.optcom.2004.01.002.
URL http://www.sciencedirect.com/science/article/pii/S0030401804000033 78

[125] H. E. Hwang, C. H. T. and W. N. Lie. Fast double-phase retrieval in fresnel domain using modified gerchberg-saxton algorithm for lensless optical security systems. *Optics Express*. **17** 16 (2009) pp. 13700–13710. doi:10.1364/OE.17.013700.
URL http://www.opticsexpress.org/abstract.cfm?URI=oe-17-16-13700 78

[126] O. Ripoll, V. Kettunen and H. P. Herzig. Review of iterative fourier-transform algorithms for beam shaping applications. *Optical Engineering*. **43** 11 (2004) pp. 2549–2556. doi:10.1117/1.1804543.
URL http://dx.doi.org/10.1117/1.1804543 79, 81, 86

[127] R. W. Gerchberg and W. O. Saxton. A practical algorithm for the determination of the phase from image and diffraction plane pictures. *Optik*. **35** (1972) pp. 237–246. 80

[128] J. R. Fienup. Iterative method applied to image reconstruction and to computer-generated holograms. *Optical Engineering*. **19** 3 (1980) pp. 193297–193297–. doi:10.1117/12.7972513.
URL http://dx.doi.org/10.1117/12.7972513 81

[129] D. Prongué, H. P. Herzig, R. Dändliker and M. T. Gale. Optimized kinoform structures for highly efficient fan-out elements. *Applied Optics*. **31** 26 (1992) pp. 5706–5711. doi:10.1364/AO.31.005706.
URL http://ao.osa.org/abstract.cfm?URI=ao-31-26-5706 81

[130] V. Arrizón, M. Testorf, S. Sinzinger and J. J.. Iterative optimization of phase-only diffractive optical elements based on a lenslet array. *Journal of the Optical Society of America A, Optics and Image Science*. **17** 12 (2000) pp. 2157–2164. doi:10.1364/JOSAA.17.002157.
URL http://josaa.osa.org/abstract.cfm?URI=josaa-17-12-2157 82

[131] M. Pasienski and B. D.. A high-accuracy algorithm for designing arbitrary holographic atom traps. *Optics Express*. **16** 3 (2008) pp. 2176–2190. doi:10.1364/OE.16.002176.
URL http://www.opticsexpress.org/abstract.cfm?URI=oe-16-3-2176 82, 83, 86

[132] A. L. Gaunt and Z. Hadzibabic. Robust digital holography for ultracold atom trapping. *Sci. Rep.*. **2** 721 (2012) pp. 1–5. doi:10.1038/srep0072.
URL http://dx.doi.org/10.1038/srep00721 82, 83

[133] P. Senthilkumaran, F. Wyrowski and H. Schimmel. Vortex stagnation problem in iterative fourier transform algorithms. *Optics and Lasers in Engineering*. **43** 1 (2005) pp. 43 – 56. doi:10.1016/j.optlaseng.2004.06.002.
URL http://www.sciencedirect.com/science/article/pii/S0143816604001423 83

[134] F. Wyrowski. Diffractive optical elements: iterative calculation of quantized, blazed phase structures. *Journal of the Optical Society of America A, Optics and Image Science*. **7** 6 (1990) pp. 961–969. doi:10.1364/JOSAA.7.000961.
URL http://josaa.osa.org/abstract.cfm?URI=josaa-7-6-961 85

REFERENCES

[135] H. Ohadi, R. L. Gregory, T. Freegarde, Y. G. Rubo, A. V. Kavokin and P. G. Lagoudakis. Dissipative phase locking of exciton-polariton condensates. *ArXiv e-prints*. 1406.6377.
URL http://arxiv.org/abs/1406.6377 94, 95, 97, 98, 99, 103, 104

[136] G. Tosi, G. Christmann, N. Berloff, P. Tsotsis, T. Gao, Z. Hatzopoulos, P. Savvidis and J. Baumberg. Geometrically locked vortex lattices in semiconductor quantum fluids. *Nat Commun*. **3** (2012) p. 1243. doi:10.1038/ncomms2255.
URL http://dx.doi.org/10.1038/ncomms2255 104, 110, 111

[137] I. Khalatnikov. Introduction to the Theory of Superfluidity, W.A. Benjamin Inc., New York, Amsterdam 1965. 113

[138] M. Vojta. Quantum phase transitions. *Reports on Progress in Physics*. **66** 12 (2003) p. 2069.
URL http://stacks.iop.org/0034-4885/66/i=12/a=R01 114

[139] M. Wouters, T. C. H. Liew and V. Savona. Energy relaxation in one-dimensional polariton condensates. *Phys. Rev. B*. **82** (2010) p. 245315. doi:10.1103/PhysRevB.82.245315.
URL http://link.aps.org/doi/10.1103/PhysRevB.82.245315 114, 116

[140] L. M. Sieberer, S. D. Huber, E. Altman and S. Diehl. Nonequilibrium functional renormalization for driven-dissipative bose-einstein condensation. *Phys. Rev. B*. **89** (2014) p. 134310. doi:10.1103/PhysRevB.89.134310.
URL http://link.aps.org/doi/10.1103/PhysRevB.89.134310 116

[141] T. K. Paraïso, D. Sarchi, G. Nardin, R. Cerna, Y. Leger, B. Pietka, M. Richard, O. El Daïf, F. Morier-Genoud, V. Savona and B. Deveaud-Plédran. Enhancement of microcavity polariton relaxation under confinement. *Phys. Rev. B*. **79** (2009) p. 045319. doi:10.1103/PhysRevB.79.045319.
URL http://link.aps.org/doi/10.1103/PhysRevB.79.045319 116

[142] G. Franchetti, N. G. Berloff and J. J. Baumberg. Exploiting quantum coherence of polaritons for ultra sensitive detectors. *ArXiv e-prints*. 1210.1187.
URL http://arxiv.org/abs/1210.1187 117

[143] A. Amo, T. C. H. Liew, C. Adrados, R. Houdre, E. Giacobino, A. V. Kavokin and A. Bramati. Exciton-polariton spin switches. *Nat Photon*. **4** 6 (2010) pp. 361–366. doi:10.1038/nphoton.2010.79.
URL http://dx.doi.org/10.1038/nphoton.2010.79 117

[144] D. Sanvitto, S. Pigeon, A. Amo, B. D. D. G. M., I. Carusotto, R. Hivet, F. Pisanello, V. G. Sala, P. S. S. Guimaraes, R. Houdre, E. Giacobino, C. Ciuti, B. A. A. and G. Gigli. All-optical control of the quantum flow of a polariton condensate. *Nat Photon*. **5** 10 (2011) pp. 610–614. doi:10.1038/nphoton.2011.211.
URL http://dx.doi.org/10.1038/nphoton.2011.211 119

[145] F. Veit, M. Amann, M. Bayer, A. Lffler, S. Hfling and A. Forchel. Relaxation dynamics of optically imprinted polariton wires. *Proc. SPIE*. **8260** (2012) pp. 82600O–82600O–7. doi:10.1117/12.906367.
URL http://dx.doi.org/10.1117/12.906367 119

[146] F. Dubin, R. Melet, T. Barisien, R. Grousson, L. Legrand, M. Schott and V. Voliotis. Macroscopic coherence of a single exciton state in an organic quantum wire. *Nat Phys*. **2** 1 (2005) pp. 32–35. doi:10.1038/nphys196.
URL http://dx.doi.org/10.1038/nphys196 126

[147] G. Roumpos, M. Lohse, W. H. Nitsche, J. Keeling, M. H. Szyma?ska, P. B. Littlewood, A. Lffler, S. Hfling, L. Worschech, A. Forchel and Y. Yamamoto. Power-law decay of the spatial correlation function in exciton-polariton condensates. *Proceedings of the National Academy of Sciences*. **109** 17 (2012) pp. 6467–6472. doi:10.1073/pnas.1107970109. http://www.pnas.org/content/109/17/6467.full.pdf+html.
URL http://www.pnas.org/content/109/17/6467.abstract 126, 129

[148] P. W. H. Pinkse, A. Mosk, M. Weidemüller, M. W. Reynolds, T. W. Hijmans and J. T. M. Walraven. Adiabatically changing the phase-space density of a trapped bose gas. *Physical Review Letters*. **78** (1997) pp. 990–993. doi:10.1103/PhysRevLett.78.990.
URL http://link.aps.org/doi/10.1103/PhysRevLett.78.990 131

[149] C. Sun, S. Jia, C. Barsi, S. Rica, A. Picozzi and J. W. Fleischer. Observation of the kinetic condensation of classical waves. *Nat Phys*. **8** 6 (2012) pp. 470–474. doi:10.1038/nphys2278.
URL http://dx.doi.org/10.1038/nphys2278 132

[150] H. Bahlouli, A. D. Alhaidari, A. Al Zahrani and E. N. Economou. Electromagnetic wave propagation in an active medium and the equivalent schrödinger equation with an energy-dependent complex potential. *Phys. Rev. B*. **72** (2005) p. 094304. doi:10.1103/PhysRevB.72.094304.
URL http://link.aps.org/doi/10.1103/PhysRevB.72.094304 132

[151] Z. Vörös, D. W. Snoke, L. Pfeiffer and K. West. Direct measurement of exciton-exciton interaction energy. *Physical Review Letters*. **103** (2009) p. 016403. doi:10.1103/PhysRevLett.103.016403.
URL http://link.aps.org/doi/10.1103/PhysRevLett.103.016403 136, 160

[152] A. Filinov, N. V. Prokof'ev and M. Bonitz. Berezinskii-kosterlitz-thouless transition in two-dimensional dipole systems. *Physical Review Letters*. **105** (2010) p. 070401. doi:10.1103/PhysRevLett.105.070401.
URL http://link.aps.org/doi/10.1103/PhysRevLett.105.070401 136, 161

[153] M. Fleischhauer and M. D. Lukin. Dark-state polaritons in electromagnetically induced transparency. *Physical Review Letters*. **84** (2000) pp. 5094–5097. doi:10.1103/PhysRevLett.84.5094.
URL http://link.aps.org/doi/10.1103/PhysRevLett.84.5094 136, 161

[154] C. Liu, Z. Dutton, C. H. Behroozi and L. V. Hau. Observation of coherent optical information storage in an atomic medium using halted light pulses.. *Nature*. **409** 6819 (2001) pp. 490–3. doi:10.1038/35054017.
URL http://dx.doi.org/10.1038/35054017 136, 161

[155] M. Yanik, W. Suh, Z. Wang and S. Fan. Stopping light in a waveguide with an all-optical analog of electromagnetically induced transparency. *Physical Review Letters*. **93** 23 (2004) pp. 1–4. doi:10.1103/PhysRevLett.93.233903.
URL http://link.aps.org/doi/10.1103/PhysRevLett.93.233903 136, 161

[156] L. V. Butov, A. Ivanov, A. Imamoglu, P. B. Littlewood, A. Shashkin, V. Dolgopolov, K. Campman and A. C. Gossard. Stimulated scattering of indirect excitons in coupled quantum wells: Signature of a degenerate bose-gas of excitons. *Physical Review Letters*. **86** 24 (2001) pp. 5608–5611. doi:10.1103/PhysRevLett.86.5608.
URL http://link.aps.org/doi/10.1103/PhysRevLett.86.5608 136, 142

[157] L. V. Butov. Cold exciton gases in coupled quantum well structures. *Journal of Physics: Condensed Matter*. **19** 29 (2007) p. 295202. doi:10.1088/0953-8984/19/29/295202.
URL http://stacks.iop.org/0953-8984/19/i=29/a=295202 136, 141, 142

[158] A. A. High, J. R. Leonard, A. T. Hammack, M. M. Fogler, L. V. Butov, A. V. Kavokin, K. L. Campman and A. C. Gossard. Spontaneous coherence in a cold exciton gas. *Nature*. **483** 7391 (2012) pp. 584–588. doi:doi:10.1038/nature10903.
URL http://dx.doi.org/10.1038/nature10903 136

[159] A. T. Hammack, N. A. Gippius, S. Yang, G. O. Andreev, L. V. Butov, M. Hanson and A. C. Gossard. Excitons in electrostatic traps. *Journal of Applied Physics*. **99** 6 (2006) p. 066104. doi:10.1063/1.2181276.
URL http://dx.doi.org/10.1063/1.2181276 136

[160] A. A. High, E. E. Novitskaya, L. V. Butov, M. Hanson and A. C. Gossard. Control of exciton fluxes in an excitonic integrated circuit. *Science*. **321** 5886 (2008) pp. 229–231. doi:10.1126/science.1157845. http://www.sciencemag.org/content/321/5886/229.full.pdf.
URL http://www.sciencemag.org/content/321/5886/229.abstract 136, 160

REFERENCES

[161] A. A. High, A. T. Hammack, J. R. Leonard, S. Yang, L. V. Butov, T. Ostatnický, M. Vladimirova, A. V. Kavokin, T. C. H. Liew, K. L. Campman and A. C. Gossard. Spin currents in a coherent exciton gas. *Physical Review Letters*. **110** (2013) p. 246403. doi:10.1103/PhysRevLett.110.246403.
URL http://link.aps.org/doi/10.1103/PhysRevLett.110.246403 136

[162] K. Kristinsson, O. Kyriienko and I. A. Shelykh. Terahertz laser based on dipolaritons. *Phys. Rev. A*. **89** (2014) p. 023836. doi:10.1103/PhysRevA.89.023836.
URL http://link.aps.org/doi/10.1103/PhysRevA.89.023836 136, 162

[163] D. Ahn and S. L. Chuang. Exact calculations of quasibound states of an isolated quantum well with uniform electric field: Quantum-well stark resonance. *Phys. Rev. B*. **34** (1986) pp. 9034–9037. doi:10.1103/PhysRevB.34.9034.
URL http://link.aps.org/doi/10.1103/PhysRevB.34.9034 137

[164] S. Adachi. GaAs, AlAs, and $Al_xGa_{1-x}As$: Material parameters for use in research and device applications. *Journal of Applied Physics*. **58** 3 (1985) pp. R1–R29. doi:10.1063/1.336070.
URL http://dx.doi.org/10.1063/1.336070 137, 151

[165] J. E. Golub, K. Kash, J. P. Harbison and L. T. Florez. Long-lived spatially indirect excitons in coupled GaAs/$Al_xGa_{1-x}As$ quantum wells. *Phys. Rev. B*. **41** (1990) pp. 8564–8567. doi:10.1103/PhysRevB.41.8564.
URL http://link.aps.org/doi/10.1103/PhysRevB.41.8564 142

[166] K. Bergmann, H. Theuer and B. W. Shore. Coherent population transfer among quantum states of atoms and molecules. *Rev. Mod. Phys.*. **70** (1998) pp. 1003–1025. doi:10.1103/RevModPhys.70.1003.
URL http://link.aps.org/doi/10.1103/RevModPhys.70.1003 144, 158, 159, 160

[167] S. I. Tsintzos, P. G. Savvidis, G. Deligeorgis, Z. Hatzopoulos and N. T. Pelekanos. Room temperature GaAs exciton-polariton light emitting diode. *Applied Physics Letters*. **94** 7 071109. doi:10.1063/1.3082093.
URL http://dx.doi.org/10.1063/1.3082093 145, 146, 147

[168] J. L. Jewell, J. P. Harbison, A. Scherer, Y. H. Lee and L. Florez. Vertical-cavity surface-emitting lasers: Design, growth, fabrication, characterization. *IEEE Journal of Quantum Electronics*. **27** 6 (1991) pp. 1332–1346. doi:10.1109/3.89950.
URL http://ieeexplore.ieee.org/xpl/articleDetails.jsp?arnumber=89950 145

[169] J. Szczytko, L. Kappei, J. Berney, F. Morier-Genoud, M. T. Portella-Oberli and B. Deveaud. Determination of the exciton formation in quantum wells from time-resolved interband luminescence. *Physical Review Letters*. **93** (2004) p. 137401. doi:10.1103/PhysRevLett.93.137401.
URL http://link.aps.org/doi/10.1103/PhysRevLett.93.137401 151

[170] C. Coulson, G. Christmann, P. Cristofolini, C. Grossmann, J. J. Baumberg, S. I. Tsintzos, G. Konstantinidis, Z. Hatzopoulos and P. G. Savvidis. Electrically controlled strong coupling and polariton bistability in double quantum wells. *Phys. Rev. B*. **87** (2013) p. 045311. doi:10.1103/PhysRevB.87.045311.
URL http://link.aps.org/doi/10.1103/PhysRevB.87.045311 153, 161

[171] L. V. Butov. Photoluminescence kinetics of indirect excitons in GaAs/$Al_xGa_{1-x}As$ coupled quantum wells. *Physical Review B*. **59** 3 (1999) pp. 1625–1628. 154

[172] L. V. Butov. Condensation and pattern formation in cold exciton gases in coupled quantum wells. *Journal of Physics: Condensed Matter*. **16** 50 (2004) pp. R1577–R1613. doi:10.1088/0953-8984/16/50/R02.
URL http://stacks.iop.org/0953-8984/16/i=50/a=R02 154

[173] S. Yang, A. Mintsev, A. Hammack, L. Butov and A. Gossard. Repulsive interaction in the macroscopically ordered exciton state in GaAs/$Al_xGa_{1-x}As$ coupled quantum well structures. *Physical Review B*. **75** 3 (2007) pp. 1–4. doi:10.1103/PhysRevB.75.033311.
URL http://link.aps.org/doi/10.1103/PhysRevB.75.033311 154

[174] K.-J. Boller, A. Imamolu and S. E. Harris. Observation of electromagnetically induced transparency. *Physical Review Letters*. **66** (1991) pp. 2593–2596. doi:10.1103/PhysRevLett.66.2593.
URL http://link.aps.org/doi/10.1103/PhysRevLett.66.2593 158

[175] L. V. Hau, S. E. Harris, Z. Dutton and C. H. Behroozi. Light speed reduction to 17 metres per second in an ultracold atomic gas. *Nature*. **397** February (1999) pp. 594–598. doi:10.1038/17561.
URL http://dx.doi.org/10.1038/17561 158

[176] N. V. Vitanov, T. Halfmann, B. W. Shore and K. Bergmann. Laser-induced population transfer by adiabatic passage techniques.. *Annual Review of Physical Chemistry*. **52** 1 (2001) pp. 763–809. doi:10.1146/annurev.physchem.52.1.763. pMID: 11326080. http://dx.doi.org/10.1146/annurev.physchem.52.1.763.
URL http://dx.doi.org/10.1146/annurev.physchem.52.1.763 158

[177] J.-J. Su, N. Y. Kim, Y. Yamamoto and A. H. MacDonald. Ferminoic physics in dipolariton condensates. *Physical Review Letters*. **112** (2014) p. 116401. doi:10.1103/PhysRevLett.112.116401.
URL http://link.aps.org/doi/10.1103/PhysRevLett.112.116401 160, 162, 168

[178] M. Mücke, E. Figueroa, J. Bochmann, C. Hahn, K. Murr, S. Ritter, C. J. Villas-Boas and G. Rempe. Electromagnetically induced transparency with single atoms in a cavity. *Nature*. **465** 7299 (2010) pp. 755–758. 161

[179] M. D. Lukin and A. Imamoglu. Controlling photons using electromagnetically induced transparency. *Nature*. **413** 6853 (2001) pp. 273–276. 161

[180] D. F. Phillips, A. Fleischhauer, A. Mair, R. L. Walsworth and M. D. Lukin. Storage of light in atomic vapor. *Physical Review Letters*. **86** (2001) pp. 783–786. doi:10.1103/PhysRevLett.86.783.
URL http://link.aps.org/doi/10.1103/PhysRevLett.86.783 161

[181] D. Møller, L. Madsen and K. Mølmer. Quantum gates and multiparticle entanglement by rydberg excitation blockade and adiabatic passage. *Physical Review Letters*. **100** 17 (2008) pp. 1–4. doi:10.1103/PhysRevLett.100.170504.
URL http://link.aps.org/doi/10.1103/PhysRevLett.100.170504 161

[182] C. Adrados, A. Amo, T. C. H. Liew, R. Hivet, R. Houdré, E. Giacobino, A. V. Kavokin and a. Bramati. Spin rings in bistable planar semiconductor microcavities. *Physical Review Letters*. **105** 21 (2010) pp. 2–5. doi:10.1103/PhysRevLett.105.216403.
URL http://link.aps.org/doi/10.1103/PhysRevLett.105.216403 162

[183] D. Bajoni, E. Semenova, A. Lemaître, S. Bouchoule, E. Wertz, P. Senellart, S. Barbay, R. Kuszelewicz and J. Bloch. Optical bistability in a GaAs-based polariton diode. *Physical Review Letters*. **101** (2008) p. 266402. doi:10.1103/PhysRevLett.101.266402.
URL http://link.aps.org/doi/10.1103/PhysRevLett.101.266402 162

[184] O. Kyriienko, A. V. Kavokin and I. A. Shelykh. Superradiant terahertz emission by dipolaritons. *Physical Review Letters*. **111** (2013) p. 176401. doi:10.1103/PhysRevLett.111.176401.
URL http://link.aps.org/doi/10.1103/PhysRevLett.111.176401 162

[185] O. Kyriienko, I. A. Shelykh and T. C. H. Liew. Tunable single-photon emission from dipolaritons. *Phys. Rev. A*. **90** (2014) p. 033807. doi:10.1103/PhysRevA.90.033807.
URL http://link.aps.org/doi/10.1103/PhysRevA.90.033807 162

[186] H. Ohadi, A. Dreismann, F. Pinsker, P. Cristofolini, R. B. Balili, Z. Hatzopoulos, P. G. Savvidis and J. J. Baumberg. Spontaneous and long-lived antiferromagnetic coupling of exciton-polariton condensates. *Unpublished*. 167

[187] M. Steger, G. Liu, B. Nelsen, C. Gautham, D. W. Snoke, R. Balili, L. Pfeiffer and K. West. Long-range ballistic motion and coherent flow of long-lifetime polaritons. *Phys. Rev. B*. **88** (2013) p. 235314. doi: 10.1103/PhysRevB.88.235314.
URL `http://link.aps.org/doi/10.1103/PhysRevB.88.235314` 167

[188] G. A. Cirino, P. Verdonck, R. D. Mansano, J. C. Pizolato, D. B. Mazulquim and L. G. Neto. Digital Holography: Computer-Generated Holograms and Diffractive Optics in Scalar Diffraction Domain, Holography - Different Fields of Application, InTech 2011. doi:10.5772/21361. 169

[189] B. C. Kress and P. Meyrueis. Digital Diffractive Optics: An Introduction to Planar Diffractive Optics and Related Technology, Wiley 2000. 171

[190] B. E. A. Saleh and M. C. Teich. Fundamentals of Photonics, 2nd Edition, Wiley 2007. iSBN: 978-0-471-35832-9. 178, 179